UNIVERSITÀ DEGLI STUDI DI NAPOLI FEDERICO II

PhD IN CHEMICAL SCIENCES

XXIX CYCLE

A MOLECULAR APPROACH TO STUDY STRUCTURE AND PROPERTIES OF POLYMERS

SUPERVISORS
PROF. CLAUDIO DE ROSA
PROF. FINIZIA AURIEMMA

COORDINATOR
PROF. LUIGI PADUANO

PhD STUDENT
CHIARA SANTILLO

Index

Chapter 2: Crystal Structures of New Polymers obtained from 1,3-dienes with New Catalytic Systems

Chapter 3: Crystalline Block Copolymers prepared by Living Organometallic Catalysts

A molecular approach to study structure and properties of polymers

Description of the thesis work

Understanding the physical and mechanical properties of polymeric materials at molecular level is still a challenge in polymer science and requires a full understanding of the relationships between molecular structure produced by a given polymerization process, crystallization and morphology generated in various processing conditions and mechanical properties.

A possibility to achieve this objective is offered by the development of novel methods of controlled synthesis of polymers that have increased our control over the molecular structure of the produced macromolecules, in terms of molecular masses and their distribution, stereo- and regioregularity, type and distribution of defects and molecular architecture, such as stereospecific polymerization by organometallic catalysis, controlled radical and anionic polymerizations and strategies of combined polymerizations. A real breakthrough has been the development of single-center metallocene and post metallocene catalysts that has allowed expanding the already great versatility of heterogeneous Ziegler-Natta catalysts toward a perfect control of molecular structure of stereoregular polyolefins and polydienes. These systems have afforded a unique opportunity for controlling the final physical properties that can be retro-designed through design of catalyst structure and polymerization method In particular, this possibility has been clearly demonstrated in the case of isotactic and syndiotactic polypropylene and isotactic polybutene.

The main aim of the present project of thesis is to exploit the concept of **retro-design** of the physical properties, that is, to identify the best

molecular architecture, synthetic approach, and processing conditions that ensure to obtain the target properties.

In this thesis were studied materials prepared with different synthetic strategies aimed at producing the desired molecular structure:
a) Organometallic catalysts for polymerization of dienes to stereoregular polydienes and successive hydrogenation for producing novel molecular architectures;
b) Organometallic non-metallocene catalysts for producing semicrystalline block copolymers.

The study of novel systems produced with a new generation of catalysts based on complexes of transition metals and lanthanides with various ligands as phosphines, imines, imino-pyridines, cheto-imines is reported in the **Chapter 1**. These systems are active and stereospecific in the polymerization of dienes, giving highly stereoregular polydienes and a whole series of olefin homopolymers and copolymers from successive hydrogenation reaction. Most of these new polymers cannot be obtained through the simple stereospecific polymerization of the corresponding monomers.
In particular in the **Chapter 2**, the crystal structure of isotactic 1,2-poly((E)-3-methyl-1,3-pentadiene) and the crystal structure of isotactic poly((R,S)-3-methyl-1-pentene) obtained from successive hydrogenation reaction, are presented.
Isotactic 1,2-poly((E)-3-methyl-1,3-pentadiene) is one of the very few examples of crystalline isotactic 1,2-polydienes described in the literature, the other ones being isotactic 1,2-polybutadiene, isotactic 1,2-poly(4-methyl-1,3-pentadiene), and isotactic 3,4-polyisoprene. Moreover, only the

crystal structure of isotactic 1,2-polybutadiene and isotactic 1,2-poly(4-methyl-1,3-pentadiene) are known.

Isotactic poly-(3-methyl-1-pentene) is the ideal example of a polyolefin which can be either chiral, containing a "true" asymmetric atom on the side group, with corresponding optical activity, or not chiral when the two enantiomeric R and S monomeric units are randomly enchained with compensation of the chirality of the lateral groups. Therefore the determination of the crystal structure of random copolymer allowed the study of the effect of the chirality of the lateral groups and the effect of intramolecular chirality compensation on the conformation of the chains and the packing of chains in the crystals.

In **Chapter 3** are presented novel polymeric materials, such as crystalline block copolymers based on isotactic polypropylene (iPP) and polyethylene (PE). This new class of block copolymers has been synthesized only recently thanks to the development of metal-based insertion polymerization methods able to ensure a high stereochemical control in living olefin polymerization.

These systems allow the study of the effect of confinement on the crystallization behavior under different crystallization conditions, and of the relationships between phase separation of incompatible polymer blocks and crystallization. The final morphology of these systems is path dependent, being affected by the competition between crystallization and phase separation.

Moreover, physical properties of these double crystalline block copolymers can be easily tailored by controlling the molecular parameters, such as block lengths, composition etc. The influence of different composition and block lengths on crystallization behavior, morphology and mechanical properties of these systems is examined.

Chapter 1

Characterization of Stereoregular Polydienes and related Hydrogenated Polymers obtained from 1,3-dienes with New Catalytic Systems

1.1 Introduction

The stereospecific polymerization of conjugated dienes with catalysts based on transition metals began in 1954, immediately after the first results obtained for the polymerization of propylene [1]. The first generation of catalysts was obtained by a combination of $TiCl_4$ or $TiCl_3$ with aluminum-alkyls, i.e. catalytic systems previously employed for ethylene and propylene. Subsequently, many other transition metals and lanthanide catalytic systems were proposed and examined, leading to a breakthrough in the field of conjugated diolefin polymerization [1-3].

With the advent of MAO as alkylating agent, at the beginning of the 1980s, new catalytic systems were introduced, in some cases much more active and stereospecific than those based on common aluminum-alkyls [4-7]. In particular, MAO allowed the use of catalyst precursors such as cyclopentadienyl derivatives of transition metals, practically inactive in combination with the normal aluminum-alkyls, providing highly active and stereospecific catalytic systems, also capable of polymerizing monomers such as (Z)-1,3-pentadiene [8-10] and 4-methyl-1,3-pentadiene [11], which could not be polymerized with the common Ziegler-Natta catalysts. Starting from the 2000s, a new generation of catalysts emerged which was based on some complexes of transition metals and lanthanides with various ligands containing donor atoms such as P, N, O (e.g., phosphines, imines, imino-pyridines, cheto-imines) in combination with MAO. These systems have proved particularly active and able to provide polydienes with a

controlled microstructure (i.e., *cis*-1,4; 1,2; mixed *cis*-1,4/1,2 with a variable 1,2 content) [12]. The same systems have also allowed to synthesize novel stereoregular poly(1,3-diene)s from different monomers such as isoprene, 1,3-pentadiene, 1,3-hexadiene, 3-methyl- 1,3-pentadiene, 1,3-heptadiene, 1,3-octadiene, and 5-methyl-1,3-hexadiene [12-14]. These polymers may not be industrially relevant, given the high cost of substituted butadienes, however they were quite interesting from a scientific perspective, indeed, this has allowed to establish connections between the catalyst structure, monomer structure and polymer microstructure, thus obtaining information on the influence of catalyst and monomer structure on the polymerization regio- and stereoselectivity. At the same time, the availability of all these highly stereoregular polymers may allow, to synthesize, via hydrogenation reaction with p-toluenesulfonyl hydrazide, a whole series of olefin homo-and copolymers which were not obtainable through the simple stereospecific polymerization of the corresponding monomers. In particular, by hydrogenation of iso- and syndiotactic cis-1,4 polydienes is it possible to obtain ethylene-α-olefin alternating copolymers (Figure 1.1).

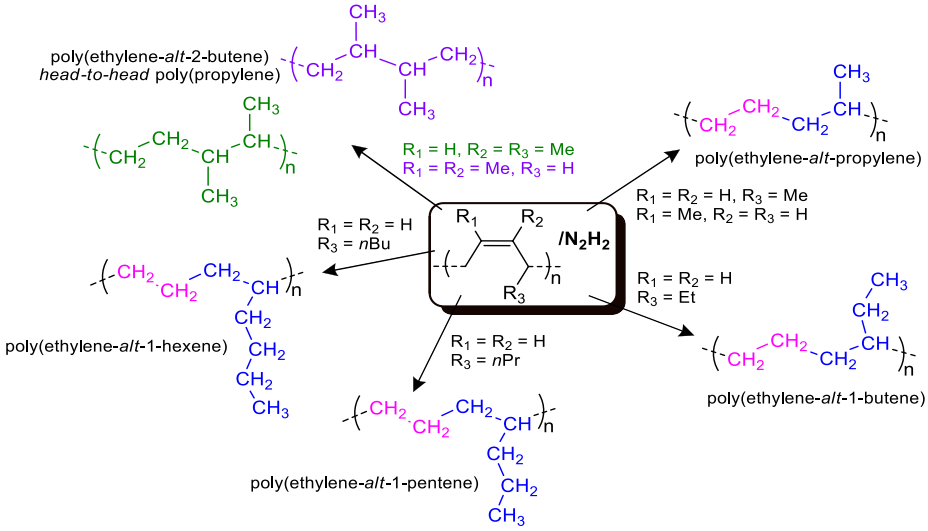

Figure 1.1: Saturated olefin copolymers which can be obtained by hydrogenation of Poly(1,3-diene)s with a 1,4 structure.

Instead, after hydrogenation of stereoregular 1,2 polydienes (isotactic and syndiotactic) novel stereoregular branched polyolefins can be obtained (Figure 1.2).

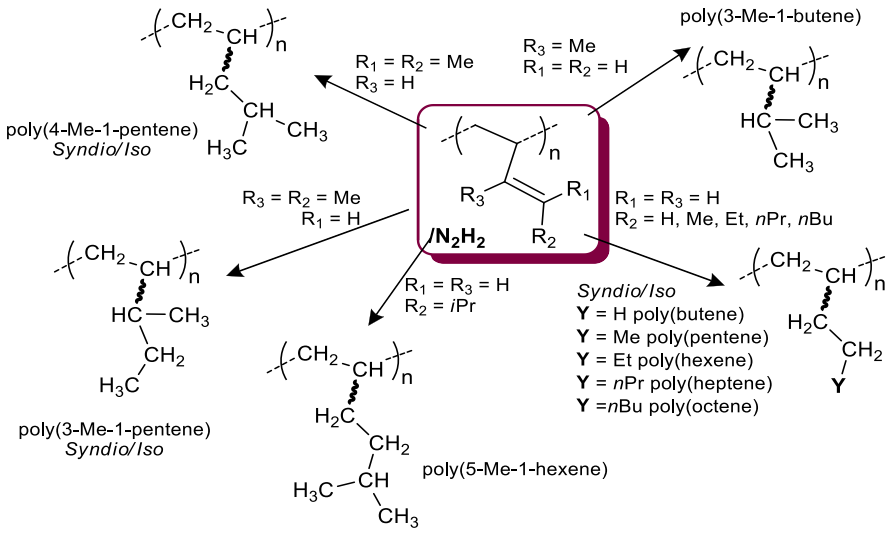

Figure 1.2: Saturated olefin polymers which can be obtained by hydrogenation of Poly(1,3-diene)s with a 1,2 structure.

1.2 Materials

1.2.1 Materials.

All polydienes and hydrogenated polymers studied in this Chapter have been provided by Professor Ricci of the Institute for Macromolecular Studies of the CNR of Milan (CNR-ISMAC). The samples of the studied alternating copolymers, the stereoregular 1,2 polydienes and the branched polyolefins are listed in the Tables 1.1-1.3. The schemes of the hydrogenation reactions and the structures of the studied polymers before and after hydrogenation are shown in the Figure 1.3. Most of the polymers synthesized as described above and reported in the Tables 1.1-1.3 are new polymers, never reported before, or with a new stereochemistry (as the ethylene/2-butene alternating copolymers). A preliminary structural characterization of these materials by X-ray diffraction and DSC is

reported. This analysis has shown that some of the new polymers are crystalline and other are not able to crystallize, notwithstanding the regularity in the constitution and configuration. In the case of the new crystalline polymers, the resolution of the crystal structure has been performed and models of chain conformation and chains packing are reported.

Table 1.1. Code of the hydrogenated alternating copolymers, polymerized monomer, catalytic system, polydienes with a 1,4 structure obtained before hydrogenation and alternating copolymers obtained after hydrogenation reaction of the corresponding polydienes.

Code of hydrogenated polymer	Monomer	Catalyst	Polydiene	Hydrogenated Alternating Copolymer
G1247AcR	1,3-pentadiene	$AlEt_2Cl/Nd(OCOC_7H_{15})_3/Al(^iBu_3)$	isotactic cis-1,4-poly (1,3-pentadiene)	isotactic ethylene/propylene
MM400AcR	1,3-pentadiene	$CoCl_2(P^tBu_2Me)_2$/ MAO	syndiotactic cis-1,4-poly(1,3-pentadiene)	syndiotactic ethylene/propylene
MM166AcR	isoprene	$CoCl_2(P^iPrPh_2)_2$ /MAO	cis-1,4-poly(isoprene)	atactic ethylene/propylene
MM349AcR	(*E*,*E*)-2,4-hexadiene	$AlEt_2Cl/Nd(OCOC_7H_{15})_3/Al(^iBu_3)$	diisotactic trans-1,4-poly(2,4-hexadiene)	racemo-di-isotactic ethylene/2-butene
G1178AcR	(*E*)-3-methyl-1,3-pentadiene	$AlEt_2Cl/Nd(OCOC_7H_{15})_3/Al(^iBu_3)$	isotactic cis-1,4-poly(3-methyl-1,3-pentadiene)	isotactic ethylene/2-butene
MM340AcR	(*E*)-3-methyl-1,3-pentadiene	Ni(acac)2/MAO	syndiotactic cis-1,4-poly(3-methyl-1,3-pentadiene)	syndiotactic ethylene/2-butene
MM352AcR	2,3-dimethyl-1,3-butadiene	$FeCl_2(bipy)_2$/MAO	cis-1,4-poly(2,3 dimethyl-1,3-butadiene)	atactic ethylene/2-butene
MM107	1,3-hexadiene	$AlEt_2Cl/Nd(OCOC_7H_{15})_3/Al(^iBu_3)$	isotactic cis-1,4-poly(1,3-hexadiene)	isotactic ethylene/1-butene
G1181AcR	1,3-octadiene	$AlEt_2Cl/Nd(OCOC_7H_{15})_3/Al(^iBu_3)$	isotactic cis-1,4-poly(1,3-octadiene)	isotactic ethylene/hexene
MM78AcR	1,3-octadiene	$CoCl_2(P^tBu_2Me)_2$/ MAO	syndiotactic cis-1,4-poly(1,3-octadiene)	syndiotactic ethylene/hexene
MM130AcR	isoprene	$CoCl_2(P^iPrPh_2)_2$ /MAO	cis-1,4-alt-3,4 poly(isoprene)	propylene/ethylene/3-methyl-butene terpolymer

Table 1.2. Code of the stereoregular 1,2 polydienes, polymerized monomer, catalytic system and polydienes with a 1,2 structure obtained before hydrogenation.

Code	Monomer	Catalyst	Polydiene
MM151	3-methyl-1,3-pentadiene	$CoCl_2(PnPrPh_2)_2$/ MAO	isotactic 1,2-poly((E)-3-methyl-1,3-pentadiene)
MM152	3-methyl-1,3-pentadiene	$CoCl_2(PMePrPh_2)_2$/ MAO	isotactic 1,2-poly((E)-3-methyl-1,3-pentadiene)

Table 1.3. Code of the hydrogenated branched polyolefins, polymerized monomer; catalytic system; polydienes with a 1,2 or 3,4 structure obtained before hydrogenation, and branched polyolefins obtained after hydrogenation reaction of the respective polydienes.

Code of hydrogenated polymer	Monomer	Catalyst	Polydiene	Hydrogenated Branched Polyolefin
MM183AcR	3-methyl-1,3-pentadiene	$CoCl_2(PnPrPh_2)_2$/ MAO	isotactic 1,2-poly((E)-3-methyl-1,3-pentadiene)	isotactic poly((R,S)-3-methyl-1-pentene)
MM184AcR	3-methyl-1,3-pentadiene	$FeCl_2(bipy)_2$/MAO	syndiotactic 1,2-poly((E)-3-methyl-1,3-pentadiene)	syndiotactic poly((R,S)-3-methyl-1-pentene)
MM412AcR	isoprene	$FeCl_2(bipy)_2$/MAO	syndiotactic 3,4 poly(isoprene)	syndiotactic poly(3-mehyl-butene)

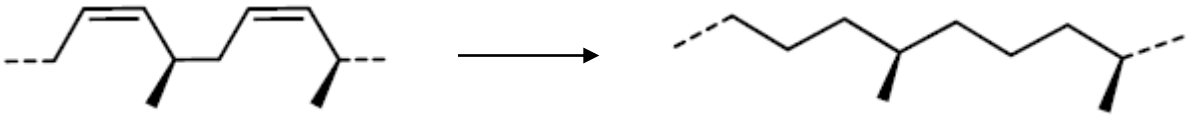

A

isotactic cis-1,4-poly (1,3-pentadiene)

G1247AcR: isotactic ethylene/propylene

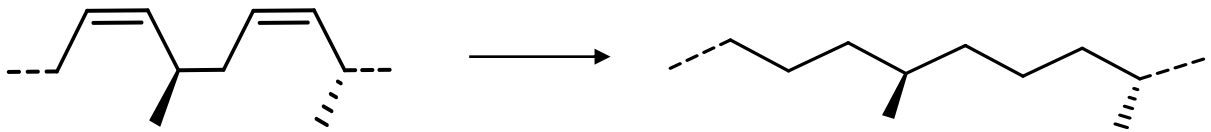

B

syndiotactic cis-1,4-poly(1,3-pentadiene)

MM400AcR: syndiotactic ethylene/propylene

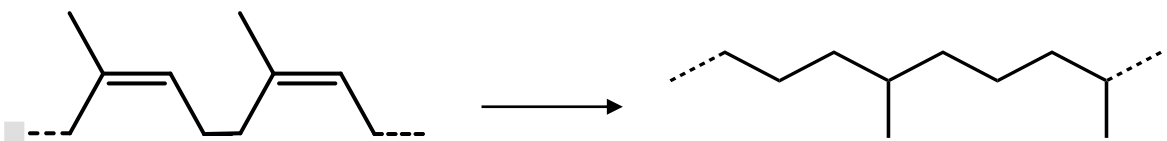

C

cis-1,4-poly(isoprene)

MM166AcR: atactic ethylene/propylene

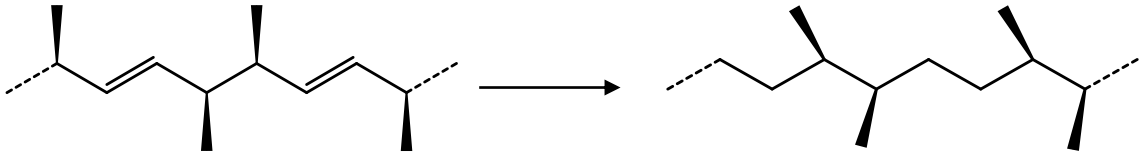

diisotactic trans-1,4-poly(2,4-hexadiene)

MM349AcR: racemo-di-isotactic ethylene/2-butene

D

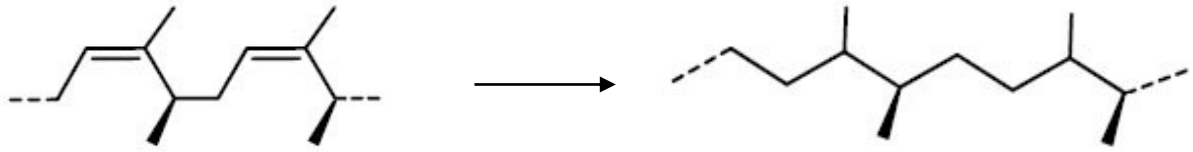

isotactic cis-1,4-poly(3-methyl-1,3-pentadiene)

G1178AcR: isotactic ethylene/2-butene

E

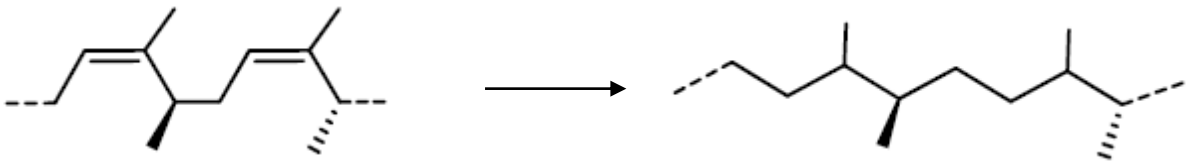

syndiotactic cis-1,4-poly(3-methyl-1,3-pentadiene)

MM340AcR: syndiotactic ethylene/2-butene

F

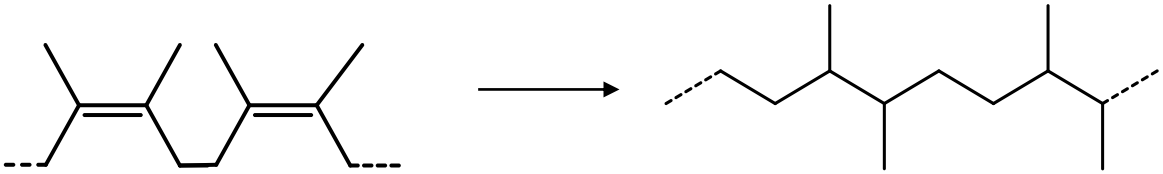

cis-1,4-poly(2,3 dimethyl-1,3-butadiene)

MM352AcR: atactic ethylene/2-butene

G

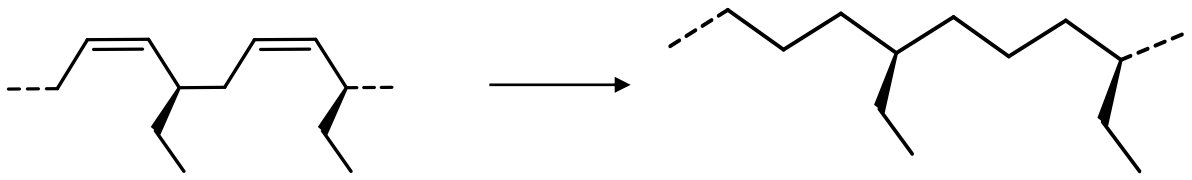

isotactic cis-1,4-poly(1,3-hexadiene)

MM107: isotactic ethylene/1-butene

H

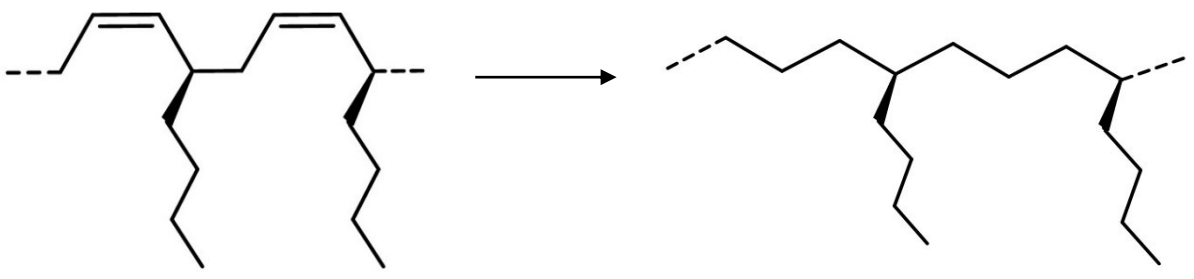

isotactic cis-1,4-poly(1,3-octadiene)

G1181AcR: isotactic ethylene/hexene

I

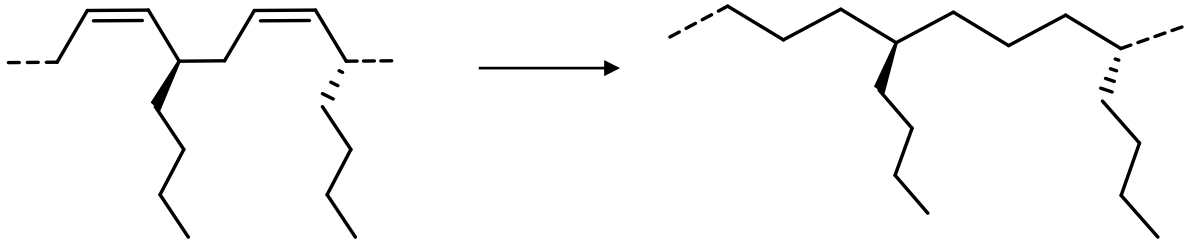

syndiotactic cis-1,4-poly(1,3-octadiene)

MM78AcR: syndiotactic ethylene/hexene

L

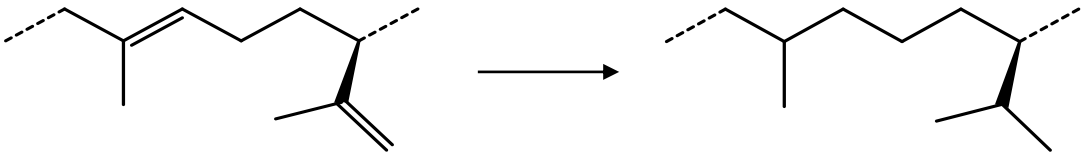

cis-1,4-alt-3,4 poly(isoprene)

MM130AcR: propylene/ethylene/3-methyl-butene terpolymer

M

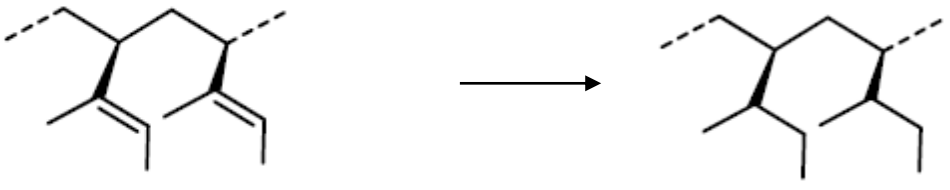

MM151, MM152:
isotactic 1,2-poly((E)-3-methyl-1,3-pentadiene)

MM183AcR:
isotactic poly((R,S)-3-methyl-1-pentene)

N

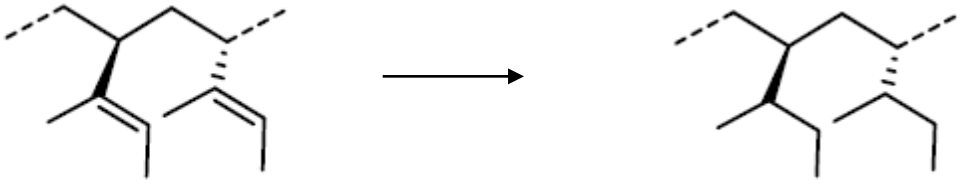

syndiotactic 1,2-poly((E)-3-methyl-1,3-pentadiene) **MM184AcR** syndiotactic poly((R,S)-3-methyl-1-pentene)

O

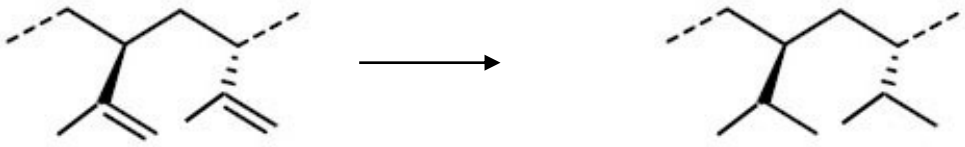

syndiotactic 3,4 poly(isoprene) **MM412AcR**: syndiotactic poly(3-mehyl-butene)

P

Figure 1.3. Schemes of the hydrogenation reactions and structures of the 1,2 or 1,4-polydienes before hydrogenation and of alternating stereoregular copolymers and of stereoregular branched polyolefins obtained after hydrogenation of polydienes.

1.2.2 Polymer characterization.

The as-polymerized samples were characterized by structural and thermal analysis.

X-ray powder diffraction profiles were obtained with Ni-filtered Cu Kα radiation with an automatic Philips diffractometer.

Thermal analysis was performed with a differential scanning calorimeter Mettler Toledo (DSC-822) in a flowing N_2 atmosphere. A scanning rate of 10 °C/min has been used to record the first heating, cooling and second heating scans.

1.3 Structural characterization

1.3.1 Alternating ethylene/propylene copolymers.

The samples of alternating ethylene/propylene copolymer G1247AcR, MM400AcR and MM166AcR have been prepared by hydrogenation of isotactic cis-1,4-poly(1,3-pentadiene), syndiotactic cis-1,4-poly(1,3-pentadiene) and cis-1,4-poly(isoprene), respectively (Figure 1.3 A-C). The precursors stereoregular polydienes, isotactic cis-1,4-poly(1,3-pentadiene), and syndiotactic cis-1,4-poly(1,3-pentadiene), were prepared by polymerization of 1,3-pentadiene with different catalytic sistems, $AlEt_2Cl/Nd(OCOC_7H_{15})_3/Al(^iBu_3)$ and $CoCl_2(P^tBu_2Me)_2/MAO$, respectively. Instead, cis-1,4-poly(isoprene) was prepared by polymerization of isoprene with $CoCl_2(P^iPrPh_2)_2$ /MAO.

In principle, since the hydrogenation reaction of poly(1,3-pentadiene)s does not lead to the formation of new asymmetric carbon atoms, it is reasonable to assume that the tacticity of the diene polymer precursors (isotactic, or syndiotactic) is maintained in the resulting alternating ethylene/propylene copolymers. Therefore, the samples of alternating ethylene/propylene copolymers G1247AcR, MM400AcR and MM166AcR are isotactic, syndiotactic and atactic, respectively (Figure 1.3A-C).

The X-ray powder diffraction profiles of the as-prepared samples G1247AcR, MM400AcR and MM166AcR are reported in Figure 1.4. All as-prepared samples show broad diffraction profiles with absence of Bragg reflections, indicating that all samples are amorphous. The diffraction peaks observed in the X-ray powder diffraction profile of the sample MM400AcR, at values of 2θ =11.7° 13.4° 26.8° and 33.7°, are due to the presence of products resulting from the decomposition of p-toluene-sulfonyl hydrazide utilized for the hydrogenation reaction rather than to the presence of crystallinity in the polymer sample.

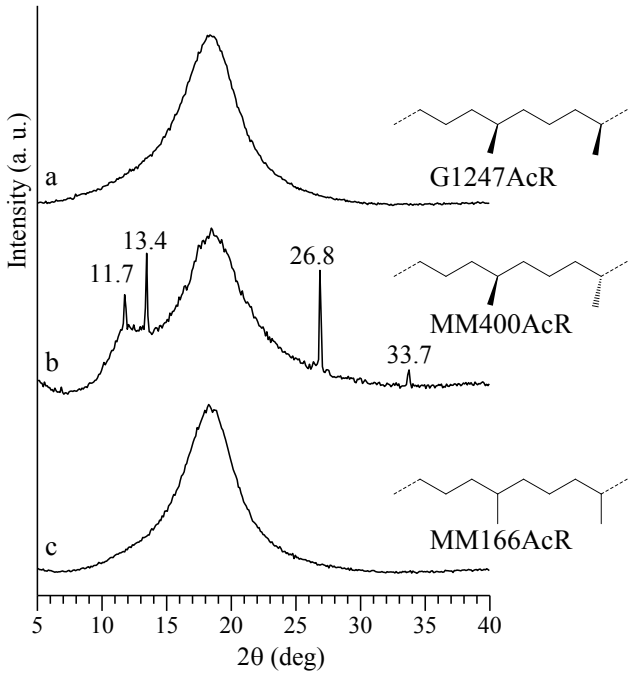

Figure 1.4. X-ray powder diffraction profiles of as-prepared samples of alternating ethylene/propylene copolymers corresponding to the hydrogenated polymers G1247AcR (isotactic ethylene/propylene) (a), MM400AcR (syndiotactic ethylene/propylene) (b) and MM166AcR (atactic ethylene/propylene) (c).

The DSC curves recorded during first heating, successive cooling from the melt and second heating of the melt-crystallized samples, recorded at

scanning rate of 10 °C/min, are reported in Figure 1.5. The DSC curves of the samples G147AcR and MM166AcR show absence of any signal.

The endothermic peaks at 35°C and 73°C observed in the first heating scan of the sample MM400AcR are probably due to traces of products of the hydrogenation reaction still present in the polymer. The successive cooling and second heating scans show absence of exothermic or endothermic phenomena.

Structural and thermal analysis of alternating ethylene/propylene copolymers revealed that all as-prepared samples are amorphous and do not crystallize after cooling from the melt as confirmed from the absence of endothermic peaks in the DSC curves of second heating of the samples. These data indicate that the alternating ethylene/propylene copolymer G147AcR and MM400AcR have a regular stereochemical structure but are not able to crystallize probably for kinetic reason.

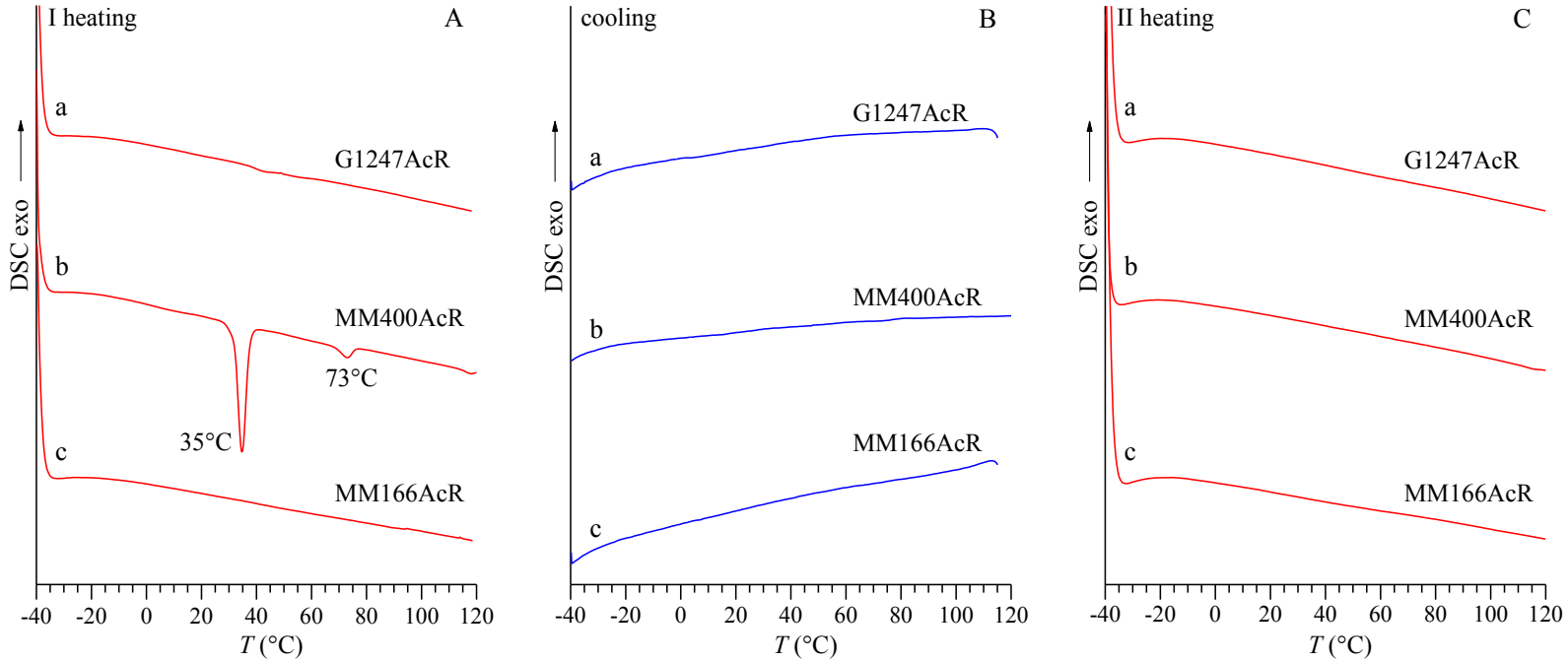

Figure 1.5. DSC curves recorded during first heating (A), successive cooling (B) and second heating scans (C) of as-prepared samples of alternating ethylene/propylene copolymers corresponding to the hydrogenated polymers G1247AcR (isotactic ethylene/propylene) (a), MM400AcR (syndiotactic ethylene/propylene) (b) and MM166AcR (atactic ethylene/propylene) (c). All DSC curves are recorded at scanning rate of 10 °C/min.

1.3.2. Alternating ethylene/2-butene copolymers.

Samples of alternating ethylene/2-butene copolymers of different stereochemistry have been prepared by hydrogenation of diisotactic *trans*-1,4 poly(*E*,*E*-2,4-hexadiene), isotactic and syndiotactic *cis*-1,4 poly(*E*-3-methyl-1,3-pentadiene) and *cis*-1,4-poly(2,3-dimethyl-1,3-butadiene), as shown in Figure 1.3D-G. The precursor polydienes have been prepared with different catalytic systems as shown in the Figure 1.6

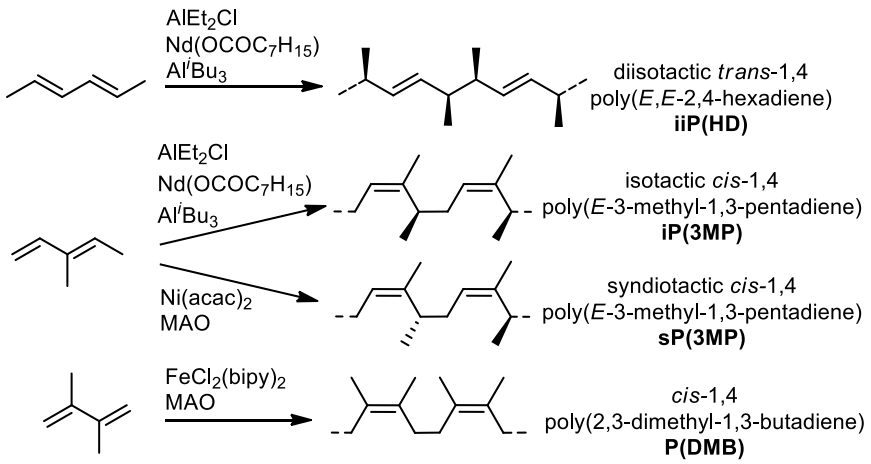

Figure 1.6. Polymerization of (*E*,*E*)-2,4-hexadiene, 3-methyl-1,3-pentadiene, and 2,3-dimethyl-1,3-butadiene.

Diisotactic *trans*-1,4 poly(*E*,*E*-2,4-hexadiene) and isotactic *cis*-1,4 poly(*E*-3-methyl-1,3-pentadiene) were synthesized by polymerizing (*E*,*E*)-2,4-hexadiene and (*E*)-3-methyl-1,3-pentadiene, respectively, with the catalytic system $AlEt_2Cl/Nd(OCOC_7H_{15})_3/Al(^iBu)_3$, syndiotactic *cis*-1,4-poly(*E*-3-methyl-1,3-pentadiene) was obtained by polymerizing (*E*)-3-methyl-1,3-pentadiene with $Ni(acac)_2$/MAO (acac = acetylacetonate), while *cis*-1,4-poly(2,3-dimethyl-1,3-butadiene) was synthesized by polymerizing 2,3-dimethyl-1,3-butadiene with $FeCl_2(bipy)_2$/MAO (bipy = bipyridine) (Figure 1.6).

The poly(1,3-diene)s were hydrogenated with diimide, formed by thermal decomposition of p-toluene-sulfonyl hydrazide (TSH), obtaining four samples of perfectly alternating ethylene/2-butene copolymers of different stereochemistry (samples MM349AcR, G1178AcR, MM340AcR and MM352AcR). In principle, when the hydrogenation reaction does not lead to the formation of new centers of asymmetry, as in the case of the hydrogenation of the diisotactic *trans*-1,4 poly(*E*,*E*-2,4-hexadiene), the tacticity of the starting poly(1,3-diene) (*i.e.,* diisotactic) is maintained in the corresponding saturated polymer, and the sample MM349AcR is, therefore, di-isotactic (Figure 1.3D). In particular, the polymerization of (*E*,*E*)-2,4-hexadiene with the catalytic system $AlEt_2Cl/Nd(OCOC_7H_{15})_3/Al(^iBu)_3$ produces a di-isotactic *trans*-1,4-poly(*E*,*E*-2,4-hexadiene) (Figure 1.6) with a relative *racemo* configuration of two adjacent tetrahedral stereoisomeric centers. The successive hydrogenation of the *racemo*-di-isotactic *trans*-1,4-poly(*E*,*E*-2,4-hexadiene) produces the alternating ethylene/2-butene copolymer with a *racemo*-di-isotactic structure (Figure 1.3D and Figure 1.7A). The *racemo*-di-isotactic alternating ethylene/2-butene copolymer produced by hydrogenation of the di-isotactic *trans*-1,4-poly(*E*,*E*-2,4-hexadiene) (sample MM349AcR) is a novel stereoregular polymer never reported before.[15]

In the other three samples, instead, the hydrogenation leads to the formation of new chiral carbons, resulting in the formation of two adjacent tetrahedral stereoisomeric centers (Figure 1.3E-G), and the hydrogenated polymers are substantially atactic for the new chiral carbon, as expected, given the non-stereoselective nature of the hydrogenation reaction with TSH, while the stereoregularity of the second carbon (isotactic or syndiotactic) is maintained. Therefore, the samples G1178AcR and MM340AcR are isotactic and syndiotactic, respectively, for one of the two adjacent

tetrahedral stereoisomeric centers and atactic for the second one (Figure 1.7B,C), and the sample MM352AcR is atactic for both the two adjacent tetrahedral stereoisomeric centers (Figure 1.7D). This stereochemistry of the four different alternating ethylene/2-butene copolymers has been confirmed by NMR analysis [15].

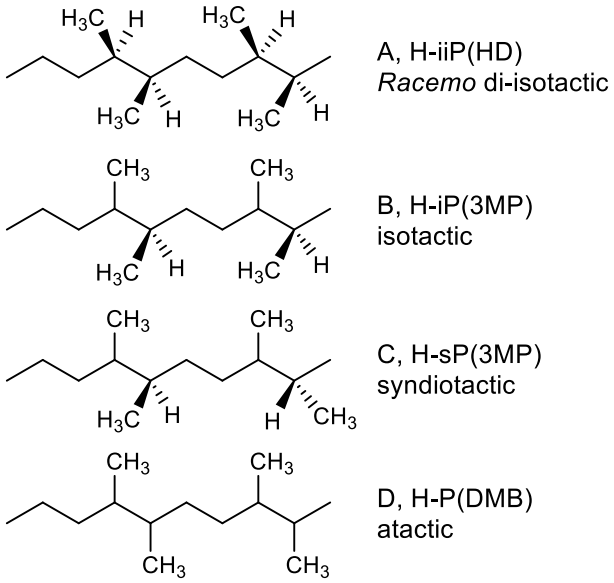

Figure 1.7. Molecular structures of the hydrogenated polymers and corresponding stereochemistry: A) MM349AcR is *racemo*-di-isotactic; B) G1178AcR is isotactic for one of the two adjacent tetrahedral stereoisomeric centers and atactic for the second one; C) MM340AcR is syndiotactic for one of the two adjacent tetrahedral stereoisomeric centers and atactic for the second one; D) MM352AcR is atactic for both the two adjacent tetrahedral stereoisomeric centers

The X-ray powder diffraction profiles and the DSC thermograms of as-prepared samples of the four samples of alternating ethylene/2-butene copolymers are reported in Figure 1.8 and Figure 1.9, respectively. It is apparent that all samples show broad diffraction profiles with absence of Bragg reflections, indicating that all samples are amorphous (Figure 1.8). The diffraction patterns do not change upon thermal treatments, and the samples do not crystallize even after annealing at relatively high temperatures. According to the X-ray diffraction profiles, in the DSC

curves recorded during first heating successive cooling and second heating, only the glass transition is observed (Figure 1.9). The samples G1178AcR MM340AcR and MM352AcR show a glass transition at nearly −20 °C, whereas the sample MM349AcR shows a glass transition at nearly −29 °C. Only the glass transition at the same temperatures is observed in the successive cooling scans with absence of exothermic signals.

The endothermic peak at 73°C visible in the first heating scan of the sample MM349AcR is due to the presence of impurities in the sample such as the diimide utilized in the hydrogenation reaction. This peak disappears in the DSC thermogram recorded during second heating.

As expected from the structures of Figure 1.7, the atactic polymers G1178AcR, MM340AcR and MM352AcR are not able to crystallize, even when one of the two adjacent tetrahedral stereoisomeric centers has a regular succession of configurations, isotactic (sample G1178AcR) or syndiotactic (sample MM340AcR).

Contrary to the *meso*-di-isotactic alternating ethylene/2-butene copolymer prepared with Ziegler-Natta catalysts from the copolymerization of ethylene with *cis*-2-butene [16–19], which is a crystalline polymer melting at 130–135 °C.[16-20], the *racemo*-di-isotactic ethylene/2-butene copolymer (sample MM349AcR) is not able to crystallize, notwithstanding the regular relative configurations of two adjacent tetrahedral stereoisomeric centers (*racemo*), and the regular succession of configurations, di-isotactic, of successive monomeric units along the chain. This is probably related to the fact that the conformation of the *racemo*-di-isotactic copolymer is different from the $(T_3G^+T_3G^-)_n$ of the *meso*-di-isotactic copolymer, although this conformation is energetically feasible also for the *racemo*-di-isotactic structure. [16,20,21] In fact, the conformation of the chains of the *racemo*-di-isotactic alternating ethylene/2-butene copolymer would be helical with succession of torsion

angles $(TTTG^{+})_n$ that is, probably, not able to crystallize for packing or kinetics reasons.

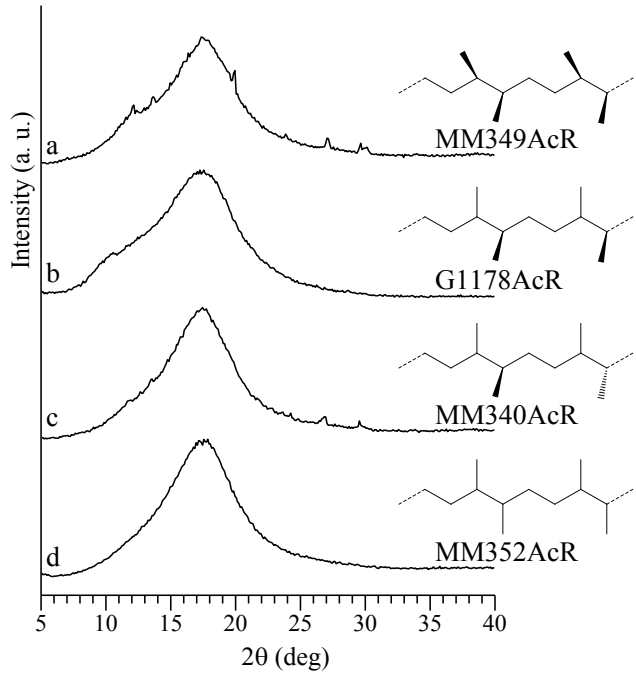

Figure 1.8. X-ray powder diffraction profiles of as-prepared samples of alternating ethylene/2-butene copolymers corresponding to the hydrogenated polymers MM349AcR (racemo di-isotactic ethylene/2-butene) (a), G1178AcR (isotactic ethylene/2-butene) (b), MM340AcR (syndiotactic ethylene/2-butene) (c) and MM352AcR (atactic ethylene/2-butene) (d).

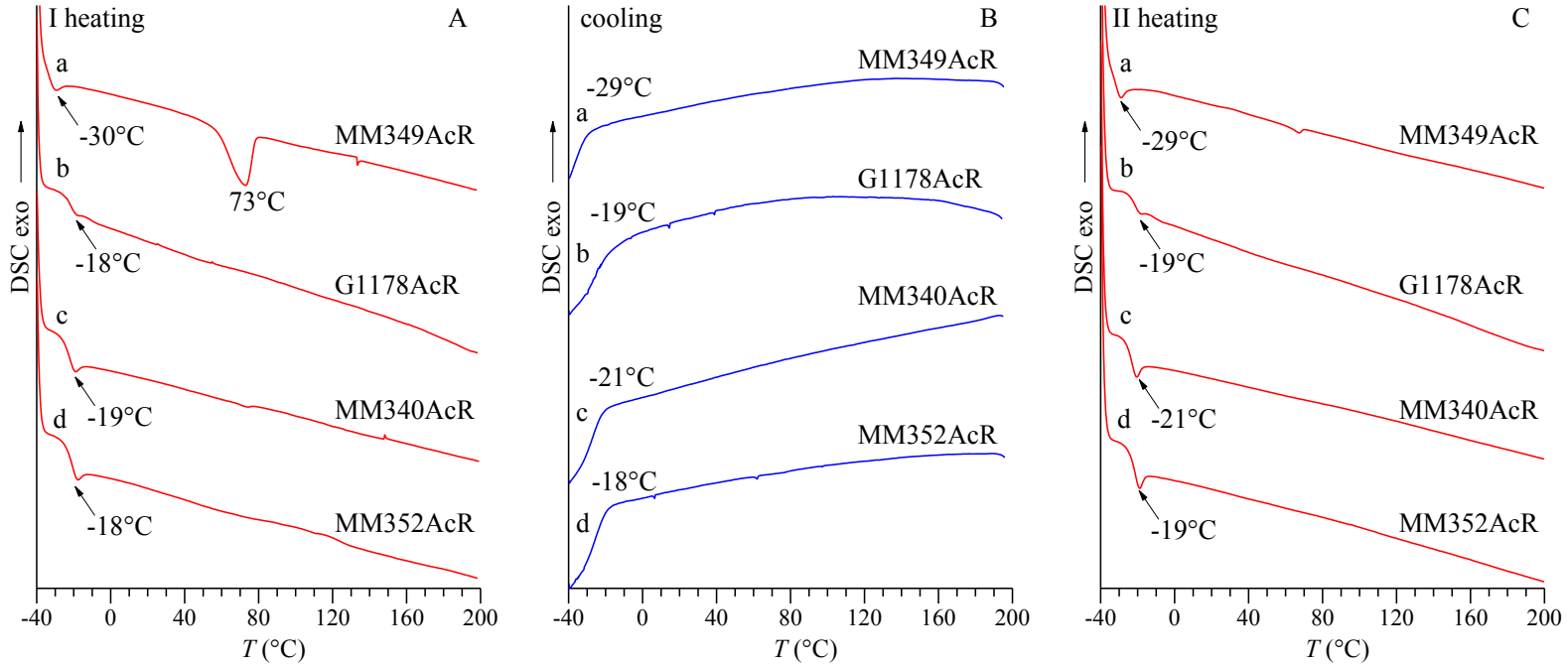

Figure 1.9. DSC curves recorded during first heating (A), successive cooling (B) and second heating scans (C) of as-prepared samples of alternating ethylene/2-butene copolymers corresponding to the hydrogenated polymers MM349AcR (racemo di-isotactic ethylene/2-butene) (a), G1178AcR (isotactic ethylene/2-butene) (b), MM340AcR (syndiotactic ethylene/2-butene) (c) and MM352AcR (atactic ethylene/2-butene) (d). All DSC curves have been recorded at scanning rate of 10 °C/min.

1.3.3 Alternating ethylene/1-butene copolymer.

The alternating isotactic ethylene/1-butene copolymer (MM107) was obtained from hydrogenation of isotactic cis-1,4-poly(1,3-hexadiene) (Figure 1.3H), which was prepared polymerizing 1,3-hexadiene with the catalytic system $AlEt_2Cl/Nd(OCOC_7H_{15})_3/Al(^iBu_3)$.

The X-ray diffraction profile of the as-prepared sample MM107 is shown in Figure 1.10, and the DSC curves recorded during first heating, successive cooling from the melt and second heating of the melt-crystallized samples, recorded at scanning rate of 10 °C/min, are reported in Figure 1.11.

Both X-ray diffraction and DSC data indicate the absence in this sample of a non-negligible crystallinity.

The sample MM107 does not crystallize after annealing or cooling from high temperature as confirmed from the absence of exothermic peaks or endothermic peaks in the DSC cooling and heating curves.

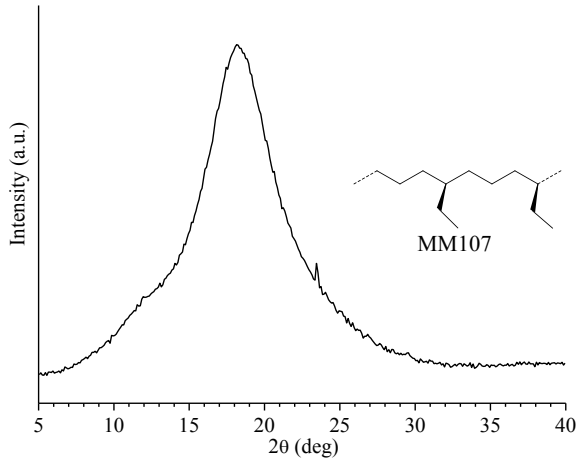

Figure 1.10. X-ray powder diffraction profile of as-prepared sample MM107 (alternating ethylene/1-butene copolymer).

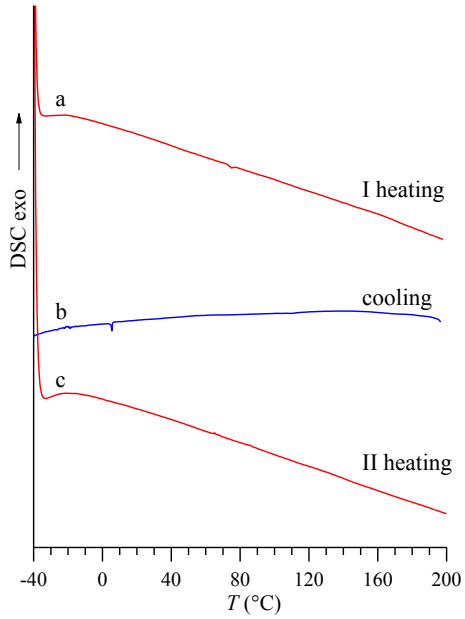

Figure 1.11. DSC curves recorded during first heating (a), successive cooling (b) and second heating scans (c) of as-prepared sample MM107 (alternating ethylene/1-butene copolymer). All DSC curves have been recorded at scanning rate of 10 °C/min.

1.3.4 Alternating ethylene/hexene copolymers.

The X-ray powder diffraction profiles of the samples of isotactic ethylene/hexene alternating copolymer (G1181AcR) and syndiotactic ethylene/hexene alternating copolymer (MM78AcR) are reported in Figure 1.12. These copolymers were obtained after hydrogenation of isotactic and syndiotactic cis-1,4-poly(1,3-octadiene), respectively (Figure 1.3 I, L), which were synthetized polymerizing 1,3-octadiene with $AlEt_2Cl/Nd(OCOC_7H_{15})_3/Al(^iBu_3)$ and $CoCl_2(P^tBu_2Me)_2/MAO$ respectively. The isotactic alternating ethylene/hexene copolymer show broad diffraction profile with absence of Bragg reflections, indicating that the sample is amorphous.

The X-ray diffraction profile of the sample MM78AcR of the alternating syndiotactic ethylene/hexene copolymer presents reflections due probably only to the presence of impurities in the sample. However, we cannot exclude the presence of some crystallinity due to the polymer.

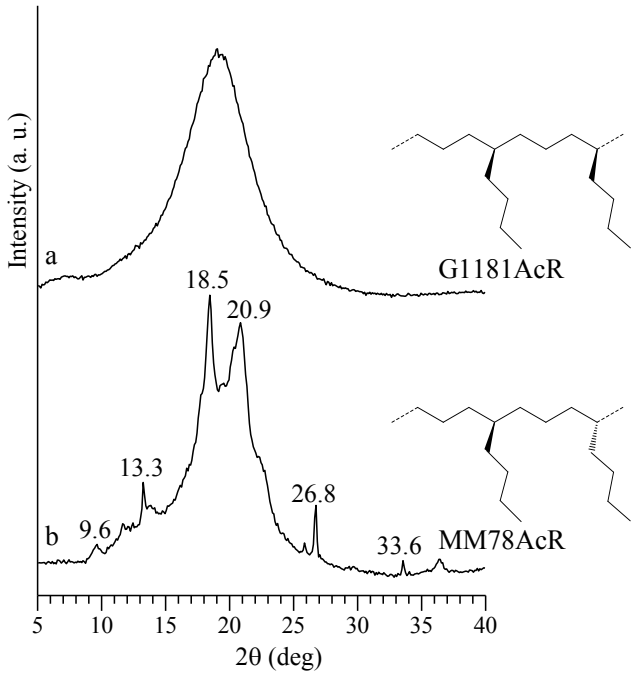

Figure 1.12. X-ray powder diffraction profiles of as-prepared samples of alternating ethylene/hexene copolymers corresponding to the hydrogenated polymers G1181AcR (isotactic ethylene/hexene) (a) and MM78AcR (syndiotactic ethylene/hexene) (b).

The DSC curves of the as-prepared samples of alternating ethylene/hexene copolymers are shown in Figure 1.13. The first heating curve, the successive cooling and second heating scans, acquired at scanning rate of 10°C/min, are reported. This data confirm that the copolymer G1181AcR is amorphous and do not crystallize even after cooling from high temperature.

In the first DSC heating curve of the as-received sample MM107, several endothermic peaks at temperatures between 30°C and 70°C and one exothermic peak at 187°C, are present. As discussed above, the presence of these peaks may be attributable, probably, to the presence of diimide in the sample. In the successive cooling from the melt no crystallization phenomena are observed and the DSC curve recorded during second heating show absence of any signal.

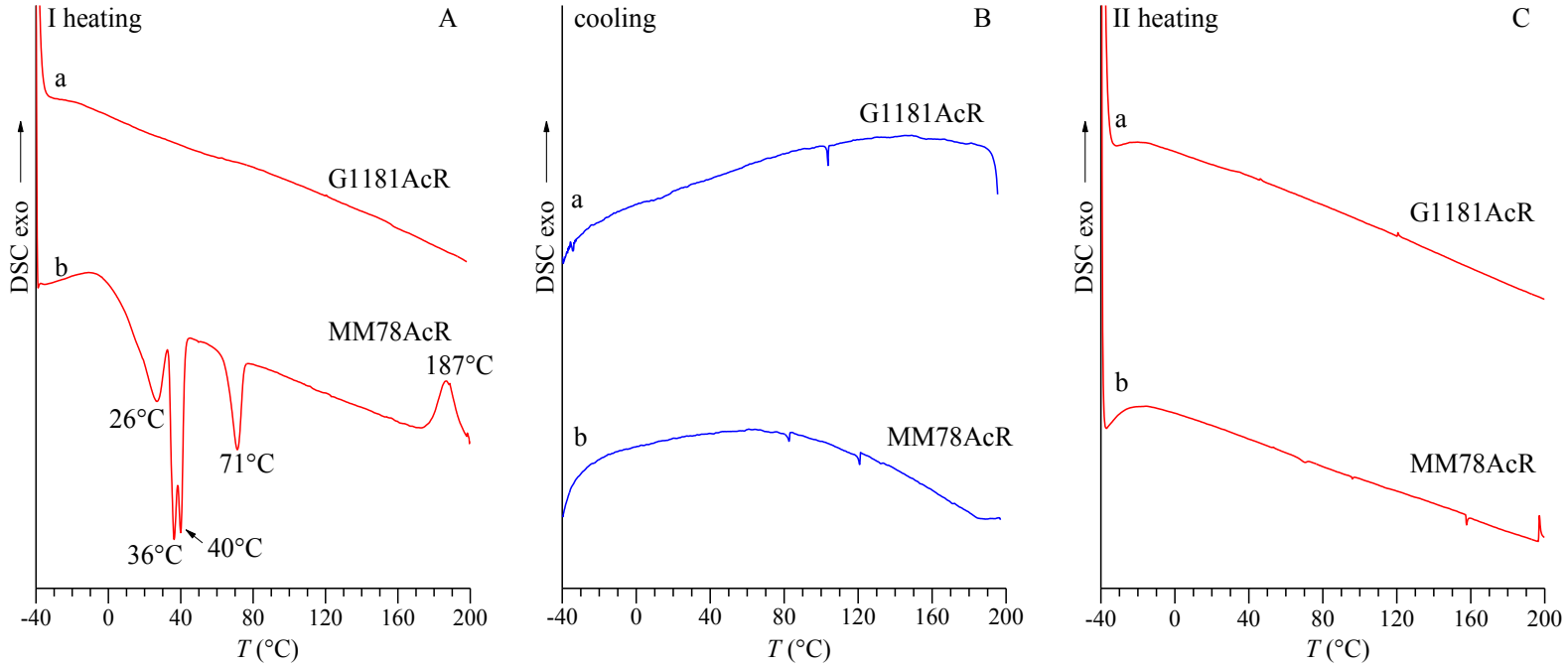

Figure 1.13. DSC curves recorded during first heating (A), successive cooling (B) and second heating scans (C) of as-prepared samples of alternating ethylene/hexene copolymers corresponding to the hydrogenated polymers G1181AcR (isotactic ethylene/hexene) (a) and MM78AcR (syndiotactic ethylene/hexene) (b). All DSC curves have been recorded at scanning rate of 10 °C/min.

1.3.5 Propylene/ethylene/3-methyl-butene copolymer.

The polymerization of isoprene with system $CoCl_2(P^iPrPh_2)_2$/MAO leads to the formation of cis-1,4-alt-3,4-poly(isoprene) [13]. The successive hydrogenation reaction with diimide of cis-1,4-alt-3,4-poly(isoprene) provides the alternating propylene/ethylene/3-methyl-butene terpolymer (Figure 1.3M) (sample MM130AcR). The X-ray powder diffraction profile of as-prepared sample is reported in Figure 1.14 whereas, the curves resulting from DSC analysis are presented in Figure 1.15. It is apparent from the diffraction profile that the as-prepared sample is amorphous and the DSC curves, recorded during first heating successive cooling and second heating scans, show only a glass transition at nearly -13°C confirming the absence of crystallinity.

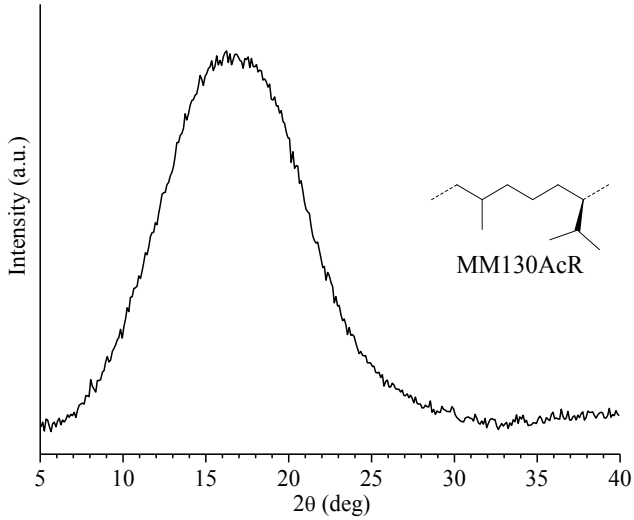

Figure 1.14. X-ray powder diffraction profiles of as-prepared sample MM130AcR (propylene/ethylene/3-methyl-butene terpolymer).

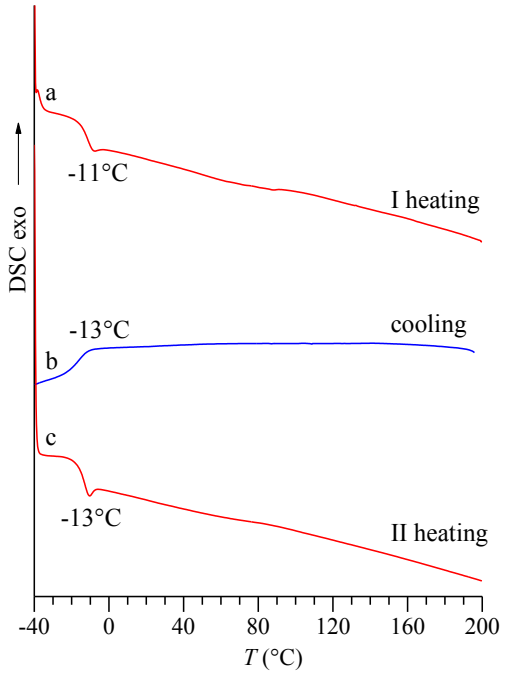

Figure 1.15. DSC curves recorded during first heating (a), successive cooling (b) and second heating scans (c) of as-prepared sample MM130AcR (propylene/ethylene/3-methyl-butene terpolymer). All DSC curves have been recorded at scanning rate of 10 °C/min.

1.3.6 Isotactic 1,2-poly((E)-3-methyl-1,3-pentadiene).

The isotactic 1,2-poly((*E*)-3-methyl-1,3-pentadiene) is obtained by polymerizing 3-methyl-1,3-pentadiene with the catalytic systems $CoCl_2(PRPh_2)_2$/MAO (R = methyl, ethyl, n-propyl, isopropyl and cyclohexyl) [22]. The synthesis and a preliminary characterization of this new polymer has been reported recently in the licterature [22]. The complexes $CoCl_2(PRPh_2)_2$ in combination with MAO were found to be highly active and stereoselective for the 1,2-polymerization of various dienes (e.g., butadiene, 1,3-pentadiene, 1,3-hexadiene, 1,3-heptadiene, 1,3-octadiene and 5-methyl-1,3-hexadiene). [6,9] The same catalytic systems promote the polymerization of 3-methyl-1,3-pentadiene, giving a polymer with an essentially isotactic E-1,2-structure.[22] The isotactic content was found to depend on the type of catalyst used (i.e., type of phosphine ligand

bonded to the cobalt atom). The polymers obtained with the catalytic systems having minimally hindered ligands (e.g., PMePh2, PEtPh2, PnPrPh2) were found to be highly crystalline and highly isotactic ([mm] ≥ 90%).[22]

In particular, the samples MM151 and MM152 were synthesized, with the catalytic sistems $CoCl_2(PnPh_2)_2$/MAO (nP = n-propyl) and $CoCl_2(PMePh_2)_2$/MAO (Me = methyl) respectively.

The molecular characteristics of the samples are reported in Table 1.4.

Both samples are highly regular with concentration of 1,2 units of 99%, and highly isotactic, with concentration of mm tried higher than 90 % [22].

Table 1.4. Molecular characteristics of the samples of the isotactic 1,2 ((*E*)-3-methyl-1,3-pentadiene). Catalytic system; percentage of 1,2 units, concentration of mm triad ([mm]), molecular weight (M_w) and index of polydispersity (M_w/M_n). [22]

Code	**Catalyst**	**1,2 %**[a]	**[mm] %**[a]	M_w **(g mol^{-1})**[b]	M_w/M_n[b]
MM151	$CoCl_2(PnPrPh_2)_2$/ MAO	~99	≥ 90	81 000	1.2
MM152	$CoCl_2(PMePrPh_2)_2$/ MAO	~99	≥ 90	89 000	1.2

a. The content of 1,2 units and the content of mm triads have been determined by ^{13}CNMR.
b. Determined by GPC [22].

The X-ray powder diffraction profiles of as- prepared samples MM151 and MM152 are reported in Figure 1.16. The polymers are crystalline and show similar diffraction profiles.

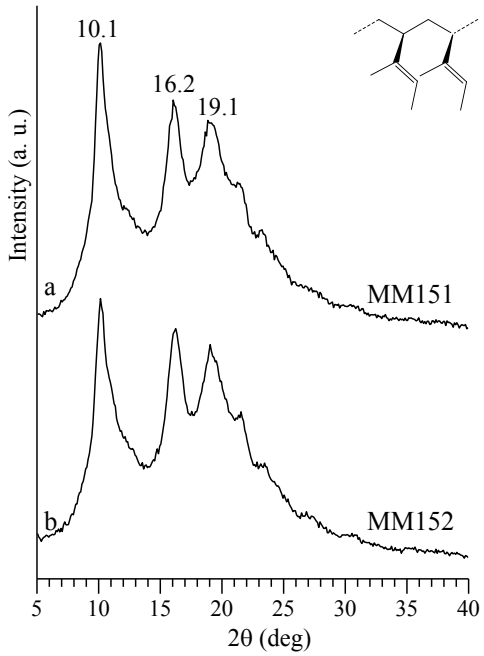

Figure 1.16. X-ray powder diffraction profiles of as-prepared samples MM151 (a) and MM152 (b) of isotactic 1,2-poly((*E*)-3-methyl-1,3-pentadiene) obtained with $CoCl_2(PnPrPh_2)_2$/MAO (a) and with $CoCl_2(PMePrPh_2)_2$/MAO (b) catalytic systems.

The DSC curves recorded during first heating, successive cooling from the melt and second heating of the melt-crystallized samples, recorded at scanning rate of 10 °C/min, are reported in Figure 1.17.

The sample MM151 shows in the first heating scan two endothermic peaks at 93 °C and 110 °C, whereas, the sample MM152 shows two endothermic peaks at higher temperatures, 101 °C and 122 °C.

The presence of more than one endothermic peak in the heating scans of as-prepared samples could be explained by the presence of different sizes or by occurrence of recrystallization phenomena during heating.

The samples MM151 and MM152 do not crystallize after cooling from the melt, in fact only the glass transition at about 30°C is observed in DSC curves recorded during cooling and second heating.

In the Chapter 2 the resolution of the crystal structure of the isotactic 1,2-poly((*E*)-3-methyl-1,3-pentadiene) from X-ray diffraction data is described.

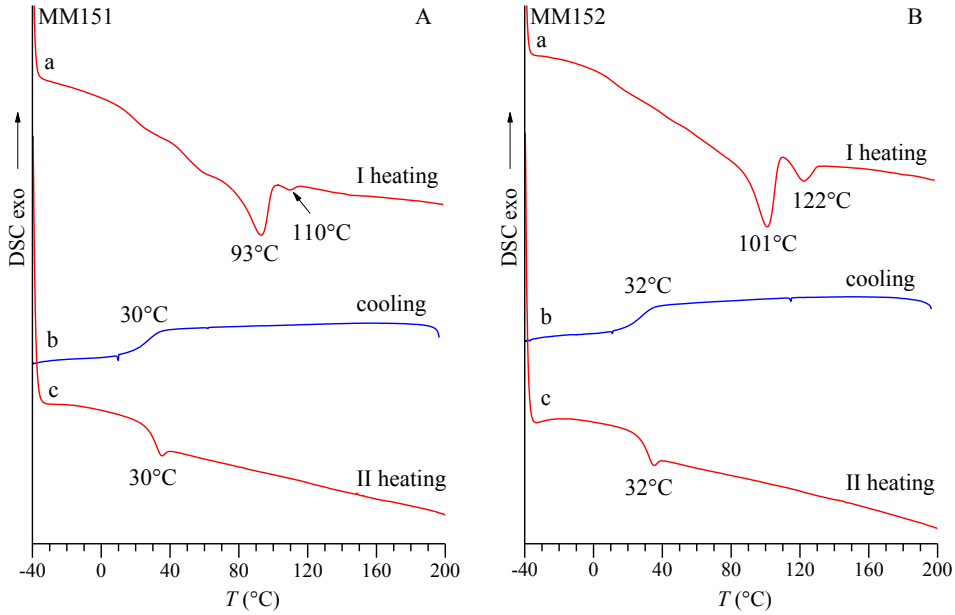

Figure 1.17. DSC curves recorded during first heating (a), successive cooling (b) and second heating scans (c) of as-prepared samples of isotactic 1,2-poly((*E*)-3-methyl-1,3-pentadiene) corresponding to the stereoregular 1,2 polydienes MM151 obtained with $CoCl_2(P^nPrPh_2)_2$/MAO catalytic system (A) and MM152 obtained with $CoCl_2(PMePrPh_2)_2$/MAO catalytic system (B). All DSC curves have been recorded at scanning rate of 10 °C/min.

1.3.7 Isotactic poly((R,S)-3-methyl-1-pentene).

The hydrogenation reaction of isotactic 1,2-poly((*E*)-3-methyl-1,3-pentadiene) with *p*-toluenesulfonyl hydrazide, preserves the isotactic configuration of the backbone, but leads to the formation of a new stereoisomeric carbon on the site chains (Figure 1.3N). Due to the non stereospecificity of the hydrogenation reaction the new asymmetric carbon in the successive monomeric units assume statistical *R*/*S* configurations (Figure 1.3N). This procedure has allowed for the first time the preparation of a purely random copolymer of the two enantiomeric (*R*) and (*S*)-3-

methyl-1-pentene monomers. In fact, using heterogeneous Ziegler_Natta catalyst, starting from a mixture of *R* and *S* 3-methyl-1-pentene monomers, only the monomer with S configuration was polymerized and only the isotactic poly((*S*)-3-methyl-1-pentene) has been reported in the literature [23-25].

X-ray powder diffraction profile of the as-prepared sample MM183AcR of isotactic poly((*R*,*S*)-3-methyl-1-pentene) is reported in Figure 1.18. The profile is characterized by two strong, sharp, and very close reflections at 2θ = 9.5° and 10.4° and a strong reflection at 2θ = 16.6° indicating that the sample is crystalline.

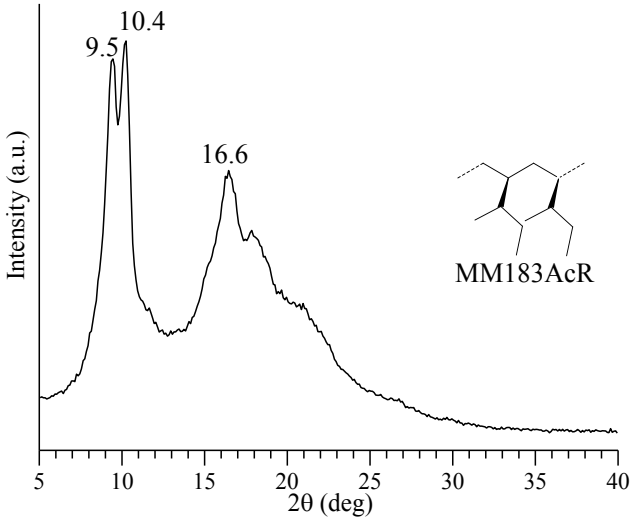

Figure 1.18. X-ray powder diffraction profiles of as-prepared sample MM183AcR of isotactic poly((*R*,*S*)-3-methyl-1-pentene).

The DSC heating curve of the as-polymerized sample MM183AcR, the successive cooling curve from the melt to low temperature, and the successive heating curve of the melt-crystallized sample are reported in Figure 1.19. The as-polymerized sample is crystalline with melting temperature of 198 °C and crystallizes from the melt by cooling at 10

°C/min at nearly 160 °C. A glass transition temperature of about 43 °C has been evaluated in both heating and cooling DSC scans.

In the Chapter 2 the resolution of the crystal structure of the isotactic poly((*R*,*S*)-3-methyl-1-pentene) is reported [26, 27].

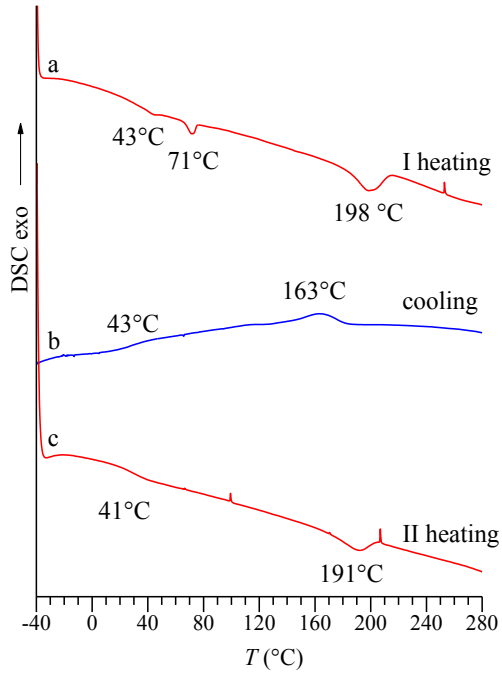

Figure 1.19. DSC curves recorded during first heating (a), successive cooling (b) and second heating scans (c) of as-prepared sample MM183AcR of isotactic poly((R,S)-3-methyl-1-pentene). All DSC curves have been recorded at scanning rate of 10 °C/min.

1.3.8 Syndiotactic poly((R,S)-3-methyl-1-pentene.

Another new polymer is the syndiotactic poly((*R*,*S*)-3-methyl-1-pentene) sample (MM184AcR) obtained by hydrogenation of syndiotactic 1,2-poly((*E*)-3-methyl-1,3-pentadiene) (Figure 1.3 O) which in turn was prepared polymerizing 3-methyl-1,3-pentadiene with the catalytic system $Fe(bipy)_2Cl_2$/MAO (bipy = bipyridine). Therefore, polymerizing 3-methyl-1,3-pentadiene with different systems as $CoCl_2(PRPh_2)_2$/MAO and $Fe(bipy)_2Cl_2$/MAO (bipy = bipyridine), stereoregular 1,2 poly(3-methyl pentadiene) isotactic and syndiotatic, respectively have been obtained. The

successive hydrogenation allowed the preparation of isotactic (section 1.3.7) and syndiotactic poly((*R*,*S*)-3-methyl-1-pentene) (Figure 1.3 N, O). The X-ray diffraction profile of the sample MM184AcR of syndiotactic poly((*R*,*S*)-3-methyl-1-pentene) is reported in Figure 1.20. The profile is characterized by two halos centered at 2θ = 11° and 19° indicating absence of crystallinity.

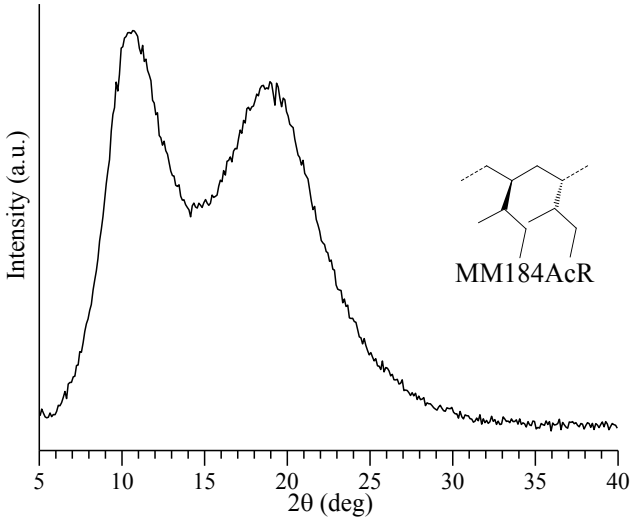

Figure 1.20. X-ray powder diffraction profiles of as-prepared sample MM184AcR (syndiotactic poly((R,S)-3-methyl-1-pentene)).

The DSC curves of first heating, successive cooling, and second heating, reported in Figure 1.21, give the same information of absence of crystallinity. The small endothermic peaks observed at low temperatures in the first heating curve, are probably due to the presence of impurities in the as-received sample. In the successive cooling at low temperature and in the second heating curve, absence of any signal was observed.

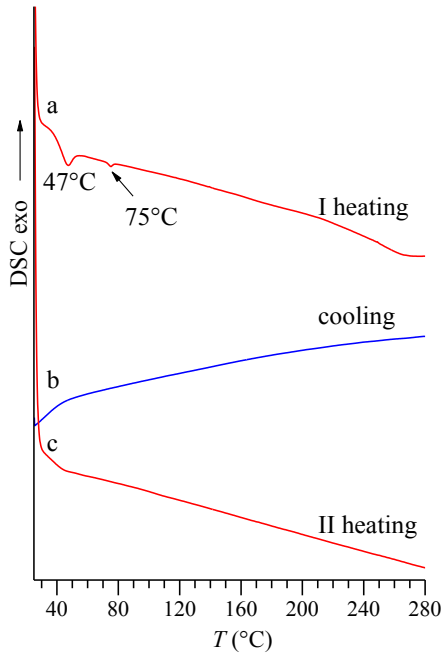

Figure 1.21. DSC curves recorded during first heating (a), successive cooling (b) and second heating scans (c) of as-prepared sample MM184AcR (syndiotactic poly((R,S)-3-methyl-1-pentene)). All DSC curves have been recorded at scanning rate of 10 °C/min.

1.3.9 Syndiotactic poly(3-methyl-butene).

The polymerization of isoprene with the catalytic system $FeCl_2(bipy)_2$/MAO allows to obtain the syndiotactic 3,4 poly(isoprene). The successive hydrogenation of the syndiotactic 3,4 poly(isoprene) gave a new polymer (Figure 1.3P): the syndiotactic poly(3-methyl-butene) (sample MM412AcR). The X-ray powder diffraction profile of the as-prepared sample MM412AcR shown in Figure 1.22 indicate that the sample is amorphous. According with the X-ray data, in the DSC curves recorded during first heating, successive cooling at low temperature and second heating only the glass transition at about 12°C has been observed (Figure 1.23). However, we have observed that the sample MM412AcR is able to crystallize by annealing of a stretched sample. The X-ray fiber diffraction pattern of a compression molded film of the sample MM412AcR stretched at 250% deformation and annealed at 70°C under

tension is shown in Figure 1.24. It is apparent that the diffraction pattern presents sharp reflections on the equator a broad reflection on the layer lines and a clear meridional reflection. This indicated that the sample of syndiotactic poly(3-methyl-butene) crystallizes by stretching and annealing in a disordered crystalline form.

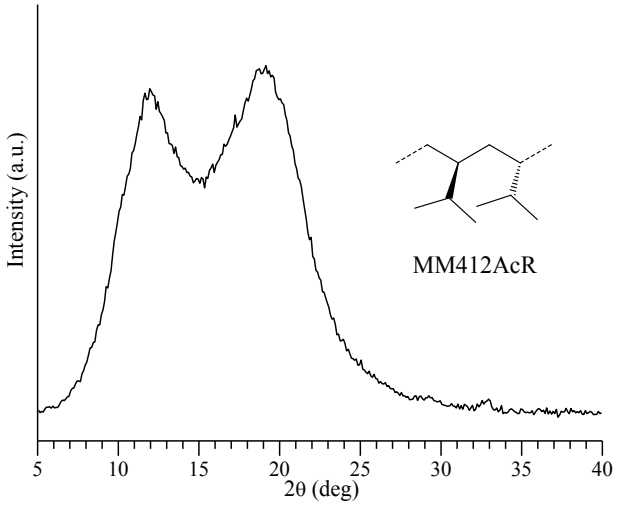

Figure 1.22. X-ray powder diffraction profiles of as-prepared sample MM412AcR of syndiotactic poly(3-methyl-butene).

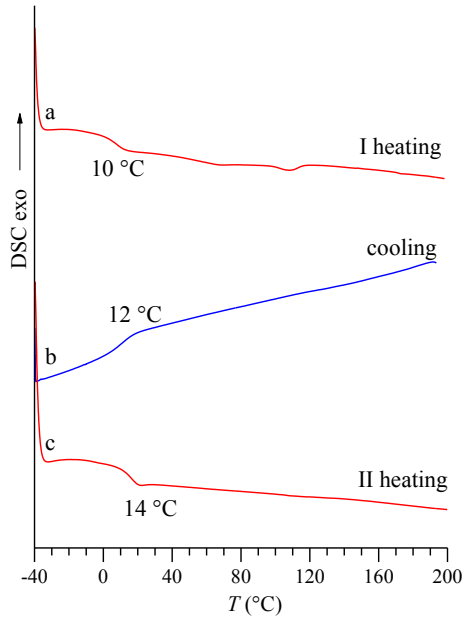

Figure 1.23. DSC curves recorded during first heating (a), successive cooling (b) and second heating scans (c) of as-prepared sample MM412AcR of syndiotactic poly(3-methyl-butene). All DSC curves have been recorded at scanning rate of 10 °C/min.

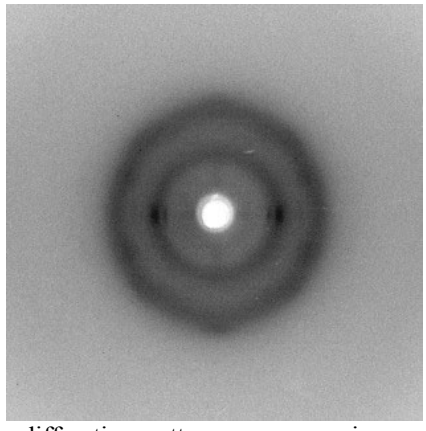

Figura 1.24: X-ray fiber diffraction pattern a compression molded film of the sample MM412AcR of syndiotactic poly(3-methyl-butene) stretched at 250% deformation and annealed at 70°C under tension.

1.4 Conclusions

Structural and thermal analysis of stereoregular polydienes and related hydrogenated polymers obtained with innovative catalytic systems has been reported.

New catalytic systems based on some complexes of transition metals and lanthanides with various ligands containing donor atoms such as P, N, O (e.g., phosphines, imines, imino-pyridines, cheto-imines) in combination with MAO are able to polymerize different types of substituted butadienes, giving polymers with different structure from different monomers. For example, the system $CoCl_2(PRPh_2)_2$/MAO (with R an alkyl group) gives a highly syndiotactic 1,2-polymer from 1,3-pentadiene, but a 1,2 isotactic polymer from 3-methyl-1,3-pentadiene [12]. The same monomer, however, does not exhibit the same behavior with all the catalysts: 3-methyl-1,3-pentadiene gives a highly isotactic 1,2-polymer when polymerized with $CoCl_2(PMePh_2)_2$/MAO, but a highly syndiotactic 1,2-polymer when polymerized with $FeCl_2(bipy)_2$/MAO [12].

The successive hydrogenation of iso- and syndiotactic cis-1,4 polydienes allows to obtain new ethylene-α-olefin alternating copolymers. Most of these new polymers cannot be obtained through the simple stereospecific polymerization of the corresponding monomers and are expected to show interesting mechanical and, probably, elastomeric properties.

From the stereoregular 1,2 polydienes (isotactic and syndiotactic) novel stereoregular branched polyolefins can be prepared. For instance isotactic poly((*R*,*S*)-3-methyl-1-pentene), syndiotactic poly((*R*,*S*)-3-methyl-1-pentene), syndiotactic poly(3-methyl-butene) are new polymers and the crystal structure and the physical properties of these systems are not known. The crystal structures of isotactic poly((*R*,*S*)-3-methyl-1-pentene) and its precursor before hydrogenation isotactic 1,2-poly((*E*)-3-methyl-1,3-pentadiene) are reported in the Chapther2.

Bibliography Chapter 1

[1] L. Porri, A. Giarrusso, Conjugated diene polymerization. In *Comprehensive Polymer Science*; G., Eastmond, A. Edwith, S. Russo, P. Sigwalt, Eds.; Pergamon Press Ltd.: Oxford, **1989**, *4*, Part II, 53.

[2] S. K. H. Thiele, D. R. Wilson, *J. Macromol. Sci. Part C: Polymer Reviews,* **2003**, *C43,* 581.

[3] L. Friebe, O. Nuyken, W. Obrecht, *Adv. Polym. Sci.*, **2006**, *204*, 1.

[4] G**.** Ricci, S. Italia, C. Comitani, L. Porri *Polym Commun* **1991**, *32*, 514.

[5] G. Ricci, L. Porri *Polymer* **1997**, *38*, 4499.

[6] G. Ricci G, L. Zetta, E. Alberti, T. Motta, M. Canetti, F. Bertini *J Polym Sci, Part A: Polym Chem,* **2007**, *45*, 4635.

[7] V. Venditto, C. De Rosa, G. Guerra, R. Napolitano *Polymer* **1992**, *33*, 3547.

[8] G. Ricci, S. Italia, L. Porri *Macromolecules* **1994**, *27*, 868.

[9] G. Ricci, E. Alberti, L. Zetta, T. Motta, F. Bertini, R. Mendichi, P. Arosio, A. Famulari, S. V. Meille, *Macromolecules* **2005**, *38*, 8353.

[10] P. Longo, G. Guerra, F. Grisi, S. Pizzuti, A. Zambelli *Macromol Chem Phys* **1998**, *199*, 149.

[11] G. Ricci, L. Porri, *Macromol. Chem. Phys.* **1997**, *198*, 3647.

[12] G. Ricci, A. Sommazzi, F. Masi, M. Ricci, A. Boglia, G. Leone *Coord. Chem. Rev.*, **2010**, *254*, 661.

[13] G. Ricci, G. Leone, A. Boglia, A.C. Boccia, L. Zetta *Macromolecules,* **2009***, 42*, 9263.

[14] A. C. Boccia, G. Leone, A. Boglia, G. Ricci *Polymer* **2013**, *54*, 3492.

[15] G. Ricci, G. Leone, A. C. Boccia, I. Pierro, G. Zanchin, M. Mauri, M. Scoti, A. Malafronte, F. Auriemma, and C. De Rosa *Macromolecules* Publication date (web) January 18, **2017.**

[16] P. Corradini, P. Ganis, P. *Makromol. Chem.* **1963**, *62*, 97.

[17] G. Natta, G. Allegra, I. W. Bassi, P. Corradini, P. Ganis, **1962**, *58*, 242.

[18] G. Natta, G. Dall'Asta, G. Mazzanti, I Pasquon, A. Valvassori, A. Zambelli, *J. Am. Chem. Soc.* **1961**, *83*, 3343.

[19] G. Natta, G. Dall' Asta, G. Mazzanti, I. Pasquon, A. Valvassori, A. Zambelli, *Makromol. Chem.* **1962**, *54*, 95.

[20] F. Auriemma, C. De Rosa, P. Corradini, *Macromol. Chem. Phys.* **2004**, *205*, 390.

[21] C. De Rosa, F. Auriemma, *Crystal and Crystallinity in Polymers* Wiley: **2014**.

[22] G. Ricci, G. Leone, A. Boglia, F. Bertini, A. C. Boccia, L. Zetta *Macromolecules*, **2009**, *42*, 3048.

[23] G. Natta, P. Pino, G. Mazzanti, P. Corradini, U. Giannini, Rend. Accad. Naz. Lincei (VIII) **1955**, *19*, 397.

[24] P. Pino, F. Ciardelli, G. Montagnoli *J. Polym. Sci.*, Part C **1968**, *16*, 3265.

[25] L. Oliva, P. Longo, A. Zambelli, *Macromolecules* **1996**, *29*, 6383.

[26] C. De Rosa, F. Auriemma, C. Santillo, R. Di Girolamo, G. Leone, A. Boccia, G. Ricci *Macromolecules* **2015***, 48*, 5251.

[27] C. De Rosa, F. Auriemma, C. Santillo, R. Di Girolamo, G. Leone, G. Ricci *CrystEngComm* **2015**, *17*, 6006.

Chapter 2

Crystal Structures of New Polymers obtained from 1,3-dienes with New Catalytic Systems

2.1 Introduction

In this Chapter the crystal structures of isotactic 1,2-poly(*E*)-3-methyl-1,3-pentadiene) (iP3MPD12) and isotactic poly((*R*,*S*)-3-methyl-1-pentene) (iP(*R*,*S*)3MP), obtained from successive hydrogenation reaction of the first, are presented. As show in Figure 1.3N, iP3MPD12 is the isotactic polydiene precursor of the saturated iP(R,S)3MP, which has been, indeed obtained by hydrogenation of iP3MPD12.

As already mentioned above, a crystalline iP3MPD12 was obtained by polymerizing 3-methyl-1,3-pentadiene with the catalytic system $CoCl_2(PnPrPh_2)_2$/MAO. This polymer represents the third example of 1,2 isotactic polydiene described in the literature; the other ones being 1,2 isotactic polybutadiene (iPBuD12) [1] and 1,2 isotactic poly(4-methyl-1,3-pentadiene) (iP4MPD12) were reported.[2]

The crystal structure of iPBuD12 is characterized by chains in 3/1 helical conformation, that are packed in a trigonal unit cell with parameters $a = b$ = 17.3 Å, c = 6.5 Å, according to the space group $R3c$ or $R\bar{3}c$ [3]. The structure of iP4MPD12 is instead characterized by chains in 18/5 helical conformation, packed in a tetragonal unit cell with parameters $a = b$ = 17.8 Å, c = 36.5 Å, according to the space group $I\bar{4}c2$ [4]. According to the different structure of the side groups, the chain conformation and the crystal structure of iP3MPD12 is expected to be different from those of iPBuD12 and iP4MPD12.

The saturated polymer iP(R,S)3MP was obtained by hydrogenation of iP3MPD12 (Figure 1.3N). The high isotacticity of the precursor iP3MPD12 ([mm]>90%) was preserved after hydrogenation in the iP(R,S)3MP chains resulting in a random enchainment of the two enantiomeric monomers unit (*S*)3MP and (*R*)3MP. The crystals of the achiral iP(R,S)3MP [5,6] reported in this chapter is compared with that of the chiral poly((*S*)-3-methyl-1-pentene) (iP(S)3MP) [7]

Isotactic poly(3-methyl-1-pentene) (iP3MP) is the ideal example of a polyolefin which can be either chiral, containing a "true" asymmetric atom on the side group, with corresponding optical activity, or not chiral when the two enantiomeric R and S monomeric units are randomly enchained with compensation of the chirality of the lateral groups. This allows the effect of the chirality of the lateral groups and the effect of intramolecular chirality compensation on the conformation of the chains and the packing of chains in the crystals to be studied and compared. Both the chiral monomer (S)-3-methyl-1-pentene ((S)3MP) and the racemic mixture (R,S)-3-methyl-1-pentene ((R,S)3MP) polymerize to isotactic polymers in the presence of Ziegler–Natta or metallocene catalysts.[7,8,9] The polymerization of the chiral monomer (S)3MP produces a chiral isotactic polymer, poly(S)-3-methyl-1-pentene) (iP(S)3MP). The polymerization of the racemic mixture (R,S)3MP gives an isotactic copolymer, poly((R,S)-3-methyl-1-pentene) (iP(R,S)3MP), where the two enantiomeric monomers (R)3MP and (S)3MP should be enchained.[8] However, the polymer produced with a Ziegler–Natta catalyst was separated into fractions having optical activity of opposite sign by adsorption chromatography on highly crystalline iP(S)3MP.[8] This indicated that copolymers of the two enantiomeric monomeric units, with prevalence of S or R monomeric units in the optically active polymers, were obtained,[8] due to the stereoselectivity of the polymerization by heterogeneous catalysts which

gives rise to the dominant formation of macromolecules by one single monomeric antipode.[8] The same polymer was also obtained with single-center homogeneous metallocene catalysts.[9] Therefore, a purely statistical copolymer of the two monomeric antipodes was not obtained with heterogeneous or homogeneous stereoselective catalysts. A different route for the synthesis of a purely random achiral copolymer iP(R,S)3MP could be the stereospecific polymerization of 3-methyl-1,3-pentadiene to isotactic 1,2-poly(3-methyl-1,3-pentadiene) and successive hydrogenation. The isotactic stereoregularity could be preserved after hydrogenation and a purely statistical copolymer of the two enantiomeric monomers with intramolecular compensation of chirality could be obtained with this procedure. In this paper, we report the synthesis of a purely random achiral copolymer iP(R,S)3MP by hydrogenation of isotactic 1,2-poly(E-3-methyl-1,3-pentadiene) (iP3MPD12). The obtained polymer iP(R,S)3MP is highly isotactic and crystalline and the crystal structure was resolved by X-ray diffraction analysis. We found that the crystal structure of iP(R,S)3MP [5,6] is different from that of chiral iP(S)3MP [7].

2.2 Materials and Methods

2.2.1 Materials.

Sample MM151 of isotactic 1,2-poly(*E*)-3-methyl-1,3-pentadiene) (iP3MPD12) and sample MM183AcR of isotactic poly((*R*,*S*)-3-methyl-1-pentene) (iP(*R*,*S*)3MP) studied in this Chapter are provided by Professor Ricci of the Institute for Macromolecular Studies of CNR of Milan (CNR-ISMAC). The sample MM151 of iP3MPD12 was prepared with a new class of catalysts based on cobalt phosphine complexes $CoCl_2(PnPrPh_2)_2$/MAO (with nP = n-Propyl). The sample MM183AcR of iP(*R*,*S*)3MP was prepared by successive hydrogenation of iP3MPD12 with p-toluenesulfonyl hydrazide. Both polymers iP3MPD12 and iP(*R*,*S*)3MP

present high molecular mass (around 90 000 g/mol) and are highly isotactic, with concentration of isotactic triad mm higher than 90%. Therefore, according to the synthetic strategy, the high isotacticity of iP3MPD12 ([mm] ≥ 90%) is preserved after hydrogenation.

2.2.2 Polymer characterization.

X-ray powder diffraction profiles were obtained with Ni-filtered Cu Kα radiation with an automatic Philips diffractometer.

Unoriented films used for structural analysis of iP3MPD12 and iP(*R*,*S*)3MP were obtained by compression molding of as-polymerized samples.

The powders of iP3MPD12 were heated at ≈140°C between perfectly flat brass plates under a press at very low pressure, kept at ≈140°C for 5 min, and cooled to room temperature. Crystalline oriented fibers were obtained by stretching strips cut from compression molded films at room temperature up to the maximum possible deformation of ε = 500% before failure and successive annealing at 60°C for ≈18 h.

For the iP(*R*,*S*)3MP, the as-prepared sample were heated at ≈240°C between flat brass plates under a press at low pressure, kept at ≈240°C for 5 min, and cooled to room temperature. Crystalline oriented fibers were obtained by extrusion of melt in a syringe and stretching.

X-ray fiber diffraction patterns of stretched fiber have been recorded on a BAS-MS imaging plate (FUJIFILM) using a cylindrical camera and processed with a digital imaging reader Perkin Elmer Cyclone Plus (storage phosphor system).

2.2.3 Determination of the helical parameters of complex helices.

Helical conformation is the most common and preferred conformations assumed by chains of synthetic polymers. In fact most of isotactic and syndiotactic polymers crystallize in helical conformation.[10,11]

Helices consist of periodic one-dimensional objects with periodicity *c* made up of a structural motif repeating regularly along one axis, trough a translation vector *p* or "unit height" parallel to the helix axis and a simultaneous rotation *t* or "unit twist" around the axis. The parameters that characterize the helical repetition of the motif are therefore the helical radius *r*, and the number of units *M* and the number of turns *N* included in the identity period *c*. The unit height *p* and the unit twist *t* are, therefore, defined as the translation along the helix axis per residue and the angle of rotation about the helix axis per residue, respectively. The unit height *p* and the unit twist *t* are related to *M* and *N* through the relationships: $p = c/M$; $t = 360\ N/M$.

Another important parameter used for characterization of helical conformations is the helical pitch *P*, corresponding to the axial length of the helix in one turn $P = c/N$. Therefore the ratio P/p corresponds to the ratio M/N. If *P* and *p* are commensurable, the ratio P/p is rational and may be expressed as the ratio M/N of two integer numbers.

The case of helices characterized by a ratio P/p equal to an irrational number implies that it is not possible to find a suitable couple of integer numbers *M* and *N* whose ratio is equal to P/p. Complex helices with incommensurable *P* and *p* parameters are quite common in synthetic polymers, and arise from small distortions of the P/p ratio from an ideal rational value. In particular, a small twisting of a simple helix characterized by small integer values of *M* and *N* parameters may result in a dramatic increase of the chain periodicity *c*, whereas the P/p value changes only slightly, giving rise to helices with high values of *M* and *N*.

Noncommensurable helical parameters correspond to helices where each residue advances a distance p parallel to the z (helix) axis and rotates by an angle t around the z axis with p and t remaining finite numbers. Therefore, for helices with noncommensurable P and p parameters the chain repetition period is virtually absent, i.e., $c \rightarrow \infty$, even though the ratio $c/M = p$ is still a finite number.[10,12]

The conformation of several helical polymers has been determined by considering the effects on the X-ray fiber diffraction patterns caused by helical geometry, exploiting the tendency of polymer substances to form fibers with a high degree of orientation of the helical chains parallel to the fiber axis.[13] The general theory used to perform diffraction analysis of helical structures was first published by Cochran, Crick, and Vand (CCV). [14] The CCV theory establishes that the diffraction intensity on the lth layer line in the X-ray fiber diffraction of a helical structure may be obtained from the square of the structure factor $F(\xi, \psi, l/c)$, which can be calculated from the following equation:

$$F_l\left(\xi, \Psi, \frac{l}{c}\right) = f\left(\xi, \Psi, \frac{l}{c}\right) \sum_n J_n(2\pi\xi r) \exp\left[in\left(\Psi + \frac{\pi}{2}\right)\right] \quad (1)$$

where ξ, ψ, and $\zeta = l/c$ are the cylindrical coordinates of a point in reciprocal space, f is the form factor of a helical residue, and J_n is the Bessel function of order n. As shown in the illustration of the Bessel functions of Figure 2.1, the amplitude of the Bessel function $J_n(R)$ for small values of R decreases rapidly as n increases. The order n of the Bessel functions in the summation is determined according to the selection rule:[14]

$$\zeta = n/P + m/p \quad (2)$$

where m is an integer number. By multiplying both members by the periodicity c, the selection rule may be also written as:

$$l = m\,M + n\,N \quad (3)$$

More generally, for a *M*/*N* helix, based on this selection rule, strong meridional reflections are generally expected on layer lines with $l = \pm mc/p = \pm mM$, where the zero-order Bessel function contributes. Furthermore the diffraction intensity in zones of reciprocal space close to the meridian (at low ξ value) is higher the lower the order of Bessel functions contributing to the structure factor.

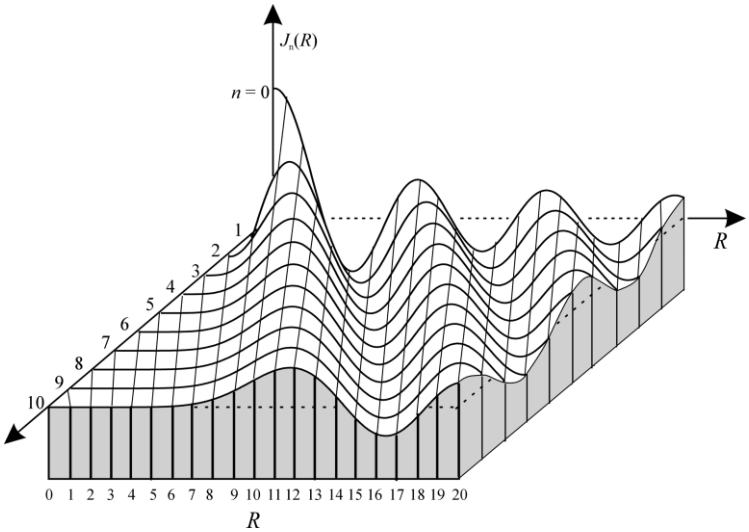

Figure 2.1. Bessel functions of first kind $J_n(R)$ for n from 0 to 10. For negative values of n, the relationship $J_{-n}(R) = (-1)^n J_n(R)$ holds.

For a helix with incommensurable parameters, planes at height $\zeta = n/P + m/p$ fill the whole reciprocal space, and the layer spacing $c^* = 1/c$ becomes small as c increases and in the limit of $c \rightarrow \infty$, $c^* \rightarrow 0$. In practice, as demonstrated in the original paper by CCV [14] it is possible to approximate the true values of P/p by some rational fraction $P'/p' = M/N$, which accounts for all the features of the diffraction pattern. Consequently, the selection rule of equation 2 for a true helix (helical parameters P and p) can be rewritten for an approximate helix (helical parameters P' and p') in the same manner:

$$\zeta' = n/P' + m/p' \qquad (4)$$

Using the approximate values *P'* and *p'*, a given Bessel function, whose position along ζ is defined by *m* and *n*, moves in the reciprocal space by a quantity $\Delta\zeta = \zeta - \zeta'$:

$$\zeta - \zeta' = \Delta\zeta = n\left(\frac{1}{P} - \frac{1}{P'}\right) + m\left(\frac{1}{p} - \frac{1}{p'}\right) = n\left(\frac{\Delta P}{PP'}\right) + m\left(\frac{\Delta p}{pp'}\right) \quad (5)$$

According to this equation, if the deviations ΔP and Δp are small, the Bessel function in question will move only a small distance in the reciprocal space $\Delta\zeta$, especially if *n* and *m* are also small. With increasing the identity period *c*, the number of structural units included in the identity period *M* also increases and the Bessel functions that for a simpler helix contribute to the diffraction intensity on the same layer line ζ, are split on different layer lines and the closely spaced layer lines become mostly filled by Bessel functions of high order. Therefore, for the majority of the layer lines, the intensity is quite small, and the lowest order Bessel functions remain confined in layer lines close to positions given by the simple helix corresponding to the commensurable approximation of *P* and *p*.

A precise determination of the ratio *P*/*p* may be obtained resorting to the graphical method proposed by Mitsui. [15] To this aim, selection rule of equation 2 is rewritten, multiplying both sides by *P* or *p* to obtain the following equations:

$$\zeta_{rel} = \zeta P = n + m\, P/p \quad (6)$$

or

$$\zeta'_{rel} = \zeta p = n\, p/P + m \quad (7)$$

From diagrams as in Figure 2.2, where ζ'_{rel} is reported as a function of *p*/*P*, it is possible to visualize the change of the distribution of the diffraction intensity as a function of the ratio *p*/*P*; therefore, the plots of Figure 1.4 can be utilized for an accurate determination of helical parameters.

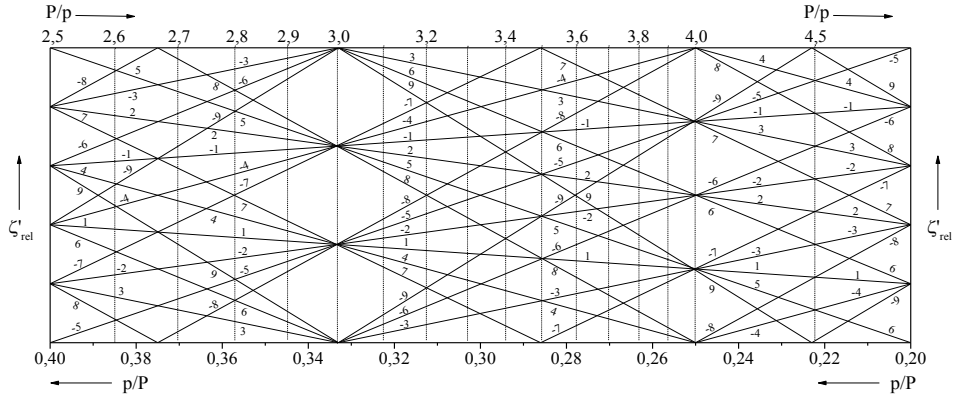

Figure 2.2. Graphic representation of ζ'_{rel} as a function of p/P. Numbers close to the straight lines denote the values of the order n of the Bessel function.[15]

A possible procedure for the use of the diagram ζ'_{rel} vs. p/P (Figure 2.2) is as follows:

(a) Plot the observed values of ζ, determined from the X-ray fiber diffraction pattern, on a transparent paper after scaling by multiplication for the experimental value of the unit height p. Mark the relative intensities of the layer lines.

(b) Set the transparent paper parallel to the ordinate of the plot of Figure 2.2, and try to find the best fit by sliding the paper along the p/P-axis, until a satisfactory agreement between the observed spacing of the layer lines along ζ'_{rel} and a reasonable correspondence of the order n of the Bessel function to the relative intensities are obtained.

(c) The so obtained value of the p/P ratio is used to find a suitable commensurable nontrivial approximation of the M and N parameters. Once the (m, n) values have been assigned to each layer, the index l of the layer line can be calculated using the selection rule $l = m\,M + n\,N$. The identity period c may be then calculated as the weighted average of l/ζ_{obs}.

A new method for the determination of the best M and N helical parameters of complex helices from fiber diffraction data was developed in my

research group by Professors F. Auriemma and C. De Rosa (ADR Method). [10, 12] This method has the advantage of giving simultaneously all possible solutions and it is more suitable for the implementation in a software work-package for solving helical structures. The method consists in performing an indexing of the observed layer lines by evaluating for each observed value of ζ_{obs} trial values of the identity period c, as $c = l/\zeta_{obs}$ with l an integer number corresponding to the trial value of the index l of the layer line. Solutions are selected among those that allow indexing all observed layer lines for identical values of c within the experimental error. The problem may be formally stated by solving the following system of discrete equations, using the identity period c as a parameter.

$$\begin{cases} \zeta_1^{-1} l_1 = c \\ \zeta_2^{-1} l_2 = c \\ \dots\dots\dots\dots. \\ \zeta_n^{-1} l_n = c \end{cases} \quad (8)$$

The system may be reformatted to a matrix formula that is suitable for electronic computing:

$$(\mathbf{ZE})^{-1}\ \mathbf{L} = c\ \mathbf{J} \quad (9)$$

where **Z** is the row vector of order 1 x k whose elements are the observed values of ζ (the ζ_{obs} values), **E** is the unit matrix of order k x k, **L** is the column vector of order k whose elements are the values of l that allow for indexing the observed layer lines, c is the parametric variable corresponding to the identity period of the chain and **J** is the column vector of order k whose elements are equal to 1. Equation 9 is numerically solved admitting as solutions only the values of c for which the elements of the column vector **L** are integer numbers.

In the successive step, for any given solution labeled i, characterized by a value of the chain periodicity c_i, the corresponding values of helical parameters M_i and N_i are found, exploiting all additional available

structural information. In particular knowing the value of unit height p, the value of M_i is calculated as the nearest integer number (nint) close to the ratio $M_i = \text{nint}(c_i/p)$. The value of N_i is then established by trial and error, applying the selection rule $l = m\,M + n\,N$ to find for all possible values of N_i the lowest order Bessel function that contributes to the diffraction intensity on each layer line. In this procedure the possible values for N_i are chosen numerically coincident with the values of l that index the observed layer lines for the ith solution. At this stage of analysis M_i/N_i helices with M_i and N_i values having a common factor should be discarded, because they identify solutions for which the chain periodicity c corresponds to $c = c_i/K$ with K the greatest common factor between M_i and N_i. The most reliable M_i/N_i helix is then identified as the helix that gives a distribution of the lowest order Bessel function on the various layer lines in the best qualitative agreement with the experimental intensity distribution, and that gives the best agreement between the observed (ζ_{obs}) and calculated (ζ_{calc}) values of the height of the various layer lines ζ.

2.2.4 Conformational and packing energy calculations.

The calculations of the conformational energy have been performed on a portion of isolated chains of iP3MPD12, iP(*R*)3MP, iP(*S*)3MP and iP(*R*,*S*)3MP under the constrain of the equivalence principle [10] by assuming a line repetition group s(M/N) for the polymer chain. As a consequence the sequence of the torsion angles in the main chain is of the kind $...\theta_1\theta_2\theta_1\theta_2...$ [10]. The intramolecular energy has been calculated as the sum of three terms: [10]

$E = \Sigma_b\, E_b + \Sigma_t\, E_t + \Sigma_{nb}\, E_{nb}$

where the bending E_b is the energy contribution due to deformation of bond angle (τ) from the equilibrium value, which is assumed to have the form:

$E_b = (K_b/2)(\tau-\tau_o)^2$

the torsional energy E_t is the energy contribution associated with rotation around single bonds and is usually taken as a sinusoidal function of the torsion angle θ:

$E_t = (K_t/2)(1 + \cos 3\theta)$

and the non-bonded energy E_{nb} is the energy contribution due to the non-bonded interactions between atoms separated by more than two bonds, which is assumed to be the Lennard-Jones function:

$E_{nb} = A/r^{12} - B/r^6$

The potential energy constants reported by Flory [16] have been used (Table 2.1). The non-bonded energy has been calculated by taking into account the interactions between the atoms of the first monomeric unit and the interactions between these atoms and the remaining atoms within spheres having radii twice the van der Waals distances for each pair of atoms. The geometrical parameters assumed in the present calculations are reported in Table 2.2.

The packing energy has been evaluated as half the sum of the interaction energies between the atoms of one monomeric unit and all the surrounding atoms of neighboring macromolecules. The calculations have been performed using a 6-12 Lennard-Jones potential with the constants reported by Flory et al.[16] and taking the methyl groups as a single rigid unit (Table 2.2). The conformation of the chain and the unit cell axes have been kept constant, and the interactions have been calculated within spheres of twice the sum of the van der Waals radii for each pair of atoms.

Table 2.1. Parameters of the potential functions used in the conformational and packing energy calculations. [16]

Torsion angles	K_t **(kJ/mol)**	
$C\text{-}C_{sp3}\text{—}C_{sp3}\text{-}C$	11.7	
C-C—C=C	4.2	
Bond angles	K_b **(kJ·mol^{-1}·deg^{-2})**	τ_o **(deg)**
$C_{sp3}\text{—}C_{sp3}\text{—}C$	0.184	109.47
$C\text{—}C_{sp3}\text{—}H$	0.121	109.47
$H\text{—}C_{sp3}\text{—}H$	0.100	109.47
$C_{sp3}\text{—}C_{sp2}\text{—}C_{sp2}$	0.174	125
$C_{sp2}\text{—}C_{sp2}\text{—}H$	0.101	117.5
$C_{sp3}\text{—}C_{sp2}\text{—}H$	0.098	117.5
Nonbonded interacting pair	$A\times10^{-3}$**(kJ·mol^{-1}·Å^{12})**	B **(kJ·mol^{-1}·Å^{6})**
$C_{sp3}\text{—}C_{sp3}$	1654.5	1520
$C_{sp3}\text{—}C_{sp2}$	2035.5	1870
$C_{sp3}\text{—}CH_3$	4021.8	2671
$C_{sp3}\text{—}H$	235.8	531
$C_{sp2}\text{—}C_{sp2}$	2516.5	2312
$C_{sp2}\text{—}CH_3$	4974.6	3304
$C_{sp2}\text{—}H$	295.7	664
$CH_3\text{—}CH_3$	9671.8	4723
$CH_3\text{—}H$	613.6	950
H—H	30.2	196

Table 2.2 Bond lengths and bond angles used in the conformational energy maps of iP3MPD12, iP(*S*)3MP and iP(*R*)3MP.

Bond Length (Å)	
$C_{sp3}\text{—}C_{sp3}$	1.53
$C_{sp3}\text{—}C_{sp2}$	1.51
$C_{sp2}\text{—}C_{sp2}$	1.34
$C_{sp3}\text{—}H$	1.10
$C_{sp2}\text{—}H$	1.10
Bond Angles (deg)	
C'-C"-C'	113
C"-C'-C"	111
C"-C'-H	107.9
C'-C"-H	108.9
H-C"-H	108.0

a. C' indicates a methine carbon atom; C" indicates a methylene carbon atom.

2.2.5 Structure factors calculations.

Structure factors have been calculated and compared to X-ray diffraction intensities evaluated from both X-ray powder diffraction profile and X-ray fiber diffraction patter. Calculated structure factors have been obtained as $F_c = (\sum|F_i|^2 M_i)^{1/2}$, where F_i is the structure factor and M_i the multiplicity factor in powder or fiber diffraction [10] of the reflection i (Miller indices $(hkl)_i$), and the summation is taken over all reflections included in the 2θ range of the corresponding diffraction peak observed in the X-ray powder diffraction profile or of the diffraction spot observed in the X-ray fiber diffraction pattern. A thermal factor $B = 8$ Å^2 and atomic scattering factors as in ref. [17] have been assumed. The observed structure factors, F_o, have been evaluated from the intensities I_o of the reflections observed in the powder diffraction profiles or in the fiber diffraction pattern as $F_o = (I_o/LP)^{1/2}$, where LP is the Lorentz-polarization factor for X-ray powder diffraction, [10] $LP = (1 + \cos^2 2\theta)/(\sin^2\theta\cos\theta)$, or for Xray fibre diffraction, $LP = (1 + \cos^2 2\theta)/[2(\sin^2 2\theta - \zeta^2]^{½}$, with the cylindrical coordinate $\zeta = \lambda l/c$, l and c being the order of the layer line and the chain axis, respectively, and λ the X-ray wavelength. [10]. The experimental intensities I_o have been evaluated from the powder diffraction profile by measuring the area of the peaks in the X-ray powder diffraction profile, after subtraction of a straight baseline approximating the background and of the amorphous contribution. The iP3MPD12 does not crystallized by cooling from the melt but crystallizes by aging at room temperature of the sample cooled from the melt. Therefore, the amorphous profile of the sample cooled from the melt before occurring crystallization was used as profile of the amorphous contribution. For the amorphous profile of iP(*R*,*S*)3MP the diffraction profile of the melt measured at temperature high than the melting temperature (190°C) was used.

The experimental intensities I_o have also been evaluated from the X-ray fiber diffraction patterns by measuring the integrated intensity of spots recorded on the imaging plate I_{tot} upon subtraction of background intensity I_b. as $I_o = I_{tot} - I_b$. The background intensity I_b has been approximately evaluated by measuring the integrated intensity of regions placed around each spot free of Bragg contributions, having identical area of the spots. The disagreement factor has been calculated as: $R' = (\Sigma|F_o - F_c|)/\Sigma F_o$. Simulated X-ray powder diffraction profiles and fiber diffraction patterns have been obtained with the software package [18] CERIUS^2, using the isotropic thermal factor B = 8 Å2.

For the calculation of powder diffraction data of iP3MPD, profile functions having a half-height width regulated by the average crystallite size along a, b, and c axes, $L_a = L_b = 150$ Å and $L_c = 100$ Å, respectively have been used. These values correspond to a coherence length along a, b, and c and is not a true crystallite size. Simulated X-ray fiber diffraction patterns have been obtained fixing the half-width at half-height of crystallite orientation distribution (taken to be a Gaussian function centered on the fiber axis) equal to 3.16°. For the calculation of powder diffraction profiles of iP(*R*,*S*)3MP, profile functions having $L_a = L_b = 200$ Å and $L_c = 150$ Å, respectively have been used and simulated X-ray fiber diffraction patterns have been obtained fixing the half-width at half-height of crystallite orientation distribution (taken to be a Gaussian function centered on the fiber axis) equal to 9.13°.

2.3 Crystal structure of isotactic 1,2-poly((*E*)-3-methyl-1,3-pentadiene)

The X-ray powder diffraction profile of the as-prepared sample MM151 of iP3MPD12 and of a sample prepared by compression-molding and cooling from the melt to room temperature are shown in Figure 2.3. The as-prepared sample is crystalline with melting temperature of 93 °C (see the DSC curve of Figure 1.17A) and degree of crystallinity of nearly 26%. The diffraction profile of the as-prepared sample presents intense reflections at 2θ = 10.1, 16.2 and 19.1° (Figure 2.3a).

The as-prepared sample does not crystallize from the melt, as already shown by the DSC cooling curve of Figure 1.17A that does not present any exothermic peak of crystallization. The X-ray diffraction profile of Figure 2.3b of the compression-molded sample prepared by heating the as-prepared powders at ≈140 °C under a press at very low pressure, keeping the sample at ≈140 °C for 5 min, and cooling to room temperature, shows, indeed, two broad halos centered at 2θ = 10° and 19° indicating that the sample is amorphous.

However, the amorphous sample cooled from the melt crystallizes by aging at room temperature for long time. This is revealed by the X-ray diffraction profile of the amorphous compression-molded sample aged at room temperature for 1 month of Figure 2.3c, that presents the same diffraction peaks of the at 2θ = 10.1 and 16.2° observed in the profile of the as-prepared sample (Figure 2.3a), even though a lower degree of crystallinity of 19% has been achieved. However, the crystallinity improves after annealing of the crystalline aged sample. The diffraction profile of the compression-molded and aged sample annealed at 70 °C for ≈ 20 h, shown in Figure 2.3d, shows sharp reflections in the same position of the as-prepared sample with a high degree of crystallinity of nearly 50%.

The DSC curves of the amorphous samples recorded during cooling or second heating show a glass transition temperature of iP3MPD12 of nearly 30 °C (curves b,c of Figure 1.17A).

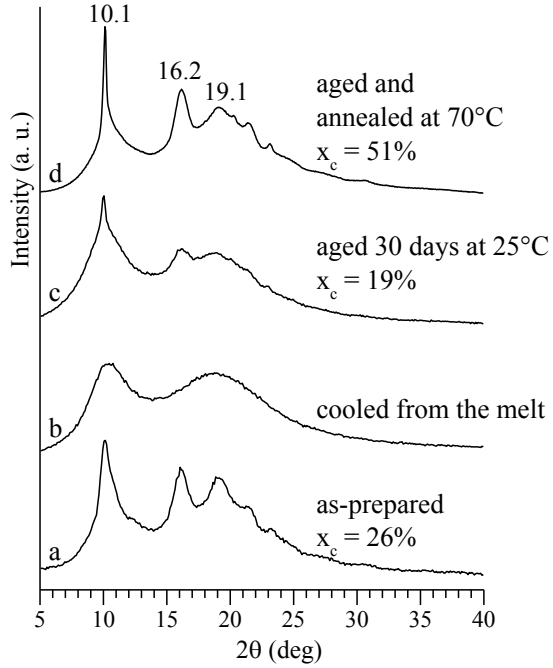

Figure 2.3. X-ray powder diffraction profiles of as-prepared sample of iP3MPD12 (a), of a sample prepared by compression molding and cooling from the melt to room temperature (b), after aging at room temperature for 30 days (c) and of the aged sample in c annealed at 70 °C for 20 h (d).

Crystalline oriented fibers of iP3MPD12 have been prepared following two procedures:

1) Stretching at high deformation up to maximum possible deformation before breaking (about 500%) the sample of high crystallinity of Figure 2.3d obtained by annealing at 70°C for ≈ 20 h of the compression-molded sample aged at room temperature for 1 month.

2) Stretching at high deformation up to maximum possible deformation before breaking (about 500%) the sample of low crystallinity of Figure 2.3c obtained by aging of the compression-molded sample at room temperature

for 1 month, and successive annealing at 60 °C for 18h of the stretched fibers kept under tension.

The X-ray fiber diffraction patterns and the corresponding equatorial profiles of the samples of iP3MPD12 obtained after each step of the two procedures are reported in Figure 2.4 and in Figure 2.5, respectively.

The bidimensional X-ray diffraction pattern of Figure 2.4A represents the initial unoriented crystalline film of iP3MPD12. All characteristic reflections of crystalline iP3MPD12 at 2θ = 10.1° 16.2° and 19.1° visible in the powder profiles of Figures 2.3 are observed. The same reflections appear more intense and well resolved in the diffraction pattern of the annealed sample of Figure 2.4B. Instead, after stretching the fiber diffraction pattern of Figure 2.4C presents broad reflections at 2θ = 10.4° on the equator and at 2θ = 16.2° on the layer line, indicating a disordered structure and fiber with very small crystals. Moreover, the strong reflections at 2θ = 10.1° and at 2θ = 16.2°, observed in the powder profiles of Figure 2.3 and in the equatorial profiles of Figures 2.4A' and 2.4B', are slightly polarized on the equator, and off the equator respectively.

Contrary to the first procedure, well oriented and crystalline fibers have been obtained with the second procedure, as shown in Figure 2.5. The X-ray diffraction pattern of Figure 2.5B of fibers obtained by stretching at high deformation the sample of low crystallinity crystallized by aging at room temperature for 1 month the amorphous compression-molded sample is similar to that of Figure 2.4C and corresponds to a disordered structure and poor crystalline fibers. Well oriented crystalline fibers with improved structural order and crystallinity have been obtained by annealing at 60°C for ≈ 18 h of the stretched sample of Figure 2.5B keeping the fibers under tension (Figure 2.5C). The strong reflection at 2θ = 10.1° is split in two very close equatorial reflections at values of 2θ = 10.1° and 10.9° as observed in Figures 2.5 C and C'. This is in agreement with the diffraction

peak at 2θ = 10.1° in the powder diffraction profiles of Figure 2.3a,d, which presents a clear shoulder that is better resolved in the fiber diffraction pattern of Figure 2.5C .

It is worth noting that that the amorphous compression-molded sample (sample of Figure 2.3b) and the sample crystallized by aging of the compression molded sample for 1 month at room temperature, with a low crystallinity of 19% (sample of Figure 2.3c), can be easily deformed up to high deformations (about 500-600%) and have shown elastomeric properties. After annealing at 70°C for several hours an increase of crystallinity degree is obtained (51%) and as a consequence a decrease of deformability and of elastic properties is observed. Therefore, an important difference between the two procedures is that in second procedure high deformations were reached by stretching of the sample with a low crystallinity degree. The successive annealing of the resulting fiber of iP3MPD12 allowed improving crystallinity and getting well oriented X-ray fiber diffraction pattern. On the contrary, in the first procedure the annealing was performed before stretching of the film. The lower possible deformation of the annealed film, allowed achieving only a disordered structure.

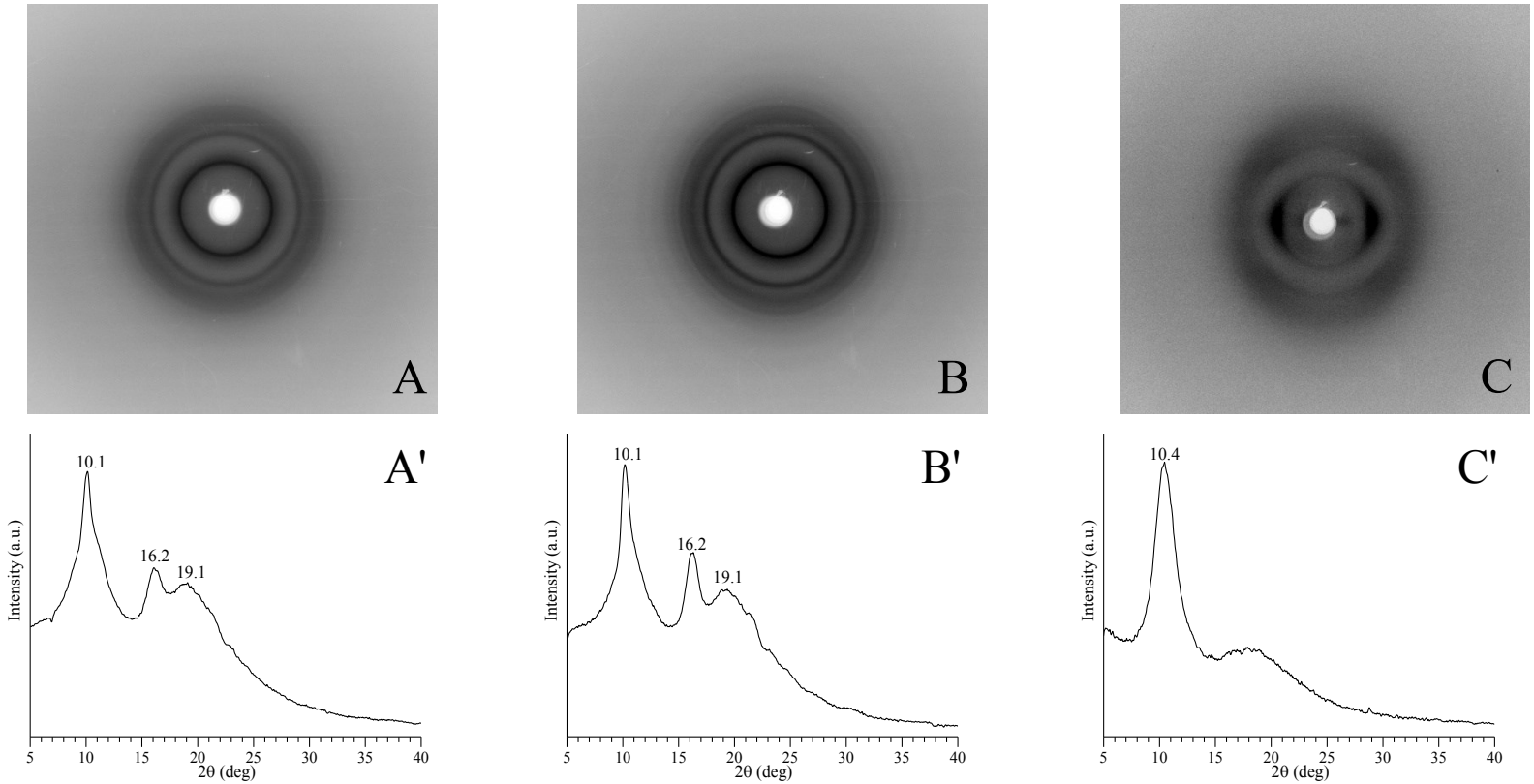

Figure 2.4. X-ray diffraction patterns (A-C), and corresponding equatorial profiles (A'-C'), of the sample crystallized by aging at room temperature for 1 month the compression-molded sample (A,A'), of the aged sample annealed at 70°C for ≈ 20 h (B,B'), and of the annealed sample stretched at high deformation (C,C').

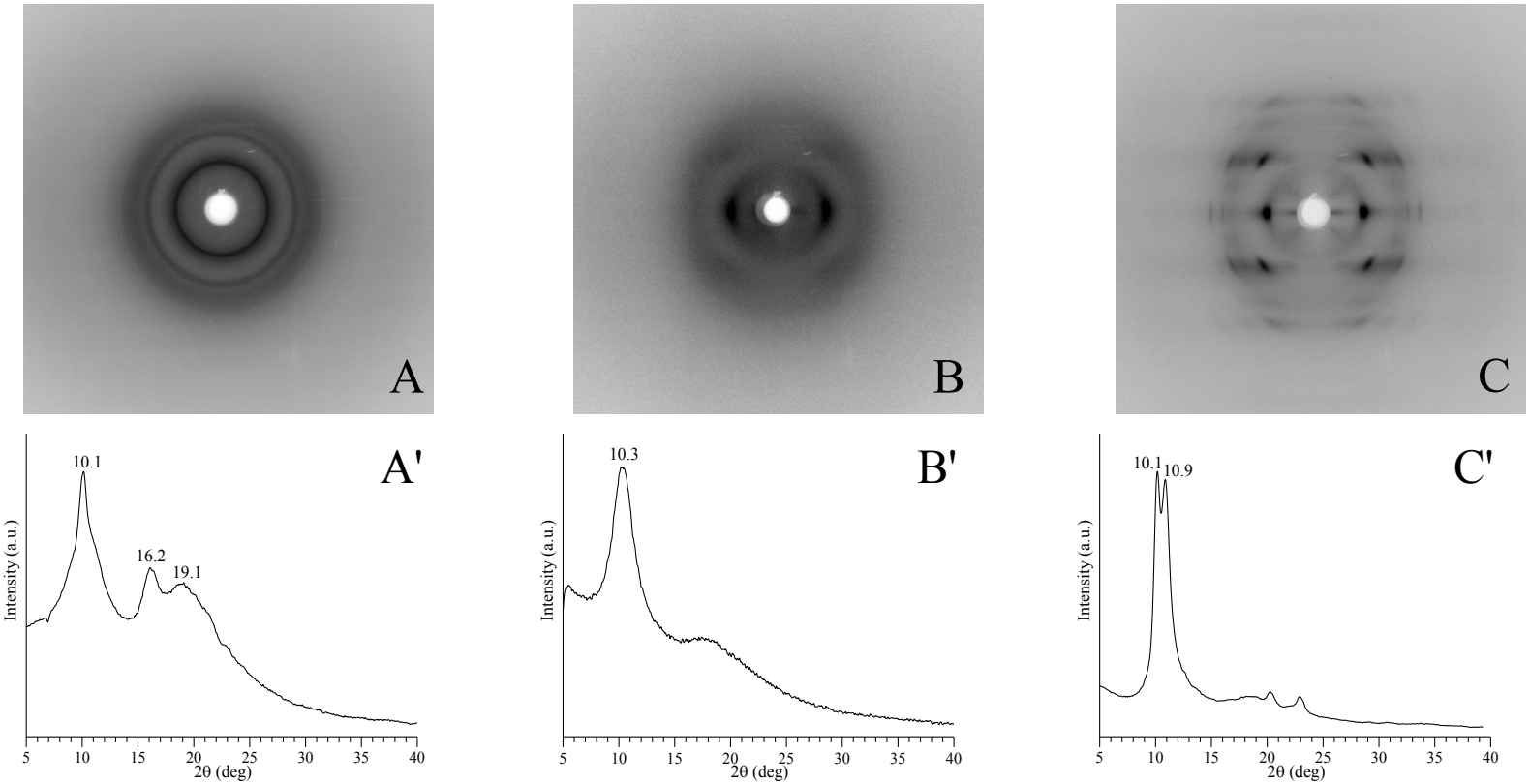

Figure 2.5. X-ray diffraction patterns (A,C), and corresponding equatorial profiles (A',C') of the sample crystallized by aging at room temperature for 1 month the compression-molded sample (A,A'), of fibers obtained by stretching the aged sample at high deformation (B,B'), and of the stretched fibers annealed at 60°C for ≈18 h (C,C').

All reflections observed in the X-ray powder diffraction profiles of Figure 2.3d and in the X-ray fiber diffraction pattern of Figure 2.5C are listed in Table 2.3 and Table 2.4 respectively. Moreover, a nearly meridional reflection at $d = p = \approx 2.1$Å has been observed in a fiber diffraction patter of the annealed fibers in tilted geometry (Figure 2.6). The corresponding approximate value of the ζ coordinate (ζ = 0.46-0.48 Å^{-1}) is reported in the tables 2.3 and 2.4.

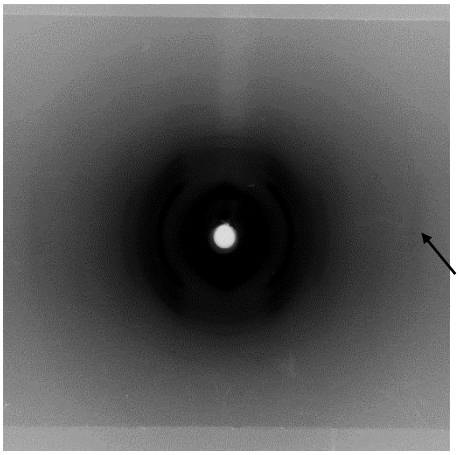

Figure 2.6: X-ray fiber diffraction patter of the annealed fiber of iP3MPD12 in tilted geometry.

Table 2.3. Diffraction angles (2θ), Bragg distances (d_o), and intensities (I_o) of the reflections observed in the X-ray power diffraction profile of Figure 2.3d.

2θ (deg)	d_o (Å)	I_o	*hkl*[a]
10.1	8.76	43	200
13.1	6.70	3	220
16.2	5.48	30	212
19.1	4.65	14	222
21.5	4.14	7	040
23.1	3.84	3	420
24.5	3.63	4	114,204
27.4	3.25	3	124
30.7	2.91	3	600,134
32.8	2.72	2	620,144

a) The Miller indices *hkl* of reflections for an orthorhombic unit cell with parameters a = 17.4 Å, b = 16.5 Å, c = 15.3 Å are also indicated.

Table 2.4. Photographic Coordinates (2x, 2y) of the diffraction spots, Diffraction angles (2θ), Bragg distances (d_o), cylindrical reciprocal coordinates (ξ and ζ), and intensities (I_o) of the reflections observed on the layer lines *l* of the X-ray fiber diffraction pattern of iP3MPD12 of Figure 2.5C.

2x (mm)	2y (mm)	2θ (deg)	d_o (Å)	ξ (Å^{-1})	ζ (Å^{-1})	*l*	I_o[b]	*hkl*[a]
20.20	0	10.1	8.76	0.114	0	0	vs	200
21.98	0	11.0	8.05	0.124	0	0	vs	020
24.78	0	12.4	7.16	0.140	0	0	vvw	120
27.30	0	13.6	6.49	0.154	0	0	vvw	220
36.12	0	18.1	4.91	0.204	0	0	vvw	320
38.18	0	19.1	4.65	0.215	0	0	vvw	230
40.72	0	20.4	4.36	0.229	0	0	m	400
46.18	0	23.1	3.85	0.260	0	0	m	420
58.20	0	29.1	3.07	0.326	0	0	vvw	440
61.68	0	30.8	2.90	0.345	0	0	vvw	600
34.62	11.98	18.3	4.85	0.195	0.067	1	vw	131
38.04	11.98	19.9	4.45	0.214	0.067	1	vw	231
11.86	23.03	12.8	6.92	0.068	0.128	2	vw	112
22.48	23.03	15.9	5.56	0.126	0.128	2	vs	212
31.08	23.03	19.2	4.63	0.174	0.128	2	w	222
36.46	23.03	21.4	4.16	0.204	0.128	2	s	132
41.06	23.03	23.3	3.81	0.229	0.128	2	vw	402
21.00	38.65	21.3	4.17	0.120	0.207	3	m	123
32.72	38.65	24.6	3.62	0.183	0.207	3	vvw	133
11.14	48.34	23.5	3.78	0.079	0.252	4	vw	114
19.14	48.34	24.7	3.60	0.116	0.252	4	m	204
30.28	48.34	27.2	3.28	0.172	0.252	4	vw	124
41.58	48.34	30.5	2.93	0.230	0.252	4	vw	134
46.52	48.34	32.2	2.78	0.256	0.252	4	vvw	144
	121	43.1	2.1	0	0.46-0.48	7	vvvw	007

a) The Miller indices *hkl* of reflections for an orthorhombic unit cell with parameters *a* = 17.4 Å, *b* = 16.5 Å, *c* = 15.3 Å are also indicated. b) vs = very strong; s = strong; m = medium; w = weak; vw = very weak, vvw = very, very weak, vvvw = very, very, very weak.

The intensity distribution of the X-ray fiber diffraction pattern of oriented fiber of iP3MPD12 (Figure 2.5C) is distributed over four off-equatorial layer lines whose height ζ_{obs} are reported in Table 2.5.

Table 2.5. Average values of the diffraction intensity (I_{obs}) on the various layer lines l having experimental cylindrical coordinates ζ_{obs} observed in the X-ray fiber diffraction pattern of Figure 2.5C. Values calculated of ζ (ζ_{calc}) and absolute values of the lowest order of the Bessel functions n that contribute to the diffraction intensity on the layer lines for 7/2 helix.

ζ_{obs} (Å^{-1})	l	I_{obs}	ζ_{calc} (Å^{-1})	n
0.067	1	vw	0.065	3
0.128	2	s	0.131	1
0.208	3	vw	0.196	2
0.252	4	m	0.261	2
0.46-0.48	7	vvvw	0.458	0

The isotactic configuration of the chain suggests that the chain conformation is helical but the indexing of the observed layer lines is nontrivial, indicating that the conformation corresponds to a complex helix. The application of ADR method [10,12] to the diffraction data of iP3MPD12 of Table 2.5 is shown in Figure 2.7. Taking in consideration only the indexing schemes for which the weighted average value of the chain periodicity c is less than 100 Å, and the standard deviation from this average is below a threshold, the most likely solution is delineated by the dotted horizontal lines in Figure 2.7. For instance, the trial values of l = 1, 2, 3, and 4, corresponding to the observed values of ζ of Table 2.5 allow indexing the observed layer lines for an identical value of c = 15.3Å; in the second step a value of M = 7 was evaluated in agreement with this value of c.

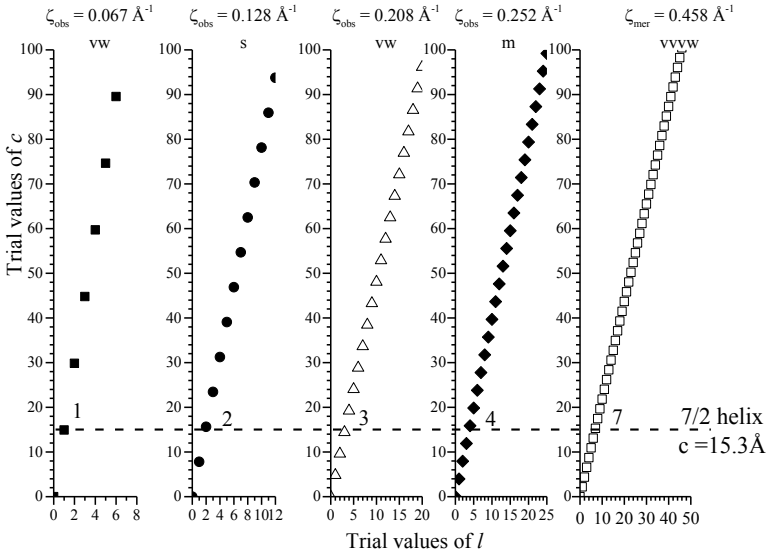

Figure 2.7. Graphical solution of parametric discrete system of eqs 8 and 9, for indexing the observed layer lines of a fiber diffraction pattern of a helical structure in the case of iP3MPD12. For each observed layer line, corresponding to the experimental values of ζ, the possible values of the identity period *c* are plotted as a function of the trial values of the index *l*. The relative experimental intensities (very weak (vw), medium (m), strong (s) observed on the layer line ζ for iP3MPD12 are indicated. The value of ζ on the meridian was evaluated in a successive step, assuming a value of $M = 7$ ($\zeta_{mer} = 7/c = 7/15.3 = 0.458$ Å^{-1}). The solutions is delineated by the dotted horizontal line that correspond to a possible indexing of the observed layer lines for an identical value of *c*.

The values of *N* was established by trial and error, applying selection rule 2' to find for all possible values of *N* (7/1, 7/2, 7/3, 7/4, 7/5 and 7/6 helices) the lowest order Bessel function that contributes to the diffraction intensity on each layer lines. The best qualitative agreement with the experimental intensity distribution was found for the 7/2 helix.

The comparison between the intensity of reflections observed on the various layer lines and the lowest order of the Bessel functions that contribute to the theoretical diffraction intensity on the various layer lines of the possible 7/2 helix, according to the CCV theory and the selection rules 2 and 3, is reported in Table 2.5. The value of ζ_{calc} are also indicated in Table 2.5.

The same solution was found by using the method of Mitsui.[15] The diagram ζ'_{rel} vs p/P was used, where the values of $\zeta'_{rel} = \zeta p$ were calculated

from the experimental values of ζ, determined from the X-ray fiber diffraction pattern and reported in Table 2.5, multiplied for a value of the unit height p = 2.18 Å ($p = c/M = 15.3/7 \approx 2.18$ Å).

The plot of Figure 2.8 shows that a satisfactory agreement between the experimental values of ζ'_{rel}, the spacing of the layer lines, and a reasonable correspondence of the order n of the Bessel function to the relative experimental intensities of reflections on the layer lines are obtained for helices with P/p = 3.5 (Table 2.5). This possible solution corresponds to the 7/2 helix.

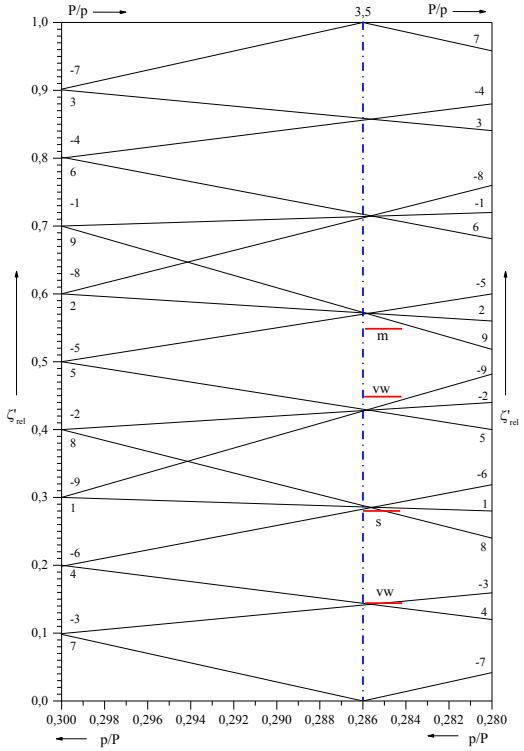

Figure 2.8. ζ'_{rel} - p/P diagram applied to the 7/2 helix of iP3MPD12. The number on the straight lines indicates the order of the Bessel functions that contribute to the diffraction intensity on the layer lines corresponding to the values of $\zeta'_{rel} = \zeta\, p$. The relative experimental intensities (very weak (vw), medium (m), strong (s) observed on the layer line ζ for iP3MPD12 are indicated. The solutions for a 7/2 helix with a ratio P/p = 3.5 (or p/P = 0.286) is delineated by the dotted vertical line.

It is worth noting that the solution of 7/2 helix for the chain conformation of iP3MPD12 is only the first nontrivial approximation of commensurable helix, with the lowest *M* and *N* integer number. Slight deviation of the ratio *P*/*p* from the value of 3.5 gives high values of *M* and *N* and incommensurable helix.

The formation of *s*(M/N) complex helical symmetry, with *M* and *N* not corresponding to very small integers, is a consequence of the bulkiness of the lateral groups [19] and corresponds to isodistortions for the torsion angles θ_1 and θ_2 of the backbone bonds from the exact gauche and trans values, as already found for various isotactic polymers.[20]

The identity period *c* = 15.3Å of iP3MPD, calculated as the weighted average of l/ζ_{obs}, is not very different to the value of the chain axis of 13.80Å found for the form I of isotactic poly(4-methyl-1-pentene) (iP4MP) that assume a 7/2 helical conformation [21] . In addition we recall that others isotactic polyolefin, as isotactic poly(1-hexene), the form I of isotactic poly((S)-4-methyl-1-hexene) and isotactic poly((R),(S)-4-methyl-1-hexene) assume the same 7/2 helical conformation as that proposed for iP3MPD12.

All reflections observed in the X-ray powder and fiber diffraction patterns are accounted for by an orthorhombic unit cell with axes *a* = 17.4Å, *b* = 16.5Å, *c* = 15.3Å. The indices *hkl* of the reflections according to this orthorhombic unit cell are reported in Table 2.3 and 2.4 respectively. The presence of two close equatorial reflections at low values of 2θ = 10.1° and 11° allowed to exclude a possible tetragonal packing, which is a typical packing of complex helices, as in the case of iP4MPD12. [4]

The calculated crystalline density of 0.869 g/cm^3, for four chains included in the unit cell, is compatible with the experimental densities of 0.882 g/cm^3 measured at 25°C by flotation on a sample having 51% crystallinity and the density of 0.884 g/cm^3 measured on an amorphous sample. According to

this structure, the calculated crystalline density is lower than the density of the amorphous phase. This feature was also found in the case of iP4MPD12 [4] and form I of iP4MP [21].

The indexing of the observed reflections indicates, disregarding the very very weak 230 reflection observed in the fiber pattern, the systematic absence of *hk*0 and 0*k*0 reflections with *k* odd and the systematic absence of *h*00 reflections with *h* odd. This suggests that a possible space group, compatible with the presence of four chains in the unit cell, could be $P2_1ab$. Models of chain conformation with 7/2 helical symmetry and of packing have been built by performing calculation of conformational and packing energy. The calculations of the conformational energy have been performed on a portion of isolated chains of iP3MPD12 shown in Figure 2.9, by application of the equivalence principle [10] to successive constitutional units by assuming a line repetition group $s(M/N)$ for the polymer chain. As a consequence, the sequence of the torsion angles in the main chain is of the kind ...$\theta_1\theta_2\theta_1\theta_2$... (Figure 2.9).

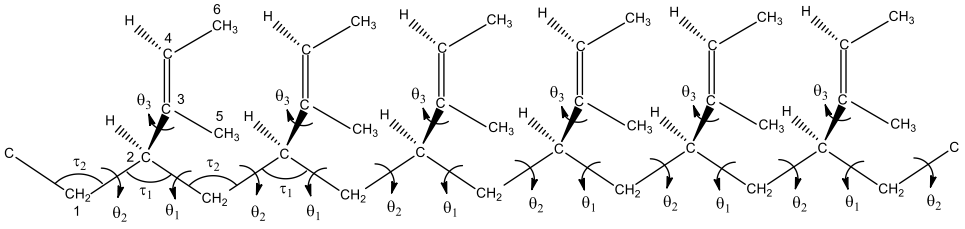

Figure 2.9. Portion of the chain of iP3MPD12 used in the conformational energy calculations with definition of the torsion angles θ_1, θ_2, and θ_3, and the bond angles τ_1 and τ_2. The torsion angle θ_3 is defined with respect to the carbon of the CH group of the ethenyl side group: θ_3 = C4−C3−C2−C1.

The conformational energy maps for chains of iP3MPD12 as a function of θ_1 and θ_2 are shown in Figure 2.10. In these maps for each pair of θ_1 and θ_2, the positions of the side groups, defined by the torsion angles θ_3, was varied in step of 5° of θ_3, to place it in the minimum-energy position

corresponding to that pair of θ_1 and θ_2. Two equivalent absolute minima observed in the map of Figure 2.10 are located in the region $\theta_1 \approx G^+$, $\theta_2 \approx T$ and $\theta_1 \approx T$, $\theta_2 \approx G^-$. The values of torsion angles and of the relative energies are reported in Table 2.6.

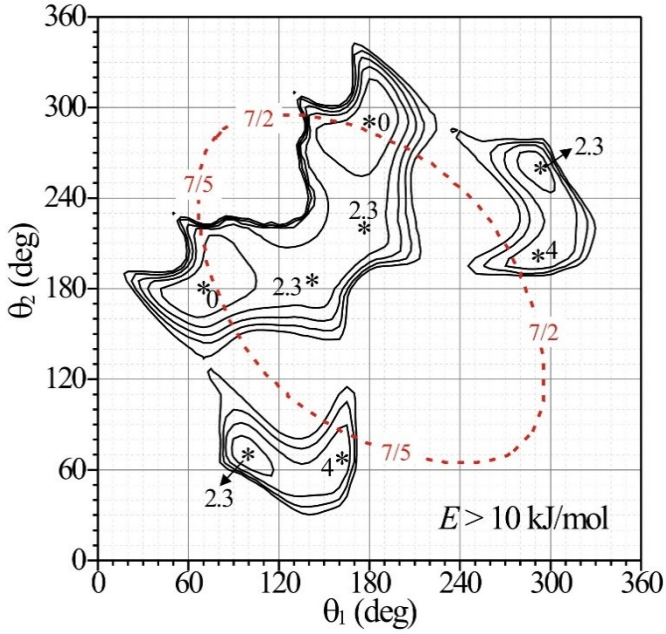

Figure 2.10. Maps of the conformation energy of iP3MPD12 as a function of θ_1 and θ_2 with θ_3 scanned every 5° in the *s*(*M*/*N*) line repetition group for $\tau_1 = 111°$ and $\tau_2 = 113°$. The curves are reported at intervals of 2 kJ/mol of monomeric units with respect to the absolute minimum of the maps assumed as zero. The values of the energy corresponding to the minima (∗) are also reported. The dashed curves represent the loci of points of couples of torsion angles θ_1 and θ_2 corresponding to the s(7/2) helical conformations.

Table 2.6. Values of torsion angles of the backbone θ_1 and θ_2, and of the lateral group θ_3 (Figure 2.9) corresponding to the minima of the conformational energy found in map of Figure 2.10 and values of the corresponding energy E scaled with respect to the absolute minimum of the map assumed as zero.

θ_1 (deg)	θ_2 (deg)	θ_3 (deg)	E (kJ/mol mu)
70	180	-115	0
180	-70	-120	0
140	-175	65	2.3
175	-140	60	2.3
100	70	90	2.6
-70	-100	30	2.6
160	65	85	4.0
-70	-160	35	4.0

The loci of points corresponding to the s(7/2) helical symmetry, with values of the unit twist $t = 2\pi\ N/M$ of 102.8°, are also reported in the maps of Figure 2.10. It is apparent that the absolute energy minimum is close the conformation with $s(7/2)$ symmetry and value of $t = 102.8°$.

The loci of the points corresponding to the $s(7/2)$ helical symmetry and to the value of the unit height $h = c/7 = 2.18$ Å are shown in the map of Figure 2.11. The pairs of values of θ_1 and θ_2 that satisfy the unit twist of the helical symmetry of 102.8° and the unit height of 2.18 Å, corresponding to the intersection points of the curves of Figure 2.11, are $\theta_1 = 81°$, $\theta_2 = 171°$ and $\theta_1 = -171°$, $\theta_2 = -81°$.

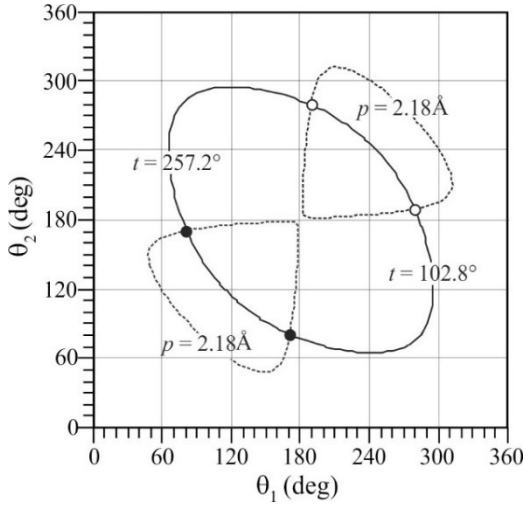

Figure 2.11. Map as a function of θ_1 and θ_2 of the loci of points for which the helical symmetry is $s(7/2)$ (continuous lines) and $h = 2.18$Å (dashed lines). The intersection points are indicated by circles.

Models of the chains of iP3MPD12 are built with the values of the dihedral angles along the main chain of $\theta_1 = 81°$, $\theta_2 = 171°$ (left-handed helix) and $\theta_1 = -171°$, $\theta_2 = -81°$ (right-handed helix). The possible conformations of the side groups have been evaluated by calculating the conformational energy of the 7/2 right-handed helix with $\theta_1 = -171°$ and $\theta_2 = -81°$ (or of the 7/2 left-handed helix with $\theta_1 = 81°$ and $\theta_2 = 171°$) varying the torsion angles θ_3. The conformational energy profile as a function of θ_3 for these fixed values of θ_1 and θ_2 are reported in Figure 2.12. Two energy minima are obtained for 7/2 helices with a value of $\theta_3 \approx G^+$ and A^-.

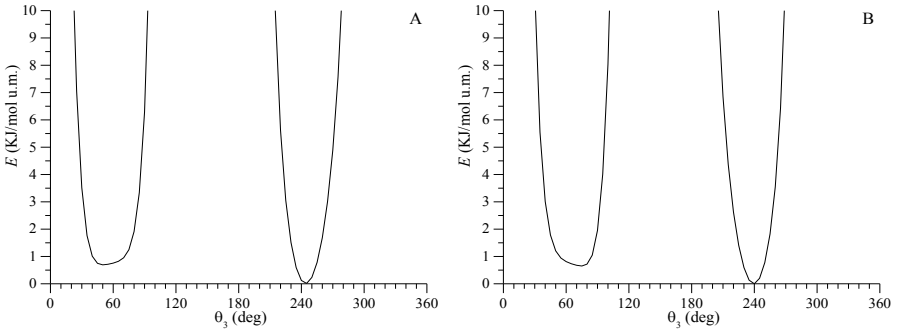

Figure 2.12. Curves of the conformational energy as a function of θ_3 for the 7/2 left-handed helix with $\theta_1 = 81°$ and $\theta_2 = 171°$ (A) and the 7/2 right-handed helix with $\theta_1 = -171°$ and $\theta_2 = -81°$.

The two possible conformations of 7/2 left-handed helix and of 7/2 right-handed helix are show in Figure 2.13 and the corresponding value of the torsion angle of the main chain and of the lateral group are reported in Table 2.7.

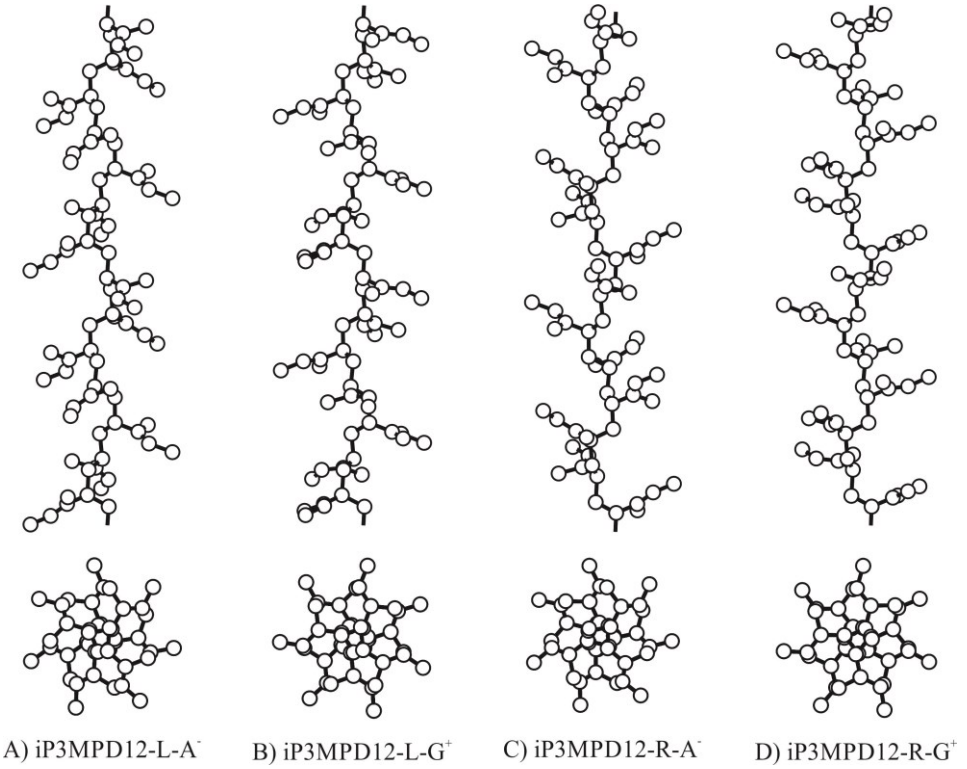

Figure 2.13. Four models of possible 7/2 conformations of the chains of iP3MPD12 found by calculations of conformational energy of Figures 2.11 and 2.12. The models correspond to the conformations defined in Table 2.7.

Table 2.7. Values of torsion angles of the backbone θ_1 and θ_2, and of the lateral group θ_3 (Figure 2.9) corresponding to the minima of the conformational energy found in the geometrical map of Figure 2.11 and in the energy profiles of Figure 2.12. Values of the corresponding energy *E* scaled with respect to the absolute minimum of the map assumed as zero are reported. In the name of model, L and R indicate left and right-handed, respectively, and A^- and G^+ indicate the value of the torsion angle θ_3 (A^- or G^+).

model of figure 2.13	θ_1 (deg)	θ_2 (deg)	θ_3 (deg)	*E* (kJ/mol mu)	helix simmetry
A) iP3MPD12-L-A^-	81	171	-115	0	7/2 left-handed
B) iP3MPD12-L-G^+	81	171	50	0.7	7/2 left-handed
C) iP3MPD12-R-A^-	-171	-81	-120	0	7/2 right-handed
D) iP3MPD12-R-G^+	-171	-81	75	0.6	7/2 right-handed

In order to find the best position of the chains inside the unit cell, calculations of the packing energy were performed for the space group $P2_1ab$. The axes of the unit cell have been maintained constant at the values a = 17.4 Å, b = 16.5 Å, c = 15.3 Å and the position of the chain axis inside the unit cell was fixed at the fractional coordinates $x/a = y/b = 0.25$. The lattice energy has been calculated varying only the orientation of the chain around its axis (defined by the angle ω, shown in Figure 2.14), and the z coordinate, which defines relative heights of the chains in the unit cell.

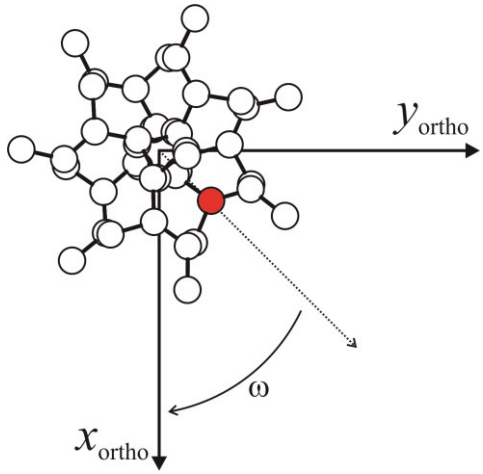

Figure 2.14. Definitions of the variables ω and z used in the packing energy calculations in the orthogonal coordinates systems. The value of ω is positive for a clockwise rotation, and z is the height of the carbon atom indicated as a filled circle.

Maps of the packing energy for the models of Figure 2.13 as a function of ω and z for the space group $P2_1ab$ are reported in Figure 2.15. The maps are periodic over $\omega = 180°$ and $z = c/2 = 7.65$Å, so only the regions with $\omega = 0\text{-}180°$ and z = 0-7.65 Å are shown. It is apparent that each map presents several equivalent energy minima; indeed, every minimum repeats identically after a rotation of $\omega = |180° - t| = 77°$, where t is the unit twist ($t = 360\times2/7) = 102.8°$), and a translation of $z = h = c/7 = 2.18$Å, where h is the unit height.

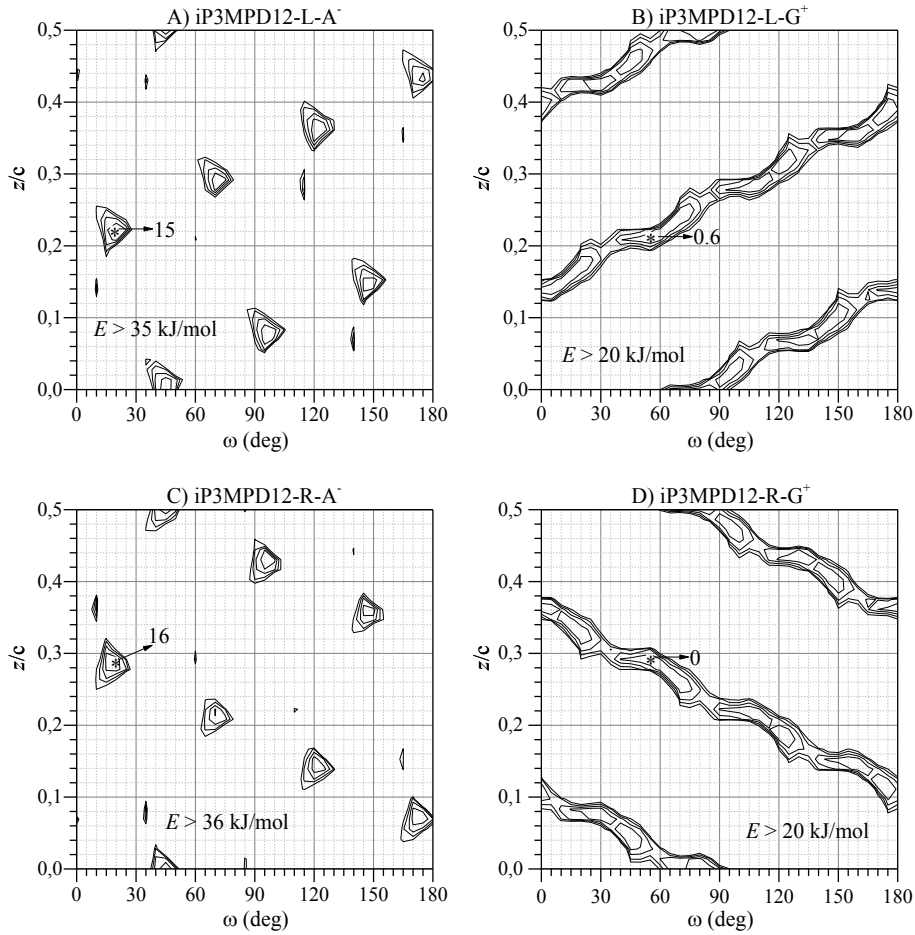

Figure 2.15. Maps of the packing energy as a function of ω and z for the monoclinic unit cell with axes a = 17.4 Å, b = 16.5 Å, c = 15.3 Å, for the space group symmetry $P2_1ab$, for models of the chain conformation of iP3MPD12 of Figure 2.13 and Table 2.7. In all models the position of the chain axis inside the unit cell was fixed at the fractional coordinates $x/a = y/b = 0.25$. The curves are drawn at intervals of 5 kJ/(mol of monomeric unit) with respect to the absolute minimum of the maps assumed as zero in (D).

The deepest minima of packing energy occur for models of iP3MPD12 having lateral group with $\theta_3 \approx G^+$ (Figures 2.15B and D). For models of chains with $\theta_3 \approx A^-$ packing energies higher than 10 kJ/mol are calculated (Figures 2.15A and 2.15C). Therefore only chains of iP3MPD12 having lateral group with $\theta_3 \approx G^+$ may be present in the unit cell. The value of ω and z indicated in Figure 2.15 are reported in Table 2.8.

Table 2.8. Values of the packing energy minima and corresponding values of ω and z found in the maps of the packing energy of Figure 2.15 for the chain models iP3MPD12-L-A^- (left-handed 7/2 chain of iP3MPD12 with $\theta_3 = A^-$) (Figure 2.13A), iP3MPD12-L-G^+ (left-handed 7/2 chain of iP3MPD12 with $\theta_3 = G^+$) (Figure 2.13B), iP3MPD12-R-A^- (right-handed 7/2 chain of iP3MPD12 with $\theta_3 = A^-$) (Figure 2.13C), iP3MPD12-R-G^+ (right-handed 7/2 chain of iP3MPD12 with $\theta_3 = G^+$) (Figure 2.13D).

model of packing	θ_1 (deg)	θ_2 (deg)	θ_3 (deg)	ω (deg)	z/c	E_{pack}[a] (kJ/mol mu)
A) iP3MPD12-L-A^-	81	171	-115	20	0.22	15
B) iP3MPD12-L-G^+	81	171	50	55	0.21	0.6
C) iP3MPD12-R-A^-	-171	-81	-120	20	0.29	16
D) iP3MPD12-R-G^+	-171	-81	75	55	0.29	0

a. The values of the packing energy E_{pack} are scaled with respect to the absolute minimum of the maps of Figure 2.15D assumed as zero.

Calculations of the structure factors were performed for different models of packing corresponding to the different positions of the chain in the unit cell which give the energy minima present in the maps of Figure 2.15D (or Figure 2.15B). A good agreement between calculated structure factors and experimental intensities observed in the X-ray powder diffraction profile of Figure 2.3d and in the X-ray fiber diffraction pattern of Figure 2.5C, is obtained for a model of chains iP3MPD12-R-G^+ with $\omega = 55°$ and $z = 4.46$ Å corresponding to the absolute minimum of the packing energy of the map of Figure 2.15D. This model of packing of iP3MPD12 that gives the best agreement is reported in Figure 2.16. A comparison between observed structure factors (F_0), evaluated from the X-ray powder diffraction profile of Figure 2.3d after the subtraction of the amorphous halo, and the structure factors calculated for the model of Figure 2.16 is reported in Table 2.9. A qualitative comparison between the calculated X-ray fiber diffraction pattern and the experimental pattern is reported in Table 2.10. The disagreement factor calculated for all observed reflections is $R = 15$ %.

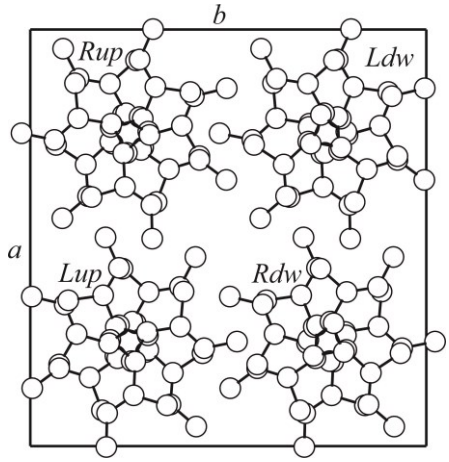

Figure 2.16. Limit ordered model of packing of chains of the chains of iP3MPD12 in 7/2 helical conformation in the orthorhombic unit cell with axes a = 17.4 Å, b= 16.5 Å, c = 15.3 Å according to the space group $P2_1ab$, corresponding to the minimum of the maps of packing energy of Figure 2.15D. The model of chains iP3MPD12-R-G^+ is considered with $\theta_3 = G^+$.

It is apparent that in the model of Figure 2.16 each right-handed helix is surrounded by four left-handed helices and vice versa.

This kind of packing is generally observed in a tetragonal lattice with chains in 4/1 helical conformation or complex *M*/*N* conformation [10]. For instance, chains of isotactic poly(*o*-methylstyrene) and isotactic poly(vinylcyclohexane) with 4/1 helical conformation are packed in the same manner in tetragonal lattices according to the space group $I4_1cd$ [22] and $I4_1/a$ [23] respectively. In the case of complex helices chains of iP4MPD12 with 18/5 helical conformation or chains of form I of iP4MP with 7/2 helical conformation are arranged in the same packing mode in tetragonal lattices according to the space group $I\bar{4}c2$ [4] and $P\bar{4}$ [21] respectively.

It is well know that depending on the conformation, the shape of a polymer chain may be approximated by a cylinder of radius *r*, corresponding to the outside envelope of the atoms of the main chain, bearing a periodic helical relief of radius *R*, corresponding to the atoms of the later groups. [10] Generally, polymers with ratio *r*/*R* in the range 0.3-0.8, crystallize in a

tetragonal lattice in which each right-handed helix is surrounded by four left-handed helices and vice versa.

In the models of chain conformation with complex *s*(7/2) helical symmetry of iP3MPD12 (Figures 2.13 and 2.16), appears that the chains have a cylindrical outside envelope, in which hollows and bulges are periodically repeated, as it occurs in a screw. Hence, the packing mode of the macromolecules of iP3MPD12 is in agreement with the shape of the helices although they do not pack in a tetragonal lattice as is generally expected, but in a orthorhombic lattice with similar axis *a* e *b* (*a* = 17.4 Å, *b* = 16.5 Å). The iP3MPD12 represents an exception to the rule of packing of chains having complex helical conformation indeed, for this polymer. Exceptions to this simple rule have been found for form III of isotactic poly(1-butene), characterized by 4_1 helical chains packed in an orthorhombic lattice with space group $P2_12_12_1$, [24] for isotactic poly(3-methyl-1-butene), characterized by 4_1 helical chains packed in a monoclinic lattice with space group $P2_1/b$, [25] and for form II of syndiotactic poly(1-butene) with complex *s*(5/3)2 helical conformation packed monoclinic lattice with space group $P2_1/a$. [26]

Another important aspect is that antichiral structures, characterized by the packing of enantiomorphous helical chains, are generally obtained through crystallographic glide planes or inversion centers. Glide planes parallel to the chain axes are able to repeat neighboring enantiomorphous and isoclined chains producing a good space filling (as in the space group $I4_1cd$), whereas inversion centers produce a packing of enantiomorphous and anticlined chains (as in the space group $I4_1/a$). [10] Therefore, in the space group $P2_1ab$ neighboring enantiomorphous chains of iP3MPD12 are isoclined and related by glide planes. As a consequence rows of enantiomorphous isoclined helices are generated along *a* and rows of enantiomorphous anticlined helices are generated along *b*.

Table 2.9. Comparison between observed structure factors $F_o = (I/LP)^{1/2}$, evaluated from the intensities I observed in the X-ray powder diffraction profile of iP3MPD12 of Figure 2.3d, and calculated structure factors, $F_c = (\Sigma|F_i|^2 \cdot M_i)^{1/2}$, for the model of packing of Figure 2.16 in the orthorhombic unit cell with axes a = 17.4 Å, b =16.5 Å, c = 15.3 Å according to the space group $P2_1ab$.

hkl	$2\theta_o$ (deg)	$2\theta_c$ (deg)	d_o(Å)	d_c(Å)	$F_o = (I_o/LP)^{1/2}$	$F_c=(\Sigma\|F_i\|^2 M_i)^{1/2}$ Model of Figure 2.16
111		9.38		9.43		73
200	10.12	10.17	8.76	8.70	632	550 } 742
020		10.72		8.25		493
201		11.70		7.56		134
211	13.11	12.88	6.70	6.87	217	32 } 190
121		13.21		6.70		107
112		13.74		6.45		75
220		14.80		5.99		268
202		15.42		5.74		116
221		15.90		5.57		184
212	16.16	16.33	5.48	5.42	849	597 } 923
122		16.60		5.34		572
031		17.13		5.18		114
311		17.21		5.15		189

131	19.10	17.89	4.65	4.96	688	122	577
013		18.21		4.87		111	
320		18.70		4.74		70	
222		18.82		4.71		166	
113		18.91		4.69		137	
321		19.59		4.53		202	
032		19.89		4.47		14	
312		19.95		4.45		100	
231		19.96		4.45		210	
203		20.18		4.40		161	
400		20.41		4.35		125	
023		20.47		4.34		169	
132		20.53		4.33		243	
213		20.89		4.25		174	
123	21.46	21.11	4.14	4.21	549	234	359
401		21.23		4.18		65	
040		21.54		4.12		126	
411		21.91		4.06		151	
322		22.04		4.03		39	
140		22.15		4.01		11	
232		22.38		3.97		43	
141		22.91		3.88		167	
223	23.15	22.91	3.84	3.88	389	47	400
331		23.03		3.86		23	
420		23.11		3.85		181	
402		23.53		3.78		199	
033		23.79		3.74		97	
313		23.85		3.73		205	
240		23.87		3.73		183	
014		23.88		3.73		14	

412		24.14		3.69		13	
133		24.34		3.66		170	
114		24.43		3.64		239	
042		24.52		3.63		61	
142	24.51	25.05	3.63	3.55	477	61	562
332		25.17		3.54		218	
204		25.44		3.50		233	
024		25.67		3.47		234	
422		25.92		3.44		256	
214		26.01		3.42		31	
124		26.18		3.40		41	
340		26.52		3.36		68	
242		26.60		3.35		117	
431		26.77		3.33		83	
511		26.82		3.32		24	
403		26.94		3.31		166	
341		27.16		3.28		50	
413		27.49		3.24		72	
051		27.65		3.23		23	
224	27.45	27.67	3.25	3.22	465	18	416
043		27.82		3.21		125	
520		27.82		3.21		64	
151		28.13		3.17		38	
143		28.29		3.15		50	
333		28.40		3.14		161	
521		28.44		3.14		142	
314		28.47		3.13		141	
432		28.65		3.12		46	
512		28.70		3.11		58	
134		28.89		3.09		116	

342		29.01		3.08		40	
423		29.07		3.07		84	
052		29.48		3.03		54	
251		29.53		3.02		122	
243		29.69		3.01		92	
440		29.85		2.99		156	
152		29.93		2.98		264	
324		30.00		2.98		17	
115		30.14		2.96		261	
522		30.22		2.96		54	
234		30.26		2.95		37	
441		30.43		2.94		66	
600		30.83		2.90		112	
531	30.71	30.96	2.91	2.89	525	47	636
205		30.98		2.89		197	
404		31.14		2.87		66	
252		31.26		2.86		51	
601		31.39		2.85		45	
215		31.46		2.84		268	
433		31.55		2.84		75	
513		31.59		2.83		59	
125		31.61		2.83		268	
414		31.61		2.83		45	
351		31.74		2.82		60	
611		31.87		2.81		93	
343		31.89		2.81		149	
044		31.91		2.80		43	
442		32.11		2.79		160	

053		32.31		2.77		90	
144		32.33		2.77		30	
334		32.42		2.76		60	
060		32.56		2.75		77	
532		32.62		2.74		124	
153		32.73		2.74		13	
620		32.73		2.74		139	
225		32.87		2.72		29	
160		32.97		2.72		60	
523		32.99		2.71		112	
424		33.02		2.71		40	
602	32.76	33.03	2.72	2.71	459	165	446
061		33.10		2.71		54	
621		33.26		2.69		32	
352		33.36		2.69		168	
612		33.49		2.67		39	
161		33.50		2.67		102	
035		33.51		2.67		20	
244		33.57		2.67		40	
540		33.69		2.66		121	
135		33.92		2.64		34	
253		33.96		2.64		120	
260		34.20		2.62		134	
541		34.22		2.62		68	

Table 2.10. Comparison between observed intensities I of X-ray fiber diffraction pattern of iP3MPD12 of Figure 2.5C, and calculated structure factors, $F_c = (\Sigma|F_i|^2 \cdot M_i)^{1/2}$, for the model of packing of Figure 2.16 in the orthorhombic unit cell with axes a = 17.4 Å, b =16.5 Å, c = 15.3 Å according to the space group $P2_1ab$. The calculated intensities I evaluated on the basis of F_c are also reported.

hkl	$2\theta_o$ (deg)	$2\theta_c$ (deg)	d_o(Å)	d_c(Å)	I_o[a]	$F_c=(\Sigma\|F_i\|^2M_i)^{1/2}$ Model of Figure 2.16	I_c[a]
200	10.09	10.17	8.76	8.70	vs	389	vs
020	10.98	10.72	8.05	8.25	vs	348	vs
120	12.36	11.87	7.16	7.45	vvw	5	vvw
220	13.65	14.79	6.49	5.99	vvw	190	s
320	18.06	18.70	4.91	4.74	vvw	50	vvw
230	19.09	19.09	4.65	4.65	vvw	—	—
400 040	20.36	24.41 21.54	4.36	4.35 4.12	m	88 89 } 125	m
420 240	23.09	23.11 23.87	3.85	3.85 3.73	m	128 130 } 182	s
340	—	26.52	—	3.36	—	48	vvw
250 440	29.1	27.82 29.85	3.07	3.21 2.99	vvw	45 111 } 120	m
600	30.84	30.83	2.90	2.90	vvw	79	vw
060	—	32.56	—	2.75	—	75	vw
620	—	32.73	—	2.74	—	98	w
160	—	32.97	—	2.72	—	42	vvw
540	—	33.69	—	2.66	—	85	w
260	—	34.19	—	2.62	—	95	w
360	—	36.15	—	2.48	—	57	vw
720	—	37.80	—	2.38	—	32	vvw
640	—	37.92	—	2.37	—	45	vvw
460	—	38.74	—	2.32	—	63	vw
111	—	9.38	—	9.43	—	36	vvw
201	—	11.7	—	7.56	—	69	vw
211	—	12.88	—	6.87	—	16	vvw
121	—	13.21	—	6.70	—	53	vw
221	—	15.90	—	5.57	—	92	w
031 311 131	18.39	17.13 17.21 17.88	4.85	5.18 5.15 4.96	vw	57 94 61 } 126	m

321 231 401 411	19.95	19.59 19.96 21.23 21.91	4.45	4.53 4.45 4.18 4.06	vw	101 105 32 75 } 167	s
141	—	22.91	—	3.88	—	83	vw
331	—	23.03	—	3.86	—	11	vvw
431	—	26.77	—	3.33	—	41	vvw
511	—	26.82	—	3.32	—	12	vvw
341	—	27.16	—	3.28	—	25	vvw
051	—	27.65	—	3.22	—	12	vvw
151	—	28.13	—	3.17	—	19	vvw
521	—	28.44	—	3.14	—	71	vw
251	—	29.53	—	3.02	—	61	vw
441	—	30.43	—	2.94	—	33	vvw
531	—	30.96	—	2.89	—	24	vvw
601	—	31.39	—	2.85	—	22	vvw
351	—	31.74	—	2.82	—	30	vvw
611	—	31.87	—	2.81	—	46	vvw
061	—	33.09	—	2.71	—	27	vvw
621	—	33.26	—	2.69	—	16	vvw
161	—	33.50	—	2.67	—	51	vw
541	—	34.22	—	2.62	—	34	vvw
451	—	34.62	—	2.59	—	56	vw
261	—	34.71	—	2.58	—	19	vvw
711	—	37.04	—	2.43	—	37	vvw
551	—	38.03	—	2.37	—	14	vvw
721	—	38.27	—	2.35	—	33	vvw
641	—	38.40	—	2.34	—	43	vvw
171	—	39.00	—	2.31	—	20	vvw
461	—	39.20	—	2.30	—	28	vvw
112	12.80	13.74	6.92	6.45	vw	38	vvw
202 212 122	15.93	15.42 16.34 16.60	5.56	5.75 5.43 5.34	vs	58 298 268 } 405	vs
222 312	19.17	18.82 19.85	4.63	4.71 4.45	w	83 50 } 97	w
132 322 232	21.38	20.53 22.04 22.38	4.16	4.33 4.03 3.97	s	121 20 21 } 124	m

402 042 332 422	23.35	23.53 24.52 25.17 25.92	3.81	3.78 3.63 3.54 3.44	vw	99 30 109 128 } 197	s
242	—	26.60	—	3.35	—	59	vw
432	—	28.65	—	3.12	—	23	vvw
512	—	28.70	—	3.11	—	29	vvw
342	—	29.01	—	3.08	—	20	vvw
052	—	29.48	—	3.03	—	27	vvw
152	—	29.93	—	2.98	—	132	m
522	—	30.22	—	2.96	—	27	vvw
252	—	31.26	—	2.86	—	26	vvw
442	—	32.11	—	2.78	—	80	vw
532	—	32.62	—	2.74	—	62	vw
602	—	33.03	—	2.71	—	83	vw
352	—	33.36	—	2.68	—	84	vw
612	—	33.49	—	2.67	—	20	vvw
062	—	34.66	—	2.59	—	22	vvw
622	—	34.82	—	2.58	—	89	vw
162	—	35.05	—	2.55	—	23	vvw
542	—	35.74	—	2.51	—	38	vvw
452	—	36.12	—	2.49	—	21	vvw
262	—	36.21	—	2.48	—	41	vvw
632	—	36.96	—	2.43	—	20	vvw
362	—	30.08	—	2.36	—	33	vvw
712	—	38.47	—	2.34	—	40	vvw
552	—	39.43	—	2.28	—	45	vvw
722	—	39.66	—	2.27	—	33	vvw
642	—	39.78	—	2.27	—	53	vw
013 113 203 023 213 123	21.3	18.21 18.91 20.18 20.47 20.89 21.11	4.17	4.87 4.69 4.40 4.34 4.25 4.21	m	56 69 80 84 87 117 } 206	s

223		22.91		3.88		23	
033		23.79		3.74		48	
313		23.85		3.73		102	
133	24.61	24.34	3.62	3.66	vvw	85 } 181	s
403		26.94		3.31		83	
413		27.48		3.25		36	
043		27.82		3.21		63	
143	—	28.29	—	3.15	—	25	vvw
333	—	28.39	—	3.14	—	81	vw
423	—	29.07	—	3.07	—	42	vvw
243	—	29.69	—	3.00	—	46	vvw
433	—	31.55	—	2.84	—	38	vvw
513	—	31.59	—	2.83	—	30	vvw
343	—	31.88	—	2.81	—	74	vw
053	—	32.31	—	2.77	—	47	vvw
523	—	32.99	—	2.71	—	56	vw
253	—	33.96	—	2.64	—	60	vw
533	—	35.23	—	2.55	—	49	vvw
603	—	35.61	—	2.52	—	48	vvw
353	—	35.92	—	2.50	—	37	vvw
613	—	36.04	—	2.49	—	63	vw
063	—	37.14	—	2.42	—	29	vvw
623	—	37.29	—	2.41	—	51	vw
163	—	37.51	—	2.39	—	25	vvw
543	—	38.16	—	2.36	—	72	vw
453	—	38.52	—	2.34	—	17	vvw
263	—	38.61	—	2.33	—	43	vvw
633	—	39.31	—	2.29	—	31	vvw
114	23.51	24.43	3.79	3.64	vw	119	m
204		25.44		3.50		116	
024	24.69	25.67	3.61	3.47	m	117 } 165	s
214		26.01		3.42		16	
124	27.2	26.18	3.28	3.40	vw	20 } 74	vw
314		28.47		3.13		71	
134	30.53	28.89	2.93	3.09	vw	58 } 61	vw
234		30.26		2.95		18	

404		31.13		2.87		33	
414		31.61		2.83		22	
044		31.91		2.80		21	
144	32.17	32.33	2.78	2.77	vvw	15 } 63	vw
334		32.42		2.76		30	
424		33.02		2.71		20	
244		33.57		2.68		20	
434	—	35.24	—	2.55	—	32	vvw
514	—	35.29	—	2.54	—	17	vvw
614	—	39.37	—	2.29	—	15	vvw

a. vs = very strong; s = strong; m = medium; w = weak; vw = very weak, vvw = very, very weak.

A direct comparison between the experimental powder diffraction profile of Figure 2.3d (after subtraction of the amorphous contribution) and the diffraction profile calculated for the model of Figure 2.16 is shown in Figure 2.17, whereas a comparison between the fiber diffraction pattern of Figure 2.5C and that calculated is shown in Figure 2.18.

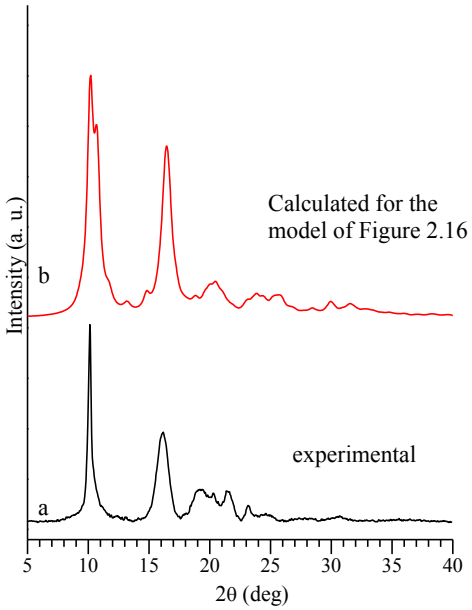

Figure 2.17. Comparison between the experimental X-ray powder diffraction profile of iP3MPD12 (a) and diffraction profile calculated for the model of packing of space group symmetry $P2_1ab$ of Figure 2.16 (b).

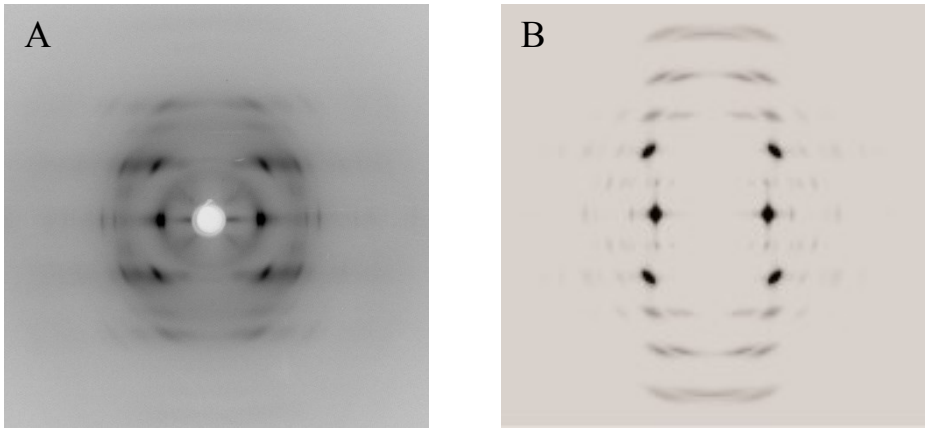

Figure 2.18. Comparison between the experimental X-ray fiber diffraction patter of iP3MPD12 (A) and the diffraction pattern calculated for the model of packing of space group symmetry $P2_1ab$ of Figure 2.16 (B).

The calculated patterns (Figure 2.17b and 2.18B) show a good agreement with the experimental X-ray powder diffraction profile (Figure 2.17a) and the fiber diffraction pattern of Figure 2.18A.

The fractional coordinates of the carbon atoms of the asymmetric unit in the model of Figure 2.16 are reported in Table 2.11.

Table 2.11. Fractional coordinates of the carbon atoms of the asymmetric unit of the model of Figure 2.16 for the crystal structure of iP3MPD12 in the orthorhombic unit cell with axes a = 17.4 Å, b = 16.5 Å, c = 15.3 Å, according to the space group $P2_1ab$.

atom	*x*/*a*	*y*/*b*	*z*/*c*	occupancy
C_1	0.269	0.202	0.254	1.0
C_2	0.283	0.285	0.297	1.0
C_3	0.324	0.140	0.289	1.0
C_4	0.400	0.146	0.299	1.0
C_5	0.277	0.065	0.314	1.0
C_6	0.453	0.081	0.335	1.0
C_7	0.289	0.280	0.397	1.0
C_8	0.210	0.276	0.440	1.0
C_9	0.335	0.350	0.432	1.0
C_{10}	0.313	0.427	0.440	1.0

C_{11}	0.414	0.319	0.457	1.0
C_{12}	0.361	0.495	0.477	1.0
C_{13}	0.214	0.284	0.539	1.0
C_{14}	0.234	0.203	0.582	1.0
C_{15}	0.138	0.316	0.574	1.0
C_{16}	0.072	0.276	0.583	1.0
C_{17}	0.150	0.404	0.599	1.0
C_{18}	-0.001	0.310	0.620	1.0
C_{19}	0.226	0.205	0.682	1.0
C_{20}	0.296	0.244	0.724	1.0
C_{21}	0.213	0.121	0.717	1.0
C_{22}	0.265	0.061	0.725	1.0
C_{23}	0.129	0.113	0.742	1.0
C_{24}	0.249	-0.022	0.761	1.0
C_{25}	0.297	0.235	0.824	1.0
C_{26}	0.245	0.298	0.867	1.0
C_{27}	0.378	0.239	0.859	1.0
C_{28}	0.421	0.306	0.868	1.0
C_{29}	0.402	0.155	0.884	1.0
C_{30}	0.502	0.308	0.904	1.0
C_{31}	0.253	0.301	0.967	1.0
C_{32}	0.205	0.234	0.009	1.0
C_{33}	0.231	0.383	0.002	1.0
C_{34}	0.160	0.413	0.010	1.0
C_{35}	0.304	0.427	0.027	1.0
C_{36}	0.141	0.496	0.046	1.0
C_{37}	0.201	0.242	0.109	1.0
C_{38}	0.274	0.208	0.152	1.0
C_{39}	0.130	0.201	0.144	1.0
C_{40}	0.118	0.122	0.153	1.0
C_{41}	0.074	0.267	0.169	1.0
C_{42}	0.046	0.083	0.189	1.0

2.4 Crystal structure of isotactic poly((*R*,*S*)-3-methyl-1-pentene)

The X-ray powder diffraction profiles of the as-polymerized sample and of the melt-crystallized compression-molded sample of iP(*R*,*S*)3MP are shown in Figure 2.19. Both diffraction profiles are characterized by two strong, sharp, and very close reflections at 2θ = 9.5° and 10.4° and a strong reflection at 2θ = 16.6°. The diffraction profile of the melt-crystallized sample presents sharper reflections and, in particular, the two close reflections at 2θ = 9.5° and 10.4° are more separated and clearly resolved.

It is worth noting that the X-ray diffraction profile of Figure 2.19 of the achiral iP(*R*,*S*)3MP is different from that of the chiral iP(*S*)3MP (see Figure 3 of ref 9), which is characterized at low values of 2θ by a single strong reflection at 2θ = 9.3° (see Figures 3b and 4 of ref 7). This indicates that the crystal structure of the copolymer of the two enantiomeric monomeric units iP(*R*,*S*)3MP is different from that of the enantiopure iP(*S*)3MP, [7] which is characterized by chains in 4/1 helical conformation packed in a tetragonal unit cell with axis a = b = 13.35 Å and c = 6.80 Å, according to the space group $I4_1$. [7] Only left-handed 4/1 helices are included in the tetragonal unit cell since the left-handed helix of iP(*S*)3MP is favored over the right-handed one because of the chirality of the lateral group. The crystal structure of iP(*S*)3MS has been described in terms of statistical disorder of the optically active chiral side groups, which assume, in the left-handed chains, randomly two different almost isoenergetic conformations, providing a gain in entropy. [7,10]

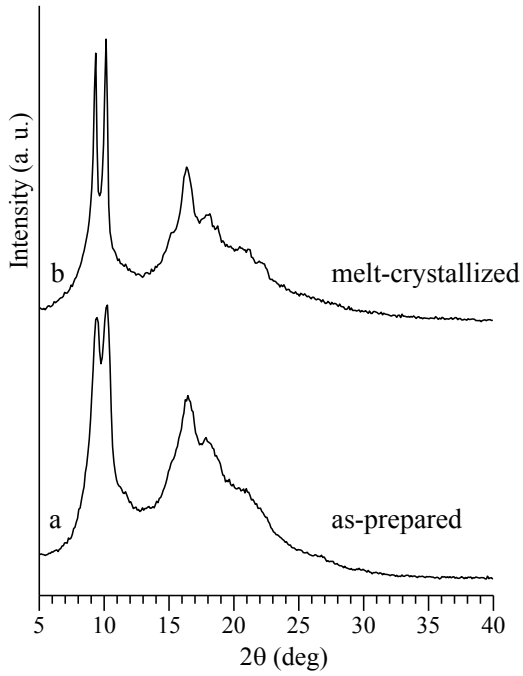

Figure 2.19. X-ray powder diffraction profiles of as-prepared (a) and melt-crystallized compression-molded sample (b) of iP(*R*,*S*)3MP.

Oriented fibers of iP(*R*,*S*)3MP have been obtained by extrusion of the melt and contemporarily stretching. The X-ray fiber diffraction pattern of iP(*R*,*S*)3MP is reported in Figure 2.20.

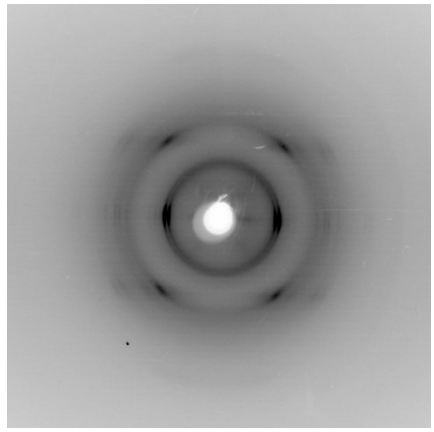

Figure 2.20. X-ray fiber diffraction pattern of oriented fiber of iP(*R*,*S*)3MP.

All the reflections observed in the powder diffraction profiles of Figure 2.19b and in the fiber pattern of Figure 2.20 are listed in Table 2.12 and 2.13 respectively.

Table 2.12. Diffraction angles (2θ), bragg distances (d_o), and intensities (I_0) observed in the X-ray power diffraction profile of Figure 2.19b.

2θ (deg)	d_o (Å)	I_o	*hkl*[a]
9.3	9.29	41	100
10.2	8.54	37	020
15.1	5.68	16	101
16.4	5.34	35	021
18.2	4.84	19	$1\bar{2}1, 2\bar{2}0$
18.8	4.69	15	200
21.2	4.17	21	121
22.1	3.98	12	201

a. The Miller indices *hkl* of reflections for a monoclinic unit cell with parameters a = 10.02 Å, b = 18.48 Å, c = 6.87 Å, and γ = 109.9° are also indicated.

Table 2.13. Photographic Coordinates (2x, 2y) of the diffraction spots, diffraction angles (2θ), bragg distances (d), cylindrical reciprocal coordinates (ξ and ζ), and intensities (I_0) of the reflections observed on the layer lines l of the X-ray fiber diffraction pattern of iP3MPD12 of Figure 2.20.

2x (mm)	2y (mm)	2θ (deg)	d_o (Å)	ξ (Å^{-1})	ζ (Å^{-1})	l	I_o[b]	*hkl*[a]
18.76	0	9.4	9.43	0.106	0	0	vs	100
20.36	0	10.2	8.69	0.115	0	0	vs	020
23.50	0	11.7	7.53	0.133	0	0	vw	$1\bar{2}0$
25.60	0	12.8	6.91	0.145	0	0	vw	110
33.56	0	16.8	5.28	0.189	0	0	vw	120
36.28	0	18.1	4.89	0.204	0	0	vvw	$2\bar{2}0$
37.72	0	18.9	4.70	0.213	0	0	w	200
40.94	0	20.5	4.34	0.230	0	0	vw	040
50.58	0	25.3	3.52	0.284	0	0	vvw	140
52.56	0	26.3	3.39	0.295	0	0	vvw	$3\bar{2}0$
17.31	26.4	15.6	5.70	0.098	0.1456	1	w	101
20.82	26.4	16.6	5.34	0.117	0.1456	1	s	021
26.00	26.4	18.3	4.85	0.146	0.1456	1	w	$1\bar{2}1$

33.60	26.4	21.2	4.20	0.188	0.1456	1	vw	121
36.00	26.4	22.0	4.03	0.201	0.1456	1	w	201

a. The Miller indices *hkl* of reflections for a monoclinic unit cell with parameters a = 10.02 Å, b = 18.48 Å, c = 6.87 Å, and γ = 109.9° are also indicated. b. vs = very strong; s = strong; w = weak; vw = very weak, vvw = very, very weak.

It is apparent that the two strong reflections at 2θ = 9.5° and 10.4° observed in the powder profile (Figure 2.19b) are equatorial reflections (Figure 2.20), whereas the strong reflection at 2θ = 16.6° is a first layer line reflection (Figure 2.20 and Table 2.13). From the fiber pattern the value of the chain axis c = 6.87 Å has been evaluated for the chains of iP(*R*,*S*)3MP. The value of the chain axis of 6.87 Å of iP(*R*,*S*)3MP is almost identical to the value of the chain axis of 6.80 Å found for the chiral iP(*S*)3MP.[7] This indicates that chains of the achiral iP(*R*,*S*)3MP assume the same 4/1 helical conformation of the chains of the chiral iP(*S*)3MP.[7] The reflections observed in the fiber pattern of Figure 2.20 and the powder diffraction profile of Figure 2.19b of iP(*R*,*S*)3MP are all accounted for by a monoclinic unit cell with parameters a = 10.02 Å, b = 18.48 Å, c = 6.87 Å, and γ = 109.9°. The calculated density with two chains in the cell is 0.932 g/cm^3, in agreement with the experimental density of 0.878 g/cm^3 measured at 25 °C by flotation on a sample with X-ray crystallinity of ≈47% (the crystalline density is 0.885 g/cm^3 evaluated from the experimental density of 0.878 g/cm^3 and the experimental density of the amorphous sample of 0.868 g/cm^3). The indices *hkl* of the reflections observed in the powder and fiber diffraction pattern according to this monoclinic unit cell are reported in Table 2.12 and 2.13 respectively. The indexing of the observed reflections indicates, disregarding in a first approximation the very weak 110 reflection observed in the fiber pattern, the systematic absence of *hk*0 reflections with k odd. This suggests that a possible space group, compatible with the presence of two chains in the unit cell, could be $P2_1/b$.

As a consequence of the choice of this monoclinic space group, the 4/1 helical symmetry of the chains is not maintained in the lattice as crystallographic symmetry, as instead occurs for the chiral iP(*S*)3MP. [7,10] The chains can be positioned in the unit cell with their chain axes coincident with the crystallographic 2_1 axes of the space group $P2_1/b$. Possible models of packing of 4/1 helical chains in the monoclinic unit cell have been found performing calculations of the conformational energy and packing energy for the space group $P2_1/b$. The calculations of the conformational energy have been performed on a portion of isolated chains of iP(*R*)3MP, iP(*S*)3MP, and iP(*R*,*S*)3MP shown in Figure 2.21, by application of the equivalence principle [10] to successive constitutional units by assuming a line repetition group *s*(*M*/*N*) for the polymer chain. As a consequence, the sequence of the torsion angles in the main chain is of the kind ...$\theta_1\theta_2\theta_1\theta_2$... (Figure 2.21).

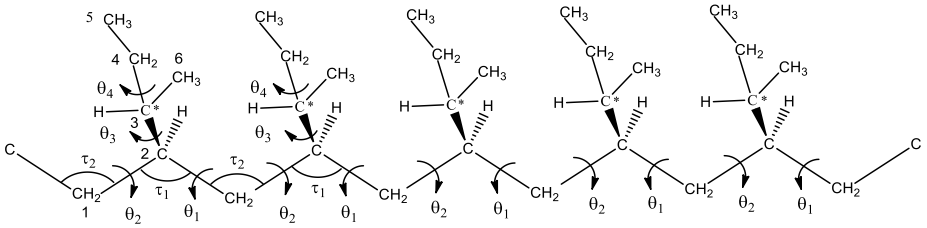

Figure 2.21. Portion of the chain of iP(*S*)3MP or iP(*R*)3MP used in the conformational energy calculations with definition of the torsion angles θ_1, θ_2, θ_3, and θ_4 and the bond angles τ_1 and τ_2. The torsion angle θ_3 is defined with respect to the carbon of the CH_2 group of the ethyl group: θ_3 = C4−C3*−C2−C1. The torsion angle θ_4 is defined with respect to the methyl group of the ethyl group: θ_4 = C5−C4−C3*−C2.

The conformational energy maps for chains of iP(*R*)3MP and iP(*S*)3MP as a function of θ_1 and θ_2 are shown in Figure 2.22. In these maps for each pair of θ_1 and θ_2, the positions of the side groups, defined by the torsion angles θ_3 and θ_4, were varied in step of 10° of θ_3 and θ_4, to place them in the minimum-energy position corresponding to that pair of θ_1 and θ_2. Two energy minima are present in both maps of Figure 2.22 in the region $\theta_1 \approx$

G^+, $\theta_2 \approx T$, or $\theta_1 \approx T$, $\theta_2 \approx G^-$. The values of torsion angles and of the relative energies are reported in Table 2.14.

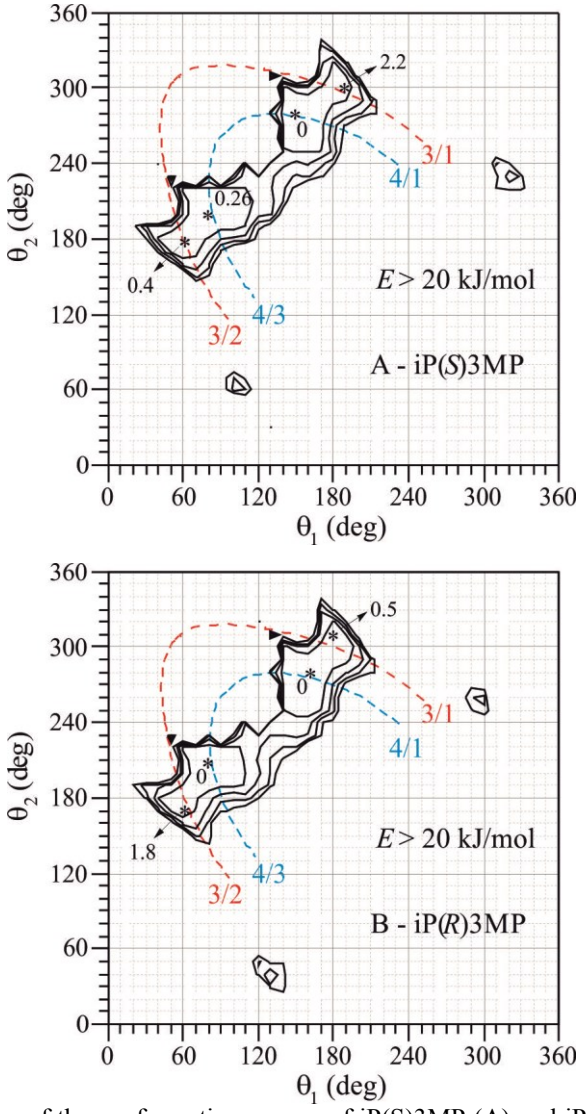

Figure 2.22. Maps of the conformation energy of iP(S)3MP (A) and iP(R)3MP (B) as a function of θ_1 and θ_2 with θ_3 and θ_4 scanned every10° in the *s*(*M*/*N*) line repetition group for $\tau_1 = 111°$ and $\tau_2 = 113°$. The curves are reported at intervals of 5 kJ/mol of monomeric units with respect to the absolute minimum of the maps assumed as zero. The values of the energy corresponding to the minima (∗) are also reported. The dashed curves represent the loci of points of couples of torsion angles θ_1 and θ_2 corresponding to the *s*(4/1) and *s*(3/1) helical conformations.

Table 2.14. Values of torsion angles of the backbone θ_1 and θ_2, and of the lateral groups θ_3 and θ_4 (Figure 2.21) corresponding to the minima of the conformational energy found in maps of Figure 2.22 of iP(*S*)3MP and iP(*R*)3MP, and values of the corresponding energy *E* scaled with respect to the absolute minimum of the maps assumed as zero[a].

θ_1 (deg)	θ_2 (deg)	θ_3 (deg)	θ_3 (deg)	*E* (kJ/mol mu)	helix symmetry
			iP(*S*)3MP		
150	-80	50	170	0	4/1 right-handed (up)
80	-160	-160	170	0.26	4/1 left-handed (down)
-170	-60	60	170	2.25	3/1 right-handed (up)
60	180	180	160	0.36	3/1 left-handed (down)
			iP(*R*)3MP		
160	-80	-70	-160	0.04	4/1 right-handed (up)
80	-150	80	-160	0	4/1 left-handed (down)
180	-50	-60	-160	0.55	3/1 right-handed (up)
60	170	60	-170	1.83	3/1 left-handed (down)

a. The "up" or "down" orientations of the chain models are also indicated. In our modeling right-handed chains are built "up" and left-handed chains are built "down".

The loci of points corresponding to the *s*(4/1) and *s*(3/1) helical symmetries, with values of the unit twist $t = 2\pi N/M$ of 90° and 120°, respectively, are also reported in the maps of Figure 2.22.[10] The absolute energy minimum is close to conformations with 4/1 helical symmetry, while the relative minimum is close to the dashed line corresponding to conformations with 3/1 symmetry. However, no polymorphic form with s(3/1) helical chains has been observed until now for iP(*S*)3MP or iP(*R*,*S*)3MP. The conformations with 4/1 helical symmetry correspond to isodistortions for θ_1 and θ_2 from the precise *gauche* and *trans* values due to the bulkiness of the lateral groups.[10]

According to this geometrical and energy analysis, models of the chains of iP(*S*)3MP, iP(*R*)3MP, and of the random copolymer iP(*R*,*S*)3MP are built with the values of the dihedral angles along the main chain of $\theta_1 = 150°$, $\theta_2 = -80°$ (or $\theta_1 = 80°$, $\theta_2 = -160°$) (Table 2.14). The possible conformations of the side groups have been evaluated by calculating the conformational energy of the 4/1 right-handed helix for $\theta_1 = 150°$, $\theta_2 = -80°$ (or the left-

handed helix for $\theta_1 = 80°$, $\theta_2 = -160°$), varying the torsion angles θ_3 and θ_4. The conformational energy maps of iP(*S*)3MP and iP(*R*)3MP as a function of θ_3 and θ_4 for these fixed values of θ_1 and θ_2 are reported in Figure 2.23.

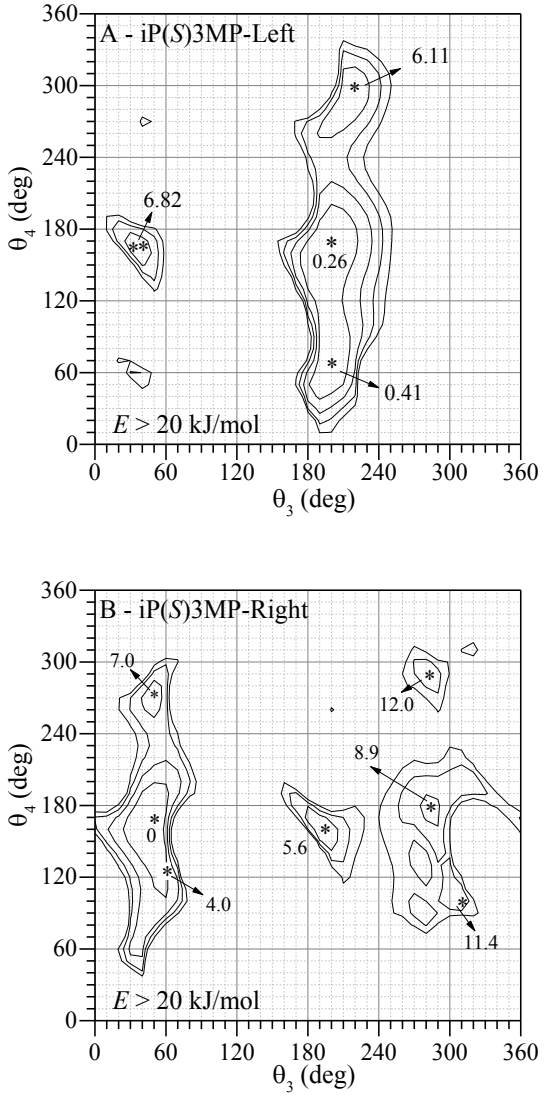

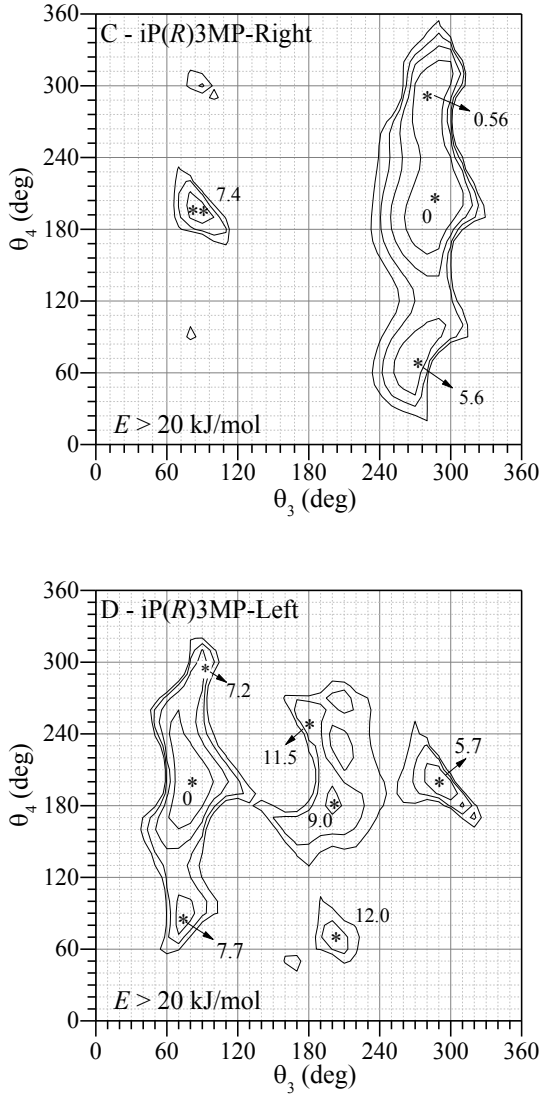

Figure 2.23. Maps of the conformational energy of iP(*S*)3MP (A, B) and iP(*R*)3MP (C, D) for backbone torsion angles $\theta_1 = 150°$, $\theta_2 = -80°$ (right-handed helix) (B, C), or $\theta_1 = 80°$, $\theta_2 = -160°$ (left-handed helix) (A, D), corresponding to the 4/1 left-handed or right-handed helix, as a function of the torsion angles θ_3 and θ_4 that define the conformation of the lateral groups. The curves are reported at intervals of 5 kJ/mol of monomeric units with respect to the absolute minimum of the maps assumed as zero. The values of energy of the minima (∗) are also reported.

The values of torsion angles and of the relative energies of minima are reported in Table 2.15. It is apparent that for iP(*S*)3MP low energy minima are obtained for only one possible value of θ_3, that is, $\theta_3 \approx$ T for the left-

handed 4/1 helix and $\theta_3 \approx G^+$ for the right-handed 4/1 helix, while θ_4 may assume different values around T and G^+ (Table 2.15). For the left-handed helix the two minima corresponding to $\theta_3 \approx T$ and two different values of θ_4 at $\theta_4 \approx T$ and $\theta_4 \approx G^+$ are isoenergetic, whereas for the right-handed 4/1 helix a deep energy minimum is obtained only for one value of θ_4, that is, for $\theta_3 \approx G^+$ and $\theta_4 \approx T$. Analogously, for iP(*R*)3MP low-energy minima are obtained for $\theta_3 \approx G^+$ for the left-handed 4/1 helix and $\theta_3 \approx G^-$ for the right-handed 4/1 helix, while θ_4 may assume different values around T and G^- (Table 12). Moreover, for the right-handed helix the two minima corresponding to $\theta_3 \approx G^-$ and two different values of θ_4 at $\theta_4 \approx T$ and $\theta_4 \approx G^-$ are isoenergetic, whereas for the left-handed 4/1 helix a deep energy minimum is obtained only for one value of θ_4, that is, for $\theta_3 \approx G^+$ and $\theta_4 \approx T$. The three possible conformations of left- and right-handed 4/1 helices of iP(*S*)3MP (two for the left-handed and one for the right-handed chain) and the three possible conformations of left- and right-handed 4/1 helices of iP(*R*)3MP (two for the right-handed and one for the left-handed chain) are shown in Figure 2.24. The six models of possible conformations are defined iP(*S*)3MP-L-TG^+ (left-handed 4/1 chain of iP(*S*)3MP with θ_3 = T and θ_4 = G^+, Figure 2.24A), iP(*S*)3MP-L-TT (left-handed 4/1 chain of iP(*S*)3MP with θ_3 = T and θ_4 = T, Figure 2.24B), iP(*S*)3MP-R-G^+T (right-handed 4/1 chain of iP(*S*)3MP with θ_3 = G^+ and θ_4 = T, Figure 2.24C), iP(*R*)3MP-R-G^-G^- (right-handed 4/1 chain of iP(*R*)3MP with θ_3 = G^- and θ_4 = G^-, Figure 2.24D), iP(*R*)3MP-R-G^-T (right-handed 4/1 chain of iP(*R*)3MP with θ_3 = G^- and θ_4 = T, Figure 2.24E), and iP(*R*)3MP-L-G^+T (left-handed 4/1 chain of iP(*R*)3MP with θ_3 = G^+ and θ_4 = T, Figure 2.24F) (Table 2.15).

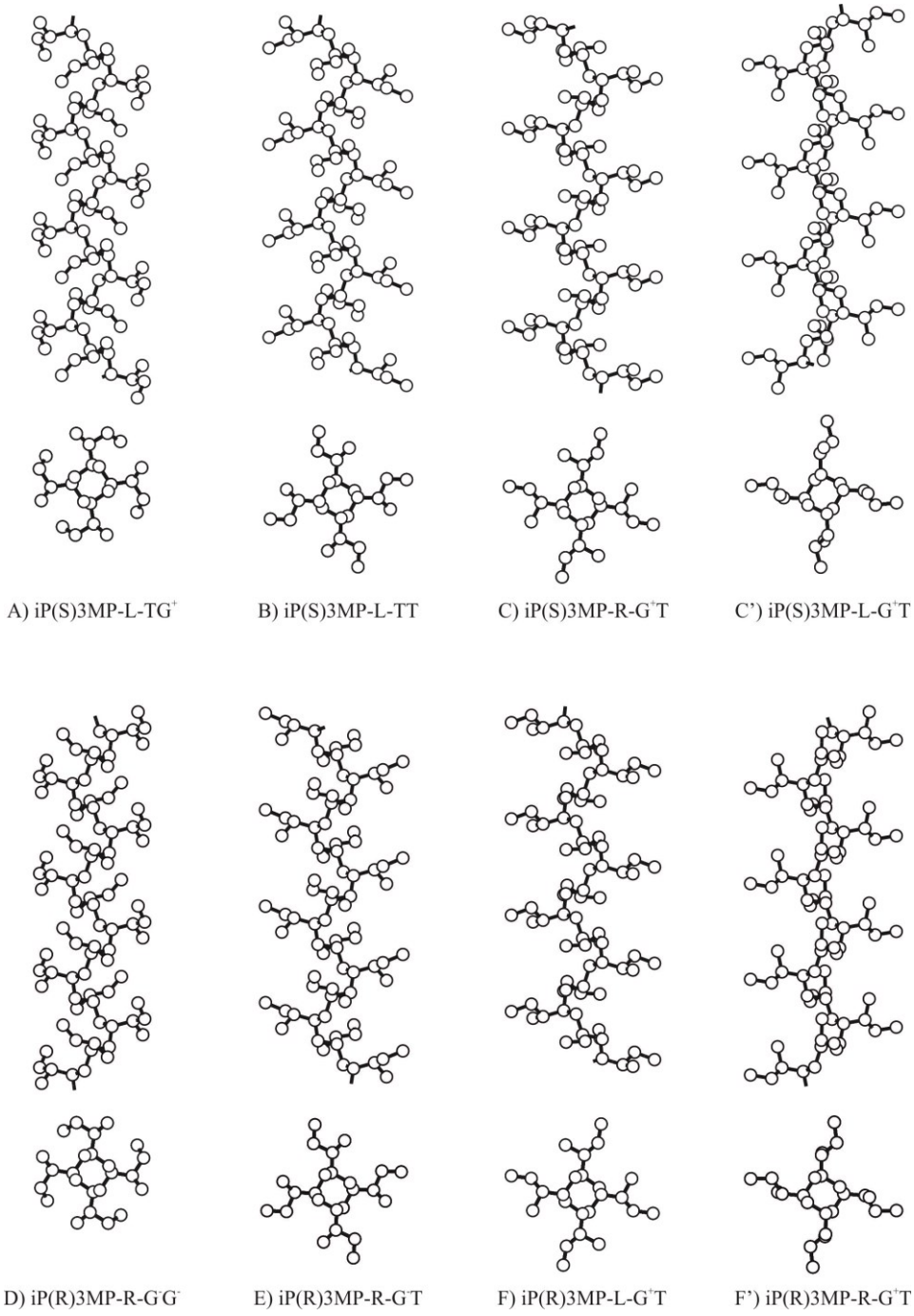

Figure 2.24. Height models of possible conformations of the chains of iP(*S*)3MP (A−C, C′) and iP(*R*)3MP (D−F, F′) found by calculations of conformational energy of Figures 2.22 and 2.23. The models correspond to the conformations defined in Table 2.15. Chains of models A, B, C′, and F are "down", and chains of models C, D, E, and F′ are "up".

Table 2.15. Height models of conformations of the chains of iP(*S*)3MP and iP(*R*)3MP corresponding to the minima of the conformational energy found in the maps of Figure 2.23[a].

model of Figure 2.24	θ_1 (deg)	θ_2 (deg)	θ_3 (deg)	θ_4 (deg)	*E* (kJ/mol mu)	helix symmetry	model
				iP(*S*)3MP			
A	80	-160	-160	70	0.41	4/1 left-handed	iP(*S*)3MP-L-TG$^+$ (down)
B	80	-160	-160	170	0.26	4/1 left-handed	iP(*S*)3MP-L-TT (down)
C	150	-80	50	170	0	4/1 right-handed	iP(*S*)3MP-R-G$^+$T (up)
C'	80	-160	40	160	6.82	4/1 left-handed	iP(*S*)3MP-L-G$^+$T (down)
				iP(*R*)3MP			
D	160	-80	-80	-70	0.56	4/1 right-handed	iP(*R*)3MP-R-G$^-$G$^-$ (up)
E	160	-80	-70	-160	0	4/1 right-handed	iP(*R*)3MP-R-G$^-$T (up)
F	80	-150	80	-160	0	4/1 left-handed	iP(*R*)3MP-L-G$^+$T (down)
F'	160	-80	90	-170	7.37	4/1 right-handed	iP(*R*)3MP-R-G$^+$T (up)

a. The values of torsion angles of the lateral groups θ_3 and θ_4 correspond to the minima of the maps of Figure 2.23 calculated with the constant values of the backbone torsion angles θ_1 and θ_2 found in the maps of Figure 2.22. The values of the conformational energy *E* are scaled with respect to the absolute minimum of the maps of Figures 2.22 and 2.23 assumed as zero. The labels A−F correspond to the model of Figure 2.24. In the symbols of models iP(*R*)3MP-X-YZ or iP(*S*)3MP-X-YZ, the label X (R or L) indicates right-handed (R) or left-handed (L) 4/1 helix, and the labels Y and Z (= T, G$^+$,or G$^-$) indicated the value of the torsion angle θ_3 and θ_4, respectively.

Besides these six low-energy models, other two models of conformation of slight higher energy are included in Table 2.15 and Figure 2.24. These models correspond to the isolated minima of the energy maps of Figure 2.23A,C (indicated with a double star) of energy ≈7 kJ/mol mu higher than the absolute minima. These local minima correspond for iP(*S*)3MP to the model iP(*S*)3MP-L-G$^+$T (Figure 2.24C') of a left-handed 4/1 helix with $\theta_3 \approx G^+$ and $\theta_4 \approx T$ (Figure 2.23A) and for iP(*R*)3MP to the model iP(*R*)3MP-R-G$^+$T (Figure 2.24F') of a right- handed 4/1 helix with $\theta_3 \approx G^+$ and $\theta_4 \approx T$ (Figure 2.23C). It is worth noting that the model iP(*S*)3MP-L-G$^+$T (Figure 2.24C') has the same conformation as the model of absolute energy minimum for the iP(*R*)3MP chain (iP(*R*)3MP-L-G$^+$T, Figure 2.24F) but opposite chirality of the lateral groups, and the model iP(*R*)3MP-R-G$^+$T (Figure 2.24F') has the same conformation as the model of absolute energy minimum for the iP(*S*)3MP chain (iP(*S*)3MP-R-G$^+$T, Figure 2.24C), but opposite chirality of the lateral groups. The high energy of the conformational models of Figure 2.24C', F' evidences the tendency of the chiral side groups to influence the chirality and the conformation of the helical chains, by destabilizing the internal energy of a helix of a given chirality by about 7 kJ/mol mu. It is also worth mentioning that the isotactic chains of iP(*R*)3MP and iP(*S*)3MP may assume two different "up" and "down" orientations, characterized by the C−C bonds connecting the side chains to the tertiary carbon atoms of the backbone pointing in the positive direction of the *z*-axis (coincident with the chain axis) defining an "up" chain, or the negative direction, defining a "down" chain. In the models of Figure 2.24, regardless of chirality of side groups, the left-handed chains are drawn down, whereas the right-handed chains are drawn up. Similar calculations have been performed for model chains of copolymer iP(*R*,*S*)3MP, and similar results as in Table 2.15 have been obtained for the lowest energy conformations. For left-handed 4/1 helix of iP(*R*,*S*)3MP the

side groups of the *R* monomeric units assume conformation with $\theta_3 \approx G^+$ and $\theta_4 \approx T$ (as in the model F of Table 2.15), and the side groups of the *S* monomeric units assume conformation with $\theta_3 \approx T$ and $\theta_4 \approx T$ (as in the model B of Table 2.15), whereas for right-handed 4/1 helix of iP(*R*,*S*)3MP the side groups of the *S* monomeric units assume conformation with $\theta_3 \approx G^+$ and $\theta_4 \approx T$ (as in the model C of Table 2.15), and the side groups of the *R* monomeric units assume conformation with $\theta_3 \approx G^-$ and $\theta_4 \approx T$ (as in the model E of Table 2.15). Models of left-handed and right-handed 4/1 helical conformation of the copolymer iP(*R*,*S*)3MP, where successive *R* and *S* monomeric units assume these conformations are shown in Figure 2.25. Although other conformations for the *S* and *R* side groups in consecutive monomeric units along the chain of iP(*R*,*S*)3MP would be also possible at low cost of conformational energy, those of Figure 2.25 correspond to the energy minima. It is worth noting that for the low-energy conformers of *R* units in a left-handed 4/1 helix with $\theta_3 \approx G^+$ and $\theta_4 \approx T$ (model F of Table 2.15 and Figure 2.24F) and *S* units in a right-handed 4/1 helix with $\theta_3 \approx G^+$ and $\theta_4 \approx T$ (model C of Table 2.15 and Figure 2.24C), the ethyl groups are in a gauche arrangement to both the CH_2 groups of the backbone ($\theta_3 \approx G^+$). For the low-energy conformers of *S* units in a left-handed 4/1 helix with $\theta_3 \approx T$ and $\theta_4 \approx T$ (model B of Table 2.15 and Figure 2.24B) and *R* units in a right-handed 4/1 helix with $\theta_3 \approx G^-$ and $\theta_4 \approx T$ (model E of Table 2.15 and Figure 2.24E), the methyl groups bonded to the chiral carbon are in a gauche arrangement to both the CH_2 groups of the backbone (the ethyl groups are in trans $\theta_3 \approx T$ and gauche $\theta_3 \approx G^-$, respectively, to one of the two CH_2 groups of the backbone). The double gauche arrangement of ethyl and methyl groups is shown in the Newman's projections in Figures 2.25A', B' and 2.25A'', B'', respectively. These results indicate that the random enchainment of *S* and *R* monomeric units in iP(*R*,*S*)3MP and the compensation of chirality make the left-handed and right-handed 4/1

helices equivalent because low-energy conformations of the chiral lateral groups are possible for both left-handed and right-handed helices (Table 2.15) and explain the experimental X-ray diffraction data that indicate a packing of enantiomorphous helices, according to the centrosymmetric space group $P2_1/b$, rather than an isomorphous packing, as in the case of iP(*S*)3MP.

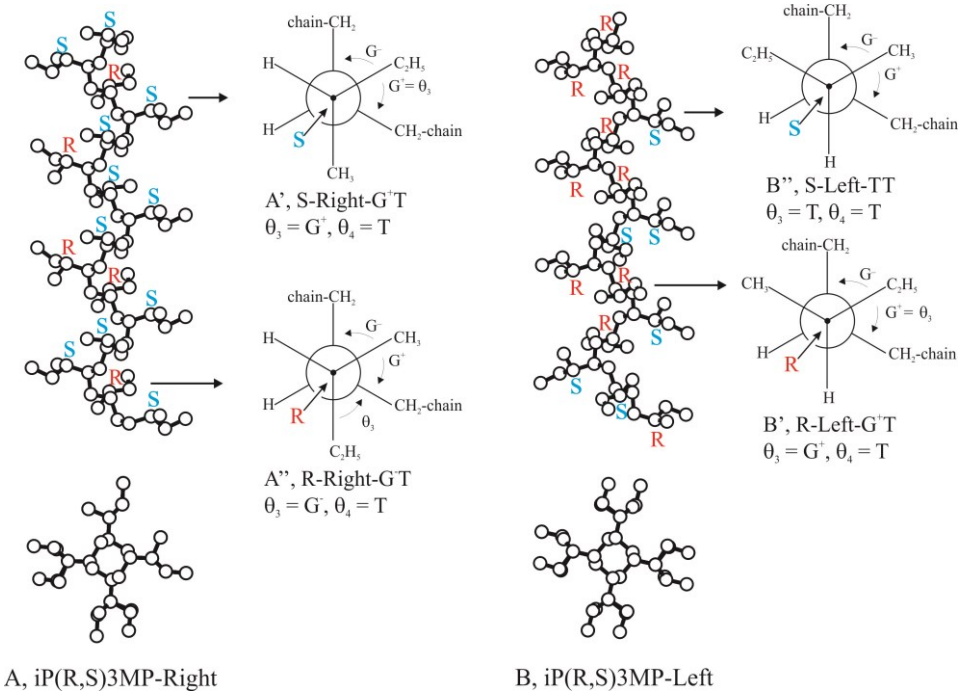

Figure 2.25. Models of right-handed and left-handed 4/1 helical conformation of the copolymer iP(*R*,*S*)3MP, where the side groups of successive R and S monomeric units assume statistically the lowest energy conformations of Figure 2.24. (A) iP(*R*,*S*)3MP chain in 4/1 right-handed helical conformation bearing S units with $\theta_3 \approx G^+$, $\theta_4 \approx T$ (A'), and R units with $\theta_3 \approx G^-$, $\theta_4 \approx T$ (A''). (B) iP(*R*,*S*)3MP chain in 4/1 left-handed helical conformation bearing R monomeric units with $\theta_3 \approx G^+$, $\theta_4 \approx T$ (B') and S units with $\theta_3 \approx T$, $\theta_4 \approx T$ (B''). The double gauche arrangements of ethyl and methyl groups are indicated in the Newman's projections of A',B' and A'',B'', respectively.

Possible models of packing for the crystals structure of iP(*R*,*S*)3MP have been found performing calculations of the packing energy of chains of the random copolymer having conformation as in Figure 2.25, for the space

group $P2_1/b$. The chains of iP(*R*,*S*)3MP are characterized by disorder in the conformations of the side groups, which assume the different conformations of Table 2.15 shown in Figure 2.24, depending on the chirality of the monomeric unit and the handedness of the helix. The possible models of packing have been found simulating the chain of the random copolymer of Figure 2.25 with the limit conformations A, B, C of iP(*S*)3MP and D, E, F of iP(*R*)3MP of Figure 2.24. The packing energy has been calculated for six limit ordered models of packing of space group symmetry $P2_1/b$ characterized by chains having the six different conformations of Figure 2.24. The six limit ordered models of packing are defined as the models of conformations of the chains of Figure 2.24 and Table 2.15. Since the position of the chain axis inside the unit cell has been fixed at the fractional coordinates $x/a = 0$, $y/b = 0.25$, coincident with the crystallographic 2_1 axes of the space group $P2_1$/b, the lattice energy has been calculated varying only the orientation of the chain around its axis (defined by the angle ω, shown in Figure 2.26), and the z coordinate, which defines the relative heights of the chains in the unit cell. The axes of the unit cell have been maintained constant at the experimental values a = 10.02 Å, b = 18.48 Å, c = 6.87 Å, and $\gamma = 109.9°$.

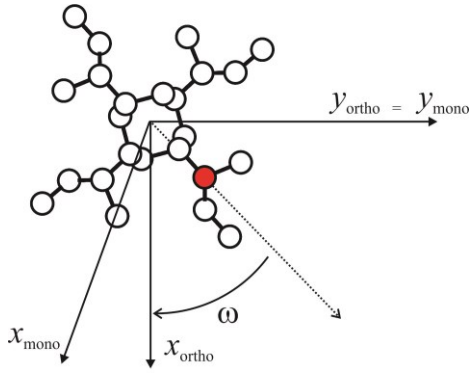

Figure 2.26. Definitions of the variables ω and z used in the packing energy calculations in the orthogonal (ortho) and monoclinic (mono) coordinates systems. The value of ω is positive for a clockwise rotation, and z is the height of the carbon atom indicated as a filled circle.

Maps of the lattice energy for the six limit ordered models of packing of the six chains of Figure 2.24A−C,D−F as a function of ω and z for the space group $P2_1/b$ are reported in Figure 2.27.

The maps are periodic over $\omega = 180°$ and $z = c/2 = 3.43$ Å; therefore, only the regions with $\omega = 0−180°$ and $z = 0−c/2 = 0−3.43$ Å are shown. The maps present one (Figure 2.27B,C,E,F) or two (Figure 2.27A,D) energy minima, which are periodically repeated after a rotation of $\omega = t = 90°$, where t is the unit twist of the 4/1 helix, $t = 2\pi/4$, and a translation of $z = h = c/4 = 1.72$ Å, where h is the unit height of the helix. The values of the energy minima and the corresponding values of ω and z are reported in Table 2.16. It is apparent that equivalent absolute energy minima are obtained for the models iP(*S*)3MP-L-TG$^+$ (left-handed 4/1 chain of iP(*S*)3MP with θ_3 = T, θ_4 = G$^+$) (Figure 2.27A) and iP(*R*)3MP-R-G$^-$G$^-$ (right-handed 4/1 chain of iP(*R*)3MP with θ_3 = G$^-$, θ_4 = G$^-$) (Figure 2.27D). Minima of slightly higher energy are obtained for the models iP(*S*)3MP-L-TT (left-handed 4/1 chain of iP(*S*)3MP with θ_3 = T, θ_4 = T) (Figure 2.27B) and iP(*R*)3MP-R-G$^-$T (right-handed 4/1 chain of iP(*R*)3MP with θ_3 = G$^-$, θ_4 = T) (Figure 2.27E) and in the maps Figures 2.27C,F for the models

iP(*S*)3MP-R-G$^+$T (right-handed 4/1 chain of iP(*S*)3MP with $\theta_3 = G^+$, $\theta_4 =$ T) and iP(R)3MP-L-G$^+$T (left-handed 4/1 chain of iP(*R*)3MP with $\theta_3 = G^+$, $\theta_4 =$ T), respectively. This indicates that the models A−F of Table 2.15 of the chains iP(*S*)3MP and iP(*R*)3MP (Figure 2.24A−F) are not only of low conformational energy but also of low packing energy in the space group $P2_1/b$. The data of Figure 2.27 and Table 2.16 also indicate that a high amount of conformational disorder may be included in the crystals due to the rotational freedom of the lateral groups defined by the values of the torsion angles θ_3 and θ_4 in S and R monomeric units of the copolymer iP(*R*,*S*)3MP, which can assume trans and gauche states at low cost of energy. The rotational freedom of the chains around the chain axis (ω) and the relative height of the chains along *c*, instead, are restricted around the minimum energy of the maps, that is, $\omega \approx 40 + n90°$ and $z/c \approx 0.1 + n0.25$, and only for the models iP(*S*)3MP-L-TG$^+$ (left-handed 4/1 chain of iP(*S*)3MP with $\theta_3 =$ T, $\theta_4 = G^+$) (Figure 2.27A) and iP(*R*)3MP-R-G$^-$G$^-$ (right-handed 4/1 chain of iP(*R*)3MP with $\theta_3 = G^-$, $\theta_4 = G^-$) (Figure 2.27D) an additional minimum of packing energy occurs for $\omega \approx 0$. The rotational freedom of the chains around the chain axis (ω) and the relative height of the chains along *c*, depend, however, on the conformation of the side groups, in particular the torsion angle θ_4. The comparison of the maps of Figure 2.27A,B and of the maps of Figure 2.27D,E shows that when the lateral groups assume conformation with $\theta_4 =$ T, as in the models iP(*S*)3MP-L-TT of Figure 2.24B with $\theta_3 =$ T and $\theta_4 =$ T, and iP(*R*)3MP-R-G$^-$T of Figure 2.24E with $\theta_3 = G^-$ and $\theta_4 =$ T, the space accessible for the packing of chains in the unit cell is more restricted and the energy minima of the maps of Figure 2.27B,E are narrower compared to those of the maps of Figure 2.27A,D of models of chains iP(*S*)3MP-L-TG$^+$ of Figure 2.24A and iP(*R*)3MP-R-G$^-$G$^-$ of Figure 2.24D with $\theta_4 = G^+$ and G^-, respectively. This indicates that even though the models of chains iP(*S*)3MP-L-TG$^+$

(Figure 2.24A) and iP(*S*)3MP-L-TT (Figure 2.24B), corresponding to the two possible values of $\theta_4 = G^+$ or T, are conformationally isoenergetic, the packing of the chain iP(*S*)3MP-L-TG^+ is more favorable in term of accessible space. Analogously, even though the models of chains iP(*R*)3MP-R-G^-G^- (Figure 2.24D) and iP(*R*)3MP-R-G–T (Figure 2.24E), corresponding to the two possible values of $\theta_4 = G^-$ or T, have the same conformational energy, the packing of the chain iP(*R*)3MP-L-G^-G^- is more favorable. This possibly indicates that the hypothesized disorder in the conformation of the lateral groups, due to the two possible values assumed by θ_4 in both S and R monomeric units of the copolymer iP(*R*,*S*)3MP in the unit cell is not completely statistical.

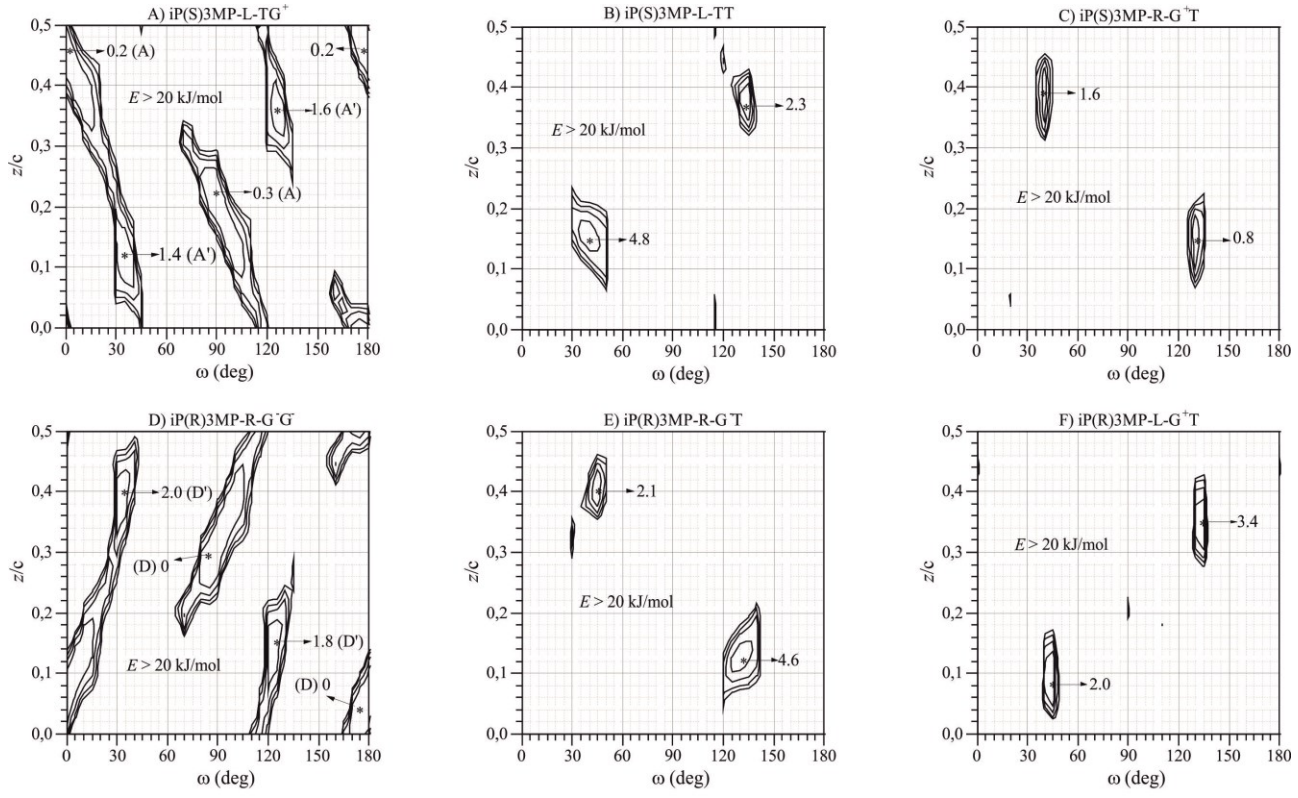

Figure 2.27. Maps of the packing energy as a function of ω and z for the monoclinic unit cell with axes a = 10.02 Å, b = 18.48 Å, c = 6.87 Å, and γ = 109.9°, for the space group symmetry $P2_1/b$, for the six limit ordered models of the chain conformation of iP(*S*)3MP or iP(*R*)3MP of Figure 2.24A-C,D-F and Table 2.15. In all models the chains have fixed 4/1 helical conformation and have their chain axes coincident with the crystallographic 2_1 helical axes of the unit cell in the space group $P2_1/b$. The curves are drawn at intervals of 5 kJ/mol mu with respect to the absolute minimum of the maps assumed as zero in (D). The energy of the relative minima (∗) are also shown.

Table 2.16. Values of the packing energy minima and corresponding values of ω and z found in the maps of the packing energy of Figure 2.27 for the chain models iP(*S*)3MP-L-TG$^+$ (left-handed 4/1 chain of iP(*S*)3MP with θ_3 = T, θ_4 = G$^+$) (Figure 2.27A), chain of iP(*S*)3MP with θ_3 = G$^+$, θ_4 = T) (Figure 2.27C), iP(*R*)3MP-R-G$^-$G$^-$ (right-handed 4/1 chain of iP(*R*)3MP with θ_3 = G$^-$, θ_4 = G$^-$) (Figure 2.27D), iP(*R*)3MP-R-G$^-$T (right-handed 4/1 chain of iP(*R*)3MP with θ_3 = G$^-$, θ_4 = T) (Figure 2.27E) and iP(*R*)3MP-L-G$^+$T (left-handed 4/1 chain of iP(*R*)3MP with θ_3 = G$^+$, θ_4 = T) (Figure 2.27F)[a]

model of paking	model of the chain	θ_1 (deg)	θ_2 (deg)	θ_3 (deg)	θ_3 (deg)	ω (deg)	z/c	E_{pack} (kJ/mol mu)	minima of the maps of Figure 2.27
				iP(*S*)3MP					
A	iP(*S*)3MP-L-TG$^+$ (down)	80	-160	-160	70	0	0.46	0.2	A
						90	0.21	0.3	
A’	iP(*S*)3MP-L-TG$^+$ (down)	80	-160	-160	70	35	0.12	1.4	A’
						125	0.37	1.6	
B	iP(*S*)3MP-L-TT (down)	80	-160	-160	170	40	0.15	4.8	B
						135	0.37	2.3	
C	iP(*S*)3MP-R-G$^+$T (up)	150	-80	50	170	40	0.39	1.6	C
						130	0.15	0.8	
				iP(*R*)3MP					
D	iP(*R*)3MP-R-G$^-$G$^-$ (up)	160	-80	-80	-70	-5	0.042	0	D
						85	0.29	0	
D’	iP(*R*)3MP-R-G$^-$G$^-$ (up)	160	-80	-80	-70	35	0.40	2.0	D’
						125	0.15	1.8	
E	iP(*R*)3MP-R-G$^-$T (up)	160	-80	-70	-160	45	0.40	2.1	E
						130	0.12	4.6	
F	iP(*R*)3MP-L-G$^+$T (down)	80	-150	80	-160	45	0.08	2.0	F
						135	0.35	3.4	

a. The values of the packing energy *E* pack are scaled with respect to the absolute minimum of the maps of Figure 2.27 assumed as zero. b. The values of the lattice energy correspond to the minima of the maps of Figure 2.27 at ω and z/c and $\approx \omega + 90°$ and $\approx z/c + 0.25$.

The six limit ordered models of packing A−C and D−F of Table 2.16, corresponding to the energy minima in the maps of Figure 2.27, are shown in Figure 2.28. Since the models C and F have identical azimuthal settings of chains (angle ω), also the projections in the ab plane are identical (Figure 2.28C,F), provided that the chains are anticlined (up and down), as for the models C, iP(*S*)3MP-R-G^{+}T (up), and F, iP(*R*)3MP-L-G^{+}T (down). Also, the models B, iP(*S*)3MP-L-TT (down), and E, iP(*R*)3MP-R-G^{-}T (up), have identical azimuthal setting and the chains are anticlined, so that the projections in the *ab* plane are identical (Figure 2.28B,E).

Calculations of structure factors have been performed for the six limit ordered models of packing of Figure 2.28 and Table 2.16 corresponding to the energy minima of the maps of Figure 2.27. A comparison between observed structure factors (F_0), evaluated from the X-ray powder diffraction profile of Figure 2.19b and the fiber diffraction pattern of Figure 2.20, and structure factors calculated (F_c) for the six limit ordered models A−F of Figure 2.28 for the space group $P2_1/b$ is reported in Tables 2.17 and 2.18, respectively. A direct comparison between the experimental X-ray powder diffraction profile of Figure 2.19b, after the subtraction of the amorphous halo, and the calculated profiles for the six limit ordered models of Figure 2.28 is reported in the Figure 2.29, whereas the calculated X-ray fiber diffraction patterns to compare with the experimental pattern of Figure 2.19 are shown in Figure 2.30. It is worth noting that the diffraction profiles calculated for the models of packing A (profile b of Figure 2.29A), B (profile c of Figure 2.29A), and C (profile d of Figure 2.29A) of Figure 2.28 are identical to those of the models D, E, and F respectively.

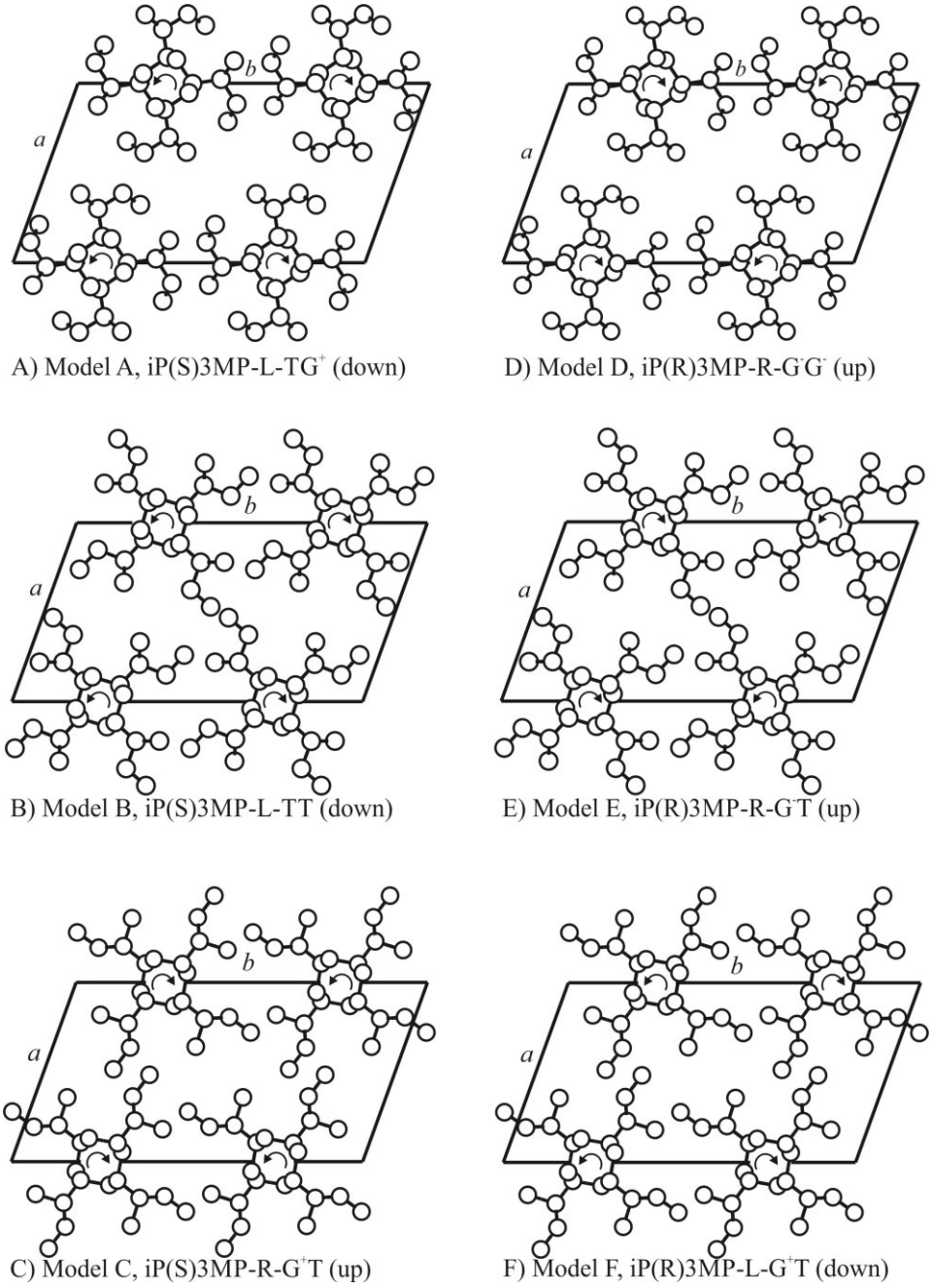

Figure 2.28. Limit ordered models of packing of chains of iP(*S*)3MP (A−C) or iP(*R*)3MP (D−F) in the monoclinic unit cell with axes a = 10.02 Å, b = 18.48 Å, c = 6.87 Å, and γ = 109.9° according to the space group $P2_1/b$, corresponding to the minima of the maps of packing energy of Figure 2.27 and Table 2.16.

A not completely satisfactory agreement between calculated structure factors and experimental intensities observed in the X-ray powder profile of Figure 2.19b and X-ray fiber diffraction pattern of Figure 2.20 has been obtained for all the limit ordered models of Table 2.16 and Figure 2.28.

The calculated diffraction profiles for every model of Figure 2.28 present basically the most important features of the experimental diffraction pattern, but with different defects. In particular, the powder and fiber diffraction patterns calculated for the models A and D of Figure 2.28A,D present a too low intensity of the 020 reflection at 2θ = 10.18° and of the 021 reflection on the first layer line at 2θ = 16.45° (Tables 2.17 and 2.18, profile b of Figure 2.29A and pattern B of Figure 2.30), compared to the experimental intensities (profile a of Figure 2.29A and Figure 2.30A). The diffraction patterns calculated for the models B and E of Figure 2.28B,E present a too low intensity of the 020 reflection at 2θ = 10.18° and too high intensities of the $1\bar{2}0$ reflection at 2θ = 11.26° and of $1\bar{1}1$, 101, and 021 reflections on the first layer line at 2θ = 15.75°, 16.96°, and 16.45°, respectively (Tables 2.17 and 2.18 and profile c of Figure 2.29A and pattern C of Figure 2.30). The diffraction patterns calculated for the models C and F of Figure 2.30C,F present almost right intensities of the equatorial 100 and 020 reflections at 2θ = 9.39° and 10.18°, respectively, and of $1\bar{1}1$, 101, and 021 reflections on the first layer line at 2θ = 15.75°, 16.96°, and 16.45°, respectively, but present a too high intensity of the 011 reflection at 2θ = 13.86° (Tables 2.17 and 2.18 and profile d of Figure 2.29A and pattern D of Figure 2.30), which is absent in the experimental powder and fiber diffraction patterns.

The packing models of the pure enantiomers iP(*R*)3MP and iP(*S*)3MP of Figure 2.27 represent only limit ordered models of the structure of the random copolymer iP(*R*,*S*)3MP. The structure of the real crystalline modification of iP(*R*,*S*)3MP is obviously disordered due to configurational

disorder in the sequence of *R* and *S* monomeric units along the chains of crystallizable stretches, as in the disordered models of chains of Figure 2.25, conformational disorder of the lateral groups, and also to the presence of structural disorder in the packing of chains. This disorder has been modeled and limit disordered models of packing have been obtained by assuming that each site of the crystalline lattice with space group symmetry $P2_1/b$ may be occupied with different probabilities by the different chains of Figure 2.24, having different chirality of the side groups, different handedness of the helical conformation, different up/down orientations, and different conformations of the lateral groups.

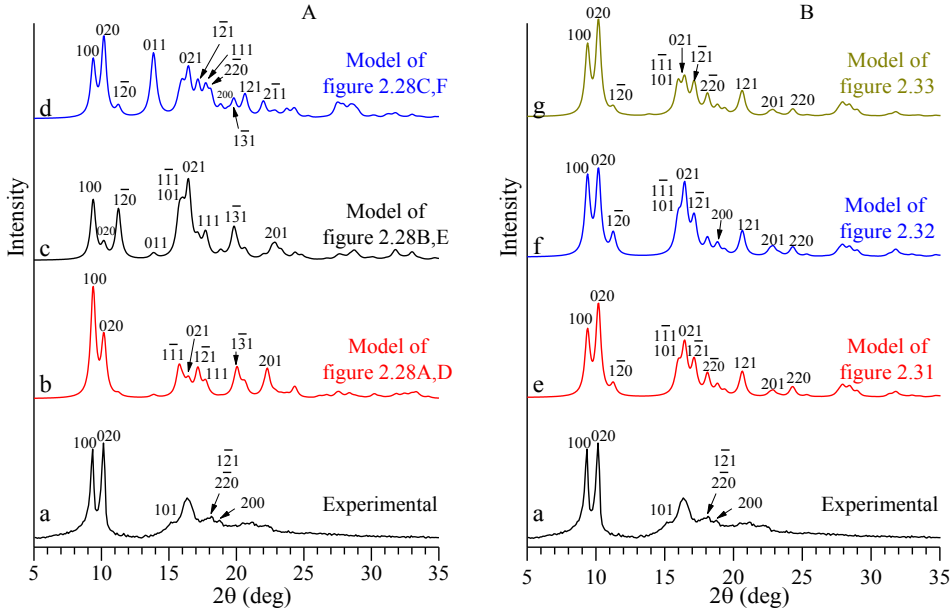

Figure 2.29. Comparison between the experimental X-ray powder diffraction profile of iP(*R*,*S*)3MP of Figure 2.19b after subtraction of the amorphous halo (a) and diffraction profiles calculated for the limit ordered models of packing of space group symmetry $P2_1/b$ of Figures 2.28A,D (b), 2.28B,E (c), and 2.28C,F (d) for the limit disordered models of Figures 2.31 (e) and 2.32(f) and for the for the limit disordered model of packing of space group symmetry $P2_1$ of Figure 2.33 (g).

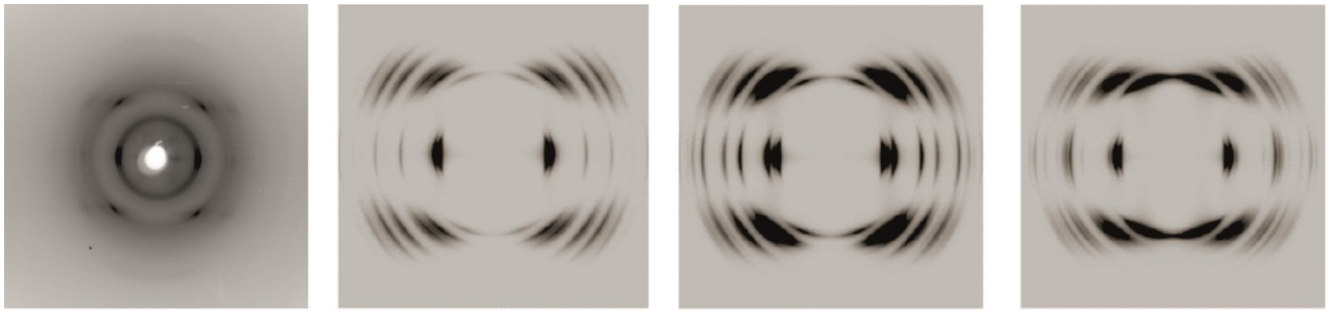

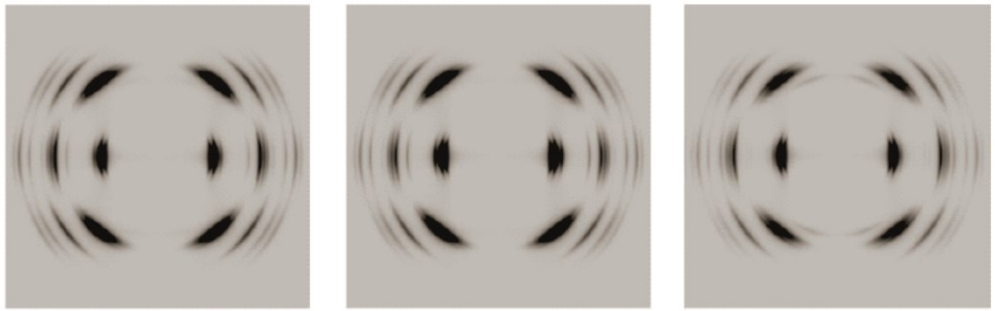

Figure 2.30. Comparison between the experimental X-ray fiber diffraction patter of iP(*R*,*S*)3MP (A) and diffraction patterns calculated for the limit ordered models of packing of space group symmetry $P2_1/b$ of Figures 2.28A,D (B), 2.28B,E (C), and 2.28C,F (D), for the limit disordered models of Figures 2.31 (E) and 2.32 (F) and for the for the limit disordered model of packing of space group symmetry $P2_1$ of Figure 2.33 (G).

Several possibilities have been considered. For limit disordered models made by a statistical occupancy on the lattice sites of helices of identical handedness but different chirality of monomeric unit and conformations of the lateral groups, the agreement between experimental and calculated diffracted intensities obtained for the limit ordered models of pure enantiomers of Figure 2.28 could not be improved. A remarkable improvement of the agreement was obtained for limit disordered models characterized by disorder in the random substitution in the sites of the lattice of chains having opposite helical handedness and opposite chirality of the lateral groups, as in the model of Figure 2.31. In this model each site of the lattice is occupied with the same probability by chains iP(*S*)3MP-R-G^+T (up) (Figure 2.24C) and iP(R)3MP-L-G^+T (down) (Figure 2.24F), having opposite chirality in the helical hand (right-handed and left-handed), opposite S and R chirality of the lateral groups, and opposite up and down orientation (anticlined chains). As shown in the limit ordered models of Figure 2.28C,F, built with these two models of chains, the chains iP(*S*)3MP-R-G^+T (up) and iP(*R*)3MP-L-G^+T (down) have not only identical projections in the ab plane (Figure 2.31A), but also similar outside envelope for the lateral side groups as shown in Figure 2.32B. The structure factors calculated for the limit disordered model of Figure 2.31 are reported in Tables 2.17 and 2.18, whereas the calculated powder diffraction profile is reported in Figure 2.29B (profile e) and the calculated fiber diffraction pattern is shown in Figure 2.30E. A very good agreement between observed and calculated diffraction profiles is obtained.

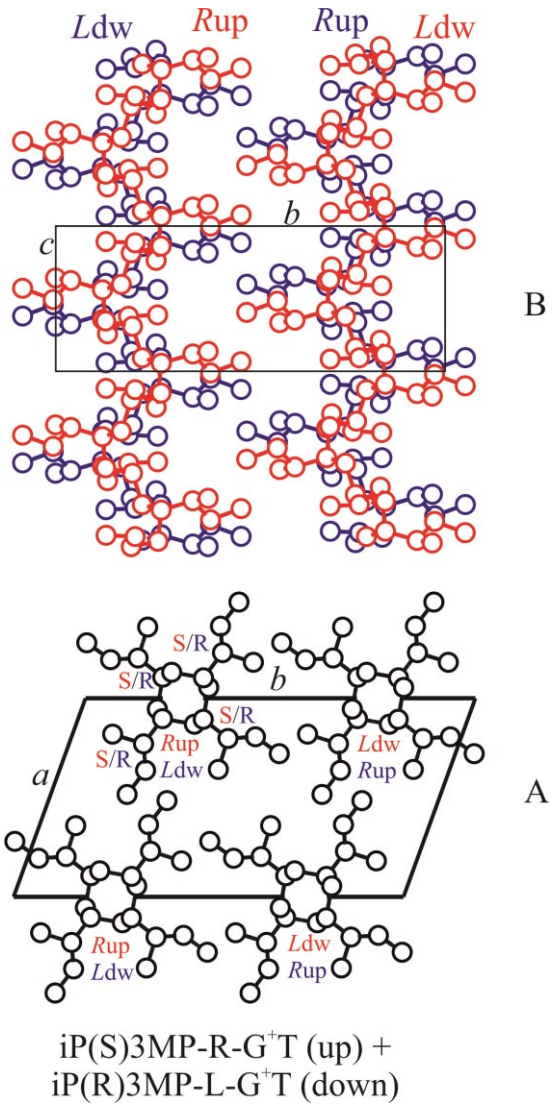

Figure 2.31. Limit disordered model of packing of iP(*R*,*S*)3MP in the monoclinic unit cell with axes a = 10.02 Å, b = 18.48 Å, c = 6.87 Å, and γ = 109.9° according to the space group $P2_1/b$ viewed in *ab* (A) and *bc* (B) projections. The crystalline lattice at $x = 0$ and $y = 0.25$ is occupied with the same probability by chains iP(*S*)3MP-R-G$^+$T (up) (chain model of Figure 2.24C) and iP(*R*)3MP-L-G$^+$T (down) (chain model of Figure 2.24F), having opposite chirality in the helical hand (right-handed and left-handed), opposite S and R chirality of the lateral groups, and opposite up and down orientation (anticlined chains). The chains iP(*S*)3MP-R-G$^+$T (up) and iP(*R*)3MP-L-G$^+$T (down) have identical projections in the *ab* plane (A) and similar outside envelope for the lateral side groups (B). *R*up and *L*dw indicate right-handed helix with up orientation and left-handed helix with down orientation, whereas *S*/*R* indicates the chirality of the methine carbons of the lateral groups.

According to the experimental diffraction pattern, in the calculated diffraction profile e of Figure 2.29B the 011 reflection at 2θ = 13.86° is absent, the intensity of the $1\bar{2}0$ reflection at 2θ = 11.26° is very low, and the intensity ratios of first layer lines and equatorial reflections in the range of 2θ = 15°−21°, in particular the 101, 021, $1\bar{2}1$, $2\bar{2}0$, and 121 reflections at 2θ = 15.96°, 16.45°, 17.14°, 18.11°, and 20.64°, respectively, are similar to those in the experimental profile. The disagreement factor calculated for both observed and nonobserved reflections is 15%. The diffraction data and the agreement indicates that in the crystals of iP(*R*, *S*)3MP chain stretches of sequences of monomeric units with prevailing *S* conf iguration tend to assume a right-handed helical conformation, whereas those of prevailing *R* configuration tend to assume a left-handed helical conformation. The prevailing combinations of (*S*/*R*)chirality−(Right/Left)-helical chirality are therefore *S*-right, *R*-left, as in chain models C, iP(S)3MP-R-G^+T (up) (Figure 2.24C) and F, iP(R)3MP-L-G+T (down) (Figure 2.24F). Disorder originates from the random substitution of helical stretches of opposite *R* and *S* configuration and helical handedness provided that they are also anticlined, that is, one up and the other down. In this model the possible disorder in the conformation of the lateral groups is not present and both S and R monomeric units are characterized by conformation of the side groups with $\theta_3 = G^+$ and θ_4 = T, as in the ordered models C and F of the pure enantiomers of Figure 2.28C,F. This conformation is characterized by the ethyl groups in a double-gauche arrangement to both CH_2 groups of the backbone (Figure 2.25A',B'). Therefore, even though the conformation of the side groups with $\theta_4 = G^+$ or G^- is slightly favored in term of packing energy (Figure 2.27A,D), the diffraction agreement indicates prevalence of the conformation of the lateral groups with θ_4 = T.

In spite of the good agreement already achieved for the model of Figure 2.31, some kind of conformational disorder should be also included in the

crystals. Moreover, even though the diffraction data indicate that in the chains of the random copolymer iP(*R*,*S*)3MP the prevailing combinations of (*S*/*R*)chirality-(Right/Left)helical chirality are *S*-right, *R*-left, disorder in this combination may be present and sequences of *S* monomeric units may also assume left-handed helical conformation and sequences of *R* monomeric units may also assume right-handed helical conformation, as in the models of chains of Figures 2.24B,C' and 7E, F', corresponding to the combinations S-left and R-right. Disorder in the succession of *R* and *S* monomeric units along the chain of iP(*R*,*S*)3MP, conformational disorder of the side groups, disorder in the helical chirality and in the up−down orientation of the chains can be modeled by assuming that each site of the crystalline lattice is occupied with a given probability by chains iP(*S*)3MP-R-G^+T (up) (Figure 2.24C), iP(*R*)3MP-L-G^+T (down) (Figure 2.24F), iP(*S*)3MP-L-TT (down) (Figure 2.23B), and iP(*R*)3MP-R-G^-T (up) (Figure 2.23E). The chain models C, iP(*S*)3MP-R-G^+T (up), and E, iP(*R*)3MP-R-G^-T (up), are isoclined (up) and isomorphous (right-handed) but have opposite S and R chirality of the lateral groups, with chirality combinations (*S*)-right-handed and (*R*)-right-handed, and different conformations of the side groups with θ_3 = G^+ or G^-. Analogously, the chain models F, iP(*R*)3MP-L-G^+T (down), and B, iP(*S*)3MP-L-TT (down), are isoclined (down) and isomorphous (left-handed) but have opposite *S* and *R* chirality of the lateral groups, with combinations (*R*)-left-handed and (*S*)-left-handed, and different conformations of the side groups with θ_3 = G^+ or T. This limit disordered model for the structure of iP(*R*,*S*)3MP is shown in Figure 2.32. In this limit disordered model, the substitution type disorder of enantiomorphous, right- and left-handed, and anticlined chains of opposite *S* and *R* chirality of the side groups of the model of Figure 2.31 is coupled with conformational disorder of the side groups and different combinations (*S*/*R*)chirality-(Right/Left)-helical chirality.

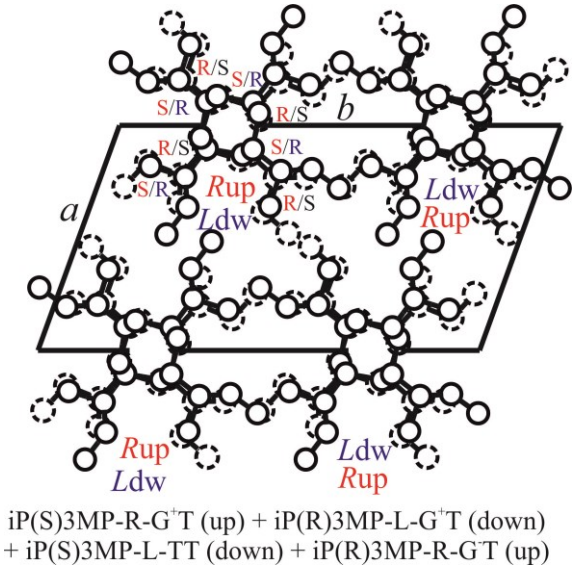

Figure 2.32. Limit disordered model of packing of iP(*R*,*S*)3MP in the monoclinic unit cell with axes a = 10.02 Å, b = 18.48 Å, c = 6.87 Å, and γ = 109.9° according to the space group $P2_1/b$. The crystalline lattice at x = 0 and y = 0.25 is occupied with the same probability by chains iP(*S*)3MP-R-G$^+$T (up) (chain model of Figure 2.24C), iP(*R*)3MP-L-G$^+$T (down) (chain model of Figure 2.24F), iP(*S*)3MP-L-TT (down) (chain model of Figure 2.24B), and iP(*R*)3MP-R-G$^-$T (up) (chain model of Figure 2.24E), having opposite chirality in the helical hand (right-handed and left-handed), opposite *S* and *R* chirality of the lateral groups, opposite up and down orientation (anticlined chains) and different combinations (*S*/*R*)chirality−(Right/Leflt)helical chirality. Rup and Ldw indicate right-handed helix with up orientation and left-handed helix with down orientation, whereas S/R indicates the chirality of the methine carbons of the lateral groups.

The degrees of different types of disorder are defined by the occupancy factors of atoms belonging to the different model chains. The occupancy factors of all atoms of the right-handed up chains are $p/2$ for iP(*S*)3MP-R-G$^+$T (up) (chain model C) and $(1 - p)/2$ for iP(*R*)3MP-R-G$^-$T (up) (chain model E), and the occupation factors of atoms of the left handed down chains are $p/2$ for iP(*R*)3MP-L-G$^+$T (down) (chain model F) and $(1 - p)/2$ for iP(*S*)3MP-L-TT (down) (chain model B). A value of the parameter p = 1 would correspond to the model of Figure 2.31, including substitution type disorder of enantiomorphous and anticlined chains of opposite *S* and *R* chirality, and no conformational disorder. The case $0.5 < p < 1$ corresponds

to the presence of stretches of left-(right-) handed 4/1 helices of a prevailing *R* (*S*) configuration, including $(1 - p)/2$ stretches of left- (right-) handed 4/1 helices of a prevailing *S* (*R*) configuration and different conformation of the lateral groups, disorder in the right/left-handed helices substitution being still present. The structure factors calculated for the limit disordered model of Figure 2.32 for the space group $P2_1/b$ for $p = 0.8$ are reported in Table 2.175 (for powder diffraction) and Table 2.18 (for fiber diffraction). The calculated diffraction profile for the model of Figure 2.32 is reported in Figure 2.29B (profile f) in comparison with the experimental X-ray powder diffraction profile, whereas the calculated fiber diffraction pattern is shown in Figure 2.30F. A good agreement between calculated and observed structure factors is obtained for the ideal limit disordered model of Figure 2.32 in all cases. In particular, for $p = 0.8$ the agreement is slightly improved with a value of the disagreement factor *R* of 14%. The fractional coordinates of carbon atoms of the asymmetric units of the model of Figure 2.32 are reported in Table 2.19.

Table 2.17. Comparison between observed structure factors $F_o = (I/LP)^{1/2}$, evaluated from the intensities I observed in the Xray powder diffraction profile of iP(*R*,*S*)3MP of Figure 2.19b, and calculated structure factors, $F_c = (\Sigma|Fi|^2 \cdot Mi)^{1/2}$, for the limit ordered models of packing of Figure 2.28 of the pure enantiomers iP(*S*)3MP and iP(*R*)3MP and the limit disordered models of packing of Figures 2.31 and 2.32 of the random copolymer iP(*R*,*S*)3MP in the monoclinic unit cell with axes $a = 10.02$ Å, $b = 18.48$ Å, $c = 6.87$ Å, and $\gamma = 109.9°$ according to the space group $P2_1/b$[a].

hkl	$2\theta_o$ (deg)	$2\theta_c$ (deg)	d_o (Å)	d_c (Å)	F_o	F_c				
						Mod. of Fig2.28 A,D	Mod. of Fig2.28 B,E	Mod. of Fig2.28 C,F	Mod. of Fig2.31	Mod. of Fig2.32
100	9.34	9.39	9.47	9.42	86	138	93	84	84	85
020	10.19	10.18	8.68	8.69	89	110	48	109	109	96
$1\bar{2}0$	–	11.26	–	7.86	–	26	102	42	42	54
011	–	13.86	–	6.39	–	35	44	142	–	–
$1\bar{1}1$	15.14	15.75	5.85	5.62	88	122	122	58	–	–
101		15.96		5.55		25 → 137	79 → 166	94 → 113	94 → 97	91 → 97
120		16.06		5.52		58	80	24	24	35
021	16.36	16.45	5.41	5.39	140	88	178	130	130	139
$1\bar{2}1$	18.16	17.14	4.88	5.17	115	125	82	110	110	104
111		17.72		5.00		93 → 156	111 → 138	106 → 176	– → 141	– → 126
$\bar{2}20$		18.11		4.90		13	3	89	89	70
200	18.74	18.84	4.73	4.71	107	19	58	64	64	63
$1\bar{4}0$		19.37		4.58		13 → 23	23 → 62	44 → 78	44 → 78	40 → 74
$1\bar{3}1$	21.17	19.81	4.20	4.48	141	55	132	93	–	–
031		20.05		4.43		144	64	2	–	–
040		20.44		4.34		50 → 187	12 → 165	26 → 149	26 → 116	18 → 107
121		20.64		4.30		93	174	113	113	105
$2\bar{1}1$	22.13	22.00	4.02	4.04	93	54	50	101	–	–
$2\bar{2}1$		22.29		3.99		158	17	9	9	10
$2\bar{4}0$		22.63		3.93		21 → 184	75 → 152	38 → 125	38 → 74	45 → 88
201		22.89		3.88		58	98	58	58	66
$1\bar{4}1$		23.33		3.81		48	72	25	25	34

$2\bar{3}1$	23-35	23.73	3.88 - 2.56	3.75	211	50	29	73	–	–
041		24.24		3.67		41	6	64	63	52
131		24.33		3.66		97	56	–	–	–
220		24.37		3.65		26	44	55	55	53
211		24.85		3.58		5	58	5	–	–
140		25.33		3.52		9	24	36	36	34
002		25.94		3.43		6	4	6	6	6
$2\bar{4}1$		26.13		3.41		44	11	11	11	7
012		26.45		3.37		30	4	20	–	–
$3\bar{2}0$		26.70		3.34		52	33	10	10	15
$1\bar{5}1$		27.41		3.25		47	23	77	–	–
$1\bar{1}2$		27.52		3.24		54	40	71	–	–
102		27.64		3.23		56	55	54	54	54
221		27.66		3.22		33	25	9	9	12
022		27.93		3.19		18	45	93	93	83
$1\bar{2}2$		28.35		3.15		72	22	42	42	29
300		28.42		3.14		27	48	52	52	52
141		28.52		3.13		11	8	58	58	49
						281	263	282	216	203

112		28.72		3.11		26	87	80	–	–
051		28.79		3.10		22	41	30	–	–
$3\bar{4}0$		28.86		3.09		32	3	5	5	4
$1\bar{6}0$		29.01		3.08		17	45	61	61	58
$2\bar{5}1$		29.28		3.05		32	13	8	–	–
$3\bar{2}1$		29.75		3.00		21	32	15	15	18
$1\bar{3}2$		30.08		2.97		13	47	35	–	–
$3\bar{1}1$		30.09		2.97		29	14	16	–	–
$2\bar{6}0$		30.23		2.96		55	10	13	13	12
032		30.25		2.95		42	18	15	–	–
$3\bar{3}1$		30.30		2.95		7	8	32	–	–
122		30.66		2.92		44	19	6	6	–
060		30.88		2.89		11	11	2	2	4
231		31.11		2.87		21	34	46	–	–
301		31.32		2.86		25	10	49	49	41
$2\bar{1}2$		31.61		2.83		33	34	16	–	–
$3\bar{4}1$		31.72		2.82		17	63	46	46	49
$2\bar{2}2$		31.82		2.81		25	80	25	25	36
$1\bar{6}1$		31.86		2.81		65	41	50	50	48
202		32.25		2.77		39	38	27	27	29
240		32.44		2.76		59	17	9	9	11
$1\bar{4}2$		32.58		2.75		41	37	19	19	23
$2\bar{3}2$		32.87		2.72		29	23	11	–	–
$2\bar{6}1$		32.98		2.72		66	46	39	39	41
151		33.04		2.71		6	83	47	–	–

042		32.25		2.69		4	13	15	15	15
132		33.32		2.69		51	8	9	–	–
311		33.33		2.69		70	10	6	–	–
320		33.48		2.68		32	11	16	16	11
061		33.58		2.67		21	35	27	27	29
212		33.71		2.66		16	9	26	–	–
$3\bar{5}1$		33.90		2.64		13	10	24	–	–
$3\bar{6}0$		34.23		2.62		48	3	17	17	13
$2\bar{4}2$		34.69		2.59		1	49	38	38	40
241		35.04		2.56		3	3	31	31	26

a. The experimental Bragg angles ($2\theta_o$) and Bragg distances (d_0) observed in the X-ray powder diffraction profile of iP(*R*,*S*)3MP of Figure 2.19b and those calculated ($2\theta_c$ and d_c) for the monoclinic unit cell with axes $a = 10.02$ Å, $b = 18.48$ Å, $c = 6.87$ Å, and $\gamma = 109.9°$ are also reported.

Table 2.18. Comparison between observed structure factors $F_o = (I/LP)^{1/2}$, evaluated from the intensities I observed in the Xray fiber diffraction pattern of iP(*R*,*S*)3MP of Figure 2.20, and calculated structure factors, $F_c = (\Sigma|Fi|^2 \cdot Mi)^{1/2}$, for the limit ordered models of packing of Figure 2.28 of the pure enantiomers iP(*S*)3MP and iP(*R*)3MP and the limit disordered models of packing of Figures 2.31 and 2.32 of the random copolymer iP(*R*,*S*)3MP in the monoclinic unit cell with axes $a = 10.02$ Å, $b = 18.48$ Å, $c = 6.87$ Å, and $\gamma = 109.9°$ according to the space group $P2_1/b$[a].

hkl	$2\theta_o$ (deg)	$2\theta_c$ (deg)	d_o (Å)	d_c (Å)	F_o	F_c				
						Mod. of Fig2.28 A,D	Mod. of Fig2.28 B,E	Mod. of Fig2.28 C,F	Mod. of Fig2.31	Mod. of Fig2.32
100	9.38	9.39	9.43	9.42	79	98	66	59	59	60
020	10.18	10.18	8.69	8.69	100	78	34	77	77	68
$1\bar{2}0$	11.75	11.26	7.53	7.86	26	18	72	29	29	38
110	12.80	12.11	6.91	7.30	24	–	–	–	–	–
120	16.78	16.06	5.28	5.52	31	41	56	17	17	25
$2\bar{2}0$	18.14	18.11	4.89	4.90	23	10	2	63	63	50
200	18.86	18.84	4.7	4.71	44	13	41	45	45	44
$1\bar{4}0$		19.37		4.58		9 → 16	16 → 44	31 → 55	31 → 55	28 → 52
040	20.47	20.44	4.34	4.34	33	35	9	18	18	13
$2\bar{4}0$		22.63		3.93		15 → 39	53 → 54	27 → 32	27 → 32	32 → 35

220 140	25.29	24.37 25.33	3.52	24.37 25.33	23	18 6 }19	31 17 }36	39 25 }47	39 25 }47	37 24 }44
$3\bar{2}0$	26.28	26.70	3.39	3.34	10	36	23	7	7	10
300	–	28.42	–	3.14	–	19	34	37	37	36
$3\bar{4}0$	–	28.86	–	3.09	–	23	2	4	4	3
$1\bar{6}0$	–	29.01	–	3.08	–	12	32	43	44	41
$2\bar{6}0$	–	30.23	–	2.96	–	39	7	9	9	9
240	–	32.44	–	2.76	–	41	12	6	6	7
320	–	33.48	–	2.68	–	23	8	11	11	7
$3\bar{6}0$	–	34.23	–	2.62	–	34	2	12	12	9
011	–	13.86	–	6.39	–	17	22	71	–	–
$1\bar{1}1$ 101	15.55	15.75 15.96	5.7	5.62 5.55	46	61 12 }62	61 39 }73	29 47 }55	– 47 }47	– 45 }45
021	16.55	16.45	5.34	5.39	71	44	89	65	65	70
$1\bar{2}1$ 111 $1\bar{3}1$ 031	18.30	17.14 17.72 19.81 20.05	4.85	5.17 5.00 4.48 4.43	52	62 42 27 72 }109	41 56 66 32 }101	55 53 47 – }89	55 – – – }55	52 – – – }52
121	21.15	20.64	4.20	4.30	35	47	37	56	56	53
$2\bar{1}1$ $2\bar{2}1$ 201 $1\bar{4}1$ $2\bar{3}1$ 041 131 211 $2\bar{4}1$	22.00	22.00 22.29 22.89 23.33 23.72 24.24 24.33 24.85 26.13	4.03	4.09 3.99 3.88 3.81 3.75 3.67 3.66 3.58 3.41	51	27 79 29 24 25 20 46 3 22 }111	25 8 49 36 14 3 28 29 5 }79	51 4 29 12 36 32 – 2 6 }77	– 4 29 12 – 32 – – 6 }54	– 5 33 17 – 26 – – 3 }46
$1\bar{5}1$	–	27.41	–	3.25	–	24	11	38	–	–
221	–	27.66	–	3.22	–	17	12	4	4	6
141	–	28.52	–	3.13	–	5	4	29	29	24
051	–	28.79	–	3.10	–	11	20	15	–	–

$2\bar{5}1$	–	29.28	–	3.05	–	16	6	4	–	–
$3\bar{2}1$	–	29.75	–	3.00	–	11	16	7	7	9
$3\,\bar{1}\,1$	–	30.09	–	2.97	–	14	7	8	–	–
$3\bar{3}1$	–	30.30	–	2.95	–	4	4	16	–	–
231	–	31.11	–	2.87	–	11	17	23	–	–
301	–	31.32	–	2.86	–	12	5	24	24	20
$3\bar{4}1$	–	31.72	–	2.82	–	9	31	23	23	25
$1\bar{6}1$	–	31.86	–	2.81	–	33	21	25	25	24
$2\bar{6}1$	–	32.98	–	2.72	–	33	23	20	20	20
151	–	33.04	–	2.71	–	3	41	24	–	–
311	–	33.33	–	2.69	–	35	5	3	–	–
061	–	33.58	–	2.67	–	11	17	14	14	14
$3\bar{5}1$	–	33.90	–	2.64	–	6	5	12	–	–
241	–	35.04	–	2.56	–	2	1	16	16	13
002	–	25.94	–	3.43	–	4	3	6	5	4
012	–	26.45	–	3.37	–	15	2	10	–	–
$1\,\bar{1}\,2$	–	26.52	–	3.24	–	27	20	36	–	–
102	–	27.64	–	3.23	–	28	27	27	27	27
022	–	27.93	–	3.19	–	9	23	46	46	42
$1\bar{2}2$	–	28.36	–	3.15	–	36	11	21	21	14
112	–	28.72	–	3.11	–	13	44	40	–	–
$1\bar{3}2$	–	30.09	–	2.97	–	7	24	18	–	–
032	–	30.25	–	2.95	–	21	9	8	–	–
122	–	30.66	–	2.92	–	22	10	3	3	–
$2\,\bar{1}\,2$	–	31.61	–	2.83	–	17	17	8	–	–
$2\bar{2}2$	–	31.82	–	2.81	–	12	40	13	13	18
202	–	32.25	–	2.78	–	20	19	14	14	15
$1\bar{4}2$	–	32.58	–	2.75	–	20	19	10	10	11
$2\bar{3}2$	–	32.87	–	2.72	–	14	12	6	–	–
042	–	33.25	–	2.69	–	2	7	8	8	7
132	–	33.32	–	2.69	–	26	4	5	–	–
212	–	33.71	–	2.66	–	8	4	13	–	–
$2\bar{4}2$	–	34.69	–	2.59	–	1	24	19	19	20

a. The experimental Bragg angles ($2\theta_o$) and Bragg distances (d_0) observed in the X-ray fiber diffraction pattern of iP(*R*,*S*)3MP of Figure 2.20 and those calculated ($2\theta_c$ and d_c) for the monoclinic unit cell with axes a = 10.02 Å, b = 18.48 Å, c = 6.87 Å, and γ = 109.9° are also reported.

Table 2.19. Fractional coordinates of the carbon atoms of the asymmetric unit (two monomeric units) of the model of Figure 2.32 for the crystal structure of iP(*R*/*S*)3MP in the monoclinic unit cell with axes a = 10.02 Å, b = 18.48 Å, c = 6.87 Å, and γ = 109.9°according to the space group $P2_1/b$.

atom	*x*/*a*	*y*/*b*	*z*/*c*	occupancy
C_1	-0.106	0.178	0.463	0.4
C_2	-0.203	0.097	0.394	0.4
C_3	-0.194	0.028	0.514	0.4
C_4	-0.279	-0.048	0.417	0.4
C_5	-0.358	0.093	0.386	0.4
C_6	0.131	0.303	0.177	0.4
C_7	0.103	0.216	0.214	0.4
C_8	0.054	0.194	0.427	0.4
C_9	0.230	0.191	0.151	0.4
C_{10}	0.363	0.221	0.280	0.4
C_{11}	0.485	0.196	0.204	0.4
C_{12}	0.181	0.103	0.133	0.4
C_1’	-0.054	0.306	0.573	0.4
C_2’	-0.103	0.284	0.786	0.4
C_3’	-0.131	0.197	0.823	0.4
C_4’	-0.230	0.309	0.849	0.4
C_5’	-0.363	0.279	0.719	0.4
C_6’	-0.485	0.304	0.796	0.4
C_7’	-0.181	0.397	0.866	0.4
C_8’	-0.106	0.178	0.037	0.4
C_9’	-0.203	0.097	0.105	0.4
C_{10}’	-0.194	0.028	-0.014	0.4
C_{11}’	-0.279	-0.048	0.083	0.4
C_{12}’	-0.358	0.093	0.114	0.4
C_1’’	0.116	0.316	0.548	0.1
C_2’’	0.221	0.394	0.620	0.1
C_3’’	0.374	0.395	0.648	0.1
C_4’’	0.470	0.469	0.746	0.1
C_5’’	0.220	0.462	0.489	0.1
C_6’’	0.040	0.190	0.081	0.1
C_7’’	0.092	0.209	0.294	0.1
C_8’’	0.139	0.297	0.333	0.1
C_9’’	0.209	0.176	0.354	0.1
C_{10}’’	0.150	0.088	0.392	0.1
C_{11}’’	0.261	0.058	0.477	0.1
C_{12}’’	0.333	0.196	0.208	0.1
C_1’’’	0.116	0.316	0.952	0.1
C_2’’’	0.139	0.297	0.167	0.1
C_3’’’	0.221	0.394	0.880	0.1
C_4’’’	0.374	0.395	0.851	0.1
C_5’’’	0.470	0.469	0.754	0.1
C_6’’’	0.220	0.462	0.011	0.1
C_7’’’	0.092	0.209	0.206	0.1
C_8’’’	0.040	0.190	0.419	0.1
C_9’’’	0.209	0.176	0.146	0.1

C_{10}'''	0.150	0.088	0.108	0.1
C_{11}'''	0.261	0.057	1.023	0.1
C_{12}'''	0.333	0.196	0.292	0.1

a. C_1−C_{12}: atoms of chain iP(*R*)-3MP-L-G^+T (down); C_1'−C_{12}': atoms of iP(*S*)-3MP-R-G^+T (up); C_1''−C_{12}'': atoms of iP(R)-3MP-R-G^-T (up); C_1'''−C_{12}''': atoms of iP(*S*)-3MP-L-TT (down).

Inspection of the X-ray fiber diffraction data of Figure 2.20 and Table 2.13 shows the presence of a very weak reflection on the equator at $2\theta = 12.8°$, indexed as 110 reflection that is absent in the calculated patterns of the models for the space group $P2_1/b$. The presence of this reflection with k odd suggests that in the very local arrangement of chains the symmetry of the space group should be lower than $P2_1/b$ and that locally, the glide plane symmetry b is not present. A possible space group that describes the very local packing of chains could be $P2_1$. A limit disordered model of packing with chains arranged as in the model of Figure 2.31 but with space group symmetry $P2_1$ is shown in Figure 2.33.

In this model the two chains included in the unit cell with chain axes at $y = 0$ and $y = 0.5$ are independent; that is, they are not related by elements of symmetry (in the model of Figure 2.31 these chains at $y = 0.25$ and 0.75 are related by the glide plane b). In the model of Figure 2.33 the two chains are assumed to be enantiomorphous and anticlined, as in the model $P2_1/b$ of Figure 2.31, but with independent settings ω and z. Also in this model each site of the crystalline lattice is occupied with the same probability by chains iP(*S*)3MP-R-G^+T (up) (chain model of Figure 2.24C) and iP(*R*)3MP-L-G^+T (down) (chain model of Figure 2.24F), having opposite chirality in the helical hand (right-handed and left-handed), opposite *S* and *R* chirality of the lateral groups, and opposite up and down orientation (anticlined chains).

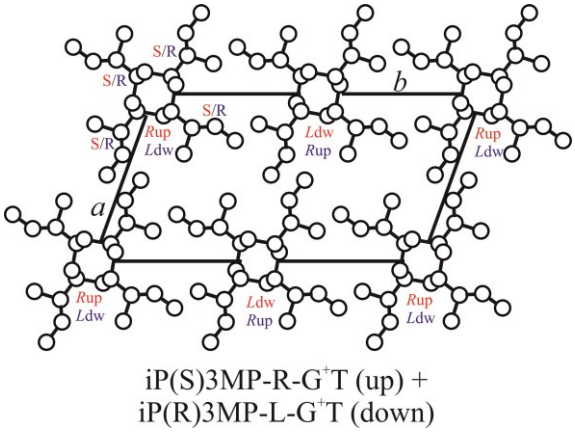

Figure 2.33. Limit disordered model of packing of iP(*R*,*S*)3MP in the monoclinic unit cell with axes a = 10.02 Å, b = 18.48 Å, c = 6.87 Å, and γ = 109.9° according to the space group $P2_1$. The two chains included in the unit cell at y = 0 and 0.5 are independent; that is, they are not related by elements of symmetry and are assumed to be enantiomorphous and anticlined, as in the model $P2_1/b$ of Figure 2.31, but with independent settings ω and z. The lattice site at $x = y = 0$ is occupied with the same probability by chains iP(*S*)3MP-R-G$^+$T (up) (chain model of Figure 2.24C) and iP(*R*)3MP-L-G$^+$T (down) (chain model of Figure 2.24F), having opposite chirality in the helical hand (right-handed and left-handed), opposite *S* and *R* chirality of the lateral groups, and opposite up and down orientation (anticlined chains). The chains iP(*S*)3MP-R-G$^+$T (up) and iP(*R*)3MP-L-G$^+$T (down) have identical projections in the *ab* plane.

The structure factors calculated for a limit disordered model of Figure 2.33 for the space group $P2_1$ are reported in Table 2.20 (powder diffraction) and Table 2.21 (for fiber diffraction), whereas the calculated powder diffraction profile is reported in Figure 2.29B (profile g) and the calculated fiber diffraction pattern is shown in Figure 2.30G. A good agreement is obtained also for this low symmetry model with a value of the disagreement factor *R* of 18%.

Additional types of disorder could also be present, as disorder in the conformation of the lateral groups and in the azimuthal setting of the chains around the chain axes and in the relative shift of the chains along *c*, compatible with the $P2_1$ space group symmetry.

Table 2.20. Comparison between observed structure factors $F_o = (I/LP)^{1/2}$, evaluated from the intensities I observed in the Xray powder diffraction profile of iP(*R*,*S*)3MP of Figure 2.19b, and calculated structure factors, $F_c = (\Sigma|Fi|^2 \cdot Mi)^{1/2}$, for the model of packing of Figures 2.33 of the random copolymer iP(*R*,*S*)3MP in the monoclinic unit cell with axes a = 10.02 Å, b = 18.48 Å, c = 6.87 Å, and γ = 109.9° according to the space group $P2_1$[a].

hkl	$2\theta_o$ (deg)	$2\theta_c$ (deg)	d_o(Å)	d_c(Å)	$F_o = (I_o/LP)^{1/2}$	$F_c=(\Sigma\|F_i\|^2M_i)^{1/2}$ Model of Figure 2.33
100	9.34	9.39	9.47	9.42	90	89
020	10.19	10.18	8.68	8.69	94	114
$1\bar{2}0$	–	11.26	–	7.86	–	33
110	–	12.11	–	7.31	–	7
011	–	13.86	–	6.39	–	20
$1\bar{3}0$	15.14	14.98	5.85	5.91	92	4
030		15.29		5.79		12
$1\bar{1}1$		15.75		5.62		6 } 106
101		15.96		5.55		104
120		16.06		5.52		12
021	16.36	16.45	5.41	5.39	147	108
$1\bar{2}1$	18.16	17.14	4.88	5.17	121	109
111		17.72		5.00		4
$2\bar{1}0$		17.75		4.99		17 } 142
$2\bar{2}0$		18.11		4.90		89
200	18.74	18.84	4.73	4.71	113	60 } 78
$1\bar{4}0$		19.37		4.58		50
$1\bar{3}1$	21.17	19.81	4.20	4.48	148	4
$2\bar{3}0$		19.84		4.48		8
031		20.05		4.43		17
040		20.44		4.34		42 } 122
130		20.55		4.32		7
121		20.64		4.30		112
210		21.15		4.20		12

$2\bar{1}1$	22.13	22.00	4.02	4.04	120	1
$2\bar{2}1$		22.29		3.99		11
$2\bar{4}0$		22.63		3.93		41
201		22.89		3.88		57
$1\bar{4}1$		23.33		3.81		30
$2\bar{3}1$		23.73		3.75		7
$1\bar{5}0$		24.09		3.69		10
041		24.24		3.67		49
131		24.33		3.66		3
220		24.37		3.65		53
						106
211	–	24.85	–	3.58	–	6
140	–	25.33	–	3.52	–	28
050	–	25.63	–	3.47	–	18
002	–	25.94	–	3.43	–	5
$2\bar{4}1$	–	26.13	–	3.41	–	9
$2\bar{5}0$	–	26.17	–	3.40	–	3
012	–	26.45	–	3.37	–	4
$3\bar{2}0$	–	26.70	–	3.34	–	27
$3\bar{1}0$	–	27.08	–	3.29	–	13
$3\bar{3}0$	–	27.31	–	3.27	–	7
$1\bar{5}1$	–	27.41	–	3.25	–	2
$1\bar{1}2$	–	27.52	–	3.24	–	7
102	–	27.64	–	3.23	–	58
221	–	27.66	–	3.22	–	22
022	–	27.93	–	3.19	–	101
230	–	28.19	–	3.16	–	8
$1\bar{2}2$	–	28.35	–	3.15	–	44
300	–	28.42	–	3.14	–	60
141	–	28.52	–	3.13	–	53
112	–	28.72	–	3.11	–	5
051	–	28.79	–	3.10	–	10
$3\bar{4}0$	–	28.86	–	3.09	–	1
$1\bar{6}0$	–	29.01	–	3.08	–	65
$2\bar{5}1$	–	29.28	–	3.05	–	4
$3\bar{2}1$	–	29.75	–	3.00	–	17
$1\bar{3}2$	–	30.09	–	2.97	–	5
$3\bar{1}1$	–	30.09	–	2.97	–	7

$2\bar{6}0$	–	30.23	–	2.96	–	1
032	–	30.25	–	2.95	–	7
150	–	30.29	–	2.95	–	14
$3\bar{3}1$	–	30.30	–	2.95	–	1
310	–	30.60	–	2.92	–	9
122	–	30.66	–	2.92	–	4
060	–	30.88	–	2.90	–	15
231	–	31.11	–	2.87	–	12
$3\bar{5}0$	–	31.22	–	2.86	–	11
301	–	31.32	–	2.86	–	40
$2\bar{1}2$	–	31.61	–	2.83	–	9
$3\bar{4}1$	–	31.72	–	2.82	–	41
$2\bar{2}2$	–	31.82	–	2.81	–	25
$1\bar{6}1$	–	31.86	–	2.81	–	48
202	–	32.25	–	2.78	–	24
240	–	32.44	–	2.76	–	2
$1\bar{4}2$	–	32.58	–	2.75	–	22
$2\bar{3}2$	–	32.87	–	2.72	–	5
$2\bar{6}1$	–	32.98	–	2.72	–	24
042	–	33.25	–	2.69	–	24
132	–	33.32	–	269	–	7
311	–	33.33	–	2.69	–	8
320	–	33.48	–	2.68	–	24
061	–	33.58	–	2.67	–	24
212	–	33.71	–	2.66	–	2
$3\bar{5}1$	–	33.90	–	2.64	–	1
$3\bar{6}0$	–	34.23	–	2.62	–	19
$2\bar{7}0$	–	34.64	–	2.59	–	2
$2\bar{4}2$	–	34.69	–	2.59	–	35
241	–	35.04	–	2.56	–	21

a. The experimental Bragg angles ($2\theta_o$) and Bragg distances (d_0) observed in the X-ray powder diffraction profile of iP(*R*,*S*)3MP of Figure 2.19b and those calculated ($2\theta_c$ and d_c) for the monoclinic unit cell with axes $a = 10.02$ Å, $b = 18.48$ Å, $c = 6.87$ Å, and $\gamma = 109.9°$ are also reported.

Table 2.21. Comparison between observed structure factors $F_o = (I/LP)^{1/2}$, evaluated from the intensities I observed in the Xray fiber diffraction pattern of iP(*R*,*S*)3MP of Figure 2.20, and calculated structure factors, $F_c = (\Sigma|Fi|^2 \cdot Mi)^{1/2}$, for the model of packing of Figures 2.33 of the random copolymer iP(*R*,*S*)3MP in the monoclinic unit cell with axes a = 10.02 Å, b = 18.48 Å, c = 6.87 Å, and γ = 109.9° according to the space group $P2_1$[a].

hkl	$2\theta_o$ (deg)	$2\theta_c$ (deg)	d_o(Å)	d_c(Å)	$F_o = (I_o/LP)^{1/2}$	$F_c=(\Sigma\|F_i\|^2M_i)^{1/2}$ Model of Figure 2.33
100	9.39	9.39	9.43	9.42	84	63
020	10.18	10.18	8.69	8.69	106	80
$1\bar{2}0$	11.75	11.26	7.53	7.86	28	23
110	12.80	12.11	6.91	7.30	25	5
$1\bar{3}0$ 030 120	16.78	14.98 15.29 16.06	5.28	5.91 5.79 5.52	32	3 9 8 } 12
$2\bar{1}0$ $2\bar{2}0$	18.14	17.75 18.11	4.89	4.99 4.90	24	12 63 } 64
200 $1\bar{4}0$	18.86	18.84 19.37	4.7	4.71 4.58	47	42 35 } 55
$2\bar{3}0$ 040 130 210 $2\bar{4}0$	20.47	19.84 20.44 20.55 21.15 22.63	4.34	4.48 4.34 4.32 4.20 3.93	35	6 30 5 8 29 } 43
$1\bar{5}0$ 220 140	25.29	24.09 24.37 25.33	3.52	3.69 3.65 3.52	24	7 37 20 } 43
050 $2\bar{5}0$ $3\bar{2}0$ $3\bar{1}0$ $3\bar{3}0$	26.28	25.63 26.17 26.70 27.08 27.31	3.39	3.47 3.40 3.34 3.29 3.26	10	13 2 19 9 5 } 25
230	–	28.19	–	3.16	–	6
300	–	18.42	–	3.14	–	42

$1\bar{6}0$	–	29.01	–	3.08	–	46
$2\bar{6}0$	–	30.23	–	2.96	–	1
150	–	30.29	–	2.95	–	10
310	–	30.60	–	2.92	–	6
060	–	30.88	–	2.90	–	10
$3\bar{5}0$	–	31.22	–	2.86	–	8
240	–	32.44	–	2.76	–	2
320	–	33.48	–	2.68	–	17
$3\bar{6}0$	–	34.23	–	2.62	–	14
$2\bar{7}0$	–	34.64	–	2.59	–	1
011	–	13.86	–	6.39	–	10
$1\,\bar{1}\,1$ 101	15.55	15.75 15.96	5.7	5.62 5.55	48	3 52 } 52
021	16.55	16.45	5.34	5.39	74	54
$1\bar{2}1$ 111	18.30	17.14 17.72	4.85	5.17 5.00	55	55 2 } 55
$1\bar{3}1$ 031 121	21.15	19.81 20.05 20.64	4.20	4.48 4.43 4.30	37	2 8 56 } 57
$2\bar{2}1$ 201 $1\bar{4}1$ $2\bar{3}1$ 041 131 211 $2\bar{4}1$	22.00	22.29 22.89 23.33 23.73 24.24 24.33 24.84 26.13	4.03	3.99 3.88 3.81 3.75 3.67 3.66 3.58 3.41	53	6 28 15 4 24 1 3 4 } 41
$1\bar{5}1$	–	27.41	–	3.25	–	1
221	–	27.66	–	3.22	–	11
141	–	28.52	–	3.13	–	26
051	–	28.79	–	3.10	–	5
$2\bar{5}1$	–	29.28	–	3.05	–	2
$3\bar{2}1$	–	29.75	–	3.00	–	9
$3\,\bar{1}\,1$	–	30.09	–	2.97	–	3
231	–	31.11	–	2.87	–	6

301	–	31.32	–	2.86	–	20
$3\bar{4}1$	–	31.72	–	2.82	–	20
$1\bar{6}1$	–	31.86	–	2.81	–	24
$2\bar{6}1$	–	32.98	–	2.72	–	12
311	–	33.33	–	2.69	–	4
061	–	33.58	–	2.67	–	12
241	–	35.04	–	2.56	–	11
002	–	25.94	–	3.43	–	3
012	–	26.45	–	3.37	–	2
$1\bar{1}2$	–	26.52	–	3.24	–	3
102	–	27.64	–	3.23	–	29
022	–	27.93	–	3.19	–	50
$1\bar{2}2$	–	28.36	–	3.15	–	22
112	–	28.72	–	3.11	–	2
$1\bar{3}2$	–	30.09	–	2.97	–	3
032	–	30.25	–	2.95	–	3
122	–	30.66	–	2.92	–	2
$2\bar{1}2$	–	31.61	–	2.83	–	5
$2\bar{2}2$	–	31.82	–	2.81	–	13
202	–	32.25	–	2.78	–	12
$1\bar{4}2$	–	32.58	–	2.75	–	11
$2\bar{3}2$	–	32.87	–	2.72	–	3
042	–	33.25	–	2.69	–	12
132	–	33.32	–	2.69	–	3
212	–	33.71	–	2.66	–	1
$2\bar{4}2$	–	34.69	–	2.59	–	18

a. The experimental Bragg angles ($2\theta_o$) and Bragg distances (d_0) observed in the X-ray fiber diffraction patern of iP(*R*,*S*)3MP of Figure 2.20 and those calculated ($2\theta_c$ and d_c) for the monoclinic unit cell with axes a = 10.02 Å, b = 18.48 Å, c = 6.87 Å, and γ = 109.9° are also reported.

2.5 Conclusion

The crystals structures of isotactic 1,2-poly((*E*)-3-methyl-1,3-pentadiene) (iP3MPD12) and isotactic poly((*R*,*S*)-3-methyl-1-pentene) (iP(*R*,*S*)3MP) have been determined by analysis of the X-ray powder and fiber diffraction patterns and conformational and packing energy calculations.

The iP3MPD12 is a stereoregular 1,2 polydiene obtained polymerizing 3-methyl-1,3-pentadiene with system $CoCl_2(PnPrPh_2)_2$/MAO. The successive hydrogenation produces the iP(*R*,*S*)3MP random copolymer.

Chains of iP3MPD12 are complex helices and by application of the Homemade and Mitsui methods was found the 7/2 helical conformation that is the first nontrivial commensurable helical approximation, with the lowest *M* and *N* integer number. This conformation with 3.5 monomeric units per pitch, fits well with the conformation of the chains of isotactic polymers of poly(4-methyl-1-pentene), poly(1-hexene), poly((S)-4-methyl-1-hexene) poly((R),(S)-4-methyl-1-hexene).

Chains of the isotactic 1,2 polydiene are packed in an orthorhombic unit cell with axes a = 17.4 Å b = 16.5 Å and c = 15.3 Å according to the space group $P2_1ab$. In the orthorhombic unit cell each right-handed helix is surrounded by four left-handed helices and vice versa. In particular, in the space group $P2_1ab$, the neighboring enantiomorphous chains of iP3MPD12 are isoclined (all up) along the *a* axis (because they related by the glide plane *a* normal to the *b* axis) and anticlined (up and down) along the *b* axis (related by the glide plane *b* normal to the *c* axis).

Generally chain with 4/1 helical conformation or complex helices with ratio r/R in the range 0.3-0.8 are packed in tetragonal lattice. Therefore, the 7/2 helices of iP3MPD12 packed in an orthorhombic unit cell, are an exception to this principle. Other examples of low symmetry packing for chains in 4/1 or complex helical conformation are the structures of form III of

isotactic poly(1-butene), isotactic poly(3-methyl-1-butene) and syndiotactic poly(1-butene).

The hydrogenation reaction of iP3MPD12 has allowed the preparation of a purely statistical copolymer of the two enantiomeric monomers, with compensation of chirality, the iP(*R*,*S*)3MP.

Chains of the hydrogenated polymer in 4/1 helical conformation are packed in a monoclinic unit cell with parameters a = 10.02 Å, b = 18.48 Å, c = 6.87 Å, and $\gamma = 109.9°$ according to the space group $P2_1/b$ or $P2_1$. A high degree of disorder is present in the crystals due to the random enchainment of the enantiomeric *R* and *S* monomeric units, whose chirality influences the handedness of the helical chains and the conformation assumed by the lateral groups. Disorder in the conformation of the lateral groups is therefore also present. In the crystals chain stretches of sequences of monomeric units in a prevailing *S* configuration tend to assume right-handed 4/1 helical conformations (combination *S*-right), whereas sequences of monomeric units in a prevailing *R* configuration tend to assume left-handed 4/1 helical conformation (combination *R*-left). Left-handed 4/1 helices for sequences of *S* monomers and right-handed helices for sequences of *R* monomers are also possible at a low cost of internal energy. In all cases the side groups are characterized by high degree of rotational disorder, due to the low energy barrier between the different rotational states. Some kind of azimuthal disorder in the relative rotation of the chains around the chain axes, compatible with the $P2_1/b$ or $P2_1$ space group symmetry, may also be present. The crystal structure of the random copolymer iP(*R*,*S*)3MP is different from that of the chiral pure enantiomer iP(*S*)3MP that is characterized by the isochiral packing of chains in 4/1 helical conformation in a tetragonal unit cell, according to the space group $I4_1$. The tetragonal crystal packing for iP(*S*)3MS is in agreement with the simple principle of packing of polymer chains in 4/1 helical conformations.

The crystal structure of iP(R,S)3MP is an example of symmetry breaking since chains in 4/1 helical conformation are not packed in a tetragonal lattice, but in a monoclinic lattice and the local symmetry of the chains is lost in the lattice. The different packing modes in the chiral and achiral isomers are driven by different entropic effects related to different types of disorder. In the structure of the pure chiral enantiomer iP(*S*)3MP, the entropic effect arising from the two possible conformational states assumed by the chiral lateral groups prevails and induces crystallization of isochiral helices. In the case of the achiral random copolymer iP(*R*,*S*)3MP the entropic effect due to the statistical substitution of helices of different chirality and clinicity prevails and induces crystallization of antichiral monoclinic structure.

Bibliography Chapter 2

[1] G. Natta, L. Porri, G. Zanini, A. Palvarini, Chim. Ind. (Milan) **1959**, *41*, 1163 (Chem. Abstr. **1961**, *55*, 20906).

[2] (a) L. Porri, M. C. Gallazzi, *Eur. Polym. J.* **1966**, *2*, 189. (b) G. Ricci, L. Porri, *Polymer* **1997**, *38*, 4499. (c) A. Proto, C. Capacchione, V. Venditto, J. Okuda *Macromolecules* **2003**, *36*, 9249.

[3] G. Natta, P. Corradini, I. W. Bassi *Rend. Fis. Accad. Lincei* **1957**, *23*, 363.

[4] G. Natta, P. Corradini, I. W. Bassi, G. Fagherazzi, *Eur. Polym. J.* **1968**, *4*, 297.

[5] C. De Rosa, F. Auriemma, C. Santillo, R. Di Girolamo, G. Leone, A. Boccia, G. Ricci *Macromolecules* **2015***, 48*, 5251.

[6] C. De Rosa, F. Auriemma, C. Santillo, R. Di Girolamo, G. Leone, G. Ricci *CrystEngComm* **2015**, *17*, 6006.

[7] V. Petraccone, P. Ganis, P. Corradini, G. Montagnoli *Eur. Polym. J.* **1972**, *8*, 99.

[8] P. Pino, F. Ciardelli, G. Montagnoli *J. Polym. Sci.*, Part C **1968**, *16*, 3265.

[9] L. Oliva, P. Longo, A. Zambelli, *Macromolecules* **1996**, *29*, 6383.

[10] C. De Rosa, F. Auriemma, *Crystals and Crystallinity in Polymers*; Wiley: Hoboken, NJ, **2014**.

[11] (a) P. Corradini In *Stereochemistry of Macromolecules*; A. Ketley, Ed.; Marcel Dekker: New York, Part III, **1968**, p 1.; (b) C. De Rosa, In *Materials Chirality*: Topics in Stereochemistry; M. M. Green, R. J. M. Nolte, E. W. Meijer, Eds.; John Wiley and Sons: Hoboken, NJ, **2003**, *24*, 71.

[12] F. Auriemma, C. De Rosa *Macromolecules* **2009**, *42*, 5179

[13] H. Tadokoro, Structure of Crystalline Polymers; John Wiley & Sons: New York, **1979**.

[14] W. Cochran, F. H. C. Crick, V. Vand *Acta Crystallogr*. **1952**, *5*, 581.

[15] (a) Y. Mitsui, *Acta Crystallogr*. **1966**, *20*, 694. (b) Y. Mitsui, *Acta Crystallogr*. **1970**, *A26*, 658.

[16] D.Y. Yoon, P. R. Sundarajan, P. J. Flory, *Macromolecules* **1975**, *8*, 765. D. Y. Yoon, P. R. Sundararajan, P. J. Flory *Macromolecules* **1975**, *8*, 776. P. R. Sundararajan, P. J. Flory *J. Am. Chem. Soc.* **1974**, *96*, 5025.

[17] D. T. Cromer, J. B. Mann *Acta Crystallogr.*, **1968**, *A24*, 321.

[18] Cerius^2 *Modeling Environment*, Molecular Simulations Inc., San Diego, CA, **1999**.

[19] P. Corradini, I. Pasquon *Rend. Fis. Accad. Lincei* **1955**, *19*, 453.

[20] P. Corradini, V. Petraccone, B. Pirozzi *Eur. Polym. J*. **1976**, *12*, 831.

[21] (a) I. W. Bassi, O. Bonsignori, G. P. Lorenzi, P. Pino, P. Corradini, P. A. Temussi *J. Polym. Phys. Sci. Polym. Phys. Ed*. **1971**, *9*, 193. (b) F.C. FranK, A. Keller, A. O'Connor *Philos. Mag*. **1959**, *8*, 200. (c) H. Kusanagi, M. Takase, Y. Chatani, H. Tadokoro, *J. Polym. Sci. Polym. Phys. Ed*. **1978**, *16*, 131.

[22] (a) G. Natta, P. Corradini, I. W. Bassi *Gazz. Chim. Ital*. **1959**, *89*,784. (b) G. Natta, P. Corradini, I. W. Bassi, *Angew. Chem. Int. Ed. Engl.* **1958**, *70*, 598. (c) P. Corradini, P. Ganis, *Nuovo Cimento, Suppl.* **1960**, *15*, 96.

[23] (a) G. Natta, P. Corradini, I. W. Bassi *Makromol. Chem.* **1959**, *33*, 247. (b) C. De Rosa, A. Borriello, P. Corradini, *Macromolecules* **1996**, *29*, 6323.

[24] G. Cojazzi, V. Malta, G. Celotti, R. Zannetti *Makromol. Chem.* **1976**, *177*, 915.

[25] P. Corradini, P. Ganis, V. Petraccone *Eur. Polym. J.* **1970**, *6*, 281.

[26] C. De Rosa and D. Scaldarella *Macromolecules* **1997**, *30,* 4153.

Chapter 3

Crystalline Block Copolymers prepared by Living Organometallic Catalysts

3.1 Introduction

Block copolymers (BCPs) consist of covalently linked chemically distinct macromolecules with linear or not linear architecture that tend to segregate into different microdomains due to their mutual repulsion. This generates the spontaneous formation of nanostructures (spheres, cylinders or lamellae) with size and periodicity that depend on the relative lengths of the blocks (Figure 3.1) [1].

The main techniques for synthesis of BCPs with defined architectures and monodisperse molecular weights are ionic (cationic, anionic, group transfer), radical (atom-transfer radical polymerization (ATRP), reversible addition fragmentation transfer (RAFT)), nitroxide-mediated polymerization (NMP), chain growth polycondensation, metal-catalyzed olefin metathesis, and ring-opening metathesis polymerization (ROMP).

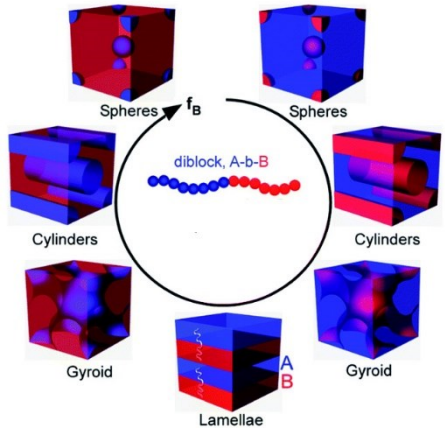

Figure 3.1. The chains of the A-B diblock copolymer, depicted as two-color chain for simplicity, self-organize such that contact between the immiscible blocks is minimized. The list of morphologies formed by di-block copolymers in the bulk is reported. The final morphology (spheres, cylinders, gyroid or lamellae) is determined primarily by the relative lengths of the two polymer blocks (f_B is the volume fraction of block B).

These methods enable consecutive enchainment of monomer units without termination and provide precise molecular weight control and the synthesis of a wide range of polymeric architectures. In particular, anionic and controlled radical polymerization techniques are well established methods for the preparation of BCPs containing blocks made up of polystyrene, poly(1,4-butadiene), polyoxyethylene, polyoxypropylene, poly(acrylates), poly(ε-caprolactone) and poly(d,l-lactide), whereas sequential living cationic polymerization is primarily used to prepare BCPs containing vinyl ether blocks or polyisobutilene. Ring opening metathesis poymerization (ROMP) has been also exploited to build blocks from cyclic olefins, especially to obtain polynorbornenes.

BCPs containing polyethylene blocks have been typically obtained by anionic polymerization of poly(1,4-butadiene) followed by hydrogenation, because ethylene polymerizes too slowly with carbanionic initiators. Hydrogenation of polydiene blocks synthesized by anionic polymerization techniques is also used to obtain blocks consisting of head-to-head polypropylene, poly(ethyl ethylene), poly(ethylene-co-propylene). However, BCPs containing stereoregular polyolefins blocks cannot be synthesized with these methodologies. BCPs containing blocks based on stereoregular polyolefin have been the subject of a small number of studies due to the difficulty of the synthetic methods.

Only in the last decade, the living insertion polymerization of unactivated olefins has emerged as a powerful tool for the synthesis of new polymeric architectures [2]. Today many efficient and selective living catalysts have been obtained for living olefin polymerization. Depending on the ligand framework of the catalyst system and the nature of the coordination metal center, linear or branched polyethylene, atactic, isotactic and syndiotactic poly(α-olefins), poly(cycloolefins), random copolymers of ethylene with higher olefins can now be efficiently synthesized in living manner,

allowing the creation of unlimited new polymer architectures, such as semicrystalline block copolymers by sequential monomer addition and/or end-functionalized macromolecules [3-7]. Examples of catalyst precursors for living polymerization of 1-alkene with high steric control, which may be used for the synthesis of new crystalline BCPs, are shown in Figure 3.2.

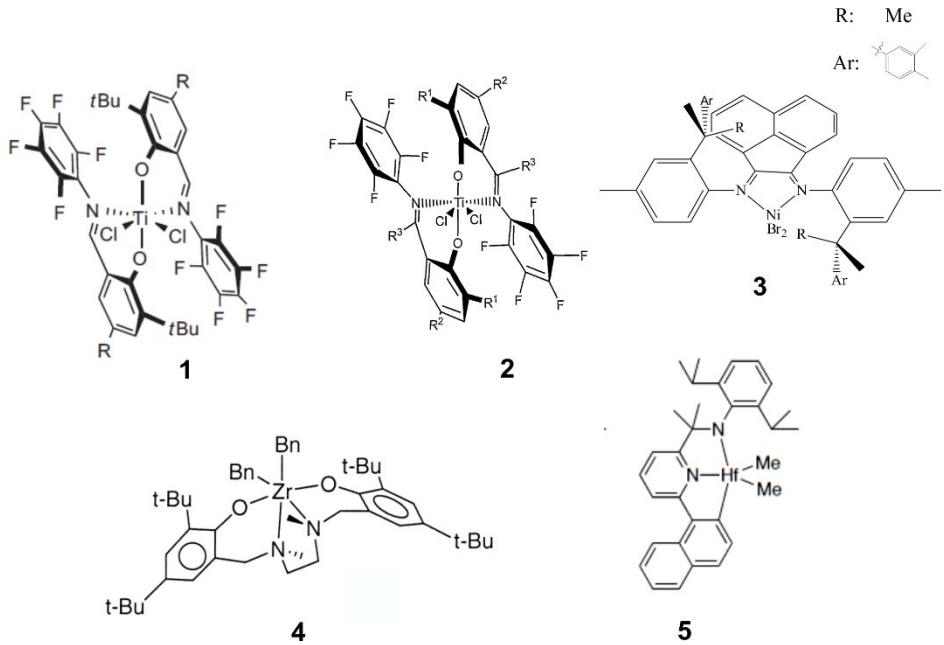

Figure 3.2. Catalyst precursors for the synthesis in a living fashion of BCPs containing tactic poly(1-alkene) blocks.

The bis(phenoxyimine) titanium complex 1 of Figure 3.2 activated with methylaluminoxane (MAO) produces BCPs containing highly stereoregular syndiotactic polypropylene (sPP) and/or polyethylene (PE) blocks alternated with rubbery blocks of ethylene-propylene random copolymers, or glassy blocks of poly(norbornene) and poly(cyclopentene) [3]. Phenoxyketimine Titanium Complexe, complex 2 of Figure 3.2 activated with MAO produces BCPs with stereoregular iPP blocks [4]. The chiral, C_2-symmetric nickel diimine complex 3 of Figure 3.2 activated with MAO produces BCPs containing iPP blocks (at low temperatures) and

regioirregular polypropylene (PP) blocks at higher temperatures [5]. The ammine-phenolate zirconium complex 4 of Figure 3.2 (Bn standing for the benzyl group) activated with $B(C_6F_5)_3$ furnishes BCPs containing highly isotactic poly(1-hexene) or poly(1-octene), iPP and PE blocks [6]. C_s-symmetric pyridylamidohafnium dimethyl precatalyst complex 5 of Figure 3.2 when activated with $B(C_6F_5)_3$ furnishes iPP, PE and isotactic poly(4-methyl-1-pentene) (iP4MP) blocks [7].

The crystallization behavior of BCPs has been extensively studied to date, so that our understanding of these complex materials has largely expanded over the past decade. [8] These studies have indicated that in semicrystalline BCPs, morphology is determined by at least two mechanisms, microphase separation in the melt and crystallization. The interplay between these two processes results in morphological richness and kinetic complexity. Extensive investigations have been carried out on semicrystalline di-block copolymers with one crystallizable block linked to an amorphous block. In these crystalline/amorphous BCPs the final morphology is governed by the composition of the BCP, the crystallization temperature T_c, the glass transition temperature T_g and the order-disorder transition temperature T_{ODT}. Depending on these factors, different microdomain structures are obtained if the crystallization occurs from a homogeneous melt or from an already microphase separated heterogeneous melt. In the latter case microphase separation precedes crystallization and provides a microstructure within which crystallization must take place, resulting in a crystallization confined within preformed microdomains or breaking out of the microphase separated structure.[9-11]

The crystallization behavior of BCPs with more than one crystalline block present a more complicated behavior since the crystallization of one block may affect the crystallization of the other block and the final morphology.

[12] In particular the morphology of the block that crystallize first, can or cannot be modified subsequently by the crystallization of the other block.

The studies performed so far on semicrystalline BCPs have mainly concerned with the crystallization behavior of block copolymers including poly(ethylene oxide), [13-16] poly(ε-caprolactone), [13,15] polyethylene [16-18] and poly(L-lactide) [14,17] blocks. The crystallization behavior of crystalline and double crystalline BCPs containing stereoregular polyolefin blocks, instead, has been less studied to date, due to the intrinsic limitations of the living polymerization methods. Recently a study of the structure and morphology of the polyethylene-*block*-syndiotactic polypropylene BCP, containing two crystallizable blocks, synthesized with a stereospecific living organometallic catalyst, was reported.[19]

Crystalline block copolymers have been also studied for their possible application as thermoplastic elastomers (TPEs).[20] The possibility to synthesize by living polymerization crystalline BCPs, based on stereoregular polyolefins with controlled architectures, allow to expand the family of TPEs and tune the elastomeric properties that derive from a combination of "hard" crystalline segments with high melting points (T_m) or high glass-transition temperatures (T_g) and "soft" segments with low T_g.

In this Chapter, a comprehensive study of the structure, the morphology and mechanical properties of novel crystalline-crystalline BCPs is reported. These materials are formed by polyethylene (PE) block linked to isotactic polypropylene (iPP).

Despite the advances in synthetic strategies, very few semi-crystalline polymers combining iPP and PE have been synthesized. The only example is from Busico and coworkers [6] wherein a modified C_2-symmetric Kol-type ligand supporting a group IV metal center was used to synthesize a PE-*b*-iPP diblock copolymer. The material was shown to be highly stereoregular (m^4 = 99%; T_m = 151 °C) and with well controlled molecular

mass (polydispersity = 1.3), but molecular weights were relatively low (M_n = 22 kg/mol). The authors suggest that lifetimes of the catalyst were limited resulting in controlled "quasi-living" polymerization.

Samples of PE-iPP *di*-block and *tetra*-block copolymers with different block lengths and controlled molecular weights, have been recently synthesized [21] by using an Hf-pyridyl amide catalyst 5 of Figure 3.2 that under proper polymerization conditions shows living behavior, maintaining high levels of stereoselectivity (m^4 = 90%).
A study of the relationships between the molecular and crystalline structure and the physical properties of these novel crystalline BCPs is reported.

3.2 Materials and Methods

3.2.1 Materials.

Samples of isotactic polypropylene-*block*-polyethylene (iPP-*b*-PE) and isotactic polypropylene-*block*-linear low density polyethylene (iPP-*b*-LLDPE) were synthesized by living polymerization with a Hf-based post-metallocene catalyst (Figure 3.3). The molecular characteristics of all the analyzed samples are reported in Table 3.1 and Table 3.2 respectively.
The LLDPE block corresponds to a random ethylene-1-octene copolymer with 1-octene concentration of 1-2 mol %.

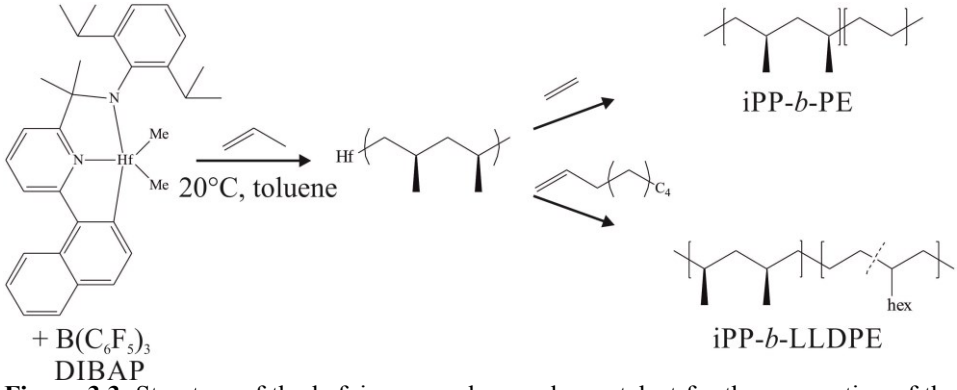

Figure 3.3. Structure of the hafnium complex used as catalyst for the preparation of the iPP-*block*-PE and iPP-*block*-LLDPE samples and sequential polymerization procedure.

Table 3.1. Code of the iPP and PE homopolymers and iPP-*b*-PE copolymers; total molecular mass (M_n); polydispersity (M_w/M_n); weight fraction (w_{iPP}) and volume fraction (f_{iPP}) of the iPP block; molecular masses of iPP ($M_{n(iPP)}$) and PE ($M_{n(PE)}$) blocks.

Code	M_n[a] (kDa)	M_w/M_n[a]	w_{iPP}[b] (wt%)	f_{ipp}[c] (v/v%)	$M_{n\,(iPP)}$[d] (kDa)	$M_{n\,(PE)}$[d] (kDa)
PE-FI-1[e]	122	1.30	0	0	–	122
RDG-1-41	139.8	1.29	100	100	139.8	–
RDG-1-91	140.1	1.23	74	74	103.4	36.7
RDG-1-127	158.0	1.27	72	68	105.3	52.7
RDG-1-138	144.7	1.30	69	65	94.6	50.1
RDG-1-166	180.6	1.26	64	52	94.6	86
RDG-1-88	163.5	1.19	52	40	64.6	98.9

a. From GPC analysis; b. determined from ^{13}C NMR spectrum; c. calculated from the molecular masses $M_{n(iPP)}$ and $M_{n(PE)}$, the densities of iPP (0.850 g/cm^3) and PE (0.853 g/cm^3) such that $f_{iPP} = (M_{n(iPP)}/0.850)/(M_{n(iPP)}/0.850 + M_{n(PE)}/0.853)$. d. estimated from total M_n and wt % of iPP or PE such that $M_{n(iPP)} = M_n w_{iPP}$. The sample PE-FI-1 has been prepared with the catalyst 1 of Figure 3.2.

Table 3.2. Code of the iPP-*b*-LLDPE copolymers; total molecular mass (M_n); polydispersity (M_w/M_n); weight fraction (w_{iPP}) and volume fraction (f_{iPP}) of the iPP block; molecular masses of iPP ($M_{n(iPP)}$) and LLDPE ($M_{n(LLDPE)}$) blocks and concentration of 1-octene [1-octene].

Code	M_n[a] (kDa)	M_w/M_n[a]	w_{iPP}[a] (wt%)	f_{ipp}[b] (v/v%)	$M_{n(iPP)}$[c] (kDa)	$M_{n(LLDPE)}$[c] (kDa)	[1-octene][d] (mol%)
JME-V-54	155	1.3	77	77	120	35	1.5
JME-IV-133	158	1.3	48	48	76	82	0.9
JME-IV-148	152	1.3	45	45	68	84	1.5
JME-IV-149	137	1.3	47	47	64	72	1.9

a. From GPC analysis; b. calculated from the molecular masses $M_{n(iPP)}$ and $M_{n(LLDPE)}$, the densities of iPP (0.850 g/cm^3) and LLDPE (0.853 g/cm^3) such that $f_{iPP} = (M_{n(iPP)}/0.850)/(M_{n(iPP)}/0.850 + M_{n(LLDPE)}/0.853)$; c. estimated from total M_n and wt % of iPP or PE such that $M_{n(iPP)} = M_n w_{iPP}$; d. determined from ^{13}C NMR spectrum.

3.2.2 Polymer characterization.

Calorimetric measurements were performed with a differential scanning calorimeter (DSC-822) by Mettler Toledo in a flowing N_2 atmosphere at a scanning rate of 10 °C/min and 2 °C/min.

Unoriented films used for the structural and mechanical analysis have been obtained by compression molding. The as-prepared samples have been heated at ≈ 180 °C between perfectly flat Teflon plates under a press at very low pressure (< 1 bar), kept at ≈ 180 °C for 5 min, and slowly cooled to room temperature (≈ 15 °C/min).

Oriented fibers have been obtained by stretching compression molded films up to a given strain ε, defined as $\varepsilon = [(L - L_0)/L_0] \times 100$, where L_0 and L the initial and final lengths of the sample, respectively.

X-ray diffraction patterns have been obtained with Ni-filtered CuKα radiation. The powder profiles were obtained with an automatic Philips diffractometer, whereas the fiber diffraction patterns were recorded on a

BAS-MS imaging plate (FUJIFILM) using a cylindrical camera and processed with a digital imaging reader Perkin Elmer Cyclone Plus (storage phosphor system).

Mechanical tests have been performed at room temperature on compression-molded films with a universal mechanical tester Zwicky by Zwick Roell, following the standard test method for tensile properties of thin plastic sheeting ASTM D882-83. Rectangular specimens 10 mm long, 5 mm wide and 0.3 mm thick have been stretched up to the break or up to a given deformation $\varepsilon = [(L_f - L_0)/L_0] \times 100$, where L_0 and L_f are the initial and final lengths of the specimen, respectively. Two benchmarks have been placed on the test specimens and used to measure elongation.

Values of tension and elastic recovery set have been measured after breaking. Ten minutes after breaking, the two pieces of the sample have been fit carefully together so that they are in contact over the full area of the break and the final total length L_r of the specimen has been obtained by measuring the distance between the two benchmarks. The tension set after breaking has been calculated as $t_b = [(L_r - L_0)/L_0] \times 100$, whereas the elastic recovery has been calculated as follows: $r_b = [(L_f - L_r)/L_r] \times 100$ and the percentage of the total strain $(L_f - L_0)$ that is recovered after breaking is obtained as $R_b = 100 \times (L_f - L_r)/(L_f - L_0) = 100 \times (\varepsilon_b - t_b)/\varepsilon_b$.

In the mechanical tests, the ratio between the drawing rate and the initial length was fixed equal to 0.1 mm/(mm × min) for the measurement of Young's modulus and 10 mm/(mm × min) for the measurement of stress−strain curves and the determination of the other mechanical properties (stress and strain at break and tension set). The reported values of the mechanical properties are averaged over at least five independent experiments.

Thin films (20-50 μm thick) of the iPP-*b*-PE samples have been prepared for polarized optical microscopy (POM) experiments. Small amounts of the

powder samples have been sandwiched between glass coverslips, melted at ≈ 180 °C and then crystallized by slow cooling to room temperature at 10 °C/min, 5 °C/min or 2.5 °C/min. Optical microphotographs of the samples have been recorded at room temperature in polarized light using a Zeiss Axioskop 40 microscope provided with a Mettler FP82 hot stage.

Time resolved small- and wide-angle X-ray scattering (SAXS and WAXS) experiments have been performed on station BM26B (DUBBLE) at the European synchrotron radiation facility (ESRF), Grenoble, France. A modified DSC Linkam hot stage has been employed that allows the transmission of X-rays through Kapton windows. The samples have been heated from 25 to 180 °C at 30 °C/min, kept at 180 °C for 1 min, then cooled from 180 to 25 °C at 10 °C/min, heated again from 25 to 180 °C at 10 °C/min and finally cooled to 25 °C at 30 °C/min. An acquisition time of 6 s, a delay time of 6 or 0 s and a wavelength of 1.0402 Å have been used to acquire the data. The sample holder scattering has been subtracted from each scan.

3.3 Characterization of isotactic polypropylene-*block*-polyethylene (iPP-*b*-PE) crystalline-crystalline block copolymers.

3.3.1 Crystallization behavior.

The X-ray powder diffraction profiles of as-prepared samples of the iPP and PE homopolymers and of iPP-PE BCPs, with different blocks lengths are reported in Figure 3.4. It is apparent that the iPP homopolymer and the iPP block in the copolymers crystallize in the α–form as indicated by the presence in the diffraction profiles of Figure 3.4 of the $(130)_{\alpha}$ reflection at $2\theta = 18.6°$. Moreover, the $(110)_{PE}$ and $(200)_{PE}$ reflections at $2\theta = 21.4°$ and 23.9°, respectively, of the orthorhombic form of PE, are also observed in the diffraction profiles of the block copolymers (Figure 3.4) indicating that both iPP and PE blocks are crystalline. The relative amount of PE crystallinity increase with increasing the PE weight fraction in the BCP.

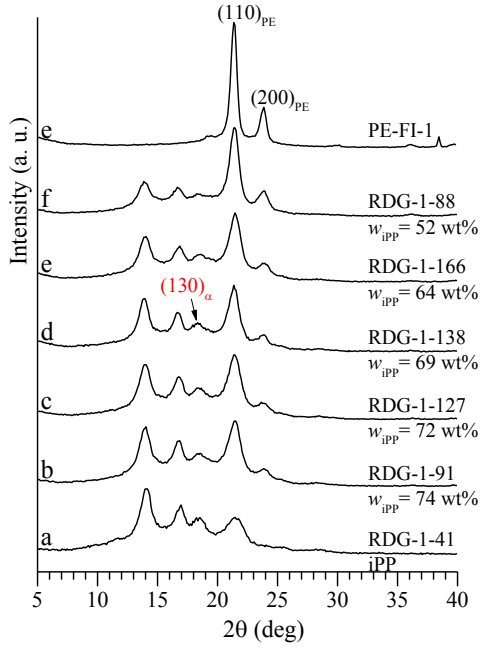

Figure 3.4 X-ray powder diffraction profiles of as-prepared samples of iPP and PE homopolymers and iPP-*b*-PE copolymers. The $(130)_{\alpha}$ reflection of α form of iPP at $2\theta = 18.6°$ and the $(110)_{PE}$ and $(200)_{PE}$ reflections at $2\theta = 21.4°$ and 23.9°, respectively, of the orthorhombic form of PE are indicated. The weight fraction of the iPP block (w_{iPP}) are also reported.

X-ray powder diffraction profiles of samples crystallized from the melt by cooling the melt (≈ 15 °C/min) to room temperature (Figure 3.5) show that the iPP homopolymer, also in this case, crystallizes mainly in α-form. In fact, the $(130)_\alpha$ reflection at 2θ = 18.6° is observed in the X-ray diffraction profile a of Figure 3.5. However, a diffraction peak with lower intensity is also detected at 2θ = 20.0° corresponding to the $(117)_\gamma$ reflection of the γ-form. Therefore, a small portion of crystals in γ-form or in a disordered modification of α and γ forms is also present.

The crystal structures of α and γ forms of iPP are very similar. The limit-ordered structural models proposed for the α and γ forms are shown in Figure 3.6. Both the α and γ forms are characterized by chains in the 3/1 helical conformation (chain periodicity c = 6.5 Å), organized to form bilayers. However, α form is characterized by a regular stacking of bilayers along the b_α-axis direction with chain axes all parallel [22-24] (Figure 3.6A), whereas the γ form is characterized by a regular packing along the c_γ-axis direction of bilayers of chains with axes oriented alternatively along two nearly perpendicular directions [23-25] (Figure 3.6 C). The angle between the axes of chains belonging to consecutive bilayers is 98.6° (or equivalently 81°), close to the angle β_α of the monoclinic unit cell of the α form. As a consequence of the structural similarity, the X-ray diffraction patterns of α and γ forms of iPP are very similar. The most intense diffraction peaks of the α form occur at 2θ = 14.2, 17.1, 18.6, 21.1, and 21.8° (d = 6.25, 5.18, 4.76, 4.18, and 4.06 Å, respectively) and correspond to $(110)_\alpha$, $(040)_\alpha$, $(130)_\alpha$, $(111)_\alpha$, and $(\bar{1}31)_\alpha$ + $(041)_\alpha$ reflections, respectively.[22-24] The most characteristic diffraction peaks of the γ form occur at 2θ = 13.8, 16.7, 20.1, 21.2, and 21.9°, (d = 6.40, 5.30, 4.42, 4.19, and 4.06 Å, respectively) and correspond to $(111)_\gamma$, $(008)_\gamma$, $(117)_\gamma$, $(202)_\gamma$, and $(026)_\gamma$ reflections, respectively.[23-25] The only remarkable difference in the diffraction patterns of α and γ forms is in the position of the third

strong peak which occurs at 2θ = 18.6° ($(130)_\alpha$ reflection) for the α form, and at 2θ = 20.1° ($(117)_\gamma$ reflection) for the γ form. An example of a disordered modification is shown in Figure 3.6B. In this structure, consecutive bilayers of chains may face each other with the chain axes either parallel (like in the α-form, Figure 3.6A) or nearly perpendicular (like in the γ-form, Figure 3.6C). The X-ray diffraction profile of samples of iPP crystallized in disordered modification intermediate between α and γ forms, show a diffuse scattering concentrates in very narrow regions of the diffraction patterns at 2θ ≈ 14°, around the $(110)_\alpha$ and $(111)_\gamma$ reflections of the α and γ forms, respectively, and in the 2θ range 18-20°, around the $(130)_\alpha$, and $(117)_\gamma$ reflections of the α and γ forms, respectively.[23,26,27]. The intensities and the positions of $(040)_\alpha$ and $(008)_\gamma$ reflection at 2θ = 17° and of $(111)_\alpha$ and $(202)_\gamma$ reflection at 2θ = 21° are not affected by the presence of α/γ disorder. [23,26,27] Therefore, the inclusion of a high degree of α/γ structural disorder in the crystalline domains implies that the $(130)_\alpha$ and $(117)_\gamma$ reflections are almost absent and only a diffuse scattering is observed in the corresponding 2θ range.

The X-ray diffraction profiles of the melt–crystallized compression molded films of iPP-*b*-PE copolymers (Figure 3.5) show a diffuse scattering in the region of the diffraction profiles at 2θ ≈ 14°, around the $(110)_\alpha$ and $(111)_\gamma$ reflections of the α and γ forms, respectively, and the presence with low intensities, of the $(130)_\alpha$ and $(117)_\gamma$ reflections at 2θ = 18.6 and 20.0° of the the α and γ forms, respectively.

In the case of a perfectly α/γ structural disorder only a broad halo in the 2θ range 18-20° should be observed. Hence, the presence of the $(130)_\alpha$ reflection of the α-form and of the $(117)_\gamma$ reflection of the γ-form, even though with low intensity, indicate that there are crystalline lamellae formed, mainly, by consecutive bilayers of chains face each other with the chain axes parallel (as in the α-form, Figure 3.6A), and, on the contrary,

crystalline lamellae formed, mainly, by consecutive bilayers of chains face each other with axes oriented alternatively along two nearly perpendicular directions (as in the γ-form, Figure 3.6C). Crystals of pure α or γ form can be also present.

The intensities of the $(110)_{PE}$ and $(200)_{PE}$ reflections at 2θ = 21.4 and 23.9° of the orthorhombic form of the PE block, increase with increasing of the length of the PE block and also a slightly increase of the crystallinity degree is observed in samples with higher weight fraction of the PE block (Figure 3.5 and Table 3.3).

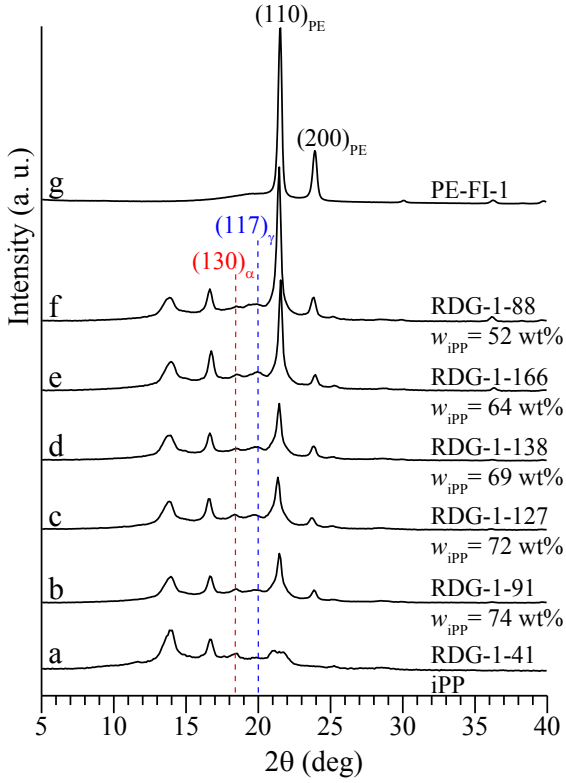

Figure 3.5 X-ray powder diffraction profiles of compression molded samples of iPP and PE homopolymers and iPP-*b*-PE copolymers. The $(130)_{\alpha}$ and the $(117)_{\gamma}$ reflections at 2θ = 18.6° and 20.0° of α and γ form respectively of iPP and the $(110)_{PE}$ and $(200)_{PE}$ reflections at 2θ = 21.4° and 23.9°, respectively, of the orthorhombic form of PE are indicated. The weight fraction of iPP block (w_{iPP}) are also reported.

Table 3.3. Code of iPP and PE homopolymers and iPP-*b*-PE copolymers, weight fractions of the iPP (w_{iPP}) and PE (w_{PE}) blocks, crystallinity degree (x_c) of compression-molded samples of iPP and PE homopolymers and iPP-*b*-PE copolymers of Figure 3.5.

Code	w_{iPP} (wt%)	w_{PE} (wt%)	x_c (%)
RDG-1-41	100	0	49
RDG-1-91	74	26	50
RDG-1-127	72	28	51
RDG-1-138	69	31	52
RDG-1-166	64	36	54
RDG-1-88	52	48	62
PE-FI-1	0	100	65

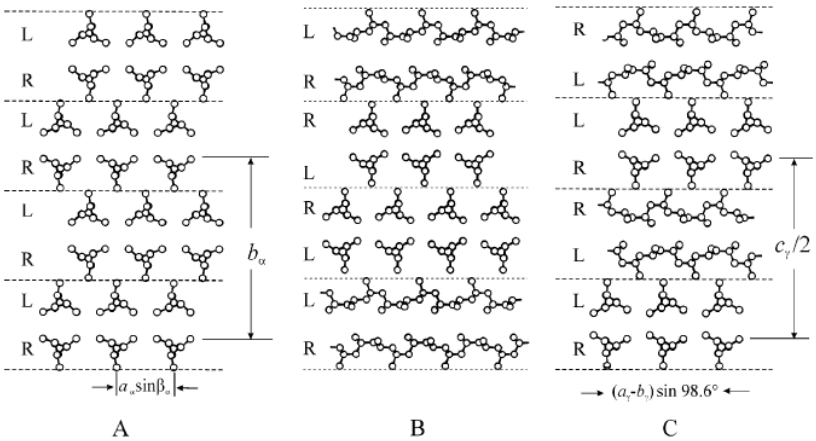

Figure 3.6. Limit ordered models of packing proposed for α (A) and γ (C) forms of iPP and model of the α/*γ* disordered modifications intermediate between α and *γ* forms (B). The dashed horizontal lines delimit bilayers of chains. Subscripts α and *γ* identify unit cell parameters referred to the monoclinic [22-24] and orthorhombic [23-25] unit cells of the α and γ forms, respectively. In the disordered model (B), consecutive bilayers of chains are stacked along b_α (c_γ) with the chain axes either parallel, as in the α form, or nearly perpendicular, as in the *γ* form. [23,26,27] Symbols R and L indicate rows of all right- and left-handed helical chains, respectively.

The DSC curves of iPP and PE homopolymers and iPP-PE BCPs, recorded during first heating, successive cooling from the melt, and second heating of the melt-crystallized samples, all recorded at 10 °C/min, are reported in Figure 3.7A-C.

The values of melting and crystallization temperatures and enthalpies are reported in Table 3.4.

The DSC heating curves of the sample RDG-1-41 (iPP homopolymer) present a melting peak at ≈ 135°C consistent with a concentration of the isotactic pentad *mmmm* of 91% (determined by solution ^{13}C NMR).

A similar stereoregularity of iPP when linked to PE block is expected, since iPP-*b*-PE samples have been synthesized with the same catalyst in the same conditions.

The shoulders in both first and second heating curves (curves a of Figure 3.7A and C) indicate the presence of crystals with different lamellar thickness and/or recrystallization phenomena.

The DSC thermograms of iPP-*b*-PE samples show only one broad peak, in the heating and cooling curves, due to the overlapping of PE and iPP melting and crystallization. In fact, the melting temperature of the iPP homopolymer is very similar to the melting temperature of the PE homopolymer (curves g of Figure 3.7A and C).

All samples, regardless of the blocks length, show a melting temperature at ≈ 130°C, slightly lower than that of iPP and PE homopolymers. Moreover, the DSC heating curves of Figure 3.7C (second heating) of all BCPs, with the exception of sample RDG-1-88 (w_{iPP} = 52%), present shoulders at a temperature higher (≈ 136°C) than that of main melting peak, indicating that these endothermic phenomena are probably due to the melting of crystals of the iPP block. This is in agreement with the absence of shoulders in the DSC heating curves of the sample RDG-1-88, presenting the lowest iPP content (52%).

It is worth noting that the main melting peak appears at temperature lower than that of the iPP and PE homopolymers (≈130 °C vs. 135 °C), probably due to confinement phenomena.

The crystallization temperatures (T_c) of the crystalline block copolymers are higher than that of iPP homopolymer (102 °C) and increase with increasing of the PE block length. These data suggest that PE crystallizes first and the crystallization of the BCPs is driven by the nucleation effect of PE to the crystallization of iPP block (Figure 3.7B and Table 3.4). In particular, the cooling curve of the sample RDG-1-88 (curve f of Figure 3.7B) with the highest weight fraction of PE block shows an exothermic peak at 113 °C with a shoulder at 105 °C. The peak at 113 °C corresponds, mainly, to the crystallization of PE, whereas the shoulder at 105 °C is probably due to the crystallization of fractions of iPP crystals. For the BCPs samples presenting PE weight fraction lower than 48% (Table 3.4), the crystallization of the two blocks seems to take place simultaneously.

The DSC analysis of as-prepared samples of iPP and PE homopolymers and iPP-*b*-PE samples was carried out also at scanning rate of 2 °C/min in an attempt to get additional details concerning melting and crystallization behavior.

The DSC curves recorded during first heating, successive cooling from the melt and second heating of the melt-crystallized samples recorded at scanning rate of 2 °C/min, are reported in Figure 3.8. The value of the melting temperatures of as-prepared samples and of the melt-crystallized samples (T_m (I) and T_m(II) respectively), of the crystallization temperatures (T_c) and corresponding values of the enthalpies are reported in Table 3.4.

It is apparent that also in this case, the iPP and PE blocks melt and crystallize, basically, at nearly the same temperature. However, all heating curves of Figure 3.8A e C recorded at 2 °C/min present an endothermic peak at ≈ 130 °C and a small peak at higher temperatures. These

endothermic phenomena are better resolved than those observed in the heating curves recorded at 10 °C/min (Figure 3.7A and C). Furthermore, when the scanning rate is slower, also the sample RDG-1-88 (curves f of Figure 3.8A and C) with the highest weight fraction of PE, shows the same melting behaviour, presenting a small shoulder at high temperature. As in the case of the DSC heating curves recorded at 10 °C/min, the peak at higher temperature is probably due to the melting of iPP crystals.

Cooling scans confirm that the presence of PE block linked to iPP produce an increase of the crystallization temperatures, probably due to a nucleation effect. The cooling curves of the samples RDG-1-91 (curve b of Figure 3.8B), RDG-1-127(curve c of Figure 3.8B), RDG-1-138 (curve d of Figure 3.8B) show exothermic peaks with shoulders at higher temperature. In these samples, it is reasonable to consider that a small fraction of PE crystals starts to crystallize just before the iPP crystallization and a small exothermic phenomenon at ≈ 110 °C in the cooling curves is observed.

For the sample RDG-1-166 with w_{PE} = 36%, higher than that of samples RDG-1-91, RDG-1-127, and RDG-1-138 a single broad peak is observed (curve e of Figure 3.8B).

The cooling curve of the sample RDG-1-88 with the highest PE content (48 wt%) (curve f of Figure 3.8B) show an exothermic peak at 116 °C and a small peak at lower temperature,109 °C. In this case, the PE block start to crystallize first at 116 °C and then, the crystallization of iPP block occurs at lower temperature.

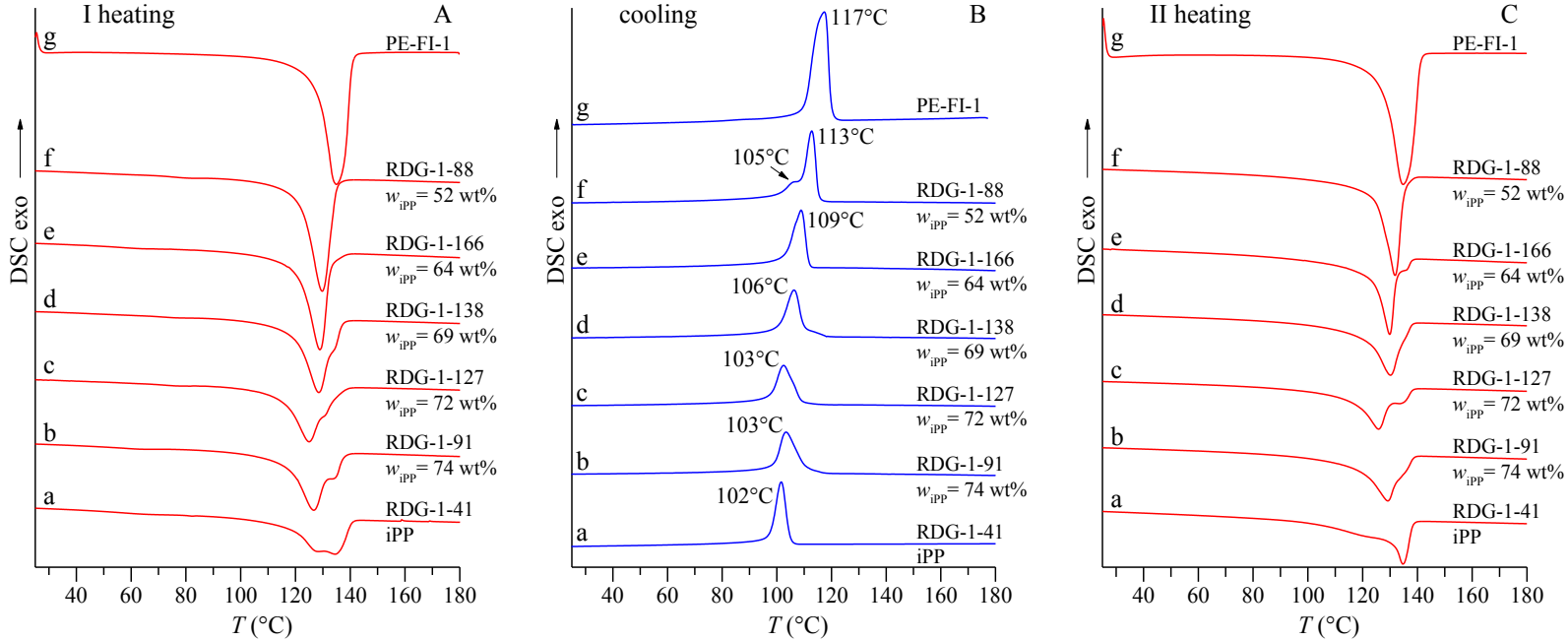

Figure 3.7. DSC curves recorded at 10°C/min during first heating (A), successive cooling (B) and second heating scans (C) of as-prepared samples of iPP and PE homopolymers and iPP-*b*-PE copolymers. The weight fraction of iPP block (w_{iPP}) and the values of the crystallization temperatures recorded during cooling from the melt are indicated.

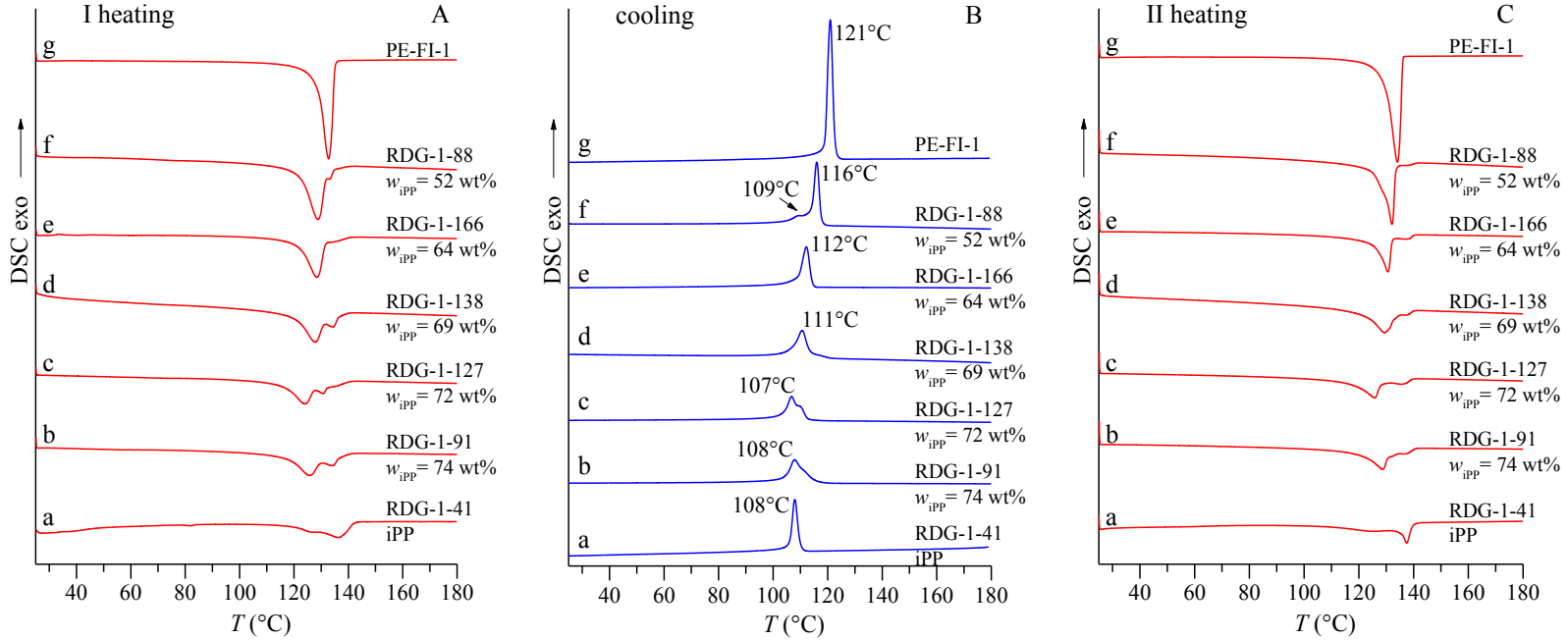

Figure 3.8. DSC curves recorded at 2°C/min during first heating (A), successive cooling (B) and second heating scans (C) of as-prepared samples of iPP and PE homopolymers and iPP-*b*-PE copolymers. The weight fraction of iPP block (w_{iPP}) and the values of the crystallization temperatures recorded during cooling from the melt are indicated.

Table 3.4. Code of the iPP and PE homopolymers and iPP-*b*-PE copolymers, weight fractions of the iPP (w_{iPP}) and PE (w_{PE}) blocks, melting temperature (T_m(I)) and melting enthalpy (ΔH_m(I)) recorded during the first heating, crystallization temperature (T_c), melting temperature (T_m(II)) and melting enthalpy (ΔH_m(II)) recorded during the second heating, crystallization enthalpy (ΔH_c) of the samples of iPP and PE hompolymers and of the iPP-*b*-PE block copolymers.

Code	w_{iPP} (wt%)	w_{PE} (wt%)	T_m(I) (°C)	T_c (°C)	T_m(II) (°C)	ΔH_m(I) J/g	ΔH_c J/g	ΔH_m(II) J/g
scan rate 10°C/min								
RDG-1-41	100	0	128,135	102	120,135	80.3	77.3	76.6
RDG-1-91	74	26	127,134	103	129,136	98.7	83.0	85.4
RDG-1-127	72	28	125,131	103	126,136	91.3	77.7	77.9
RDG-1-138	69	31	129,134	106	130,136	105.4	86.5	89.1
RDG-1-166	64	36	129	109	130,136	112.3	89.1	92.1
RDG-1-88	52	48	130	113,105	132	129.7	110.1	113.5
PE-FI-1	0	100	135	117	135	168.7	176.3	173.6
scan rate 2°C/min								
RDG-1-41	100	0	126,136	108	125,137	73.0	77.4	71.8
RDG-1-91	74	26	126,134	111,108	129,137	104.5	87.6	82.8
RDG-1-127	72	28	124,131	110,107	126,136	96.8	79.3	73.9
RDG-1-138	69	31	128,135	117,111	129,138	112.2	87.6	83.2
RDG-1-166	64	36	128,136	112	131,138	108.9	86.0	84.2
RDG-1-88	52	48	129,134	116,109	132,138	140.3	117.4	113.5
PE-FI-1	0	100	133	121	134	168.4	180.6	181.2

3.3.2 Temperature and time resolved WAXS and SAXS.

Simultaneous time and temperature-resolved wide and small angle X-ray scattering (WAXS and SAXS) experiments have been performed with synchrotron radiation at ESRF in Grenoble to further investigate the melting and crystallization behavior of iPP-PE di-block copolymers and to confirm the DSC results previously discussed.

The experiments were performed on iPP-*b*-PE samples with different block lengths (namely RDG-1-91, RDG-1-166 and RDG-1-88). The temperature profile employed was: heating from 25 to 180 °C at 30 °C /min; isotherm at 180 °C for 1 min; cooling to 25 °C at 10 °C/min, heating again to 180 °C at 10 °C/min and finally, cooling from 180 to 25 °C at 30 °C/min.

WAXS and SAXS profiles of the sample RDG-1-91 with the highest iPP weight fraction (74%), at selected temperatures, recorded during the cooling and heating scans at 10 °C/min, are reported in Figures 3.9.

The diffraction profiles recorded during cooling clearly show that, starting from the amorphous halo of the melt at 180°C (profile a of Figure 3.9A), the weak $(110)_{PE}$ reflection of PE at $2\theta = 21.3°$ appears at the beginning of the cooling at 114 °C (profile b of Figure 3.9A) while no reflections of iPP are observed at this temperature. These data indicate that the PE block crystallizes first and crystalline iPP becomes detectable at lower temperature (109 °C), as evidenced by the presence of $(110)_{\alpha}$ and $(040)_{\alpha}$ reflections of iPP in the diffraction profile d of Figure 3.9A. The SAXS profiles of the same sample, acquired during cooling from the melt at 10 °C/min are reported in Figure 3.9A'.

The absence of correlation peaks in the SAXS pattern at 180 °C (curve a of Figure 3.9A'), indicate that no microdomain structure is present in the melt. It is worth noting that the presence of phase-separated melt cannot be excluded since very small electron density difference, negligible for X-ray

scattering, between PE and iPP blocks is expected in the melt state. Rheological measurements to verify the presence of phase separated melt determine the order-disorder transition temperature are in progress.

The SAXS profiles recorded at temperatures lower than 107 °C present two broad peaks q_1^* at 0.20 nm^{-1} and q_2^* at 0.54 nm^{-1}, corresponding to a Bragg distance of 31.4 and 11.6 nm, respectively, that become more defined when the sample reach room temperature (Figure 3.9A'), indicating the formation of a microphase-separated microstructure driven by crystallization. Since the two correlation peaks appear almost simultaneously during cooling from the melt, the attribution of the two periodicities to one of the two crystalline phase (PE or iPP) is not obvious. However, the SAXS profiles of samples PE-FI-1 and RDG-1-41 of the homopolymers PE and iPP, show strong correlation peaks at $q^* \approx 0.21 nm^{-1}$ $q^* \approx 0.53$ nm^{-1} respectively (Figure 3.10 A,B), due to crystalline lamellar stacks. In the case of PE homopolymer, also a second order peak at $2q^* \approx$ 0.42 nm^{-1} is observed (Figure 3.10 A).

These data suggest that the first peak at 0.20 nm^{-1} (Figure 3.9 A') observed in the block copolymer might correspond to the lamellar stacks of PE with an average periodicity L_{SAXS} of ≈ 31 nm, and the peak at 0.54nm^{-1} (q_2^*) with a lamellar periodicity L_{SAXS} of ≈ 12 nm corresponds to the lamellar stacks of iPP since the same periodicities are present in the SAXS profiles of the melt-crystallized samples of the homopolymers PE and iPP (Figure 3.10).

SAXS profiles show that upon cooling, microphase separation driven by crystallization leads to an ordered lamellar morphology at the nanoscale. Crystallization of both blocks seems not influenced by the possible phase-separated melt structure and evolve via breakout-crystallization mechanism according with the morphological characterization discussed in paragraph 3.3.5.

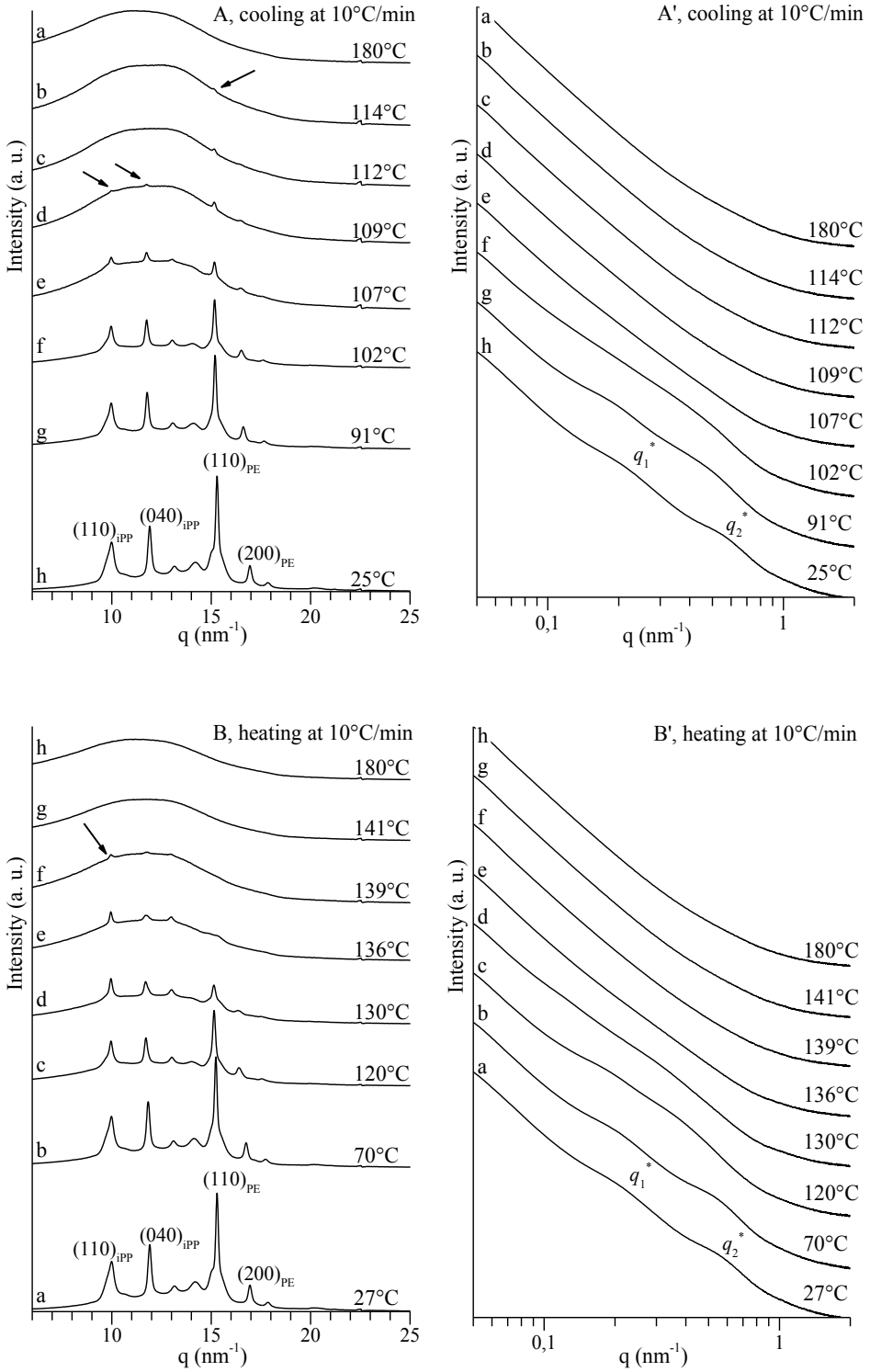

Figure 3.9. WAXS (A, B) and SAXS (A', B') profiles of the sample RDG-1-91 recorded during cooling (A, A') and heating (B, B') scan at 10°C/min at the indicated temperatures.

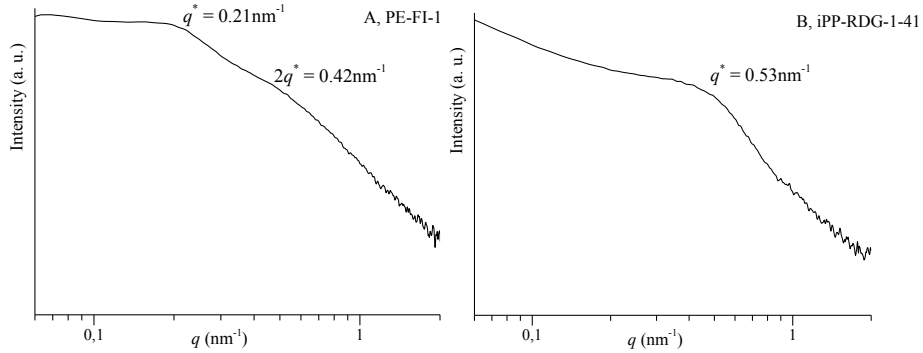

Figure 3.10. SAXS profiles recorded at 25 °C of melt-crystallized samples of PE-FI-1 (A) and iPP-RDG-141 (B) homopolymers.

The WAXS profiles of the sample RDG-1-91 recorded during heating of melt–crystallized sample (Figure 3.9B) show that the PE crystals start melting at a temperature slightly lower than that of the iPP crystals since a strong decrease of the intensity of $(110)_{PE}$ and $(200)_{PE}$ reflections of PE is observed at 130 °C (profile d of Figure 3.9). In fact, the diffraction profile recorded at 136 °C (curve e of Figure 3.9B) shows only traces of PE crystallinity that become not detectable in the diffraction profile recorded at 139 °C (curve f of Figure 3.9B) where only the $(110)_{\alpha}$ reflection of iPP, with low intensity, is present. These results are in agreement with the DSC heating curves (curve b, d of Figure 3.7C) and confirm that the small endothermic phenomenon at high temperatures (curve b of Figure 3.7C) is due to the melt of thicker/more perfect iPP crystals.

As already discussed, the two correlation peaks in the SAXS profile recorded at 27 °C (curve a of Figure 3.9B') correspond to a lamellar periodicity $L_{SAXS} \approx 31$ nm and 12 nm for PE and iPP lamellar stacks, respectively.

A small decrease of the q values, corresponding to an increase in the lamellar periodicity, is observed with increasing the temperature. In the SAXS profile recorded at 120 °C (curve c of Figure 3.9B') the two correlation peaks become very broad and partially overlapped and

disappear at higher temperatures when the samples in completely melted (curves d-h of Figure 3.9B').

Similar experiments have been performed also for the samples RDG-1-166 and RDG-1-88 presenting the weight fraction of the iPP block of 64% and 52%, respectively. The WAXS and SAXS profiles of the sample RDG-1-166, recorded during cooling and heating at 10 °C/min, are reported in Figure 3.11, whereas those of the sample RDG-1-88 are shown in Figure 3.12.

For the sample RDG-1-166 with w_{iPP} = 64 %, the WAXS profiles recorded during cooling from the melt (profile b and c of Figure 3.11A) show that PE crystallized first as in the case of the sample RDG-1-91 with higher iPP content. Moreover, in the corresponding SAXS profiles (b and c of Figure 3.11A') a broad correlation peak appears at $q_1^* \approx 0.24$ nm^{-1}, while no peaks are observed at $q \approx 0.5$ nm^{-1} in agreement with the presence of only PE crystals. This result, obtained for a sample with higher PE content respect to the sample RDG-1-91, confirms that the first correlation peak q_1^* is due to crystalline PE lamellar stacks.

The iPP block starts crystallizing at lower temperature (110 °C) as indicated by the increasing intensity of the $(110)_\alpha$ and $(040)_\alpha$ reflections in profile d of Figure 3.11A.

The SAXS data, collected at temperatures lower than 110 °C (curves d-h of Figure 3.11A'), show an increase of SAXS intensity at $q \approx 0.24$ nm^{-1} with decreasing temperature, whereas the second correlation peak q_2^* becomes detectable only at 106 °C (profile f of Figure 3.11A') when significant iPP crystallinity is developed.

The WAXS profiles recorded during heating at 10 °C/min of the melt-crystallized sample show that both blocks melting simultaneously

as shown by the progressive decrease of intensity of the PE and iPP reflections as in the case of the sample RDG-1-91. A weak peak,

corresponding to the $(110)_{\alpha}$ reflection of iPP in still present at 138 °C according with the shoulder evidenced in the DSC heating trace (curve e of Figure 3.7C) at the same temperature.

Similar results to those discussed for the samples RDG-1-91 and RDG-1-166 have been obtained from WAXS and SAXS data acquired during cooling and successive heating at 10 °C/min of the sample RDG-1-88 presenting the highest PE content (48 wt%) (Figure 3.12).

Also in this case, PE crystallizes first during cooling from the melt (Figure 3.12A). SAXS profiles show that only a correlation peak at $q_1^* \approx 0.22$ nm^{-1} due to crystalline PE lamellar stacks, is present at high temperatures (range 116-110 °C) according with the presence of $(110)_{PE}$ and $(200)_{PE}$ PE reflections and the absence of those of iPP in the WAXS profiles recorded in the same temperature range (profiles c-e of Figure 3.12A,A').

SAXS profiles, recorded at room temperature (profile h of Figure 3.12A' and profile a of Figure 3.12B'), when the sample is fully crystallized, show two well-defined correlation peaks relative to PE and iPP lamellar stacks, with periodicity of 30 and 11 nm respectively.

WAXS experiments performed by heating of the melt-crystalized sample from 25 °C to 180 °C at 10 °C/min, confirm the behaviour discussed for the other iPP-*b*-PE samples (Figure 3.12B).

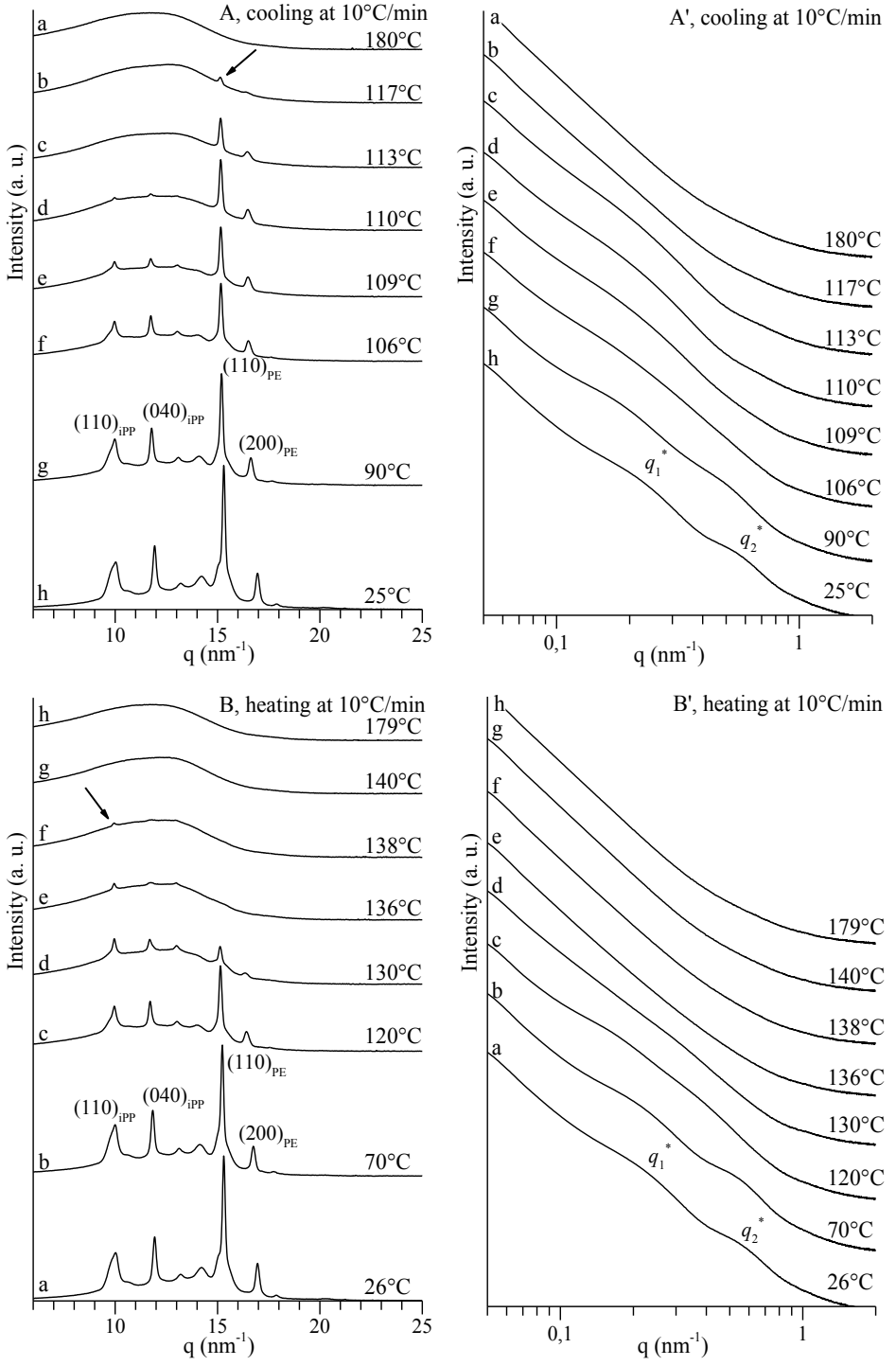

Figure 3.11. WAXS (A, B) and SAXS (A', B') profiles of the sample RDG-1-166 recorded during cooling (A, A') and heating (B, B') scan at 10°C/min at the indicated temperatures.

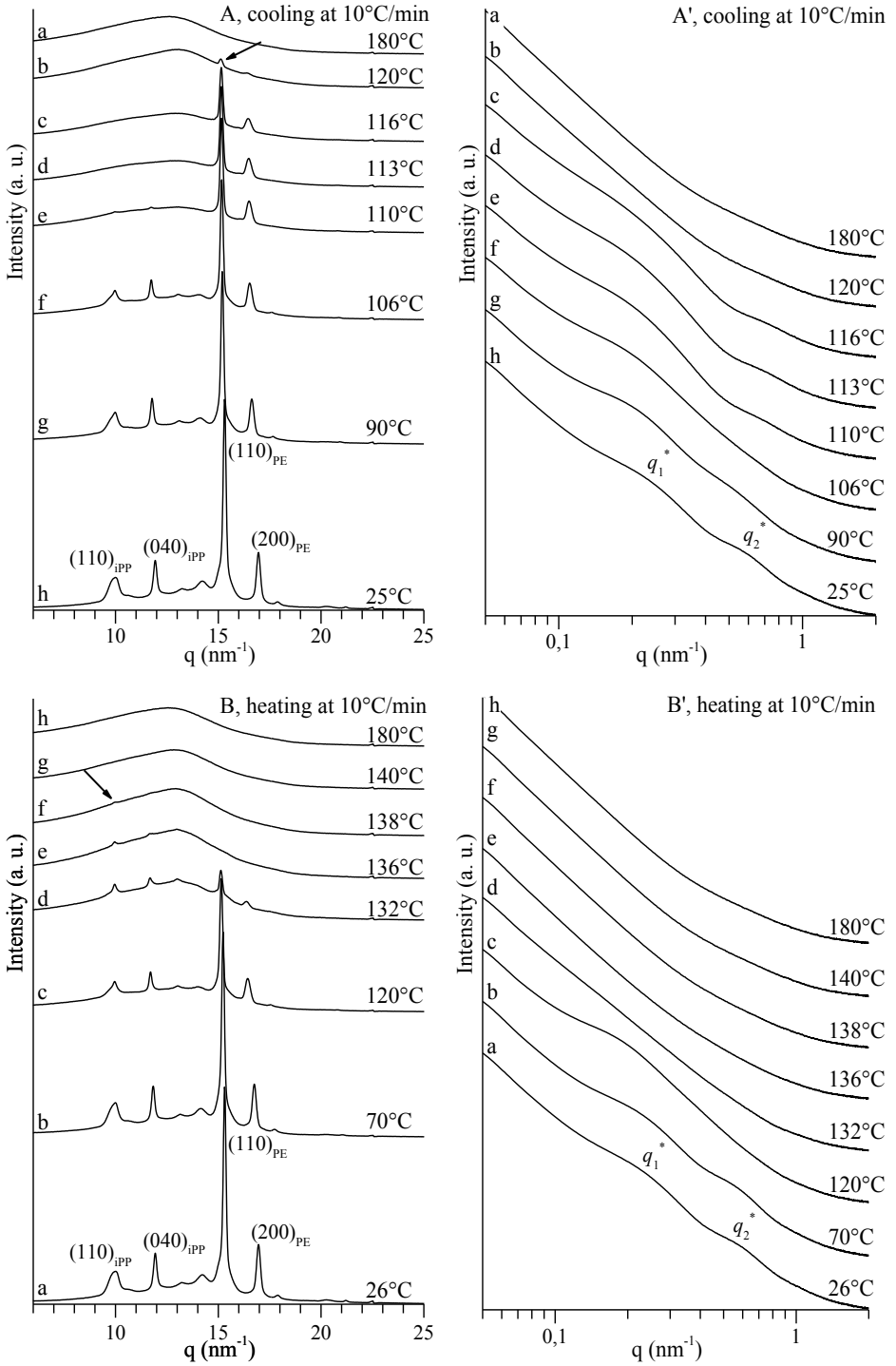

Figure 3.12. WAXS (A, B) and SAXS (A', B') profiles of the sample RDG-1-88 recorded during cooling (A, A') and heating (B, B') scan at 10°C/min at the indicated temperatures.

A comparison between the Lorentz-corrected SAXS profiles recorded at 25°C of the iPP-PE block copolymers and the two homopolymers, crystallized by cooling from the melt, is reported in Figure 3.13. The values of q_1^*, q_2^*, and the corresponding lamellar periodicities L_{SAXS1} and L_{SAXS2} are listed in Table 3.5.

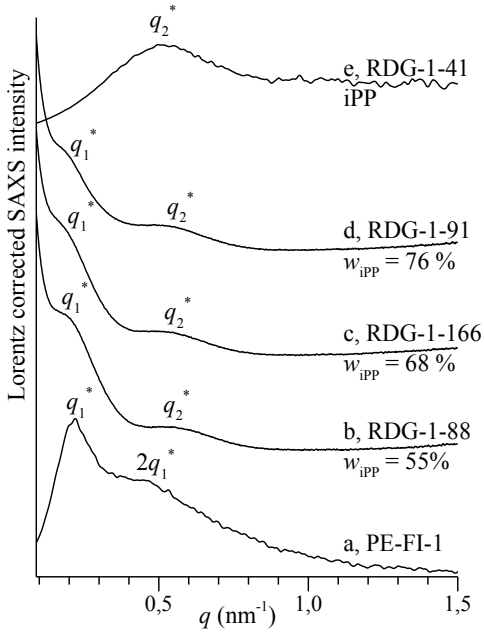

Figure 3.13. SAXS profiles after correction for the Lorentz factor recorded at 25 °C of melt-crystallized samples of PE (a) and iPP (e) homopolymers, and of iPP-*b*-PE block copolymers RDG-1-88 (b), RDG-1-166 (c), RDG-1-91 (d).

Table 3.5. Code of PE and iPP homopolymers and iPP-*b*-PE copolymers, weight fractions of the iPP (w_{iPP}) and PE (w_{PE}) blocks, position of the correlation peaks (q_1^* and q_2^*) in the SAXS profiles of Figure 3.13, and corresponding values of the lamellar periodicity (L_{SAXS1} and L_{SAXS2}).

Code	w_{iPP} (wt%)	w_{PE} (wt%)	q_1^* (nm^{-1})	q_2^* (nm^{-1})	L_{SAXS1} (nm)	L_{SAXS2} (nm)
PE-FI-1	0	100	0.21,042[a]	—	30	—
RDG-1-88	52	48	0.21	0.56	30	11
RDG-1-166	64	36	0.20	0.54	31	12
RDG-1-91	74	26	0.20	0.54	31	12
RDG-1-41	100	0	—	0.53	—	12

a. Value of the second order correlation peak ($2q_1^*$) of PE homopolymer observed in the SAXS profile a of Figure 3.13.

It is apparent that the position of the maxima q_1^* and q_2^* of the SAXS correlation peak, measured at room temperature, does not greatly depend on the BCP composition (Figure 3.13).

Since the structure formation in these samples is driven by crystallization, the nanostructure most probably consists of alternating crystalline PE and iPP domains separated by amorphous regions as shown in Figure 3.14.

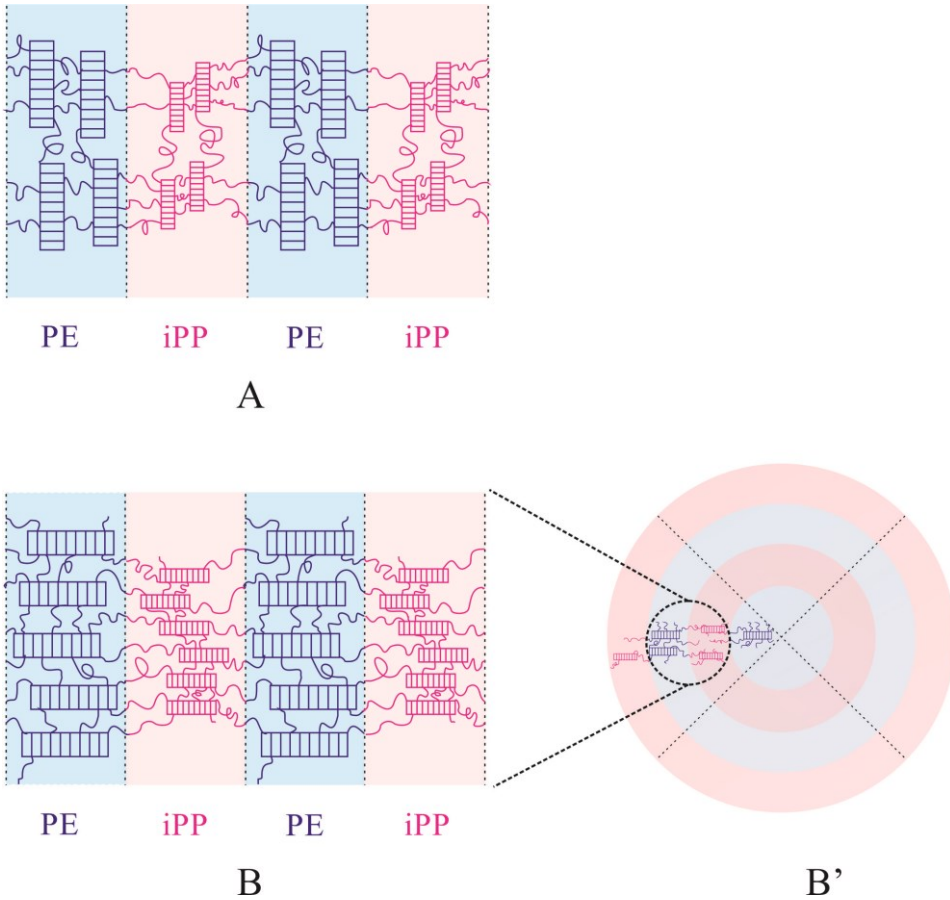

Figure 3.14. Scheme of lamellar morphology of crystalline iPP-*b*-PE block copolymers. The chain axes of the crystalline lamellae are normal to the surface of separation of nanostructured domains A and parallel in B. In B' is represented a model of spherulitic morphology formed by alternating crystalline domains of PE and iPP separated by amorphous regions in which the chain axes of the crystalline lamellae are parallel to the surface of separation of nanostructured domains.

3.3.3 Mechanical properties.

The stress-strain curves of compression molded films of iPP-*b*-PE copolymers are compared in Figure 3.15. The values of the mechanical parameters of the block copolymers and of the iPP and PE homopolymers are reported in Table 3.6. Samples of iPP-*b*-PE show deformation with necking according with high values of crystallinity and are characterized by high strength, modulus, and ductility with high deformation at break. The sample RDG-1-88 presents values of ductility and tensile strength lower than those of the other BCPs in agreement with the highest degree of crystallinity.

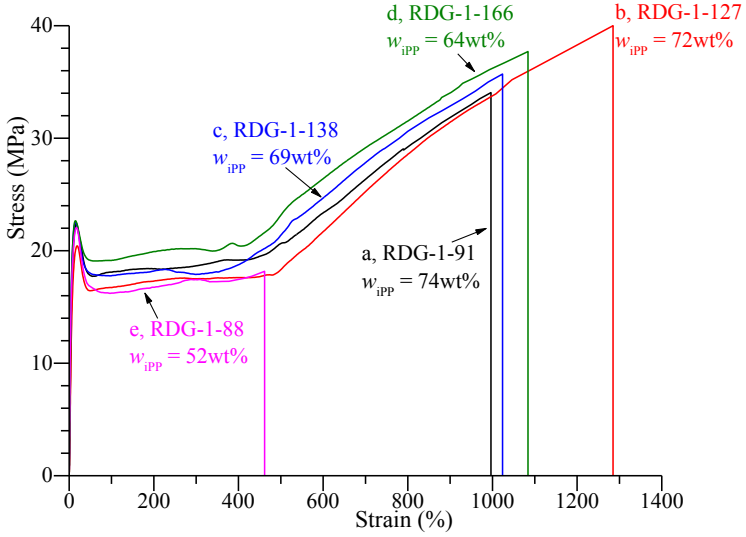

Figure 3.15. Stress-strain curves of the melt-crystallized compression molded films of iPP-*b*-PE copolymers.

Similar values of the tension set ($t_b \approx 500\%$) evaluated after break, were estimated for the block copolymers regardless the lengths of the two block. The high values of t_b and the low values of the percentage of deformation achieved at breaking which is recovered after breaking (R_b) (Table 3.6) indicate that these samples show irreversible plastic deformation with partial elastic recovery after breaking.

A comparison of the mechanical behaviors of the copolymer RDG-1-166, representative of iPP-PE samples and of iPP and PE homopolymers is shown in Figure 3.16. These data clearly indicate that iPP-*b*-PE samples show great enhancement of ductility as compared to those observed for the corresponding homopolymer samples PE and iPP. The different mechanical behavior is probably related with the chain architecture that dictate a different mechanism of deformation and/or fracture.

The results reported in Figures 3.15 and 3.16 and Table 3.6 indicate that samples of iPP-*b*-PE with weight fraction of iPP block in the range 74-64 wt% show higher ductility than those of iPP and PE homopolymers. The values of the Young's modulus are similar to those of homopolymers, moreover, higher values of the strain at the at the yield point (ε_y) were obtained for the block copolymers.

The sample RDG-1-88 with w_{iPP} = 52 wt% show, instead, value of the Young's modulus similar to that of the PE homopolymer (or a slightly higher), and lower ductility than those observed in the BCPs and the two homopolymers.

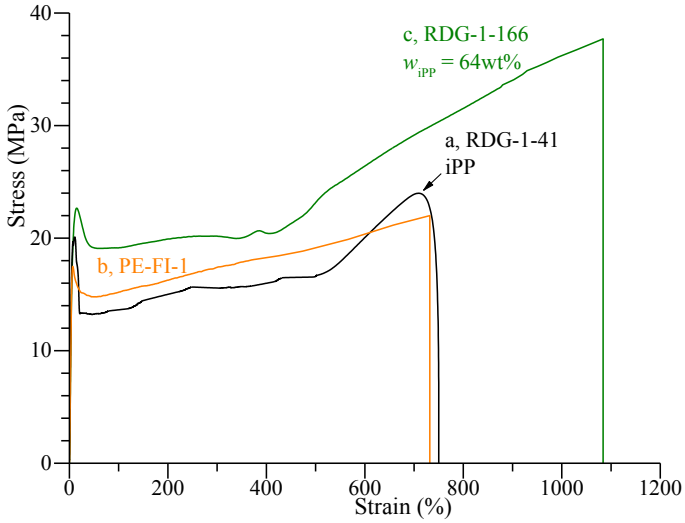

Figure 3.16. Stress-strain curves of the melt-crystallized compression molded films of iPP (a) and PE (b) homopolymers and of iPP-*b*-PE copolymer RDG-1-166 (c).

Table 3.6. Code of iPP and PE homopolymers and iPP-*b*-PE copolymers, weight fractions of the iPP block (w_{iPP}), Young's modulus (E), stress (σ_y) and strain (ε_y) at the yield point, stress (σ_b) and strain (ε_b) at break, tension set at break (t_b), percentage of deformation recovered after breaking (R_b) and X-ray crystallinity (x_c) of melt-crystallized compression molded films of iPP homopolymer and iPP-*b*-PE copolymers.

Code	w_{iPP} **(wt%)**	E **(MPa)**	σ_y **(MPa)**	ε_y **(%)**	σ_b **(MPa)**	ε_b **(%)**	t_b **(%)**	R_b **(%)**	x_c **(%)**
RDG-1-41	100	420	20	10	25	750			49
RDG-1-91	74	340	22	18	34	996	480	51	50
RDG-1-127	72	360	20	20	40	1285	516	58	51
RDG-1-138	69	400	23	16	36	1024	477	53	52
RDG-1-166	64	353	23	16	38	1084	484	55	54
RDG-1-88	52	517	22	18	18	461	490	25	62
PE-FI-1	0	460	18	7	22	732			65

These outstanding mechanical properties of iPP-PE crystalline-crystalline copolymers, are related to the block architecture structure and the structural transitions occurring during stretching (see paragraph 3.3.4).
In particular, the deformation at break and mechanical strength can be tuned by changing the lengths of the two blocks, keeping nearly constant values of elastic modulus.

3.3.4 Oriented Fibers.

A study of the structural transformations occurring during tensile deformation has been performed for the homopolymer (iPP) and iPP-PE block copolymers.
The X-ray fiber diffraction patterns of the samples RDG-1-41 (iPP homopolymer), RDG-1-91 (iPP-*b*-PE with w_{iPP} = 74 %), RDG-1-127 (iPP-*b*-PE with w_{iPP} = 72 %), RDG-1-138 (iPP-*b*-PE with w_{iPP} = 69 %) and RDG-1-166 (iPP-*b*-PE with w_{iPP} = 64 %), obtained by stretching at room-temperature compression molded films at different values of strain ε are reported in Figure 3.17, 3.18, 3.19, 3.20 and 3.21, respectively.
For the sample RDG-1-88 (iPP-*b*-PE with w_{iPP} = 52 %) with lower weight fraction of iPP block, was not possible to perform the same study because of the low ductility. This sample behave as a stiff-plastic material and was not possible to stretch it, also at very low deformations.
The X-ray diffraction pattern and the corresponding equatorial profile of the initial melt-crystallized unstretched film of the iPP homopolymer (Figure 3.17 A, A'), obtained by compression molding, show the presence of the $(130)_\alpha$ reflection of α-form and also the $(117)_\gamma$ reflection of γ-form but, with lower intensity. This indicate that the sample crystallize basically in α-form, however, a small portion of the crystals are in γ-form or in a disordered modifications of the two forms.

Crystals of iPP in γ-form or in α/γ modifications, transform, already at low deformation (ε = 100 %), in the α-form. In fact, the $(117)_\gamma$ reflection at 2θ = 20°of the γ-form is almost absent in the diffraction pattern of Figure 3.17 B and in the corresponding equatorial profile of Figure 3.17 B', whereas, the $(130)_\alpha$ reflection at 2θ = 18.6 °of the α-form is still present. A slightly polarization of the $(111)_\alpha$ and $(\bar{1}31)_\alpha + (041)_\alpha$ reflections at 2θ = 21° of the α-form on the first layer line occur by stretching of the compression molded film of iPP at value of the strain ε = 100 % (Figure 3.17 B) indicating a preferred orientation of the crystals with the chain axes parallel to the stretching direction (fiber axes). Furthermore, the broad halo in the range of 2θ = 14-18° on the equator, indicates that a small portion of crystals are, already at low deformation, in the mesomorphic form of iPP (Figure 3.17 B).

At the maximum deformation the α form transforms completely in the mesomorphic form and fibers in the pure mesomorphic form are obtained for the sample RDG-1-41, as indicated by the absence of any reflections of the α-form (Figure 3.17C).[24,29]

It is worth mentioning that, the stretching of iPP samples in α-form generally induces preferential orientation of crystals with chain axes directed parallel to the stretching direction (c_α-axis orientation), like in a standard fiber morphology. In the X-ray diffraction patterns of crystals of the α form in the normal c_α-axis orientation, the $(110)_\alpha$, $(040)_\alpha$, and $(130)_\alpha$ reflections occur on the equator (at 2θ = 14, 17, and 18.6°, respectively), whereas the reflections $(111)_\alpha$ and $(\bar{1}31)_\alpha + (041)_\alpha$ are located on the first layer line at 2θ = 21°. [23]

The stretching of the iPP crystals in γ-form induces a preferred orientation with one half of chain axes parallel to the stretching direction and the second half of chains directed at an angle of ≈ 81° with respect to the fiber axis. This preferential orientation is define as "parallel chain axis

orientation".[26] In the corresponding X-ray diffraction pattern the $(111)_\gamma$ and $(117)_\gamma$ reflections at $2\theta = 14$ and 20°, respectively, appear both on the equator and the first layer line, the $(008)_\gamma$ reflection at $2\theta = 17°$ appears on the equator, whereas the $(202)_\gamma$ and $(026)_\gamma$ reflections at $2\theta = 21°$ are located on the first layer line. [23] However, at low deformation, crystals of the γ form can assume a different kind of preferred orientation with the c_γ-axis (that is the direction of stacking of bilayers of chains, Figure 3.6C) parallel to the stretching direction and, therefore, with the two sets of chain axes directed along directions nearly normal to the stretching direction. This preferential orientation is define "perpendicular chain axis orientation" or cross-*β* [23,29,30] and the resulting diffraction pattern is characterized by the presence of a strong meridional spot at $2\theta \approx 17°$, corresponding to the $(008)_\gamma$ reflection.

During stretching of samples crystallized in a disordered modification intermediate between α and γ forms, both orientations of crystals with chain axes parallel or perpendicular to the stretching direction can be obtained. As a consequence, the existence of the diagnostic meridional reflection at $2\theta \approx 17°$ in the diffraction patterns of samples of iPP crystallized in a mixture of α and γ forms stretched at low deformations, correspond to the $(008)_\gamma$ and $(040)_\alpha$ reflections of the γ and α forms respectively, and reveals the formation of the structure cross-*β*.

In the X-ray diffraction patterns of Figure 3.17 of the sample RDG-1-41, it is apparent that the development of the fibrillar morphology occurs in the standard mode, namely, the deformation induces orientation of the crystalline lamellae with chain axes only parallel to the stretching direction. In the case of the iPP-*b*-PE copolymers, the iPP block crystallizes by cooling from the melt in a mixture of α and γ forms, as indicate by the presence of both $(130)_\alpha$ and $(117)_\gamma$ reflections at $2\theta = 18.6$ and 20.0° of α and γ form respectively, with similar intensity, in the X-ray fiber diffraction

patterns of Figures 3.18 A, 3.19 A, 3.20 A and 3.21 A and in the corresponding equatorial profiles of the unoriented samples (Figures 3.18 A', 3.19 A', 3.20 A' and 3.21 A'). As discussed in section 3.3.1, in the diffraction pattern of samples crystallized in a perfect mixture of the α and γ forms, only a diffuse scattering in the range of 2θ =18-20° should be observed. Samples of iPP-*b*-PE slowly crystallized from the melt, are characterized by crystalline lamellae in which consecutive bilayers of chains are stacked along b_α (c_γ) with the chain axes mainly, parallel, as in the α form, and by crystalline lamellae in which consecutive bilayers of chains may face each other with the chain axes mainly nearly perpendicular as in the *γ* form. On the other hand, crystals in α/γ modification more similar to the α-form and crystals in α/γ modification more similar to the γ-form may be present. Moreover, crystals of pure α-form and γ-form can be also present. This crystalline structure justify the presence in the diffraction pattern of the unoriented compression-molded films of the block copolymers of both typical reflections of the two pure forms, rather than a broad halo in the range of 2θ =18-20° (Figures 3.18A-3.21A).

The $(110)_{PE}$ and $(200)_{PE}$ reflections at 2θ = 21.4° and 23.9°, respectively, are also observed in the diffraction patterns of the unstretched samples of Figures 3.18 A,A', 3.19 A,A', 3.20 A,A' and 3.21 A,A'. This indicates that the PE block crystallizes in the common orthorhombic form.

During deformation a general orientation of both crystals of iPP and PE blocks occurs. However, for the PE block linked to the iPP block, only a polarization of the $(110)_{PE}$ and $(200)_{PE}$ reflections of the orthorhombic form of PE on the equator, that increase with increasing of the deformation, is observed. Instead, a more complex behavior has been observed for the iPP block. This behavior is also different from that observed for the iPP homopolymer.

The fiber diffraction pattern of the sample RDG-1-91 (iPP-*b*-PE with w_{iPP} = 74 %) stretched at ε = 100% (Figure 3.18B), show a reflection at 2θ ≈ 17° in a nearly meridional position and also a reflection at 2θ ≈ 20° located in the first layer line. Both reflections are not observed in the X-ray diffraction pattern of the sample RDG-1-41 (iPP homopolymer) stretched at the same deformation (Figure 3.17B). The reflection at 2θ ≈ 17° corresponds to the $(040)_\alpha$ reflection of the α–form, or the $(008)_\gamma$ reflection of the γ–form polarized, at oblique angles in nearly a meridional position on a layer line off the equator, indicating that portions of the crystals in disordered modifications intermediate between the α- and γ form, assume an orientation with the chain axes nearly perpendicular to the stretching direction (cross-*β* or perpendicular chain axis orientation). The cross-*β* orientation may be attributed to the simultaneous occurrence of two kinds of slip processes at low deformations, interlamellar and intralamellar.[23, 24, 31] Interlamellar shear leads to a location of the $(008)_\gamma$ reflection of the γ form ($(040)_\alpha$ reflection of the α form) on the meridian, whereas the intralamellar shear pushes the chain axes to align parallel to the stretching direction and thus shifts the position of the reflection at 2θ = 17° toward the equator.

The reflection at 2θ ≈ 20° correspond to the $(117)_\gamma$ reflection of crystals in γ-form or in α/γ modification more similar to the γ form, and the polarization on the layer line off the equator indicates that a portion of crystals assumes an orientation with chain axes parallel to the stretching direction.[23]

A slightly polarization of the $(111)_\alpha$, $(\bar{1}31)_\alpha$, and $(041)_\alpha$ reflections at 2θ ≈ 21° of crystals in α-form on the first layer line (Figure 3.18B), indicates that the portion of crystals of the α-form are in the normal c_α-axis orientation, therefore, with the chain axes parallel to the stretching directions.

At slightly higher deformation (200 %), portions of the crystals of the α-form transform in the mesomorphic form (Figure 3.18C). In fact, the $(110)_\alpha$, $(040)_\alpha$ and $(130)_\alpha$ reflections of the α-form are replaced by a broad halo centered at $2\theta \approx 15°$, typical of the mesomorphic form, on the equator of the diffraction pattern of Figure 3.18C. However, the diffraction pattern of Figure 3.18C shows that the $(117)_\gamma$ reflection at $2\theta \approx 20°$ is still present on the layer line even though with very low intensity indicating the presence of crystals in the γ-form or in α/γ modifications more close to the γ-form with chain axes parallel to the stretching direction not yet transformed into the mesomorphic form. Moreover, also a week $(008)_\gamma$ reflection at $2\theta \approx 17°$ is still present and polarized on the meridian. This indicates that a small portion of crystals of γ-form or in α/γ modifications more close to the γ-form, oriented with the chain axes perpendicular to the stretching direction, is also still present at this deformation (200%) and it has not yet transform into the mesomorphic form.

At very high degree of deformations (400-600%), also the crystals of γ-form transform into the mesomorphic form with high orientation of the chain axes only parallel to the stretching direction (Figure 3.18D-E).

These data indicate that crystals in α-form in the normal c_α-axis orientation, transform in the mesomorphic form at values of the strain lower that those observed for crystals of the γ-form.

At the highest deformation well oriented fibers with mixtures of crystals of the mesomorphic form of iPP and of the orthorhombic form PE are obtained (Figure 3.18E).

Similar structural transformations occur during stretching of the compression molded films of iPP-*b*-PE copolymers, regardless of the relative lengths of the iPP and PE blocks (Figures 3.19, 3.20, 3.21).

These data indicate that the development of the mesomorphic form of iPP is observed at high deformations in both the iPP homopolymer and iPP -

PE copolymers. In the case of iPP homopolymer, starting from low deformations, crystals in γ-form transform in the α-form and then the α-form transforms into mesomorphic form. The iPP crystals are oriented always with the chain axes parallel to the fiber axes at any draw ratio. In the case of BCP, crystals of iPP in α/γ forms transform in the mesomorphic form through the formation, at low value of the strain, of the structures in cross-*β* orientation. Therefore, crystalline lamellae are oriented with chain axes nearly perpendicular to the stretching direction. Crystal of α-form transform in the mesomorphic form more easily than the crystal of γ-form. At high draw ratios, the crystals tend to assume orientations with chain axes parallel to fiber axes, as in the standard fiber morphology, and are in mesomorphic form.

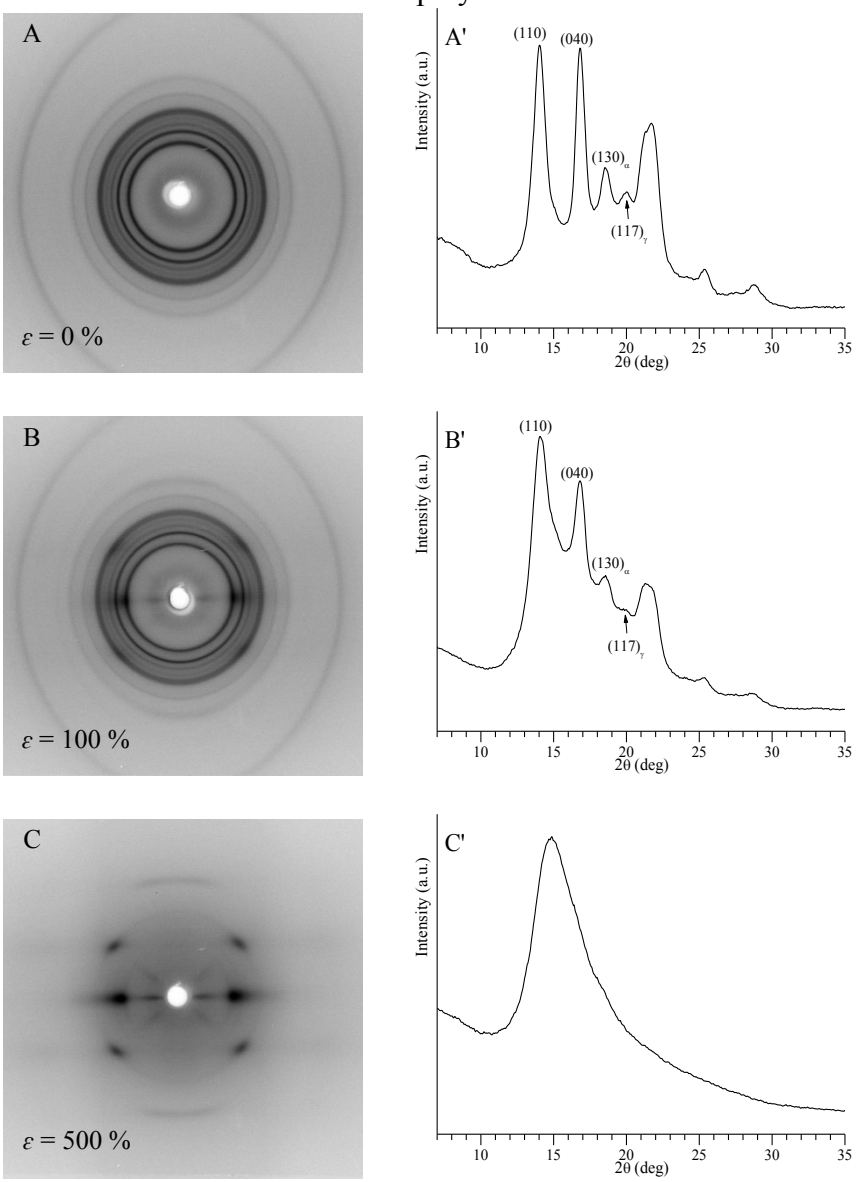

Figure 3.17. X-ray fiber diffraction patterns (A-C), and corresponding equatorial profiles (A'- C'), of the sample RDG-1-41 unoriented (A) and of oriented fibers obtained by stretching at room-temperature compression molded films at values of strain ε of 100% (B) and 500% (C).

iPP-*b*-PE RDG-1-91 with w_{iPP} = 74 wt%

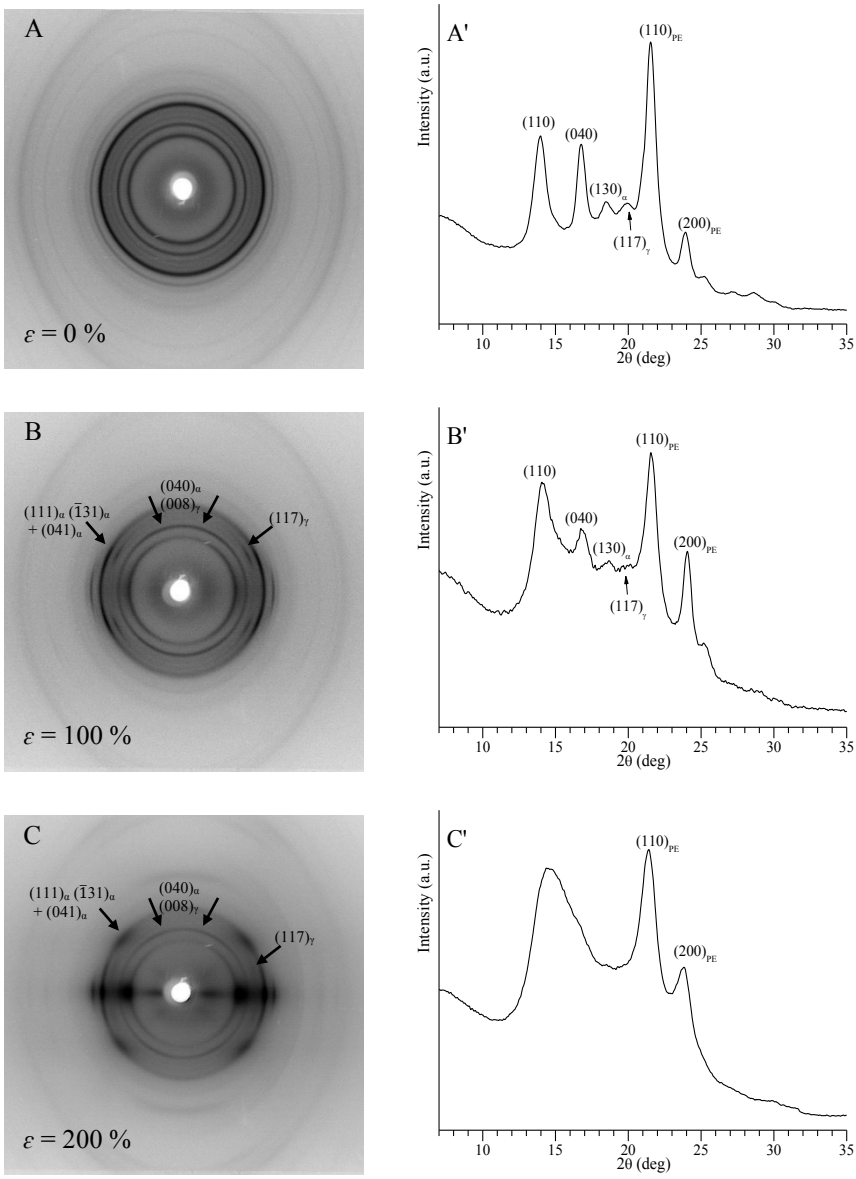

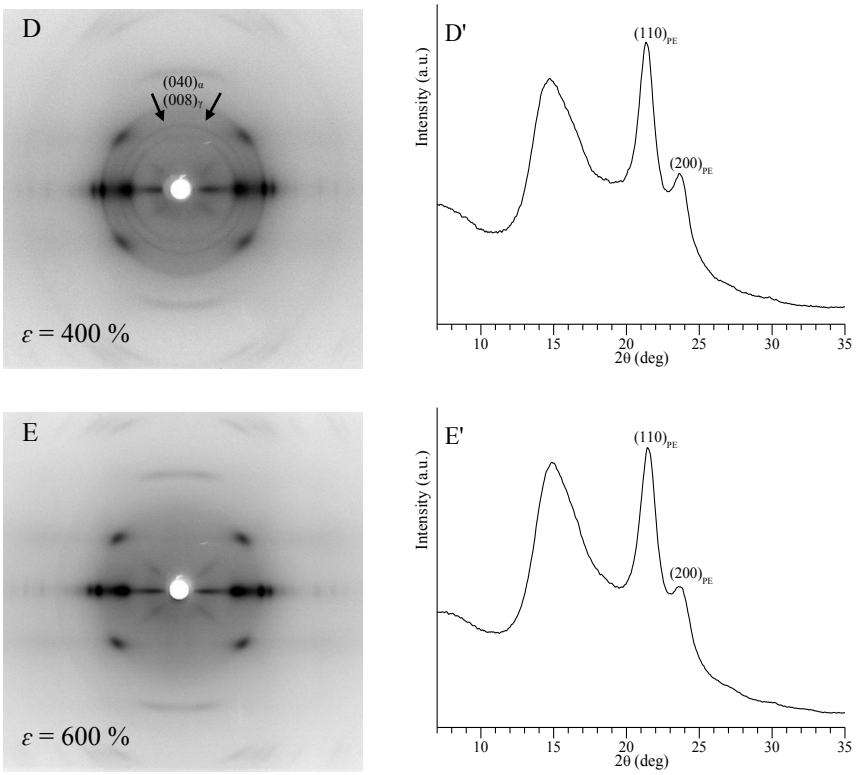

Figure 3.18. X-ray fiber diffraction patterns (A-E), and corresponding equatorial profiles (A'- E'), of the sample RDG-1-91 unoriented (A) and of oriented fibers obtained by stretching at room-temperature compression molded films at values of strain ε of 100% (B), 200% (C) , 400% (D) and 600% (E).

iPP-*b*-PE RDG-1-127 with w_{iPP} = 72 wt%

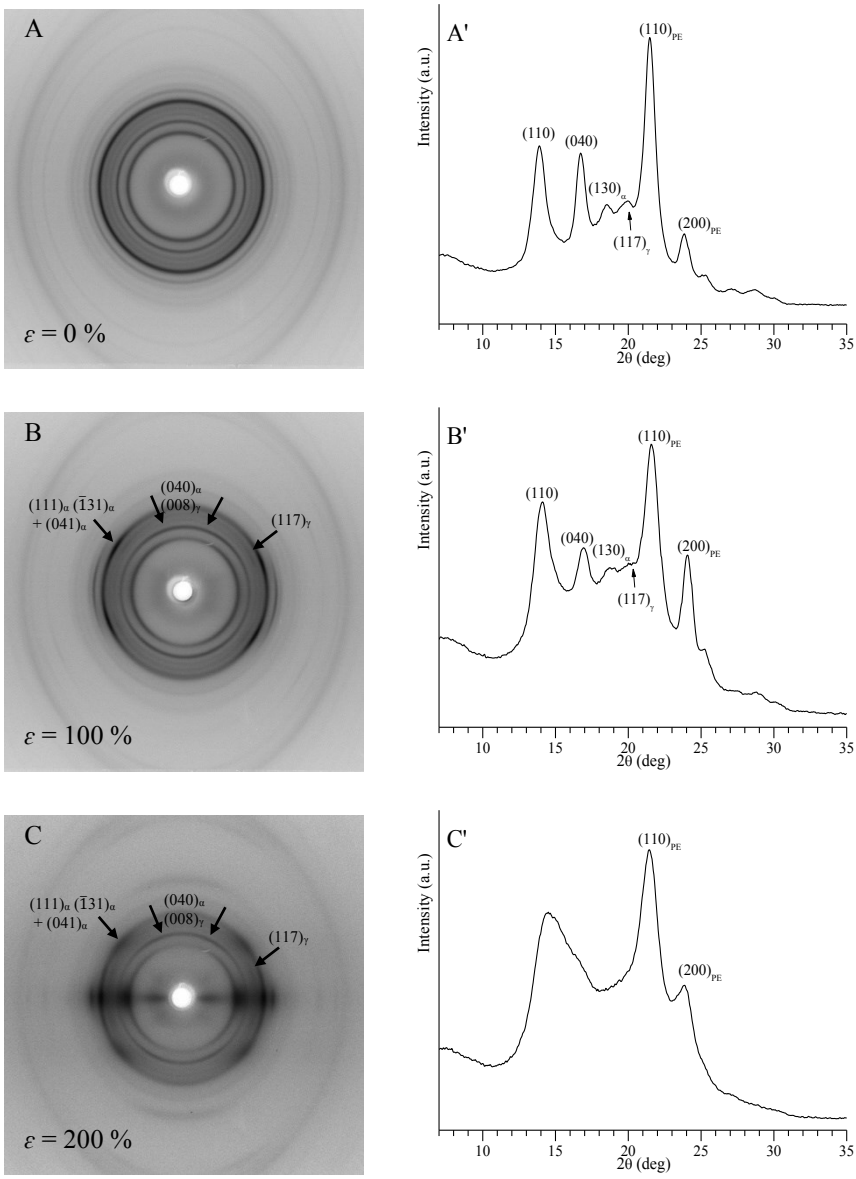

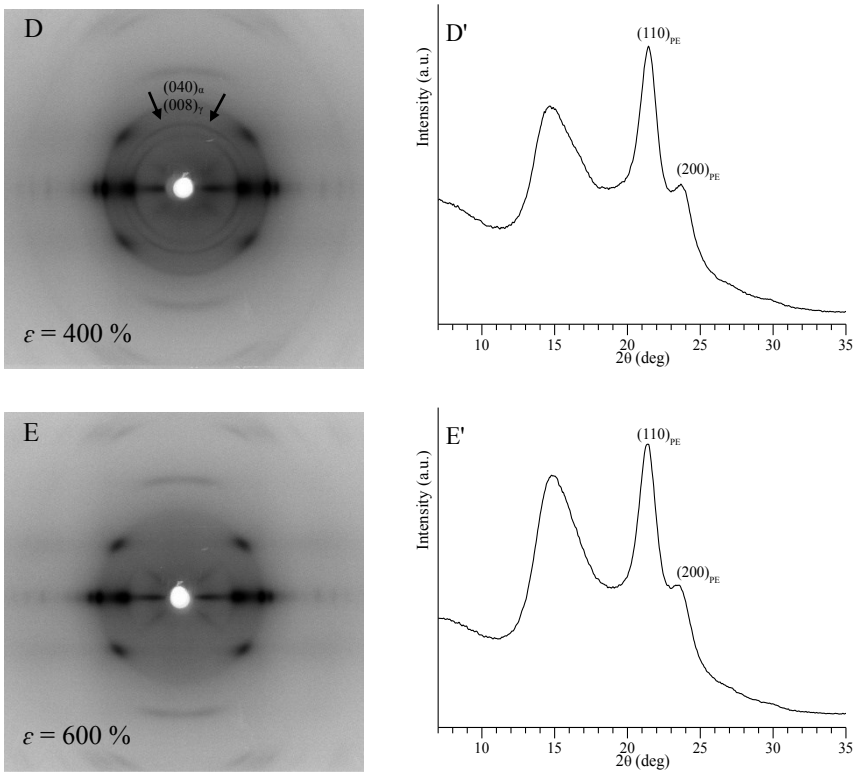

Figure 3.19. X-ray fiber diffraction patterns (A-E), and corresponding equatorial profiles (A'- E'), of the sample RDG-1-127 unoriented (A) and of oriented fibers obtained by stretching at room-temperature compression molded films at values of strain ε of 100% (B), 200% (C) , 400% (D) and 600% (E).

iPP-*b*-PE RDG-1-138 with w_{iPP} = 69 wt%

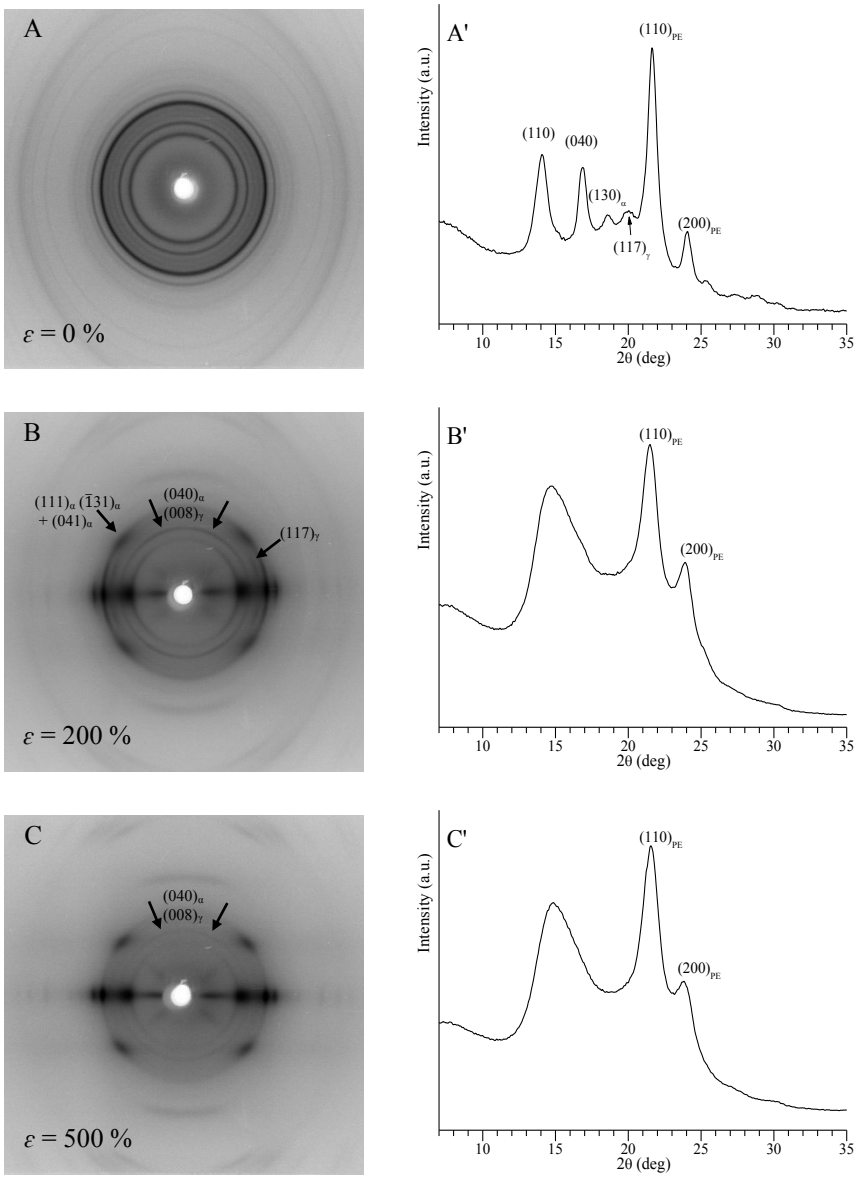

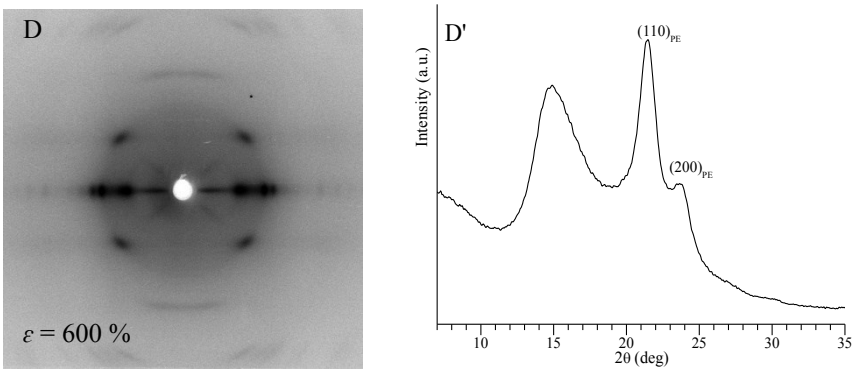

Figure 3.20. X-ray fiber diffraction patterns (A-D), and corresponding equatorial profiles (A'- D'), of the sample RDG-1-138 unoriented (A) and of oriented fibers obtained by stretching at room-temperature compression molded films at values of strain ε of 200% (B), 500% (C) and 600% (D).

iPP-*b*-PE RDG-1-166 with w_{iPP} = 64 wt%

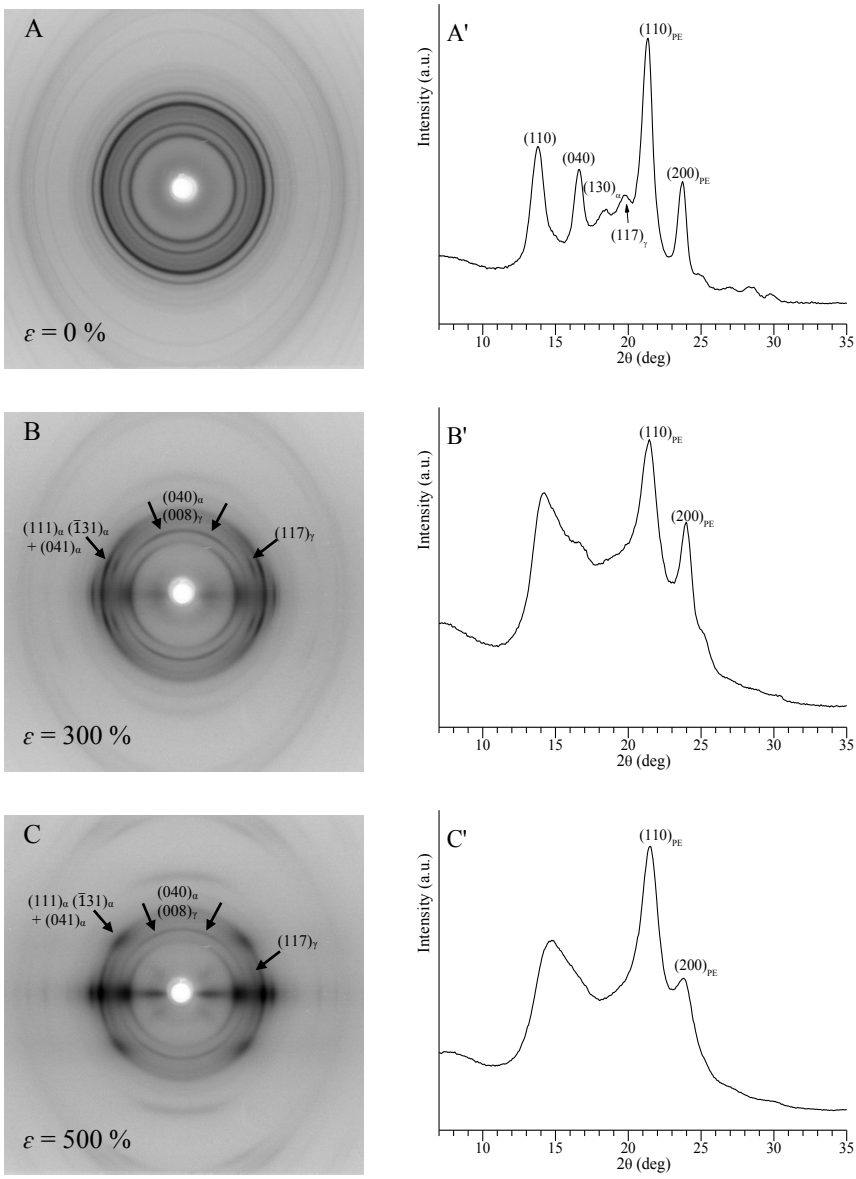

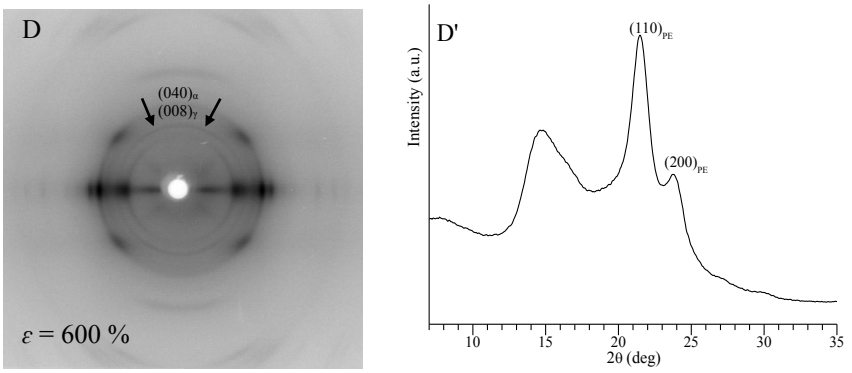

Figure 3.21. X-ray fiber diffraction patterns (A-D), and corresponding equatorial profiles (A'- D'), of the sample RDG-1-166 unoriented (A) and of oriented fibers obtained by stretching at room-temperature compression molded films at values of strain ε of 300% (B), 500% (C) and 600% (D).

3.3.5 Morphology of bulk crystallized samples.

Polarized optical microscopy (POM) images of samples of iPP homopolymer and iPP-*b*-PE crystallized from the melt at cooling rate of 10 °C/min and 5 °C/min are shown in Figures 3.22 and 3.23, respectively.

The image of Figure 3.22A of the sample RDG-1-41 show the presence of bundle-like entities, organized in a nearly 90° texture,[32] that are typical of samples of iPP in which crystals of α and γ forms can be present simultaneously. The same morphology is observed also in the POM image of the sample RDG-1-41 crystallized at 5 °C/min, where a slight increase of the crystals size is observed (Figure 3.23A).

Similar bundle-like crystals are observed in the POM images of the iPP-PE block copolymers with the highest iPP weight fraction of Figure 3.22B,C (samples RDG-1-91 and RDG-1-127 with 74 and 72 wt% of iPP).

A high concentration of bundle-like crystals, are evident in POM image of the sample RDG-1-91 presenting the highest length of iPP block (w_{iPP} = 74%) in Figure 3.22B. However, it is apparent that the crystalline structures observed for the block copolymers are smaller than those of the iPP homopolymer crystallized in the same conditions. As already discussed in

paragraph 3.1, in double crystalline di-block copolymers, depending on the block composition, the crystallization of one block may affect the crystallization and morphology of the second block, leading to the formation of less defined morphologies.

Samples of iPP-*b*-PE with similar weight fraction of iPP block (RDG-1-127 with w_{iPP} = 72% and RDG-1-138 with w_{iPP} = 69%), have similar morphology, characterized by disordered crystalline structure, and only a small increase of the crystals size is observed with decrease of the weight fraction of iPP block (Figures 3.22C and D).

In the POM images of BCPs samples with the higher length of the PE block, as in the sample RDG-1-166 with w_{iPP} = 64 wt% (Figure 3.22E), and in the sample RDG-1-88 with w_{iPP} = 52 wt% (Figure 3.22F), small banded spherulites, typical of PE are observed along with smaller birefringent entities, corresponding to iPP crystals formed at lower temperature. [33, 34]. It is worth noting that, considering the block architecture, the observation of banding is consistent with the models of Figure 3.14B,B'.

The images of Figures 3.23B-F indicate that the morphology of iPP-*b*-PE samples crystallized from the melt at cooling rate of 5 °C/min does are similar to that of the samples crystallized at 10°C/min.

The highest density of well-defined banded spherulites with average diameter between 10-20 μm is observed in the POM images of the sample RDG-1-166 of lower thickness cooled from the melt at 5 °C/min (Figure 3.24). The presence of PE banded spherulites indicate that the PE block crystallize first determining the final morphology according with the X-ray diffraction profiles of Figures 3.11A, 3.12. These data confirm that crystallization dominates the morphology, and superstructures like spherulites or bundle-like entities are observed. This crystallization behavior (break-out) is usually observed during the crystallization of

weakly segregated BCPs or when the crystallization take place from a homogeneous melt.

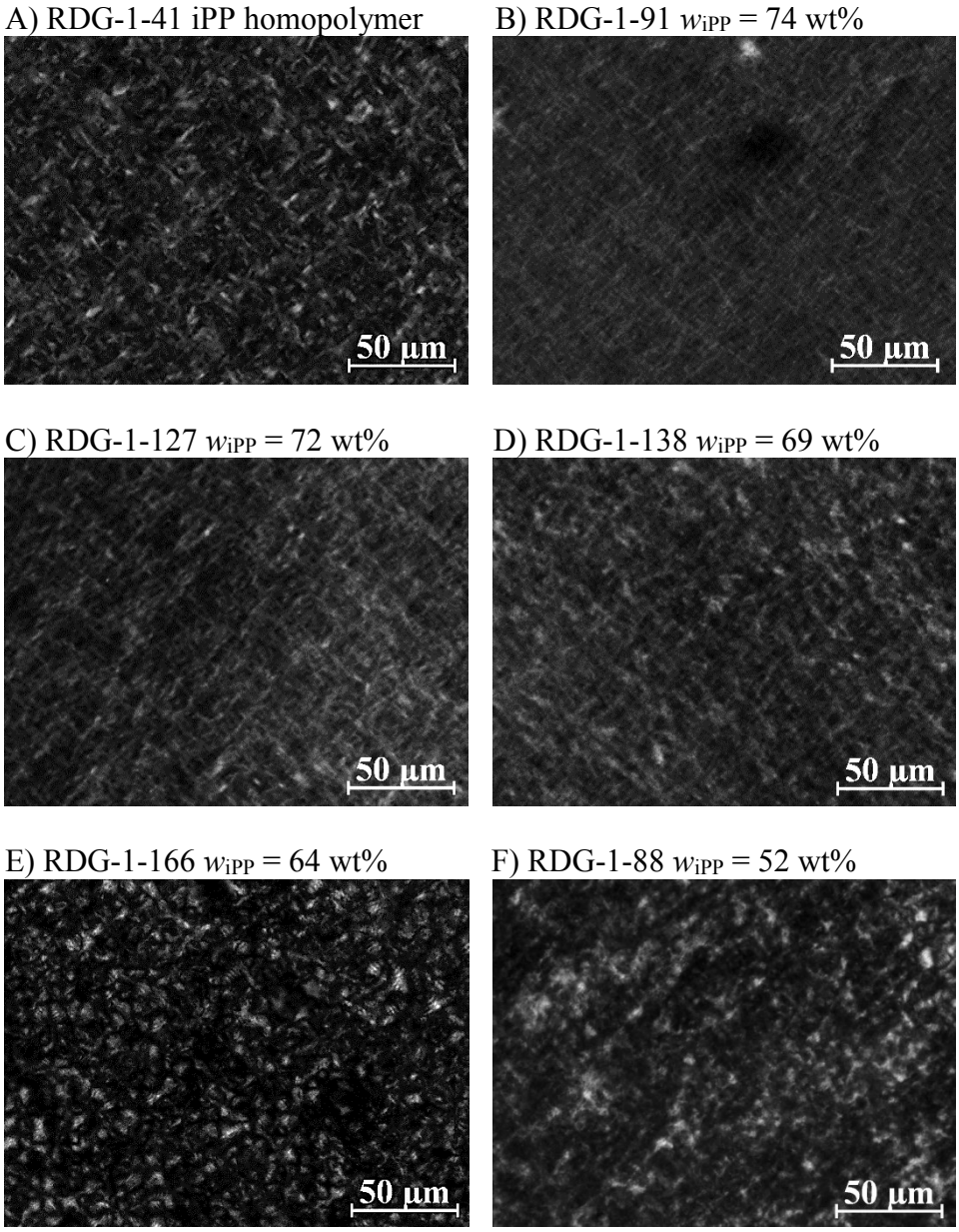

Figure 3.22. Polarized optical microscope images (crossed polars) recorded at room temperature of iPP homopolymer RDG-1-41 (A) and of iPP-*b*-PE copolymers RDG-1-91 (B), RDG-1-127 (C), RDG-1-138 (D), RDG-1-66 (E) and RDG-1-88 (F), crystallized from the melt by cooling at cooling rate of 10 °C/min to room temperature. The thickness of the films is ≈ 100 µm.

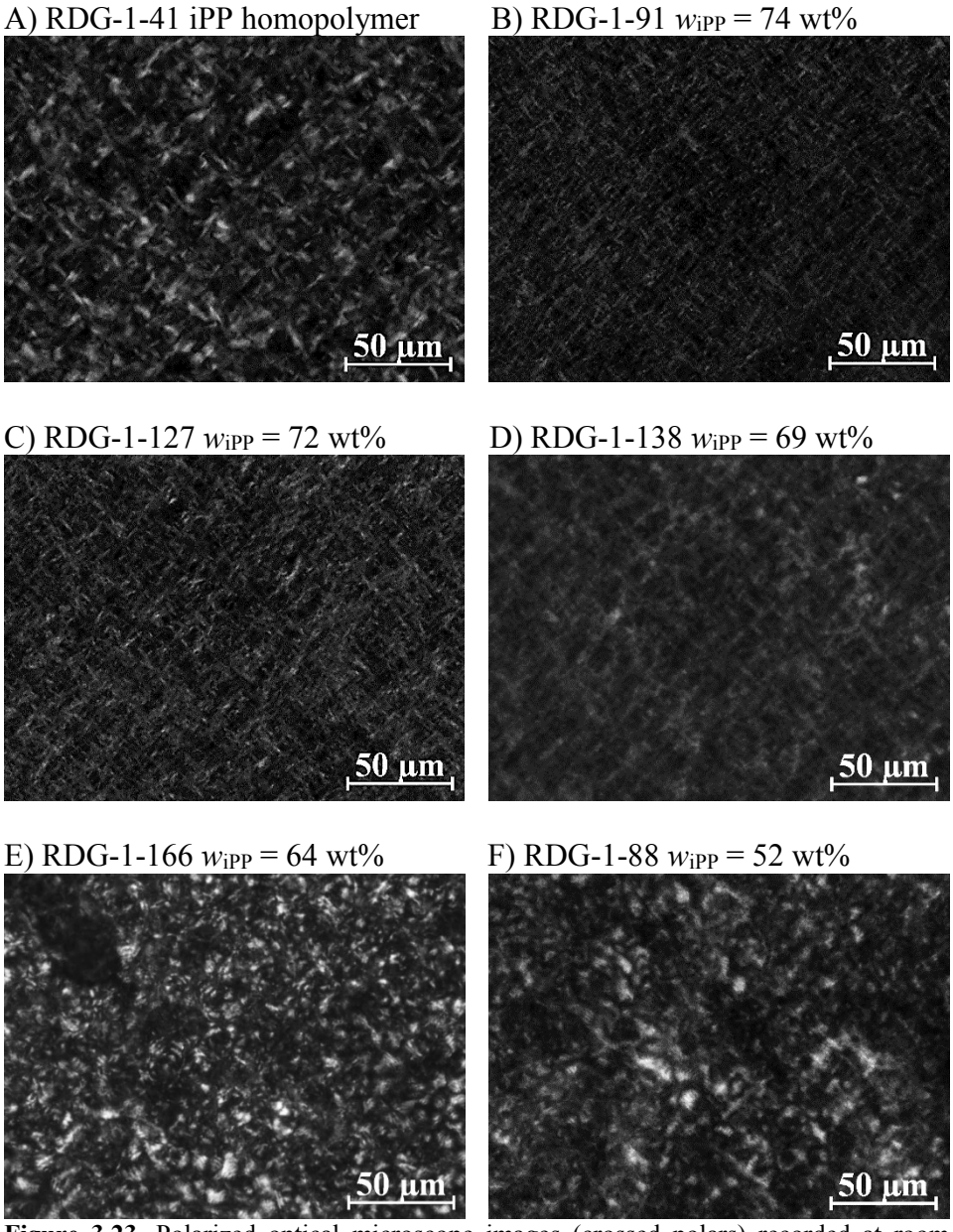

Figure 3.23. Polarized optical microscope images (crossed polars) recorded at room temperature of iPP homopolymer RDG-1-41 (A) and of iPP-*b*-PE copolymers RDG-1-91 (B), RDG-1-127 (C), RDG-1-138 (D), RDG-1-66 (E) and RDG-1-88 (F), crystallized from the melt by cooling at cooling rate of 5 °C/min to room temperature. The thickness of the films is ≈ 100 µm.

RDG-1-166 w_{iPP} = 64 wt%

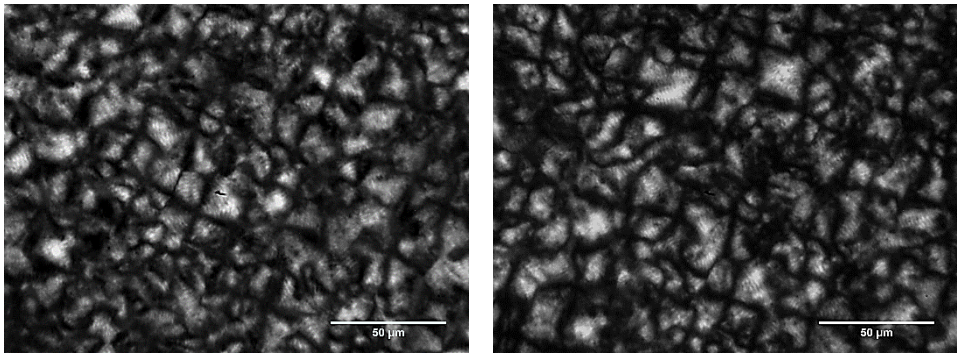

Figure 3.24. Polarized optical microscope images (crossed polars) recorded at room temperature of iPP-*b*-PE copolymer RDG-1-66 (E) crystallized from the melt by cooling at cooling rate of 5 °C/min to room temperature. The thickness of the films is ≈ 10 µm.

3.4 Characterization of isotactic polypropylene-*block*-linear low density polyethylene (iPP-*b*-LLDPE) crystalline-crystalline block copolymers.

3.4.1 Crystallization behavior.

The X-ray powder diffraction profiles of as-prepared samples of the iPP homopolymer and of iPP-LLDPE BCPs, with different blocks lengths are reported in Figure 3.25. The presence in the diffraction profiles of Figure 3.25 of the $(130)_\alpha$ reflection at $2\theta = 18.6°$ indicates that the iPP homopolymer and the iPP block in the copolymers, crystallize in the α–form. Moreover, the $(110)_{PE}$ and $(200)_{PE}$ reflections at $2\theta = 21.4°$ and 23.9°, respectively, of the orthorhombic form of PE, are present in the diffraction profiles of the block copolymers (Figure 3.25) indicating that both iPP and PE blocks are crystalline.

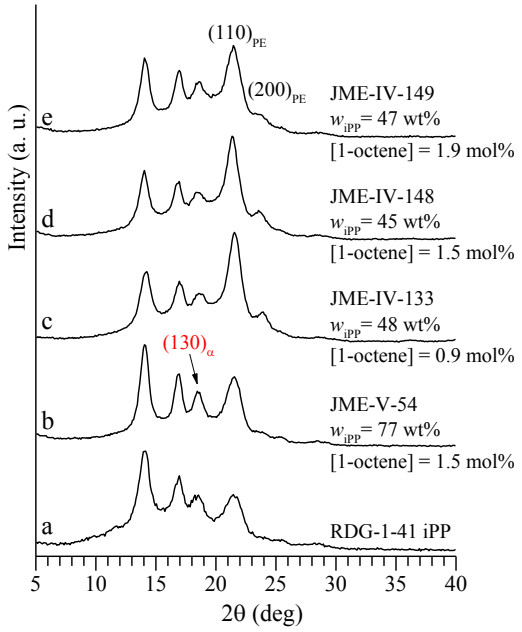

Figure 3.25. X-ray powder diffraction profiles of as-prepared samples of iPP homopolymer and iPP-*b*-LLDPE copolymers. The $(130)_\alpha$ reflection of α form of iPP at $2\theta = 18.6°$ and the $(110)_{PE}$ and $(200)_{PE}$ reflections at $2\theta = 21.4°$ and 23.9°, respectively, of the orthorhombic form of PE are indicated. The weight fraction of the iPP block (w_{iPP}) and the concentration of 1-octene ([1-octene]) are also reported.

The X-ray powder diffraction profiles of compression-molded samples slowly crystallized from the melt (≈ 15 °C/min) are reported in Figure 3.26. The iPP homopolymer sample and the iPP blocks in the copolymers, crystallize in a disordered modifications of α and γ forms, as indicated by the presence of both $(130)_\alpha$ and $(117)_\gamma$ reflections at 2θ = 18.6° and 20.0° of α and γ form respectively, in the diffraction profiles of Figure 3.26.

The same result was found when the iPP block is linked to the PE block, in fact, the diffraction profiles of the iPP-*b*-PE compression molded films of Figure 3.5, show, also in the case, the presence of the $(130)_\alpha$ and $(117)_\gamma$ reflections of α and γ form respectively, indicating that the iPP block crystallizes in a mixture of the two forms.

The polyethylene phase crystallizes in both iPP-PE and iPP-LLDPE BCPs in the orthorhombic form, as indicate by the presence of the $(110)_{PE}$ and $(200)_{PE}$ reflections at 2θ = 21.4° and 23.9° respectively, in the diffraction profiles of Figure 3.5 and 3.26.

The values of the crystallinity degrees evaluated for the iPP-*b*-LLDPE compression molded films are slightly higher than those of iPP homopolymer (Table 3.7).

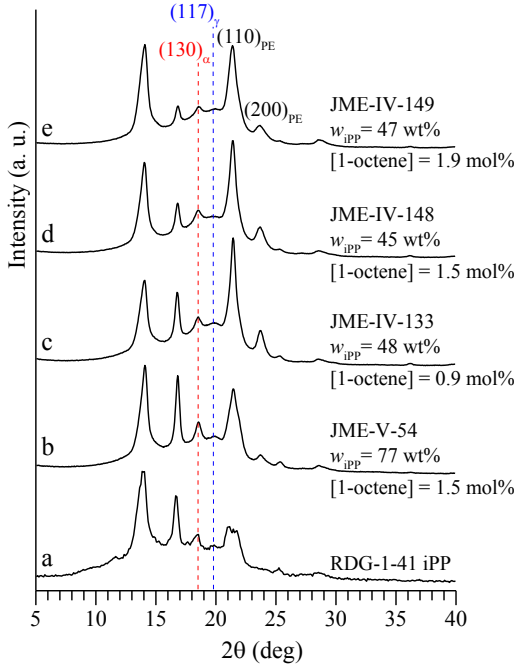

Figure 3.26. X-ray powder diffraction profiles of compression molded samples of iPP homopolymer and iPP-*b*-LLDPE copolymers. The $(130)_{\alpha}$ and the $(117)_{\gamma}$ reflections at 2θ = 18.6° and 20.0° of α and γ form respectively of iPP and the $(110)_{PE}$ and $(200)_{PE}$ reflections at 2θ = 21.4° and 23.9°, respectively, of the orthorhombic form of PE are indicated. The weight fraction of iPP block (w_{iPP}) and the concentration of 1-octene ([1-octene]) are also reported.

Table 3.7. Code of iPP homopolymer and iPP-*b*-LLDPE copolymers, weight fractions of the iPP block (w_{iPP}), concentration of 1-octene ([1-octene]), crystallinity degree (x_c) of the compression-molded samples of iPP homopolymer and iPP-*b*-LLDPE copolymers.

Code	w_{iPP} (wt%)	[1-octene] (mol%)	x_c (%)
iPP-RDG-1-41	100	—	49
JME-V-54	77	1.5	51
JME-IV-133	48	0.9	58
JME-IV-148	45	1.5	56
JME-IV-149	47	1.9	57

The DSC curves of iPP homopolymer and iPP-LLDPE BCPs, recorded during first heating, successive cooling from the melt, and second heating of the melt-crystallized samples, all recorded at 10 °C/min, are reported in Figure 3.27A-C. The values of melting and crystallization temperatures and enthalpies are reported in Table 3.8.

As already discuss in the paragraph 3.3.1 for the Figure 3.7, the isotactic pentad *mmmm* of 91% of the sample RDG-1-41 (iPP homopolymer) is in agreement with the presence of a melting peak at ≈ 135°C in the DSC heating curves a of Figure 3.27 A and C. The Hf-based post-metallocene catalyst was used for the synthesis of the iPP homopolymer and for both iPP-PE and iPP-LLDPE BCPs (Figure 3.3), therefore a similar isotacticity of iPP block when linked to PE or LLDPE block is expected.

The DSC heating curves of the sample JME-V-54 with the highest weight fraction of iPP (77%) and concentration of 1-octene of 1.5% (curves b of Figure 3.27 A and C) show a main endothermic peak at 127°C or 134°C for the first and second heating scans respectively, and a small endothermic peak at lower temperatures. The main peak at higher temperature is due to the melting of iPP block, whereas, the small peak at lower temperature corresponds to the melting of the LLDPE block.

The DSC curves of first heating of the copolymers JME-IV-133, JME-IV-148 and JME-IV-149 with similar lengths of the iPP and LLDPE blocks and concentration of 1-octene of 0.9, 1.5 and 1.9 % respectively (curves c-e of Figure 3.27A), show two endothermic peaks, corresponding to the melting of iPP and LLDPE blocks, that are better resolved in the second heating curves (curves c-e of Figure 3.27B). This indicates that the iPP and LLDPE blocks melt at different temperatures and in particular, the LLDPE block melts at temperatures lower than that of the iPP block. Furthermore, a decrease of the melting temperatures of the LLDPE block with increasing of the concentration of 1-octene is observed.

The DSC thermogram recorded during cooling from the melt of all iPP-*b*-LLDPE samples show only one exothermic peak due to the overlapping of iPP and LLDPE crystallization.

The crystallization temperatures (T_c) of the iPP-*b*-LLDPE samples with similar lengths of the iPP and LLDPE blocks, are lower than that of iPP homopolymer (curves c-e of Figure 3.27B) and a decrease of the T_c and a broadening of the crystallization peak with increasing of 1-octene content are observed.

A different melting and crystallization behavior was found for the iPP-PE BCPs. In fact in this case the two blocks melt at similar temperatures and only one melting peak with a small shoulder at higher temperatures is observed in DSC heating curves of Figure 3.7A and C. In the case of iPP-*b*-LLDPE samples, two separated melting peaks are present in the DSC heating curves of Figure 3.27A and C, indicating that the melting of the two blocks occurs at different temperatures.

Cooling scans of iPP-*b*-PE samples (Figure 3.7B and Table 3.3), have demonstrated that the presence of the PE block linked to the iPP block induces an increase of the T_c compared to the T_c of iPP homopolymer. These data have indicated that the PE crystallizes first, as also confirmed by simultaneous WAXS and SAXS experiments performed during cooling from the melt, and that the crystallization of these BCPs is driven by the nucleation effect of PE to the crystallization of iPP block (Figure 3.7B and Table 3.3). Instead, in the case of iPP-*b*-LLDPE samples, probably, iPP domains crystallize just before the LLDPE crystallization and lower values of the T_c compared to the T_c of iPP homopolymer, are observed (Figure 3.27B and Table 3.8).

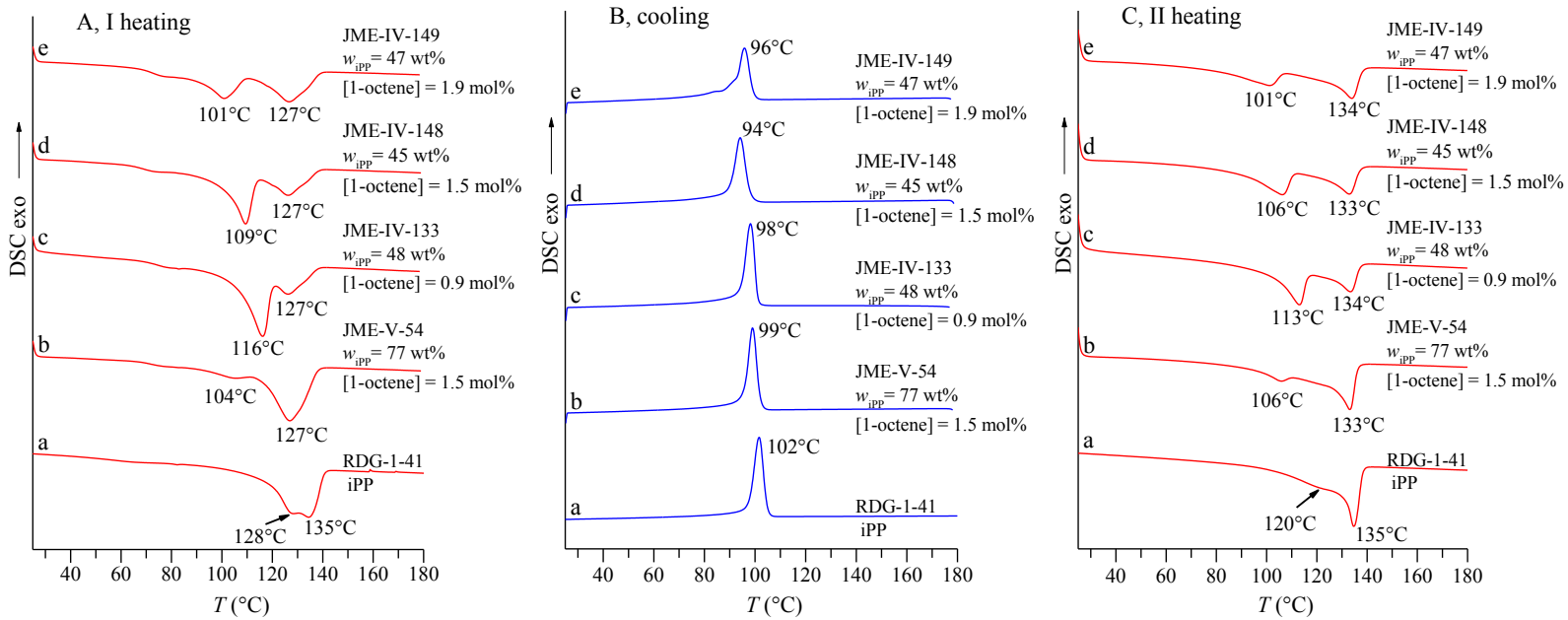

Figure 3.27. DSC curves recorded at 10°C/min during first heating (A), successive cooling (B) and second heating scans (C) of as-prepared samples of iPP homopolymer and iPP-*b*-LLDPE copolymers. The weight fraction of iPP block (w_{iPP}), the concentration of 1-octene ([1-octene]) and the values of the melting and crystallization temperatures are indicated.

Table 3.8. Code of iPP homopolymer and iPP-*b*-LLDPE copolymers, weight fraction of the iPP (w_{iPP}) block, concentration of 1-octene ([1-octene]), melting temperature (T_m(I)) and melting enthalpy (ΔH_m(I)) recorded during the first heating, crystallization temperature (T_c), melting temperature (T_m(II)) and melting enthalpy (ΔH_m(II)) recorded during the second heating, crystallization enthalpy (ΔH_c) of the samples of iPP hompolymer and of the iPP-*b*-LLDPE copolymers.

Code	w_{iPP} (wt%)	[1-octene] (mol%)	T_m(I) (°C)	T_c (°C)	T_m(II) (°C)	ΔH_m(I) J/g	ΔH_c J/g	ΔH_m(II) J/g
RDG-1-41	100	—	128,135	102	120,135	80.3	77.3	76.6
JME-V-54	77	1.5	104,127	99	106,133	94.2	76.2	69.6
JME-IV-133	48	0.9	116,127	98	113,134	106.4 (80.2+26.2)	76.4	76.9 (48.3+28.6)
JME-IV-148	45	1.5	109,127	94	106,133	100.4 (68.1+32.3)	73.4	65.2 (35.0+30.2)
JME-IV-149	47	1.9	101,127	96	101,134	91.1 (48.3+42.8)	71	69.0 (30.1+38.9)

3.4.2 Time and temperature resolved WAXS and SAXS.

Simultaneous time and temperature-resolved wide and small angle X-ray scattering (WAXS and SAXS) experiments have been performed with synchrotron radiation at ESRF in Grenoble to clarify the melting and crystallization behavior of iPP-LLDPE di-block copolymers and to confirm the DSC results previously discussed.

The temperature profile employed was: heating from 25 to 180 °C at 30°C/min; 1 min hold at 180 °C; cooling to 25 °C at 10 °C/min, heating again to 180 °C at 10 °C/min and finally, cooling from 180 to 25 °C at 30 °C/min.

WAXS and SAXS profiles of the sample JME-V-54 with 77 wt% of iPP at selected temperatures, recorded during cooling and heating scans at 10 °C/min, are reported in Figure 3.28. The SAXS data were corrected for the Lorentz factor and are also reported in Figure 3.28. It is apparent that starting from an amorphous halo of the melt at 180 °C (curve a of Figure 3.28A), during cooling the iPP block crystallizes first as indicated by the appearance of the weak $(110)_{\alpha}$ and $(040)_{\alpha}$ reflections of iPP at 103°C, while no reflections of LLDPE are observed (curve c of Figure 3.28A). The WAXS profiles recorded at lower temperatures show that only the crystallization of the iPP block occurs until 99°C (curves d-f of Figure 3.28A), whereas, the presence of crystals of LLDPE is detectable only at 88°C (curves e of Figure 3.28A), as indicated by the increase of the intensity of the reflection at q = 15 nm^{-1} (2θ = 21°) due to the $(110)_{PE}$ reflection of PE.

The absence of correlation peaks in the SAXS pattern at 180 °C (curve a of Figure 3.28A', A''), indicates that no microdomain structure is evident in the melt. However, as already discuss in the paragraph 3.3.1 for the iPP-PE block copolymers, a phase separation is expected in the melt state for these samples. Therefore, the absence of any signal in the SAXS profiles a of

Figure 3.28A', A'' can be attributable to the small electron density difference between LLDPE and iPP blocks, negligible for X-ray scattering. SAXS profiles recorded between 103°C and 99°C (curves c-f of Figure 3.28A') show an increase of the intensity at q^* value of ≈ 0.4 nm^{-1}, that is better observed in the corresponding Lorentz-corrected SAXS profiles of Figure 3.28A''. According to the WAXS profiles at these temperatures (curves c-f of Figure 3.28A) that show only reflections of iPP crystals, this correlation peak correspond to the lamellar stacks of iPP domains.

At lower temperatures, when both blocks are crystalline, only one broad correlation peak is observed at q^* = 0.5 nm^{-1} (curves h of Figure 3.28A', A''), indicating that the two correlations relative to iPP and LLDPE crystalline lamellar stacks are not distinguishable and that the iPP and LLDPE lamellar stacks have a similar periodicity L_{SAXS} ≈ 13 nm.

WAXS experiments performed by heating of the melt-crystalized sample from 25 °C to 180 °C at 10 °C/min (Figure 3.28B), show that crystals of LLDPE melt at temperature lower than that of iPP crystals, confirmed by the decrease of the intensity of the reflection at q = 15 nm^{-1} ($(110)_{PE}$ reflection of PE) during heating up to 106 °C (curves a-c of Figure 3.28B) and the presence of all iPP reflections and the absence of those of LLDPE in the diffraction profiles recorded at temperatures higher than 106°C. A decrease of the intensities of the diffraction peaks of iPP is observed in the WAXS profiles recorded during heating the sample up to 133°C and only an amorphous halo is shown in the profiles at 141°C and 180°C indicating that the sample is fully melted. These data are in agreement with the DSC second heating curve of this sample (curve b of Figure 3.27C) in which the two endothermic peaks at 106°C and 133°C are due to the melting of LLDPE and iPP crystalline domains respectively.

As already discuss, only one broad peak is present in the SAXS profile of the sample JME-V-54 recorded at 26°C (curve a of Figure 3.28B') that

probably indicate a similar lamellar periodicity $L_{SAXS} \approx 13$ nm of iPP and LLDPE lamellar stacks. A small decrease of the q value, corresponding to an increase of the lamellar periodicity of both crystalline phases, with increasing temperature, is observed. The diffraction peak appears more sharp at 111°C (curves d of Figure 3.28B',B'') when the LLDPE block is melted. This correlation peak is observed up to 120°C (curves e of Figure 3.28B',B''), where high crystallinity of the iPP block is still present in the corresponding WAXS profiles (curves d and e of Figure 3.28B). After melting, in the SAXS profiles at 141°C and 180 °C (curves g and h of Figure 3.28B',B'') no correlation peaks are observed.

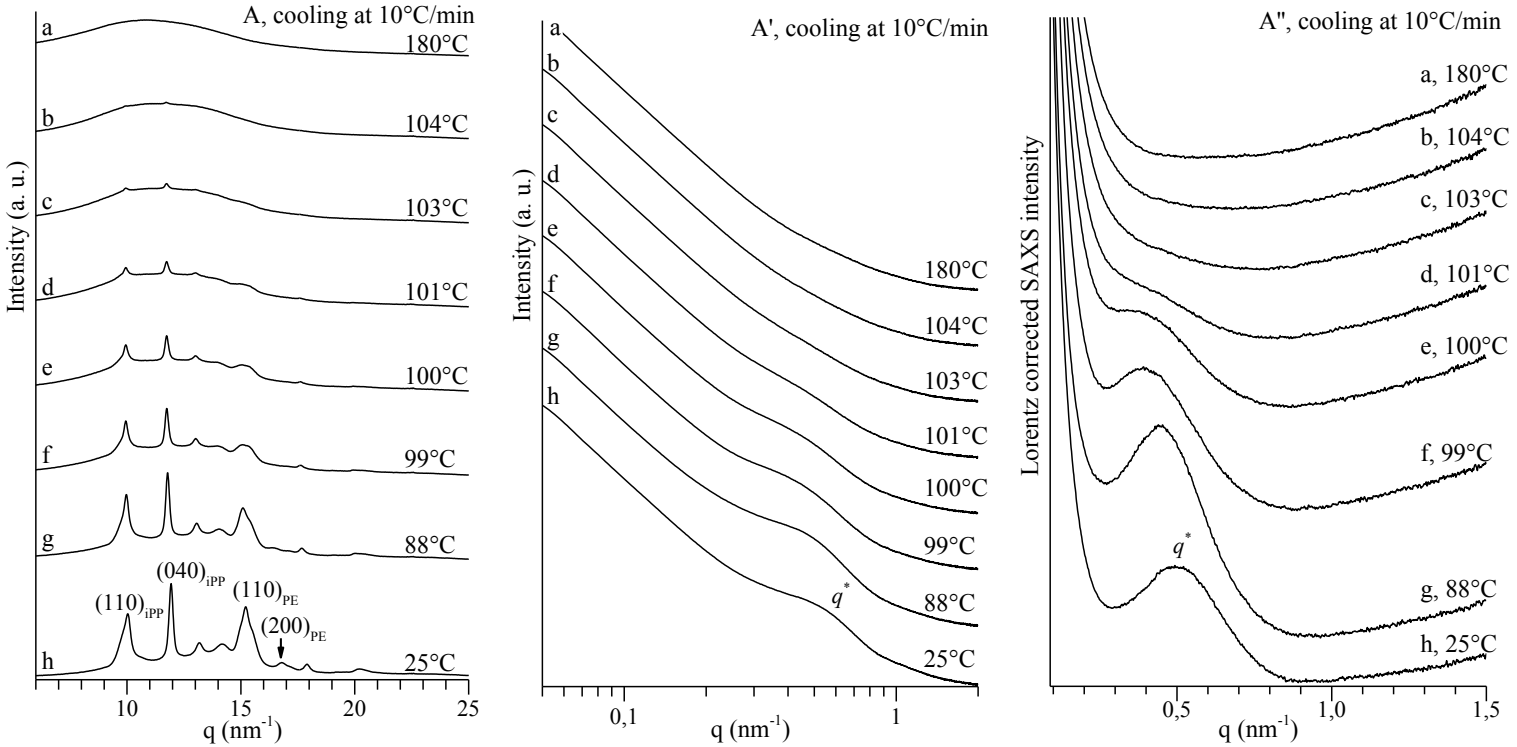
A, cooling at 10°C/min
a
180°C
b
104°C
c
103°C
d
101°C
e
100°C
f
99°C
g
88°C
h
25°C
(110)iPP
(040)iPP
(110)PE
(200)PE
Intensity (a. u.)
10
15
20
25
q (nm-1)
A', cooling at 10°C/min
a
b
c
d
e
f
g
h
180°C
104°C
103°C
101°C
100°C
99°C
88°C
25°C
q*
Intensity (a. u.)
0,1
1
q (nm-1)
A", cooling at 10°C/min
a, 180°C
b, 104°C
c, 103°C
d, 101°C
e, 100°C
f, 99°C
g, 88°C
h, 25°C
q*
Lorentz corrected SAXS intensity
0,5
1,0
1,5
q (nm-1)

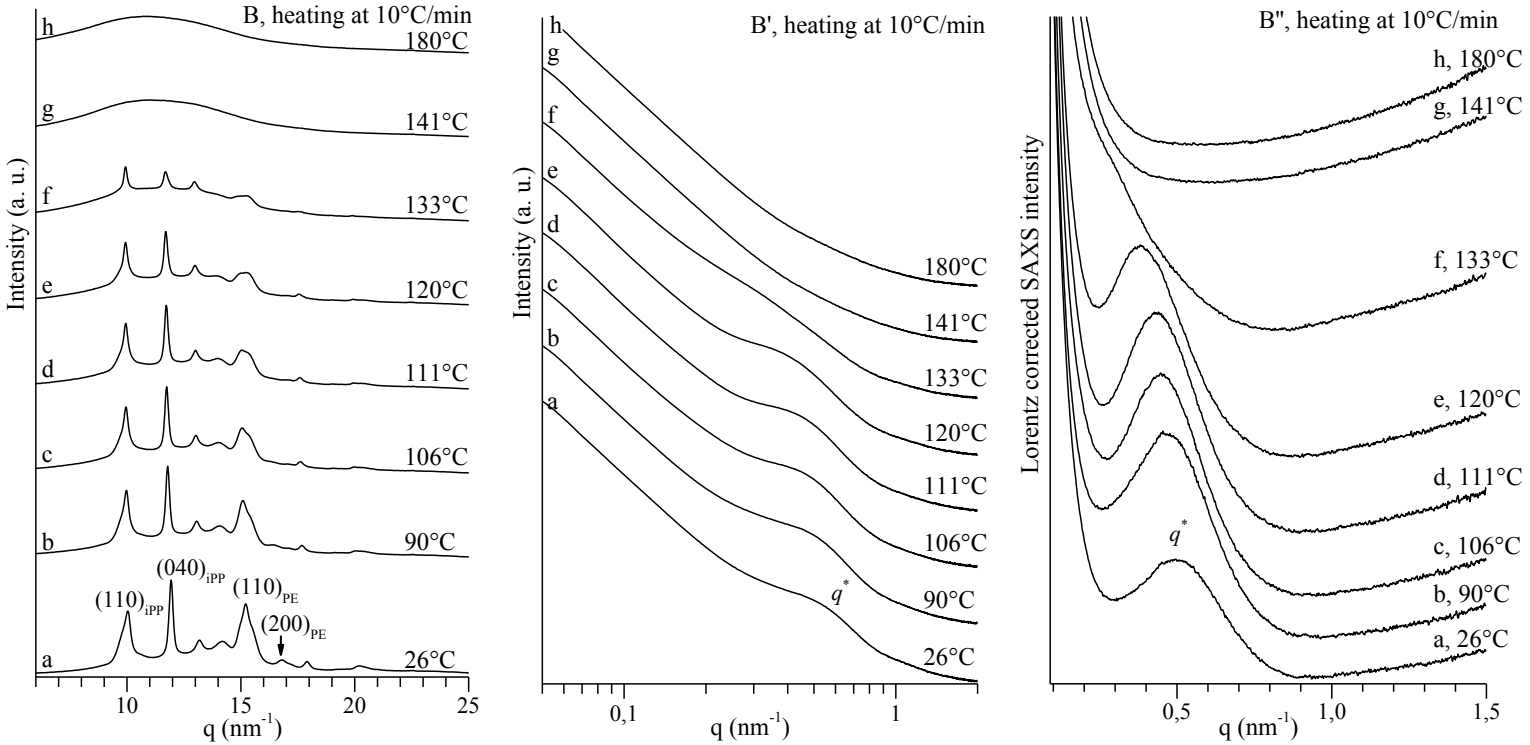

Figure 3.28. WAXS (A, B) and SAXS (A', B') profiles of the sample JME-V-54 with w_{iPP} = 77 wt% recorded during cooling (A, A') and heating (B, B') scan at 10°C/min at the indicated temperatures. The SAXS profiles after correction for the Lorentz factor are also reported (A'' and B'').

Also in the case of the sample JME-IV-133, with weigh fraction of iPP of 48 wt% and concentration of 1-octene of 0.9 mol%, the iPP block start to crystallize at higher temperatures than the LLDPE block, according with the presence of iPP reflections and absence of those of LLDPE in the WAXS profiles recorded, by cooling from the melt, at 102°C and 100°C (curves b and c of Figure 3.29A). However, crystallinity of the polyethylene phase is detected already at 98°C (curve d of Figure 3.29A) indicating that the two blocks crystallize almost simultaneously. These data are in agreement with the presence of only one exothermic peak at 98°C in the DSC cooling curve of sample JME-IV-133, recorded at the same scanning rate (curve c of Figure 3.27B).

Similar results are obtained from the SAXS profiles of Figure 3.29A' and in the corresponding Lorentz-corrected SAXS profiles of Figure 3.29A'', which show absence of any signal at 180°C (curve a of Figure 3.29A') and the appearance of a broad correlation peak centered at $q^* \approx 0.36$ nm^{-1} only at 98°C (curve d of Figure 3.29A', A''). It is worth noting that, at this temperature the PE crystallinity is very low, as revealed in the corresponding WAXS pattern (curve d of Figure 3.29A). When the crystallinity of the LLDPE block is significantly improved at 71°C (curve g of Figure 3.29A), an increase of the SAXS intensity at $q^* \approx 0.30$ nm^{-1} (curve g of Figure 3.29A'') is observed. It seems reasonable to connect this intensity increase to the formation of polyethylene lamellar stacks with lamellar periodicity slightly lower than those of the iPP crystals.

The SAXS profile recorded at room temperature, when the two blocks are fully crystallized, show the presence of a broad peak corresponding to the overlapping of LLDPE and iPP lamellar stacks.

The WAXS profiles recorded during heating at 10 °C/min of the melt-crystallized sample show that, the LLDPE block is completely melted at 117°C (curve d of Figure 3.29B), whereas crystallinity of the iPP block is

still present up to 135°C (curve f of Figure 3.29B), confirming the DSC data of the second heating scan (curve c of Figure 3.27C) which presents two well separated melting peaks at 113°C and 135°C.

The correlation peak observed in the SAXS profiles recorded at 25 °C (curve a of Figure 3.29B',B''), becomes sharper when the LLDPE block is melted at 117°C (curve d of Figure 3.29B'') indicating the presence of only crystalline lamellar stacks of iPP block. At temperature higher than 120°C absence of any SAXS intensity is observed (curves f-h of Figure 3.29B',B'').

WAXS and SAXS profiles of the samples JME-IV-148 and JME-IV-149 with 45 and 47 wt% of iPP respectively, recorded during cooling and heating scans at 10 °C/min, are reported in Figure 3.30 and 3.31, respectively. For these iPP-LLDPE block copolymers, characterized by lengths of the two blocks similar to the sample JME-IV-133 but with higher 1-octene content, similar results to those discussed for the sample JME-IV-133 were obtained. Nevertheless, the crystallization behavior of these two samples is slightly different. In fact, for these two block copolymers, the crystallization of the two blocks occurs at different temperatures. In particular, for the sample JME-IV-148 with 1.5 % of 1-octene, crystallinity of the polyethylene phase is detected at nearly 94 °C (Figure 3.30A), whereas for the sample JME-IV-149, with 1.9 % of 1-octene, the iPP block crystallizes almost completely in the range of temperatures between 105 and 92 °C and only at lower temperatures the crystallization of the LLDPE block starts (Figure 3.31A).

Therefore, in the iPP-*b*-LLDPE copolymers, with similar block lengths, the crystallizations of the LLDPE block is slower than the iPP block, and becomes increasingly slower with increasing of 1-octene content. Indeed, in the samples JME-IV-133 with 0.9 % of 1-octene the two block crystallize almost simultaneously, instead in the samples with the highest

1-octente content (1.9%) the crystallization of the two blocks occurs separately. Moreover, it is important to note that the crystallization of the polypropylene phase occurs always at ≈ 100°C regarding the concentration of comonomer (1-octene) in the polyethylene phase.

These data are in agreement with the values of the crystallization temperatures evaluated from the DSC cooling scans of Figure 3.27B, and suggest, that the presence of the comonomer (1-octene) influences the crystallization of the polyethylene phase but does not affect the crystallization of the polypropylene phase.

The structural analysis performed during heating of the melt-crystallized samples JME-IV-148 and JME-IV-149 confirm that the iPP block melts at temperatures higher than 130°C, whereas the LLDPE block melts at temperatures least 20 °C lower (Figures 3.30B and 3.31B). So, the melting of the two blocks covalently linked take place like independent phenomena, as also indicate by the presence of two endothermic peaks in the corresponding DSC curves of the second heating scans (curves d and e of Figure 3.27C). Moreover, the presence of the comonomer does not disturb the melting of the iPP domain, which melts always at the same temperature in all block copolymers. On the contrary, the LLDPE domain in the sample JME-IV-133 (with [1-octene] = 0.9 mol%) melts at temperatures higher than that of the LLDPE block in the sample JME-IV-148 (with [1-octene] = 1.5 mol%) which in turn melts at temperatures higher than that in the sample JME-IV-149 (with [1-octene] = 1.9 mol%) (Figures 3.29B-3.31B). SAXS experiments performed during cooling and heating of the samples JME-IV-148 and JME-IV-149 have indicated similar results to those discuss for the sample JME-IV-133.

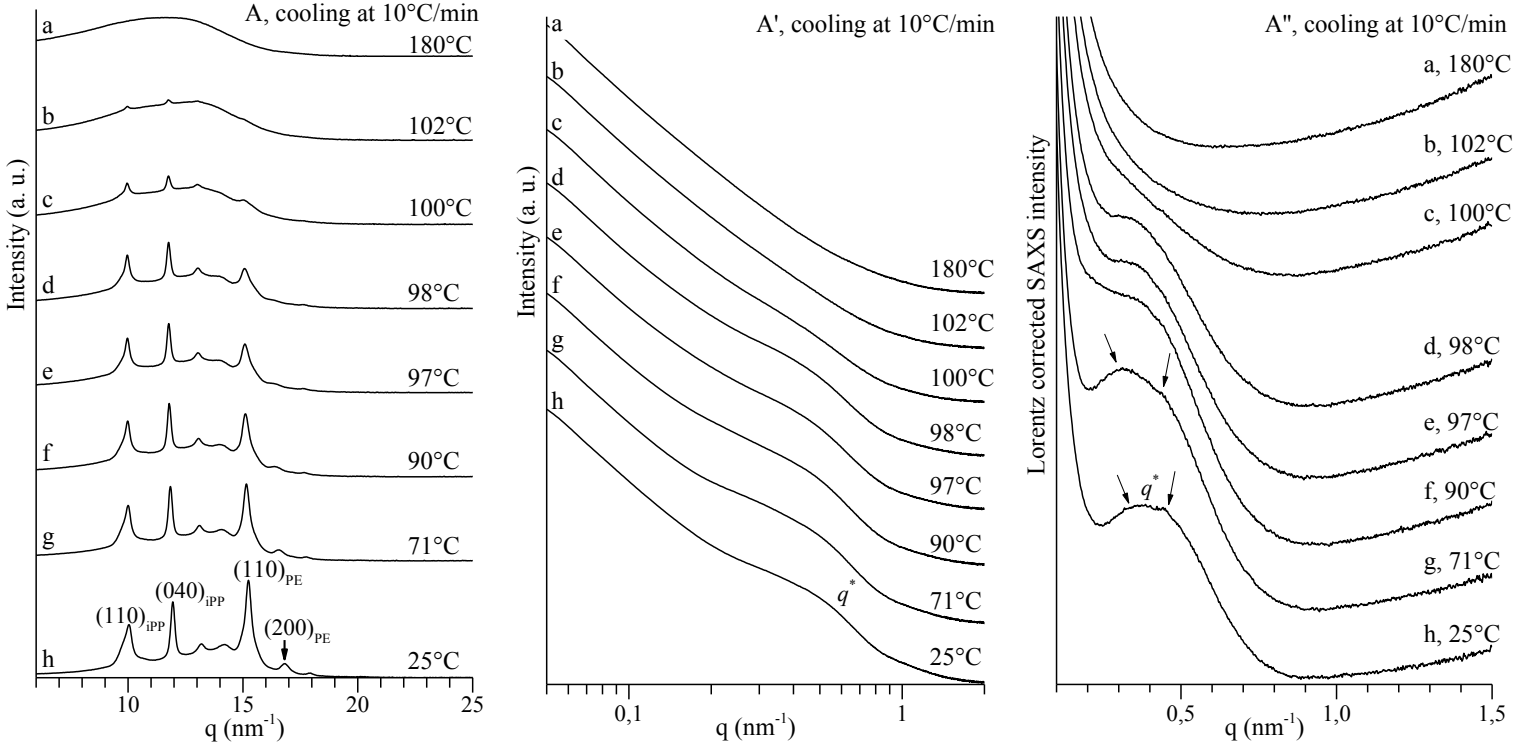
A, cooling at 10°C/min
a
180°C
b
102°C
c
100°C
d
98°C
e
97°C
f
90°C
g
71°C
h
25°C
(110)iPP
(040)iPP
(110)PE
(200)PE
Intensity (a. u.)
q (nm-1)
A', cooling at 10°C/min
q*
A", cooling at 10°C/min
a, 180°C
b, 102°C
c, 100°C
d, 98°C
e, 97°C
f, 90°C
g, 71°C
h, 25°C
Lorentz corrected SAXS intensity

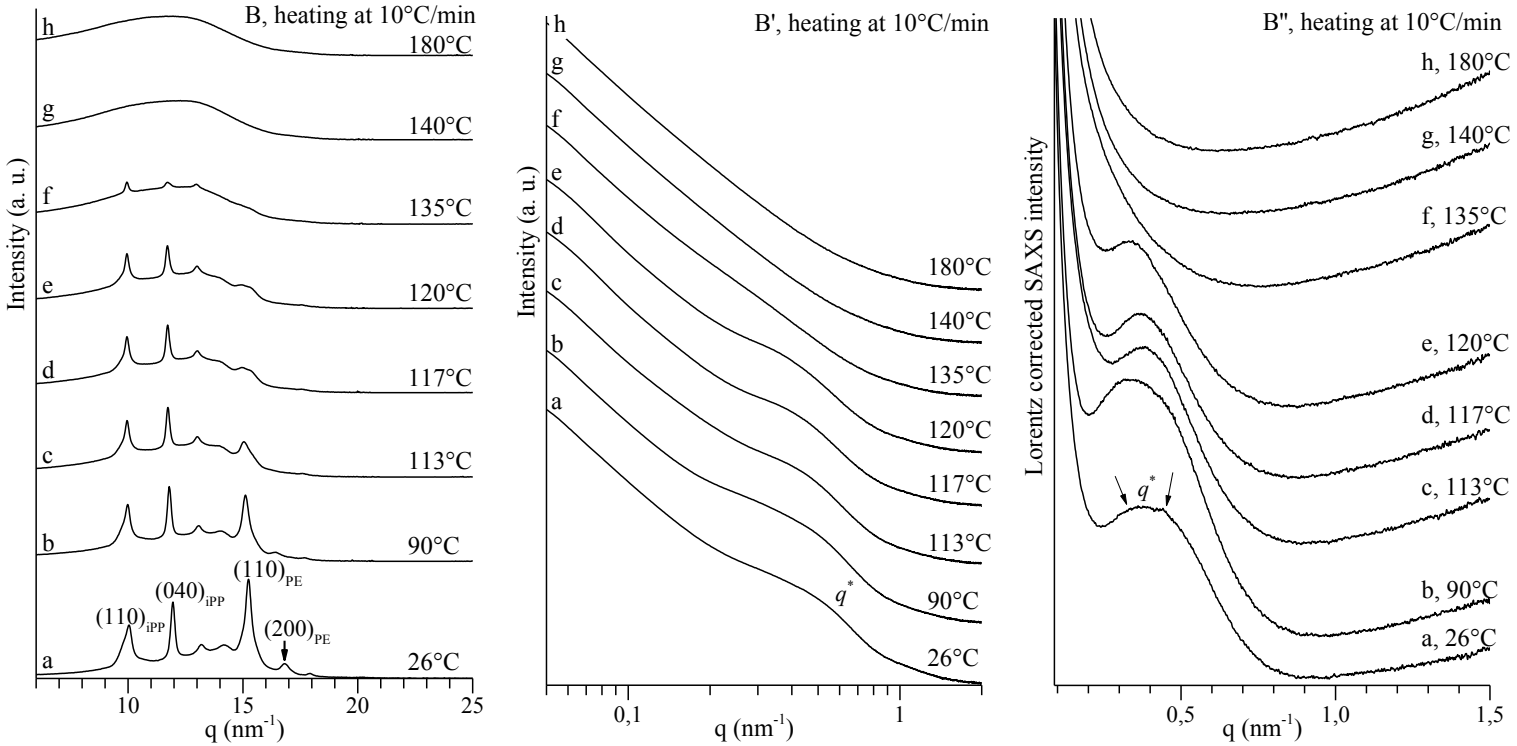

Figure 3.29. WAXS (A, B) and SAXS (A', B') profiles of the sample JME-IV-133 with 48 wt% of iPP recorded during cooling (A, A') and heating (B, B') scan at 10°C/min at the indicated temperatures. The SAXS profiles after correction for the Lorentz factor are also reported (A'' and B'')

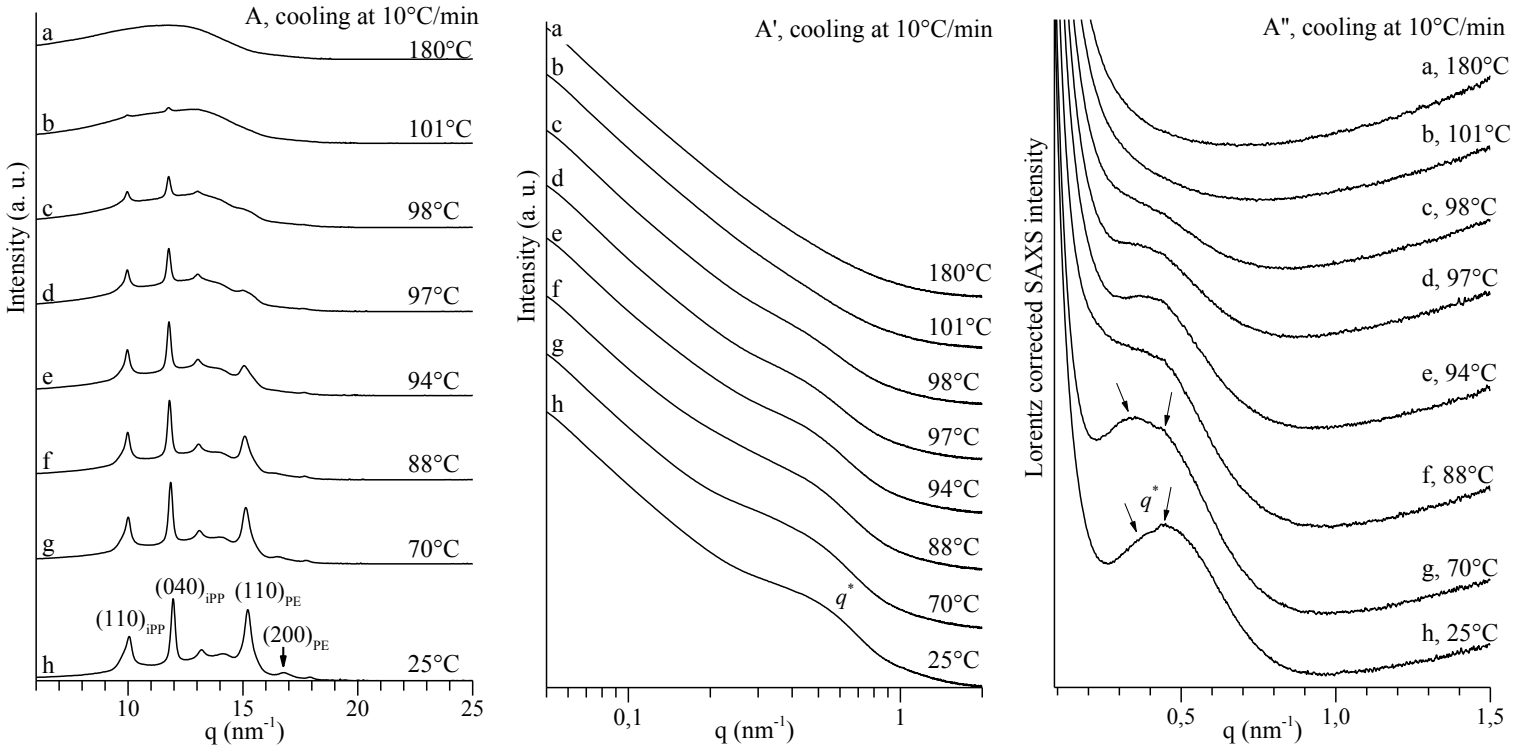
A, cooling at 10°C/min
a
180°C
b
101°C
c
98°C
d
97°C
e
94°C
f
88°C
g
70°C
h
25°C
(110)iPP
(040)iPP
(110)PE
(200)PE
Intensity (a. u.)
10
15
20
25
q (nm-1)
A', cooling at 10°C/min
a
b
c
d
e
f
g
h
180°C
101°C
98°C
97°C
94°C
88°C
70°C
25°C
q*
Intensity (a. u.)
0,1
1
q (nm-1)
A", cooling at 10°C/min
a, 180°C
b, 101°C
c, 98°C
d, 97°C
e, 94°C
f, 88°C
g, 70°C
h, 25°C
q*
Lorentz corrected SAXS intensity
0,5
1,0
1,5
q (nm-1)

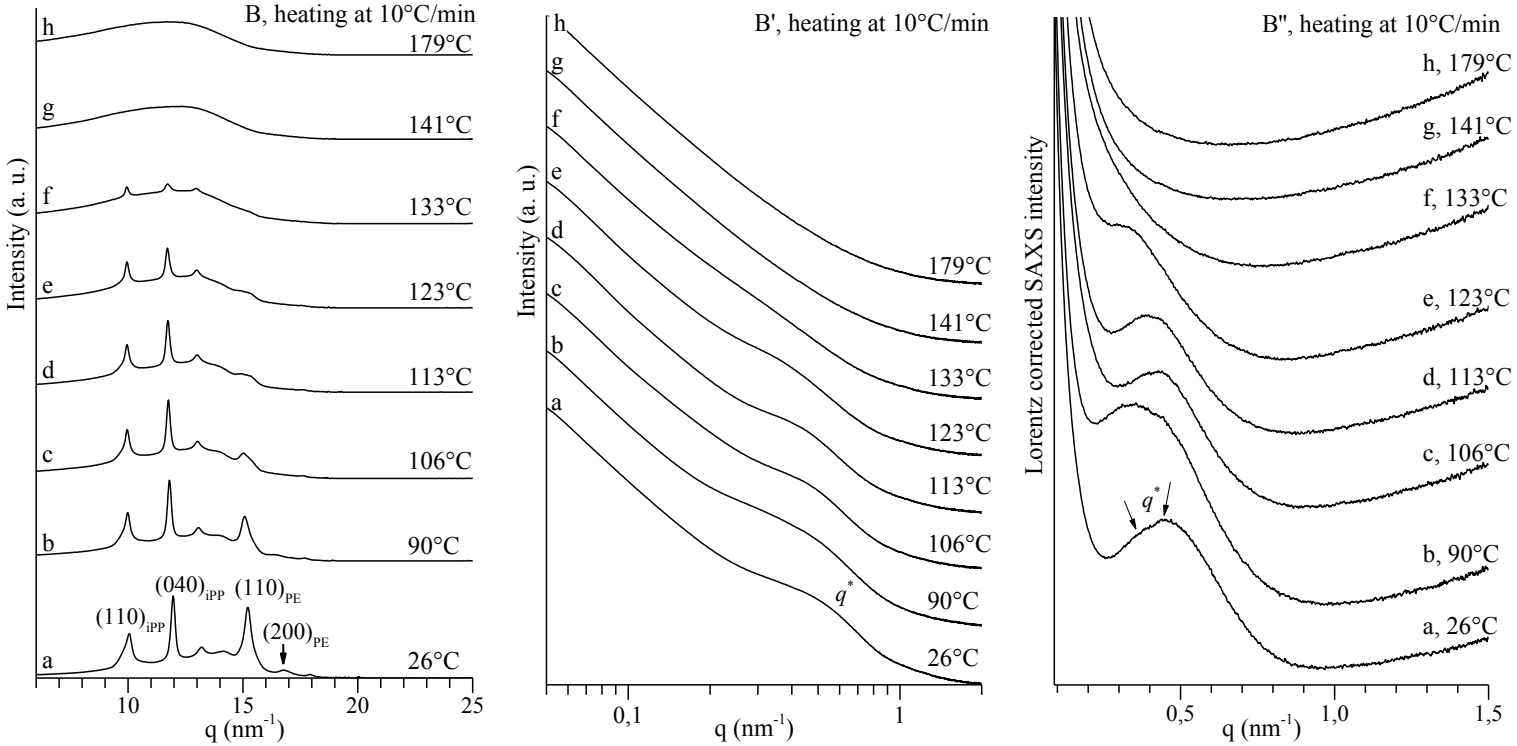

Figure 3.30. WAXS (A, B) and SAXS (A', B') profiles of the sample JME-IV-148 with 45 wt% of iPP recorded during cooling (A, A') and heating (B, B') scan at 10°C/min at the indicated temperatures. The SAXS profiles after correction for the Lorentz factor are also reported (A'' and B'').

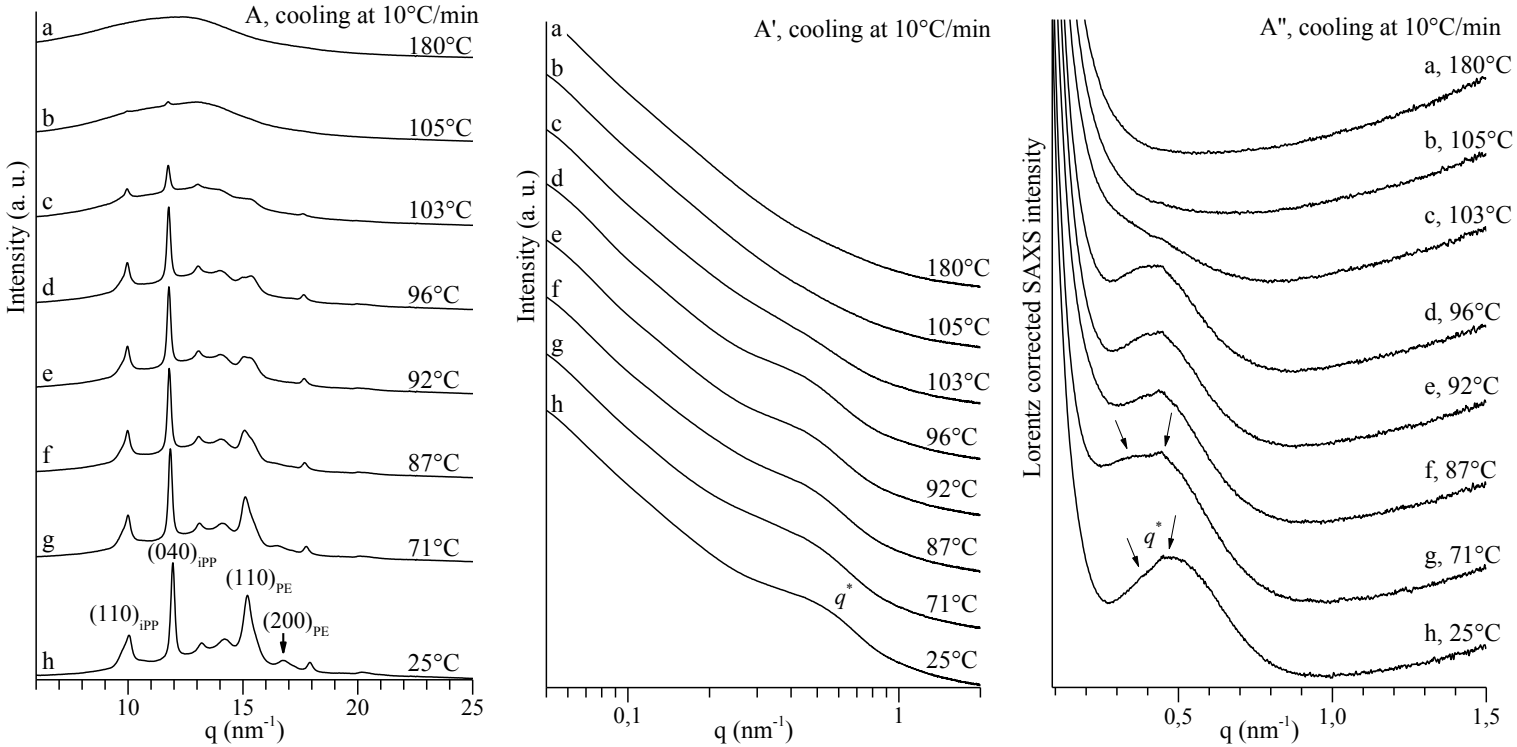
A, cooling at 10°C/min
a
180°C
b
105°C
c
103°C
d
96°C
e
92°C
f
87°C
g
71°C
h
25°C
(040)iPP
(110)PE
(110)iPP
(200)PE
Intensity (a. u.)
10
15
20
25
q (nm-1)
A', cooling at 10°C/min
a
b
c
d
e
f
g
h
180°C
105°C
103°C
96°C
92°C
87°C
71°C
25°C
q*
Intensity (a. u.)
0,1
1
q (nm-1)
A", cooling at 10°C/min
a, 180°C
b, 105°C
c, 103°C
d, 96°C
e, 92°C
f, 87°C
g, 71°C
h, 25°C
q*
Lorentz corrected SAXS intensity
0,5
1,0
1,5
q (nm-1)

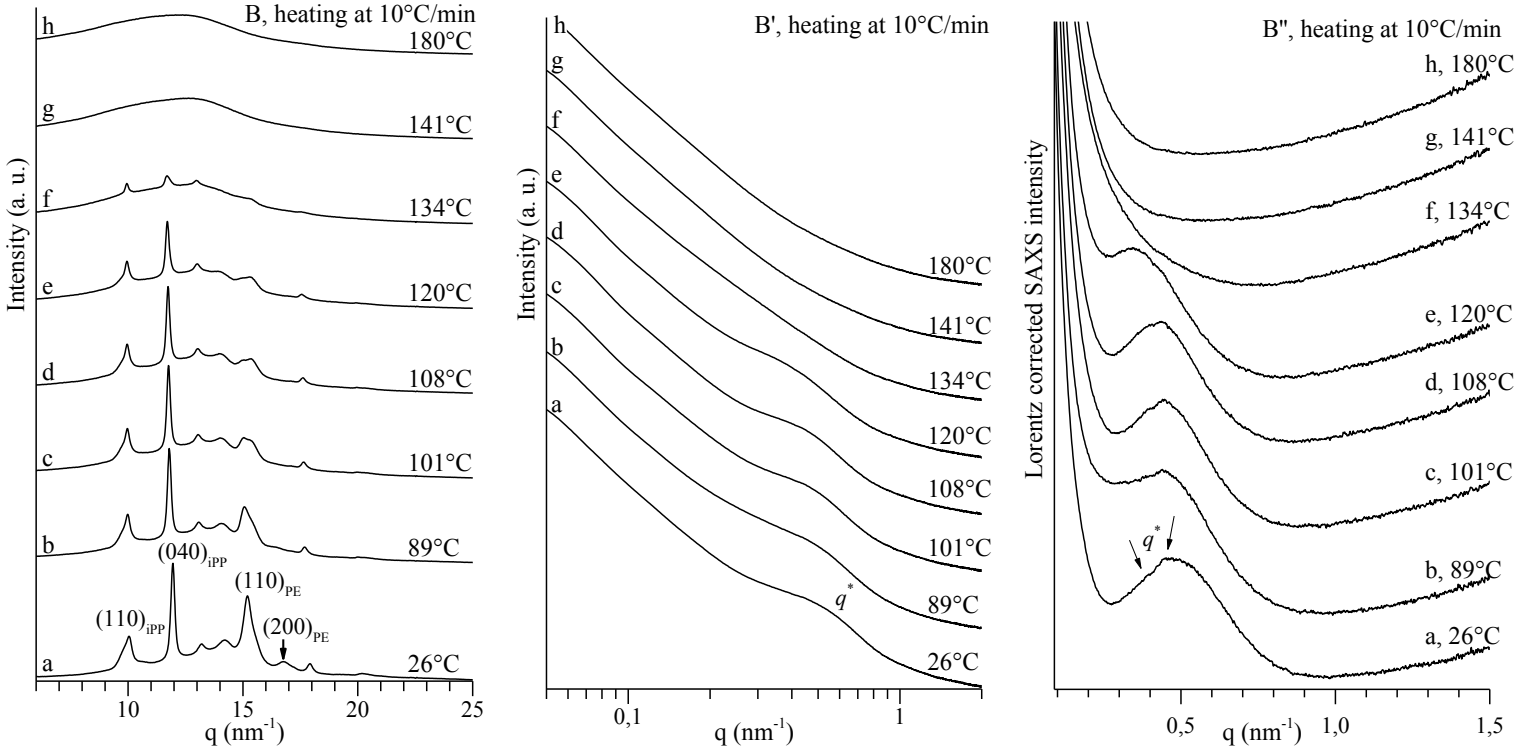

Figure 3.31. WAXS (A, B) and SAXS (A', B') profiles of the sample JME-IV-149 with 47 wt% of iPP recorded during cooling (A, A') and heating (B, B') scan at 10°C/min at the indicated temperatures. The SAXS profiles after correction for the Lorentz factor are also reported (A'' and B'').

A comparison between the Lorentz-corrected SAXS profiles recorded at 25°C of the iPP-LLDPE block copolymers and of iPP homopolymer, crystallized by cooling from the melt, is reported in Figure 3.32. The values of q^*, and the corresponding lamellar periodicities L_{SAXS} are listed in Table 3.9. For all iPP-*b*-LLDPE copolymers a broad correlation peak is present, suggesting that the correlation peaks of the two crystalline phases are overlapped and, consequently, a similar lamellar periodicity of the iPP and LLDPE domains.

In particular, the sample JME-V-54, with the longest iPP block, show the highest q^* value compared to the other BCPs samples and similar to the corresponding iPP homopolymer.

In the case of the copolymers JME-IV-133, JME-IV-148 and JME-IV-149 with similar length of the two blocks, a different shape of the correlation peak compared to that of the iPP homopolymer and of the sample JME-V-54, is observed. In fact, it has been observed the presence of a broad correlation peak with a shoulder at lower q^* value, due to crystalline lamellar stacks of the LLDPE block. This feature is more evident in the SAXS profiles of the sample JME-IV-133, with the lowest concentration of 1-octene (0.9%) (curve c of Figure 3.32), consistent with an increase of the periodicity L_{SAXS} of crystalline LLDPE domains with increasing 1-octene content. The values of q^* and of the periodicity of the two crystalline phase roughly evaluated from the peaks and shoulders in the SAXS profiles of the samples (profiles c-e of Figure 3.32) are reported in Table 3.9.

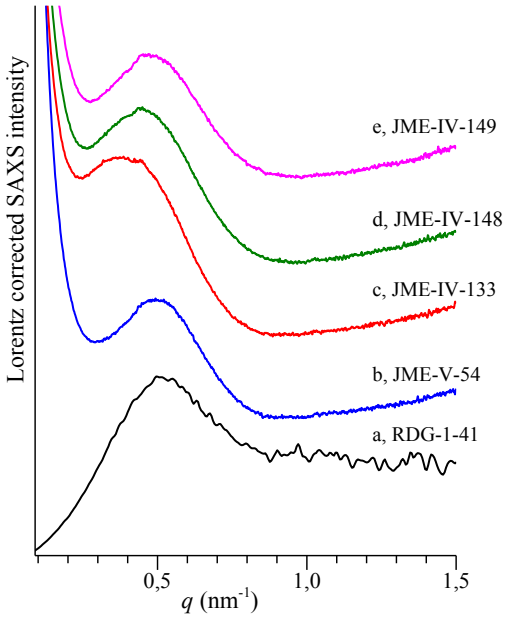

Figure 3.32. SAXS profiles after correction for the Lorentz factor recorded at 25 °C of melt-crystallized samples of iPP homopolymer (a), and of iPP-*b*-LLDPE block copolymers JME-V-54 (b), JME-IV-133 (c), JME-IV-148 (d) and JME-IV-149 (e).

Table 3.9. Code of iPP-*b*-LLDPE copolymers, weight fractions of the iPP (w_{iPP}), concentration of 1-octene ([1-octene]), position of the correlation peaks (q^*), and corresponding values of the lamellar periodicity (L_{SAXS}).

Code	w_{iPP} (wt%)	[1-octene] (mol%)	q^* (nm^{-1})	L_{SAXS} (nm)
RDG-1-41	100	—	0.54	12
JME-V-54	77	1.5	0.50	13
JME-IV-133	48	0.9	0.34,0.44	18,14
JME-IV-148	45	1.5	0.36,0.45	17,14
JME-IV-149	47	1.9	0.38,0.46	16,13

AS show in the section 3.3.2, SAXS experiments performed on samples of iPP-PE block copolymers have suggested the formation of a nanostructure, driven by crystallization, characterized by alternating crystalline PE and iPP layers, separated by amorphous regions that include the amorphous portions of chains belonging to the PE and iPP domains (Figure 3.14). In fact, in this case two correlation peaks are present in SAXS profiles recorded at 25°C of the samples crystallized by cooling from the melt

(Figure 3.13), from which two lamellar periodicities of ≈ 30 and 12 nm for crystalline PE and iPP layers, respectively, have been evaluated.

A similar nanostructure (Figure 3.14) may be proposed even in the case of iPP-LLDPE block copolymers. However, the presence of the comonomer (1-octene) in the polyethylene block, induces a decrease of the periodicity of PE lamellar stacks that becomes more similar to that of the iPP, and only one broad correlation peak (with shoulders), in the SAXS profiles of Figure 3.32 is observed.

3.4.3 Mechanical properties.

The stress strain curves of compression molded films of iPP-*b*-LLDPE copolymers are reported in Figure 3.33. The values of the mechanical parameters of the block copolymers and of the iPP homopolymer are shown in Table 3.10.

Samples of iPP-*b*-LLDPE with similar length of the two blocks (curves b-d of Figure 3.33) show similar good ductility with similar values of deformation at break around 1100−1200 %, regardless of the concentration of 1-octene. A slightly decrease of the Young's modulus (*E*) and of yield stress (σ_y) with increasing concentration of 1-octene (Table 3.10) is observed.

The sample JME-V-54, with the highest iPP block length and the same 1-octene content of the sample JME-IV-148 (1.5%), presents values of ductility, modulus, yield stress and of the tension set, measured after break, higher than those of the other BCPs (Table 3.10).

All samples of iPP-*b*-LLDPE show deformation with necking according with high values of crystallinity associated with strong strain hardening at high deformation (Figure 3.33) and high values of the tensile strength (Table 3.10).

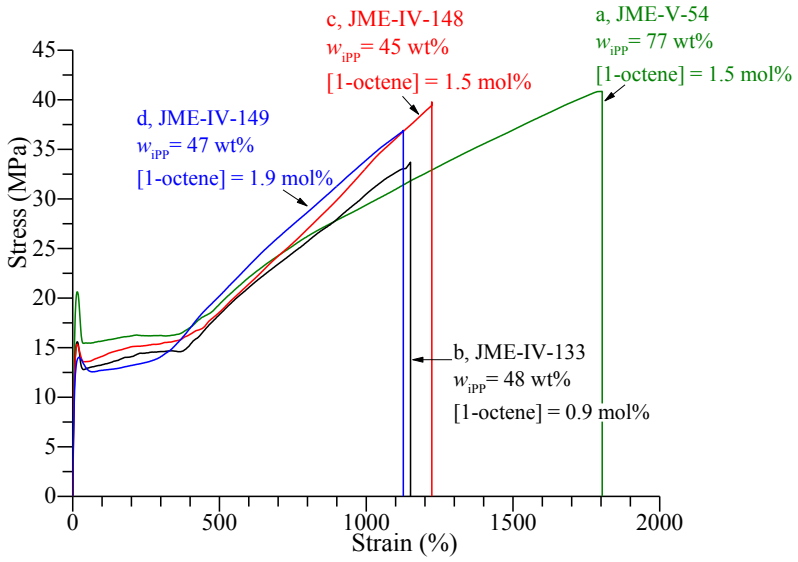

Figure 3.33. Stress-strain curves of the melt-crystallized compression molded films of iPP-*b*-LLDPE copolymers.

A comparison of the mechanical behaviors of iPP homopolymer and of the copolymers JME-V-54 and JME-IV-148, with similar concentration of 1-octene but different length of iPP block (77% and 45% respectively) is shown in Figure 3.34. The stress strain curve of the iPP-*b*-PE copolymer RDG-1-91, with weight fraction of iPP similar to the iPP-*b*-LLDPE copolymer JME-V-54, is also reported in Figure 3.34.

The data of Figures 3.34 and 3.33 indicate that the iPP-*b*-LLDPE copolymers show grater ductility than the corresponding iPP homopolymer due to the presence of LLDPE block ("soft segment") linked to the iPP block. Moreover, the block copolymer JME-V-54, with weight fraction of iPP of 77%, has value of the yield stress similar to the sample RDG-1-41 (iPP homopolymer) and higher than the sample JME-IV-48 (iPP-*b*-LLDPE copolymer) with the same 1-octene content but weight fraction of iPP of 45% (Figure 3.34 and Table 3.10).

Also in the case of the sample RDG-1-91, in which the iPP block is linked to the PE block ("hard segment"), an enhancement of the ductility of the iPP-*b*-PE copolymer (curve d of Figure 3.34) compared to the iPP homopolymer (curve d of Figure 3.34) is observed. However, the stress strain curves of Figure 3.34, reveal that lower values of deformation at break can be achieved for the sample RDG-1-91 compared to the iPP-*b*-LLDPE copolymer JME-V-54, with similar iPP block length.

These results demonstrated that different mechanical behavior may be obtained when the iPP is covalently linked to a "hard" or "soft" block. Furthermore, the mechanical properties of both iPP-PE and iPP-LLDPE BCPs, can be modulated varying the block lengths and the content of 1-octene in the case of the iPP-*b*-LLDPE.

The values of the tension set after breaking (t_b) and the high values of the percentage of the deformation which is recovered after breaking (R_b) indicate that the samples of iPP-*b*-LLDPE show a partial elastic behavior. Compared to the copolymer iPP-*b*-PE, an improvement of the elastic properties is observed for the samples iPP-*b*-LLDPE.

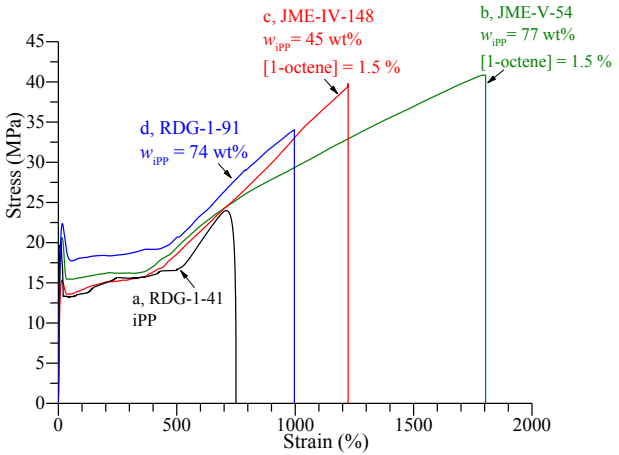

Figure 3.34. Stress-strain curves of the melt-crystallized compression molded films of iPP homopolymer (a), and of iPP-*b*-LLDPE copolymers JME-V-54 (b) and JME-IV-148 (c) and of iPP-*b*-PE copolymer RDG-1-91 (d).

Table 3.10. Code of iPP homopolymer and iPP-*b*-LLDPE copolymers, weight fractions of the iPP block (w_{iPP}), concentration of 1-octene ([1-octene]), Young's modulus (E), stress (σ_y) and strain (ε_y) at the yield point, stress (σ_b) and strain (ε_b) at break, tension set at break (t_b), percentage of deformation recovered after breaking (R_b) and X-ray crystallinity (x_c) of melt-crystallized compression molded films of iPP-*b*-LLDPE copolymers.

Code	w_{iPP} (wt%)	[1-octene] (mol%)	E (MPa)	σ_y (MPa)	ε_y (%)	σ_b (MPa)	ε_b (%)	t_b (%)	R_b (%)	x_c (%)
RDG-1-41	100	—	420	20	10	25	750			49
JME-V-54	77	1.5	300	21	16	41	1804	504	72	51
JME-IV-133	48	0.9	270	16	16	34	1151	380	65	58
JME-IV-148	45	1.5	230	15	16	40	1223	344	72	56
JME-IV-149	47	1.9	230	14	21	37	1126	380	64	57

3.4.4 Oriented Fibers.

A study of the stress induced phase transition of the iPP-LLDPE block copolymers has been performed to compare the structural transformations of iPP block, when is linked to the LLDPE or PE block in the iPP-*b*-LLDPE and iPP-*b*-PE copolymers respectively, and also with those of the corresponding iPP homopolymer.

The X-ray fiber diffraction patterns of the iPP-*b*-LLDPE samples obtained by stretching at room-temperature compression molded films at different values of strain ε are reported in Figures 3.35-3.38

As already discussed, the iPP block in the copolymers, crystallizes slowly from the melt in a disordered modification of α and γ forms as indicate by the presence of both $(130)_\alpha$ and $(117)_\gamma$ reflections at $2\theta = 18.6$ and 20.0° of α and γ form respectively, in the X-ray fiber diffraction patterns of the unoriented samples of Figures 3.35 A, 3.36 A, 3.37 A and 3.38 A. The $(110)_{PE}$ and $(200)_{PE}$ reflections at $2\theta = 21.4°$ and 23.9°, respectively, of the orthorhombic form of PE are also present in the diffraction patterns of the unstretched samples (Figures 3.35 A,A', 3.36 A,A', 3.37 A,A' and 3.38 A,A'), indicating that both iPP and LLDPE blocks are crystalline.

During stretching of the compression molded films similar transformations of iPP and LLDPE blocks are observed in all copolymers, regarding the block lengths and the concentration of 1-octene. In particular, the diffraction patterns of the sample JME-V-54 stretched at ε = 100% (Figure 3.35B) show a polarization of the $(110)_\alpha$ $(040)_\alpha$ $(130)_\alpha$ reflections of α-form and of the $(111)_\gamma$ $(008)_\gamma$ and $(117)_\gamma$ reflection of γ-form of iPP on the equator, indicating the presence of crystals with chain axes oriented parallel to the stretching direction. However, the $(040)_\alpha$ reflection of the α–form and the $(008)_\gamma$ reflection of the γ–form, both at $2\theta \approx 17°$, are also polarized in a nearly meridional position indicating the formation of the cross-β structures [23, 24], that is, crystals of iPP in α/γ disordered modifications,

close to the γ form, assume an orientation with the chain axes nearly perpendicular to the stretching direction. Therefore, crystals of disordered modifications more similar to the γ form and of disordered modifications closer to the α form are obtained at this value of deformation (ε = 100%). Because in the crystals close to the α form, the fraction of consecutive bilayers with parallel chains is prevalent over that of crystals with perpendicular chains, these crystals assume more easily the parallel chain axis orientation, whereas the crystals that assume the cross-*β* orientation are probably those characterized by structural features closer to the γ form. At 200% of deformation (Figure 3.35C), the decrease of the intensity of the meridional reflection at 2θ = 17° suggest an increase of iPP crystalline lamellae oriented with the chain axes parallel to the fiber axes.

The degree of orientation of crystals increases with increasing deformation, and a broad halo on the equator at 2θ ≈ 15° replaces the $(110)_{\alpha}$ and $(040)_{\alpha}$ reflections of the α-form in the diffraction patterns of the sample JME-V-54 recorded at values of the strain in the range 400-600% (Figures 3.35D,D' and 3.35E,E'). This correspond to the formation of iPP crystalline aggregates in mesomorphic form. [35]

Concerning the LLDPE block a slightly polarization of the $(110)_{PE}$ and $(200)_{PE}$ reflections of the orthorhombic form on the equator, is obtained by stretching the compression molded film at ε = 100% (Figure 3.35B). At higher value of the deformation a progressive decrease of the intensity of the $(200)_{PE}$ reflection and a simultaneously broadening of the $(110)_{PE}$ reflection is observed (Figure 3.35C-E). In the fiber diffraction patterns of the sample stretched at 600% (Figure 3.35E,E') the $(200)_{PE}$ reflection of the orthorhombic form of PE is almost absent and partially overlapped with the broad $(110)_{PE}$ reflection. Probably, at high deformation some crystals transform in the hexagonal form of PE, which is characterized by a single

$(100)_{PE}$ at 2θ = 20.04° [36], according to the broadening and the slight shift at lower 2θ value of the $(110)_{PE}$ reflection.

The hexagonal form of PE was already observed in random copolymers of ethylene and propylene (EP), with ethylene content between 80 and 40 mol% [24, 36]. In EP copolymers, propylene units are included in the crystalline lattice of the orthorhombic form of PE (lattice parameters a = 7.42 Å, b = 4.95 Å and c (chain axis) = 2.54 Å [24, 37]), inducing large disordered and decrease of degree of crystallinity. Therefore, these materials are amorphous at room temperature but are able to crystallize by stretching at room temperatures in a pseudo-hexagonal form, which is characterized by chains in trans-planar conformation packed in a unit cell with *b* and *c* axes similar to the orthorhombic form of PE but *a* axis nearly equal to $b\sqrt{3}$ [24, 37]. However, the broadening of the $(110)_{PE}$ reflection and the absence of the $(200)_{PE}$ reflection could be also due to the presence of small fibrillar crystals formed upon stretching by fragmentation of the starting lamellae.

Similar structural transformations of the iPP and LLDPE blocks occur by stretching of the others iPP-*b*-LLDPE samples characterized by similar block lengths. However, some differences have been observed in the behavior of the LLDPE block. The X-ray fiber diffraction profiles of the samples JME-IV-133, JME-IV-148 and JME-IV-149 stretched at values of the strain in the range 100-200% of Figures 3.36B-C 3.37B-C and 3.38B-C show an increase of the intensity in a region of 2θ between 18-20°, which becomes more evident with increasing 1-octene content in the polyethylene phase. This can be explained with the appearance of the $(001)_{PE}$ reflection of the monoclinic form of PE.[38] This indicates that at low deformation the orthorhombic form transforms in part in the monoclinic form of PE.[38] Frank, Keller and O'Connor had noticed for the first time the appearance of a strong reflection with *d* = 4.59 Å in rolled or pressed specimens of

polyethylene, which could not be indexed on the basis of the orthorhombic unit cell [39]. They suggest the possibility of a martensitic phase transformation by stress [38, 39]. Seto, Hara and Tanaka reproducing the same experiment of Frank. et al., were able to index this reflection at 2θ = 19.51° as $(001)_{PE}$ reflection on the base of a monoclinic unit cell with axes a = 8.09 Å, b = 2.53 Å, c = 4.79 Å and β = 107.9°, where the unique axis b is parallel to the molecular axis. In this unit cell, the chains assume the same trans-planar conformation as in the orthorhombic form. However, the skeletal planes of the molecules in the monoclinic form are arranged parallel to each other with an angle ϕ of the skeletal plane of the molecules against the a-axis of 90°, while in the orthorhombic form the skeletal planes of molecules at the center and corner of the unit cell are nearly perpendicular to each [38].

Hence, we suggest that during stretching of the iPP-*b*-LLDPE at low values of deformation, between 100-200%, the orthorhombic and monoclinic forms of polyethylene coexist, though the monoclinic structure is unstable [38] and gradually transform into orthorhombic form at higher values of the strain. In fact, this structural phase transition of the orthorhombic form to monoclinic form is reversible, as already demonstrated in samples of high density polyethylene [38].

At high draw ratios (600%), the presence of some PE crystals in hexagonal structures cannot be excluded.

iPP-*b*-LLDPE JME-V-54 with w_{iPP} = 77 wt% and [1-octene] = 1.5%

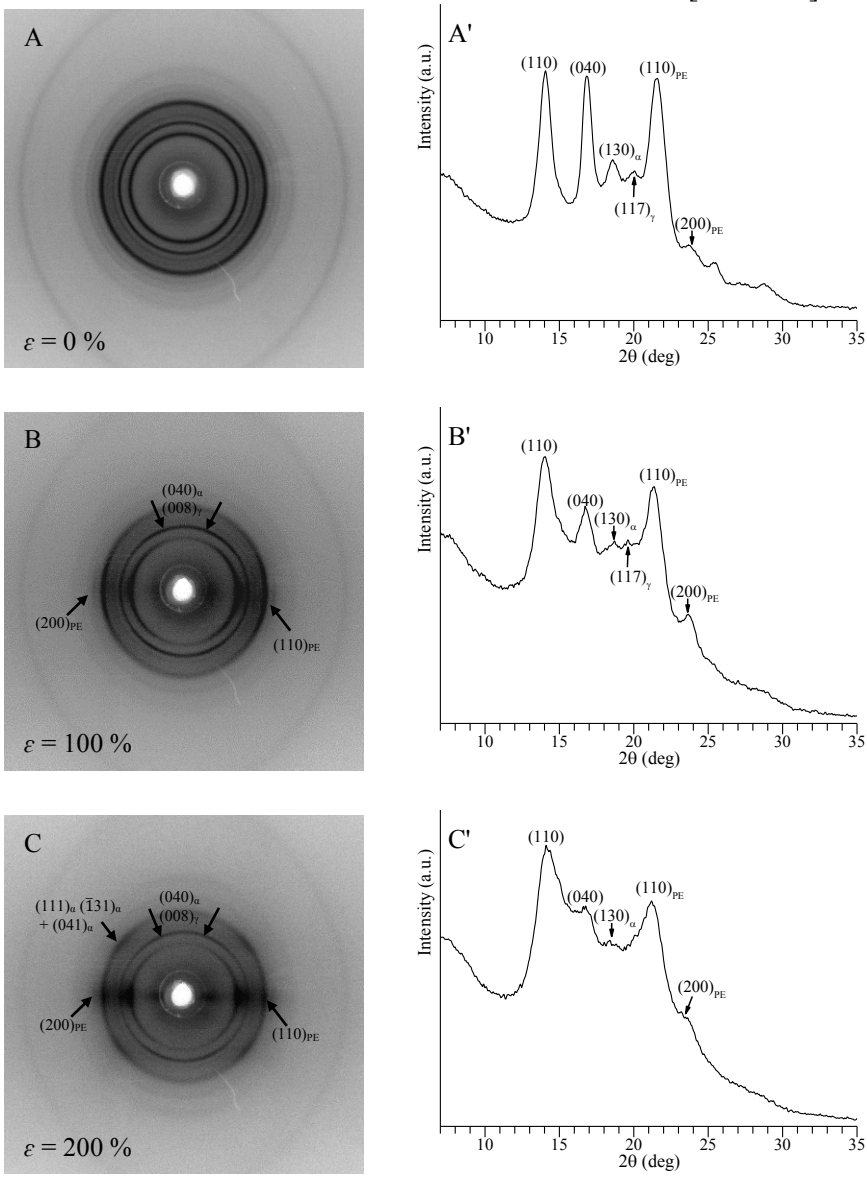

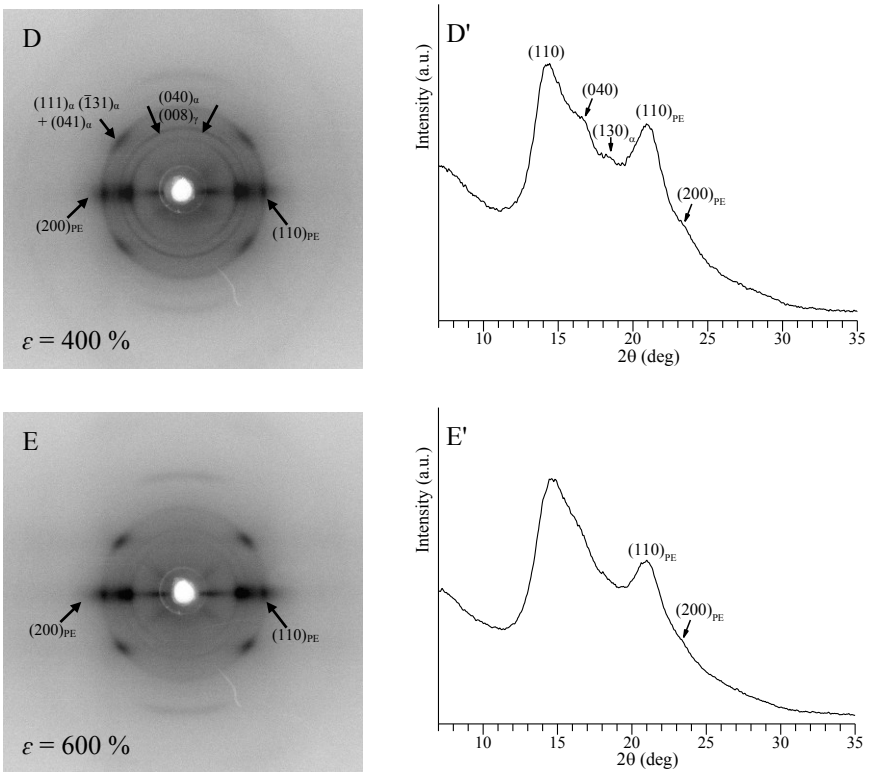

Figure 3.35. X-ray fiber diffraction patterns (A-E), and corresponding equatorial profiles (A'- E'), of the sample JME-V-54 unoriented (A) and of oriented fibers obtained by stretching at room-temperature compression molded films at values of strain ε of 100% (B), 200% (C) , 400% (D) and 600% (E).

iPP-*b*-LLDPE JME-IV-133 with w_{iPP} = 48 wt% and [1-octene] = 0.9%

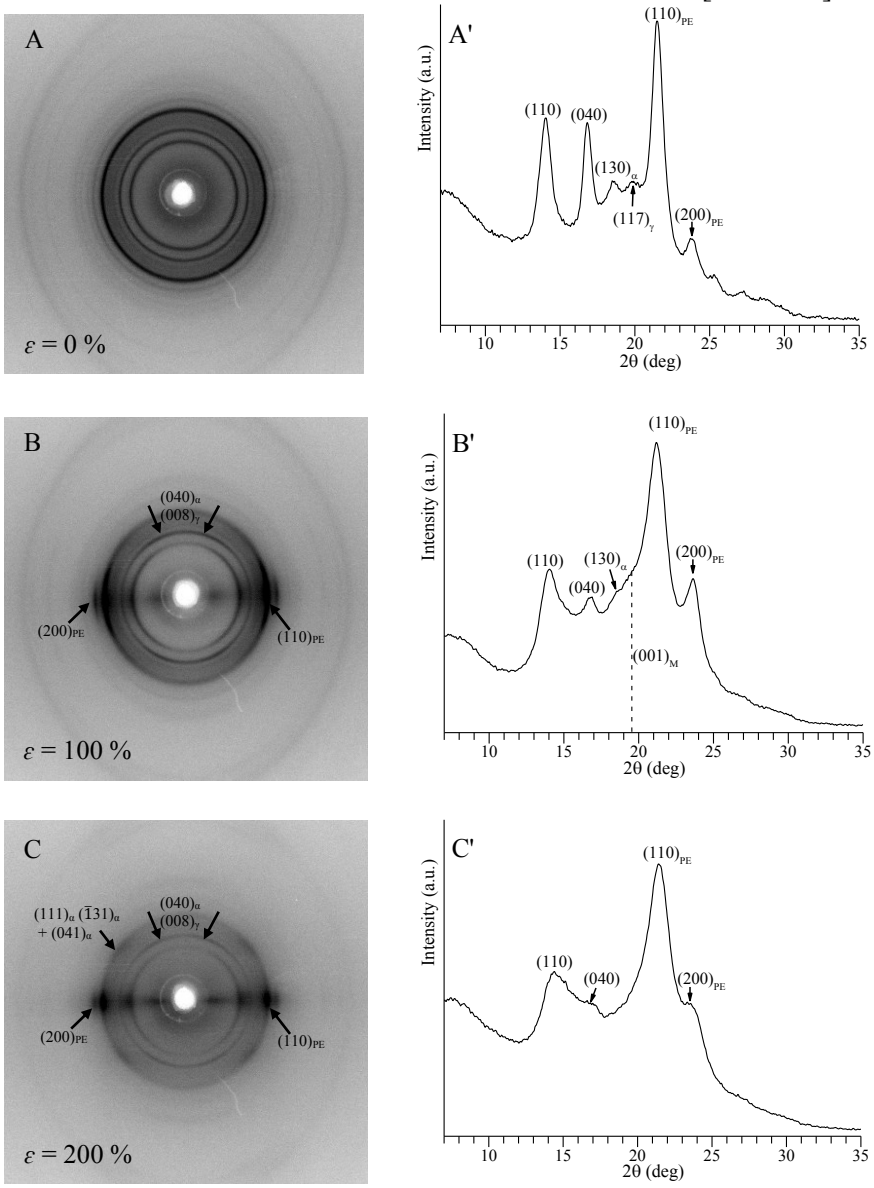

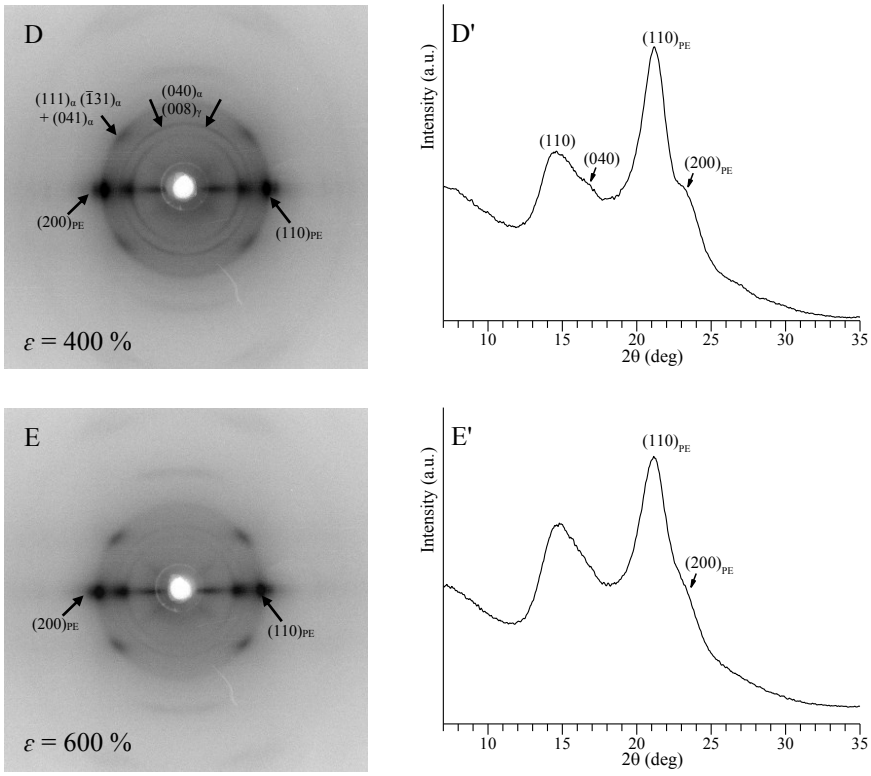

Figure 3.36. X-ray fiber diffraction patterns (A-E), and corresponding equatorial profiles (A'- E'), of the sample JME-V-133 unoriented (A) and of oriented fibers obtained by stretching at room-temperature compression molded films at values of strain ε of 100% (B), 200% (C) , 400% (D) and 600% (E).

iPP-*b*-LLDPE JME-IV-148 with w_{iPP} = 45 wt% and [1-octene] = 1.5%

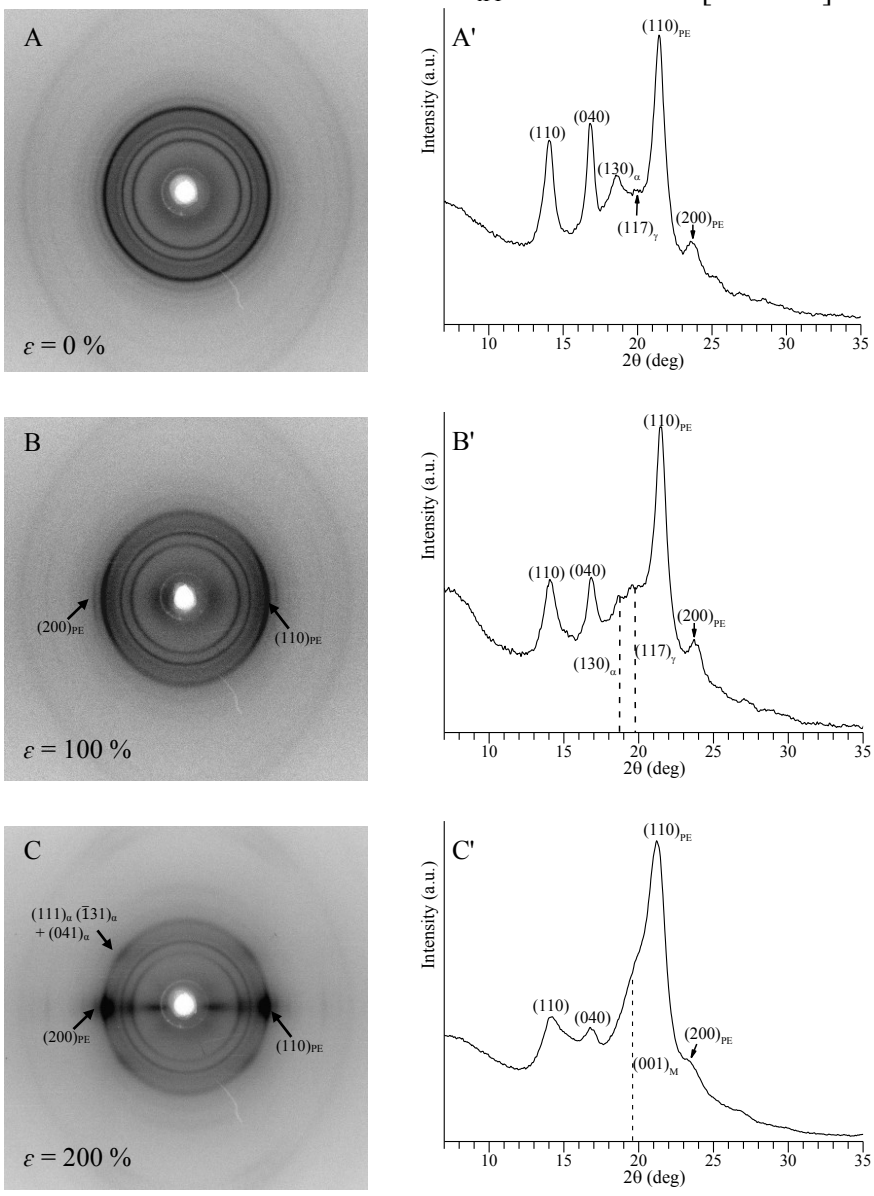

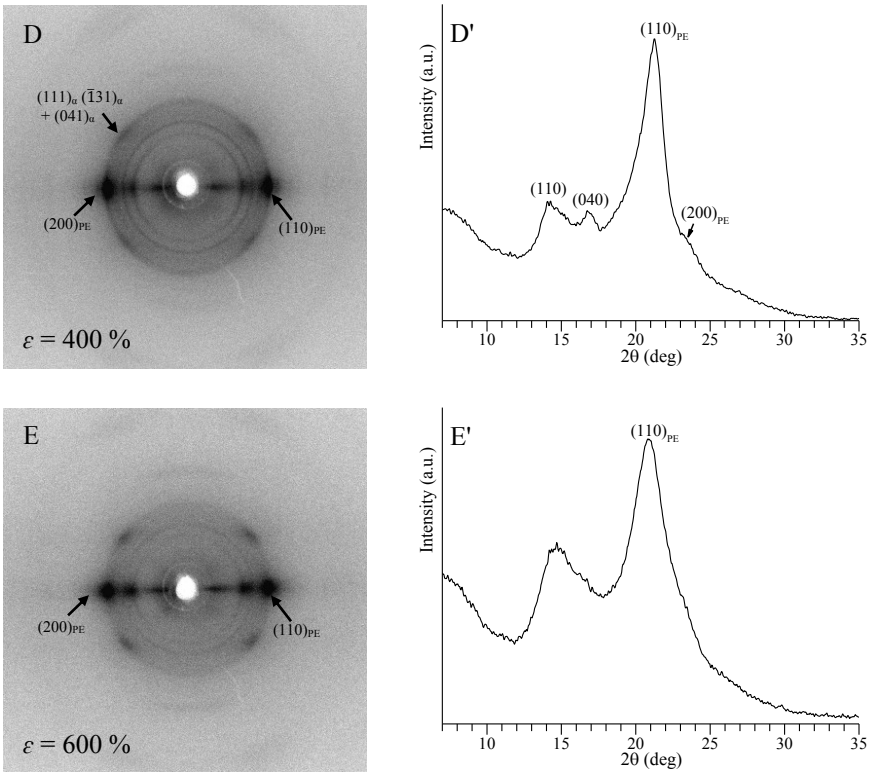

Figure 3.37. X-ray fiber diffraction patterns (A-E), and corresponding equatorial profiles (A'- E'), of the sample JME-V-148 unoriented (A) and of oriented fibers obtained by stretching at room-temperature compression molded films at values of strain ε of 100% (B), 200% (C) , 400% (D) and 600% (E).

iPP-*b*-LLDPE JME-IV-149 with w_{iPP} = 47 wt% and [1-octene] = 1.9%

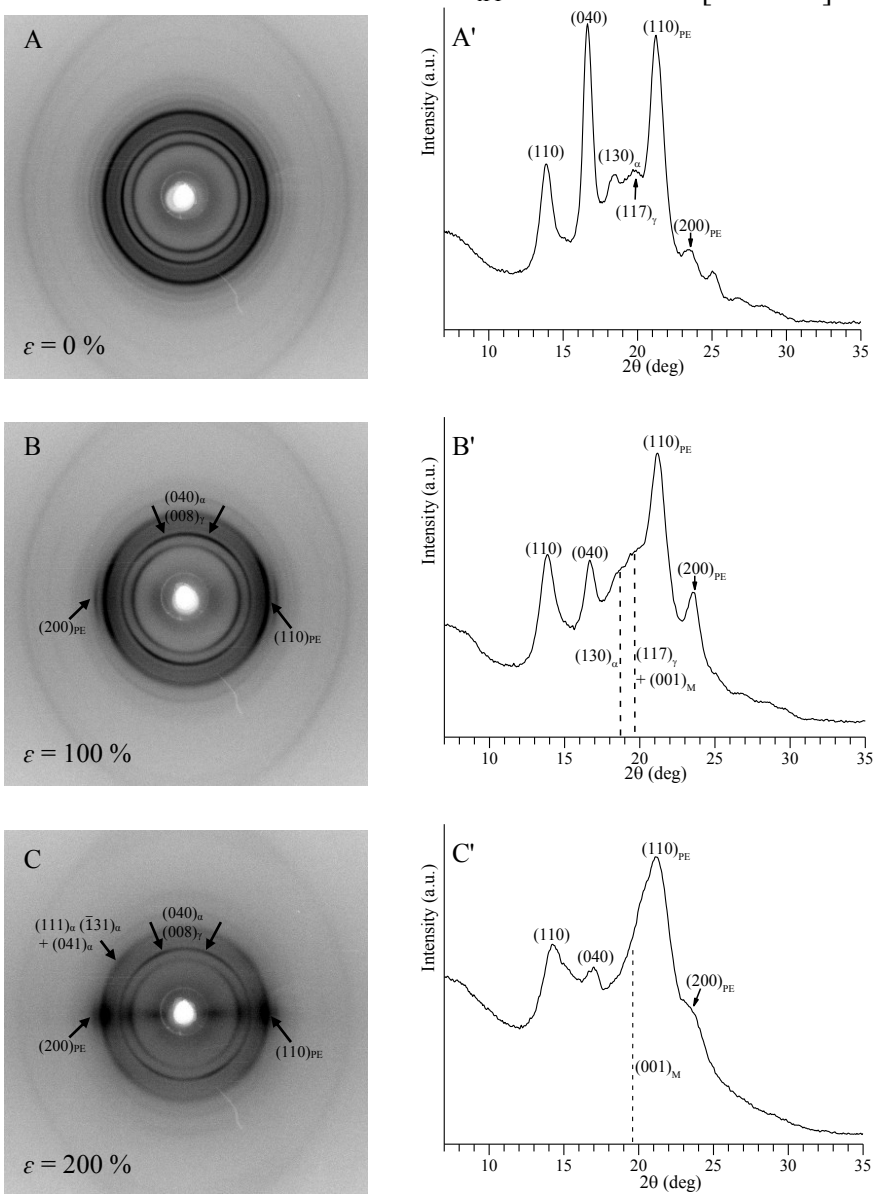

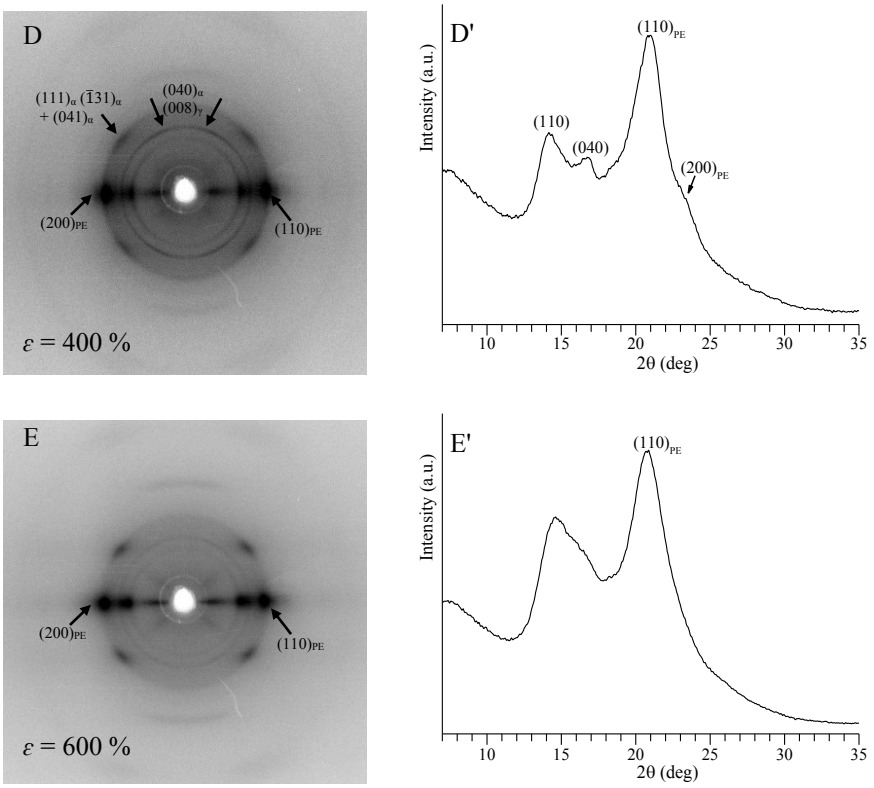

Figure 3.38. X-ray fiber diffraction patterns (A-E), and corresponding equatorial profiles (A'- E'), of the sample JME-V-149 unoriented (A) and of oriented fibers obtained by stretching at room-temperature compression molded films at values of strain ε of 100% (B), 200% (C) , 400% (D) and 600% (E).

A different structural behavior of the isotactic polypropylene and polyethylene phases were found during stretching of the iPP-*b*-PE samples (paragraph 3.3.4). As already discuss, for both iPP-*b*-PE and iPP-*b*-LLDPE copolymers the iPP block crystallizes in a mixture of α and γ forms, and the formation of the cross-*β* structures at low value of deformation (100%) is observed. However, at 200% of deformation most of the iPP crystals are in the mesomorphic form when the iPP is linked to the PE block ("hard segment"). Instead, when iPP domains are covalently linked to the LLDPE block ("soft segment"), iPP crystals in α/γ modifications are present up to 400% of deformations and only at high draw ratios (600%) transform in the mesophase. Since the iPP is the same in the two class of BCPs, this different behavior of the iPP, can be related to the different behavior of the polyethylene phase. Indeed, in the iPP-*b*-PE copolymers, no structural transitions of the PE block are observed by stretching, and only an orientation of the PE crystals in orthorhombic form is observed. In the iPP-*b*-LLDPE copolymers, the orthorhombic form of the LLDPE block transforms in the unstable monoclinic form at low deformation (100%), which transforms in the orthorhombic form at higher deformation. At high draw ratio, orthorhombic and hexagonal structures coexist. These structural phase transitions of the polyethylene phase in the iPP-*b*-LLDPE samples are more easier than the development of the mesomorphic form of the iPP. Moreover, as discuss in the paragraphs 3.3.3 and 3.4.3, both BCPs show high value of deformation at break. In the iPP-*b*-PE samples the formation of the mesomorphic form of iPP at already low deformations (200%) facilitates the further successive deformation up to very high values of the strain. Whereas, the high ductility of the iPP-*b*-LLDPE copolymer can be attributable at the structural transformations of the LLDPE block which occur at values of the deformation lower than that at which the mesomorphic form of the iPP block develops.

Furthermore, the higher values of the strain at break evaluated in both BCPs, compared to the corresponding iPP homopolymer, are due to the occurrence of these transformations that produces an effective mechanism able to gradually dissipate some amount of mechanical energy and produces a neat increase of the values of the strain at break.

3.4.5 Morphology of bulk crystallized samples.

Polarized optical microscopy (POM) images of samples of iPP-*b*-LLDPE crystallized from the melt at cooling rate of 10 °C/min and 2.5 °C/min are shown in Figures 3.39-3.42.

The POM images of the sample JME-V-54 with 77wt% of iPP block crystallized from the melt at 10°C/min (Figure 3.39A and B) reveal the presence of bundle-like entities typical of iPP crystals in a disordered modification intermediate between α and γ forms. The same crystalline supermolecular structure is observed, indeed, also for the iPP homopolymer (Figure 3.22 A) confirming that this morphology is given mainly by the iPP block in the iPP-*b*-LLDPE copolymer.

The shape of the crystalline entities does not change in the block copolymers JME-IV-133 and JME-IV-148 with similar block lengths (and 48 and 45 wt% of iPP, respectively) but smaller crystalline entities are observed (Figures 3.40-3.42).

Furthermore, in the sample JME-IV-133, the presence of same banded spherulites, due probably to the polyethylene phase, are also evident (Figure 3.40C).

As discuss in the paragraph 3.4.2, the structural analysis performed by cooling from the melt at 10°C/min on the iPP-*b*-LLDPE copolymers (Figures 3.28-3.31) has revealed that the iPP block crystallizes at temperatures higher than that of the LLDPE block. This is in agreement with the morphology of these samples that show feature typical of the polypropylene phase, rather than of the polyethylene phase. However, in the sample JME-IV-133 the two block crystallizes almost simultaneously (Figure 3.29A). Therefore, the presence of some banded spherulites in the POM images of Figure 3.40C may indicate that in some regions the crystallization of the LLDPE block determines the final morphology.

The copolymer JME-IV-149 with 47 wt% of iPP presents bundle-like entities with size similar to the sample JME-V-54 (Figure 3.42). In both BCPs, the crystallization of the iPP block is almost completed before the occurrence of the LLDPE crystallization. (Figures 3.28A and 3.31A). This can be probably due on one hand, to the highest weight fraction of iPP (77%) in the sample JME-V-54 and on the other hand, to the highest content of 1-octene (1.9%) in the sample JME-IV-149 which slows down the crystallization of the LLDPE block respect to the iPP crystallization.

Similar morphologies have been observed in all iPP-LLDPE samples, crystallized from the melt at 2.5 °C/min. The shape and the dimensions of the crystalline do not change, but in the case of the samples JME-IV-133 larger regions with banded spherulites of LLDPE, are obtained (Figure 3.40F and G). Moreover, also the images of the sample JME-IV-148 (Figure 3.41E, F) show the presence of banded spherulites typical of the PE [33, 34]. This suggests that at lower cooling rate probably the LLDPE block crystallizes at higher temperatures, more similar to that of the iPP block, determining the final morphology.

In conclusion, the iPP-LLDPE samples present morphologies similar to those observed in the iPP-PE samples (Figures 3.22-3.24). However, in the iPP-*b*-PE copolymers PE domains crystallize from the melt before the iPP domains and well defined banded spherulites with average diameter between 10-20 μm have been observed (Figure 3.24).

iPP-*b*-LLDPE JME-V-54 with w_{iPP} = 77 wt% and [1-octene] = 1.5%

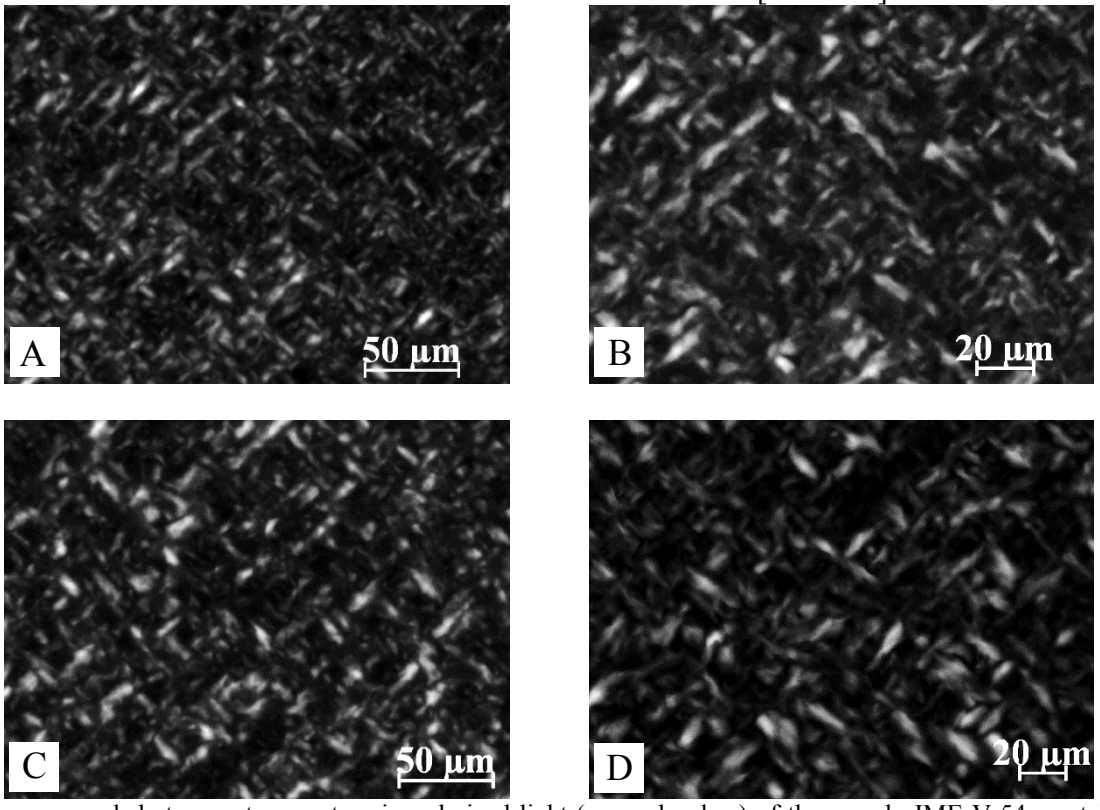

Figure 3.39. POM images recorded at room temperature in polarized light (crossed polars) of the sample JME-V-54 crystallized from the melt at cooling rate of 10 °C/min (A,B) and at 2.5°C/min (C,D) to room temperature. The thickness of the films is ≈ 100 µm.

iPP-*b*-LLDPE JME-IV-133 with w_{iPP} = 48 wt% and [1-octene] = 0.9%

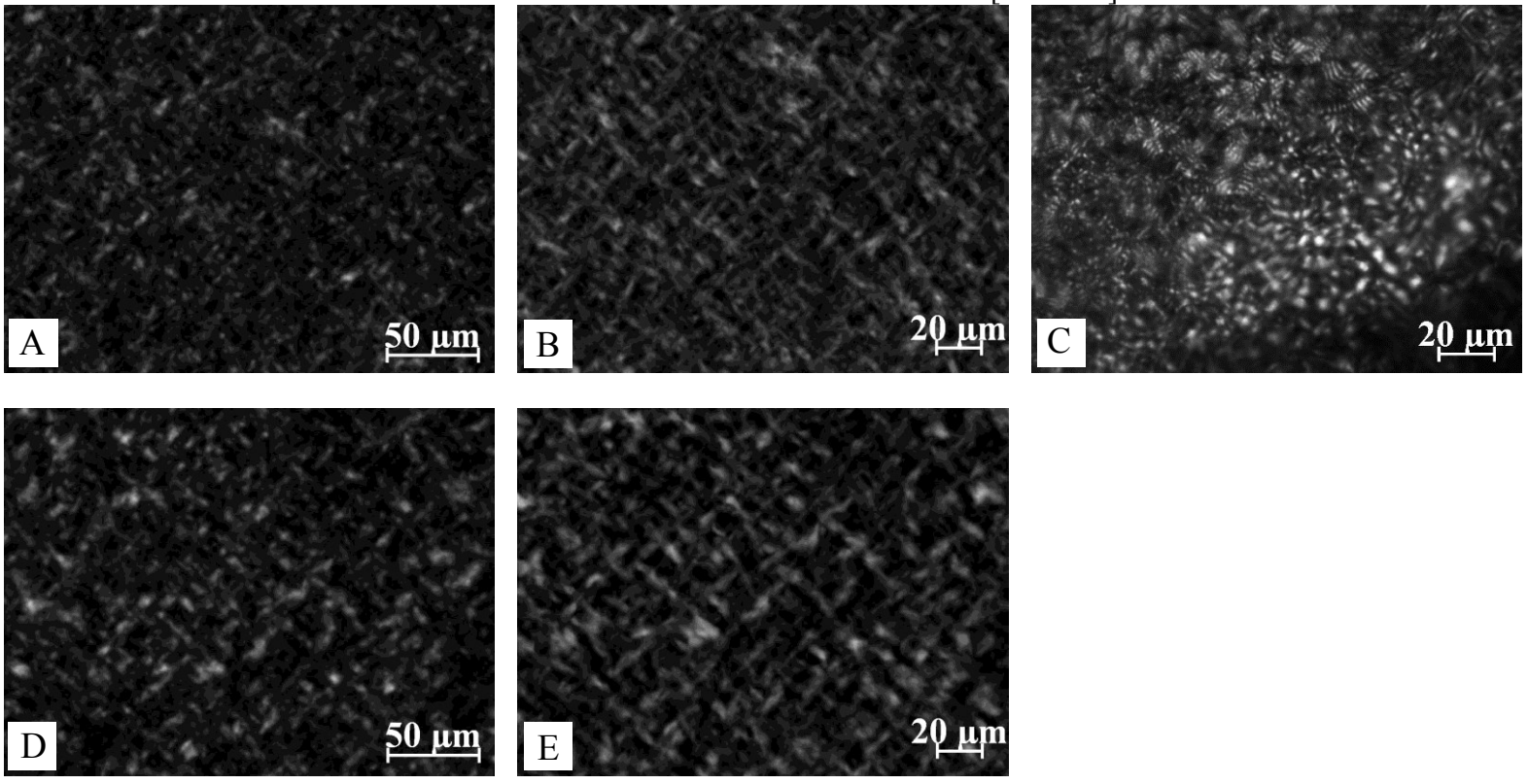

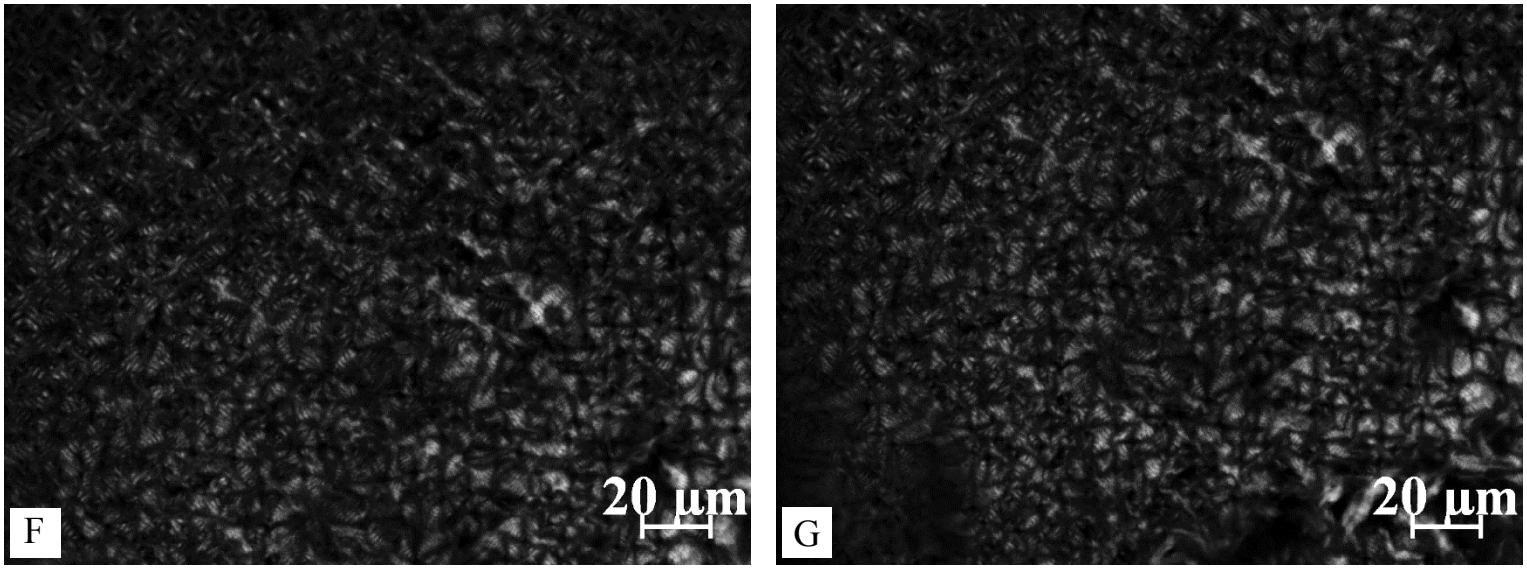

Figure 3.40. POM images recorded at room temperature in polarized light (crossed polars) of the sample JME-IV-133 crystallized from the melt at cooling rate of 10 °C/min (A-C) and at 2.5°C/min (D-G) to room temperature. The thickness of the films is ≈ 100 µm.

iPP-*b*-LLDPE JME-IV-148 with w_{iPP} = 45 wt% and [1-octene] = 1.5%

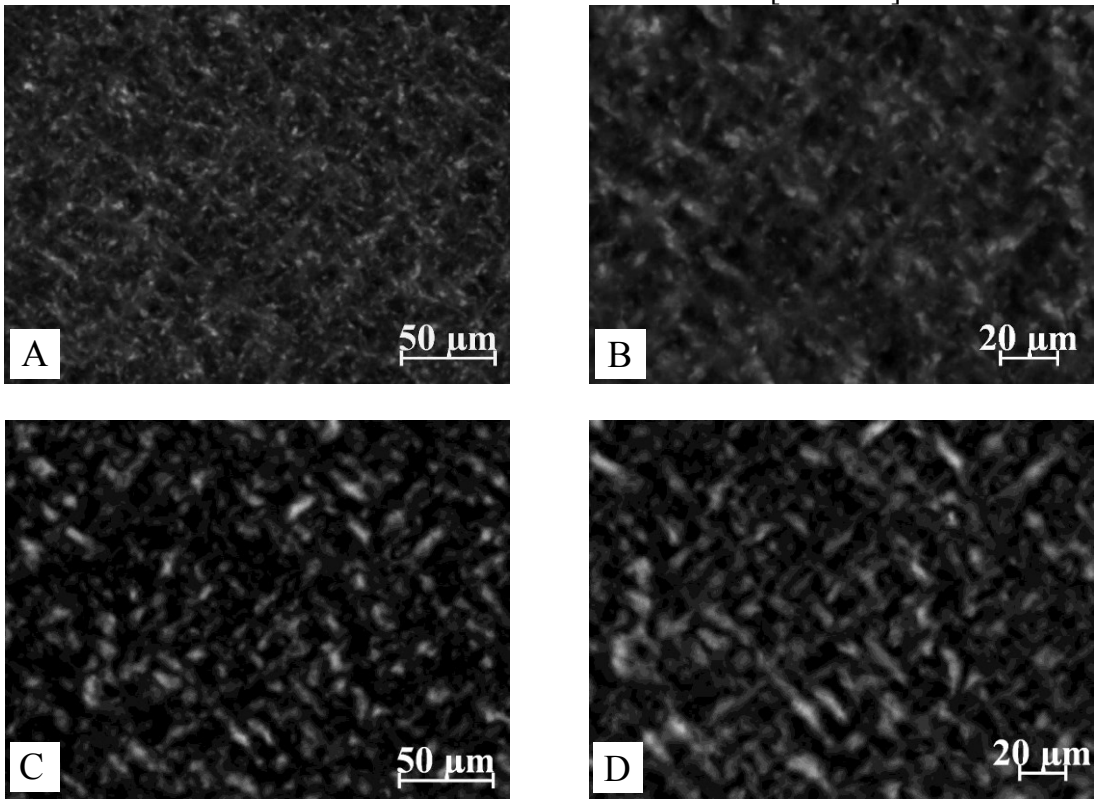

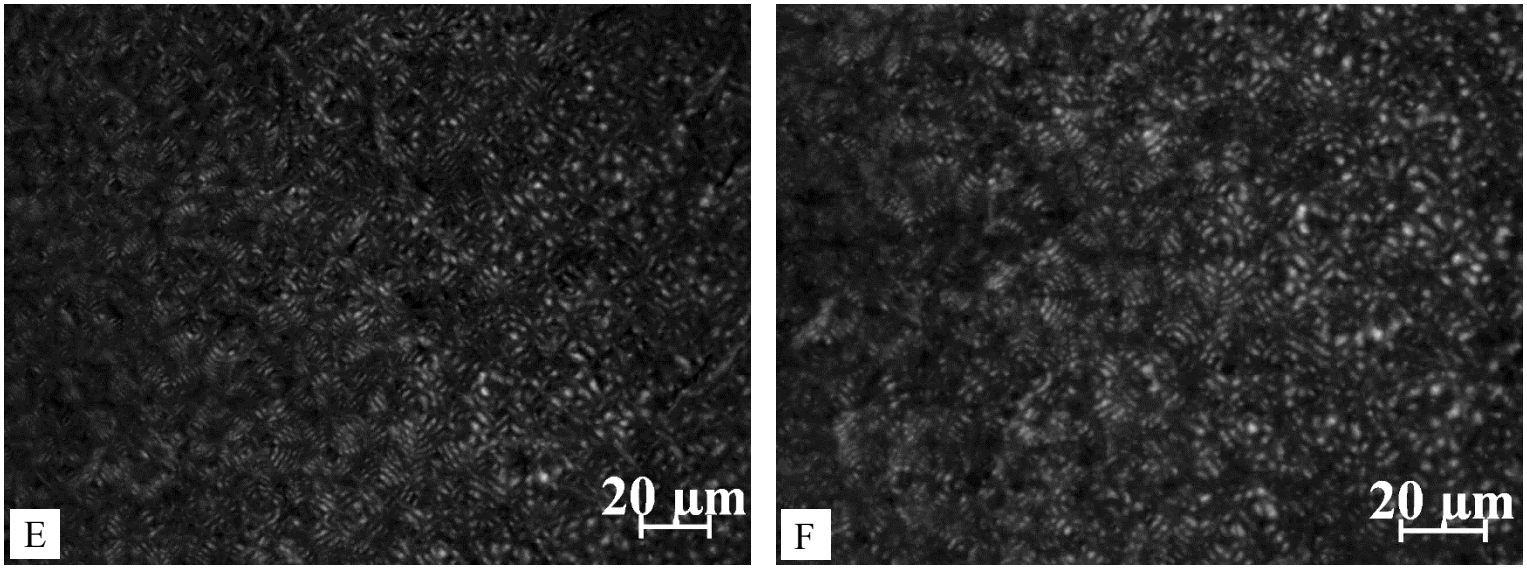

Figure 3.41. POM images recorded at room temperature in polarized light (crossed polars) of the sample JME-IV-148 crystallized from the melt at cooling rate of 10 °C/min (A,B) and at 2.5°C/min (C-F) to room temperature. The thickness of the films is ≈ 100 µm.

iPP-*b*-LLDPE JME-IV-149 with w_{iPP} = 47 wt% and [1-octene] = 1.9%

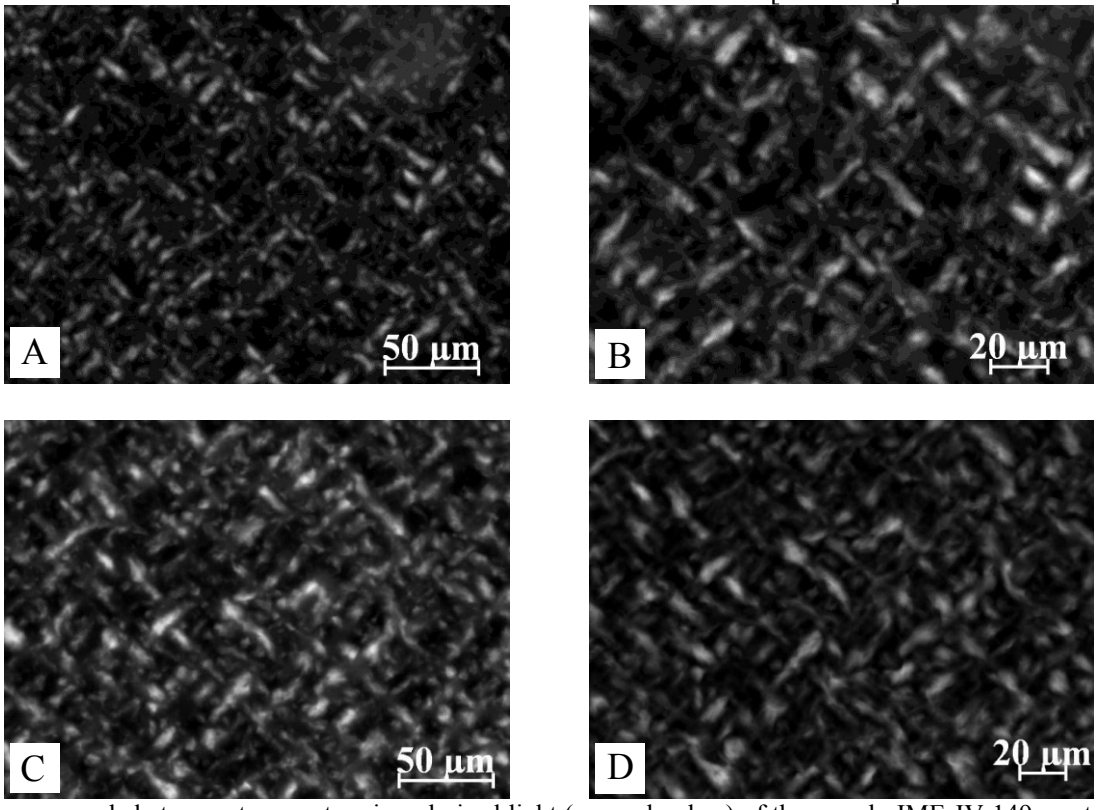

Figure 3.42. POM images recorded at room temperature in polarized light (crossed polars) of the sample JME-IV-149 crystallized from the melt at cooling rate of 10 °C/min (A,B) and at 2.5°C/min (C,D) to room temperature. The thickness of the films is ≈ 100 µm.

3.5 Conclusions

The structure, the morphology and the physical properties of crystalline-crystalline iPP-PE and iPP-LLDPE block copolymers, synthesized by living polymerization with an Hf-based post-metallocene catalyst and characterized by different block lengths have been investigated.

The DSC thermograms of all iPP-*b*-PE samples show only one broad peak (≈ 130°C) in the heating curves, due to the overlapping of PE and iPP melting. The crystallization temperatures increase with increasing the PE block length. These data suggest that PE crystallizes first and the crystallization of the block copolymers is driven by the nucleation effect of PE on the crystallization of iPP block.

In the case of iPP-*b*-LLDPE samples, the presence of the comonomer (1-octene) reduces the melting temperature of the LLDPE block that results lower than that of the iPP block and two separated melting peaks are present in the DSC heating curves of these copolymers. The crystallization temperatures are lower than that of the iPP-*b*-PE copolymers and of the iPP homopolymer and decrease with increasing 1-octene content.

Simultaneous time and temperature-resolved wide and small angle X-ray scattering (WAXS and SAXS) experiments performed with synchrotron radiation at ESRF in Grenoble have clarified the melting and crystallization behavior of iPP-*b*-PE and iPP-*b*-LLDPE copolymers. In the case of iPP-*b*-PE samples, the two blocks melt and crystallize at slightly different temperature. Crystal of PE starts melting at temperature lower than that of crystals of iPP. Instead, during cooling from the melt PE crystallizes first.

The structural analysis performed during cooling and heating of iPP-*b*-LLDPE samples have demonstrated that the presence of the comonomer (1-octene) in the polyethylene phase does not disturb the melting and crystallization of the iPP block, which melts at temperature higher than 130°C and crystallizes at ≈ 100 °C in all block copolymers. Instead, the

melting and the crystallization of the LLDPE block occurs at temperature lower than that of the iPP block. Moreover, a decrease of both melting and crystallization temperatures of polyethylene domain with increasing 1-octene content are observed.

SAXS data of both iPP-PE and iPP-LLDPE crystalline-crystalline block copolymers have shown that upon cooling, microphase separation is driven by crystallization and the obtained nanostructure most probably consists of alternating crystalline PE (or LLDPE) and iPP domains separated by amorphous regions. In the case of the iPP-*b*-PE samples lamellar periodicities of ≈ 30 and 12 nm for crystalline PE and iPP layers, respectively, have been evaluated. For the iPP-*b*-LLDPE samples, the 1-octene induces a decrease of the periodicity of PE lamellar stacks and similar lamellar periodicities of the two blocks, of ≈ 17 and 14 nm for PE and iPP domains, respectively, have been estimated.

All copolymers samples show great enhancement of ductility and mechanical strength as compared to that observed for the corresponding iPP homopolymer and in the case of the iPP-*b*-PE samples, also to that of the PE homopolymer, but with important differences in the values of elastic modulus, yield stress, and elastic properties. The different mechanical behavior is related to the different polyethylene block that is covalently linked to the polypropylene block.

Samples of iPP-*b*-PE, in which the iPP block is linked to the PE block ("hard segment"), show values of the elastic modulus and of the strain at the yield point higher than those observed in the corresponding iPP and PE homopolymers and in the iPP-*b*-LLDPE samples in which the iPP block is linked to the LLDPE block ("soft segment").

The iPP-*b*-LLDPE copolymers show an improvement of the elastic properties, according with the lower values of the tension set and the higher

values of the elastic recovery after breaking compared to those of the iPP-*b*-PE copolymers.

A study of the stress induces phase transition of the iPP-*b*-PE samples, have demonstrated that a general orientation of both crystalline blocks occur and in particular, at high deformations the iPP block is in mesomorphic form. However, crystals of iPP in α/γ disordered modifications transform in the mesomorphic form through the formation, at low value of the strain (200%), of the cross-*β* structures. Therefore, crystalline lamellae are oriented with chain axes nearly perpendicular to the stretching direction. Crystals of α-form transform in the mesomorphic form more easily than the crystals of γ-form. At high draw ratios, the crystals tend to assume orientations with chain axes parallel to fiber axes, as in the standard fiber morphology, and are in mesomorphic form.

In the case of iPP-*b*-LLDPE samples, the iPP block transforms in the mesomorphic form, through the formation of the cross-*β* structures, only at values of deformation higher than 400 %. Therefore, at values of deformation higher than those observed in the iPP-*b*-PE samples (200 %). This different behavior of the iPP block in the two classes of BCPs, can be related to the different behavior of the polyethylene phase. Indeed, in the iPP-*b*-PE copolymers, no structural transitions of the PE block are observed by stretching, and only an orientation of the PE crystals in orthorhombic form is observed. In the iPP-*b*-LLDPE copolymers, the orthorhombic form of the LLDPE block transforms in the unstable monoclinic form at low deformation (100%), which transforms in the orthorhombic form at higher deformation. At high draw ratio, orthorhombic and hexagonal structures coexist.

X-ray fiber diffraction patterns highlight the fundamental role played by the stress-induced transformations on the deformability and ductility behavior of these materials. In the iPP-*b*-PE samples the formation of the

mesomorphic form of iPP at low deformations facilitates the further successive deformation up to very high values of the strain. Instead, the high ductility of the iPP-*b*-LLDPE samples can be attributable at the structural transformations of the LLDPE block, which occur at values of the deformation lower than that at which the mesomorphic form of the iPP block develops. Furthermore, the higher values of the strain at break evaluated in both BCPs, compared to the corresponding iPP homopolymer, are due to the occurrence of these transformations that produces an effective mechanism able to gradually dissipate some amount of mechanical energy and produces a neat increase of the values of the strain at break.

POM images of iPP-PE and iPP-LLDPE crystalline-crystalline block copolymers confirm that crystallization dominates the morphology, and superstructures like spherulites or bundle-like entities are observed.

The main interest of these new materials is a possible application as phase compatibilizers of PE and iPP which are the two of the most common polymers being produced. [21] Since polyethylene and polypropylene are immiscible with one another and therefore common grades of PE and iPP do not adhere or blend, creating challenges for recycling these materials.

Recently it has been reported that iPP-PE BCPs [21] are very effective in strengthening the interface between iPP and PE and therefore can be used as additives in small amounts to blend PE and iPP since they can create molecular stitches between the two phases and make the resulting blend as tough as iPP and PE themselves. These compatibilizers open opportunities for upcycling recovered PE/iPP into equal or higher value materials with lower sorting costs.

Bibliography Chapter 3

[1] (a). F. S. Bates, G. H. Fredrickson, *Annu. Rev. Phys. Chem*. **1990**, *41*, 525. (b) L. Leibler, *Macromolecules* **1980**, *13*, 1602. (c) B. D. Olsen, X. Li, J. Wang, R. A. Segalman, *Macromolecules* **2007**, *40*, 3287. (d) W. van Zoelen, G. ten Brinke, *Soft Matter* **2009**, *5*, 1568. (e) M. Park, C. Harrison, P. M. Chaikin, R. A. Register, D. H. Adamson, *Science* **1997**, *276*, 1401.

[2] G. W. Coates, P. D. Hustad, S. Reinartz *Angew. Chem*. Int. Ed. **2002**, *41*, 2236. (b) G. J. Domski, J. M. Rose, G. W. Coates, A. D. Bolig, M. Brookhart *Prog. Polym. Sci.* **2007**, *32*, 30.

[3] J. Tian, P. D. Hustad, G. W. Coates *J. Am. Chem. Soc.* **2001**, *123*, 5134.

[4] A. F. Mason, G. W. Coates *J. Am. Chem. Soc* **2004**, *126*, 16326.

[5] A. E. Cherian, J. M. Rose , E. B. Lobkovsky , G. W. Coates *J. Am. Chem. Soc* **2005**, *127*, 13770.

[6] (a) V. Busico, R. Cipullo, N. Friederichs, S. Ronca, M. Togrou *Macromolecules* **2003**, *36*, 3806. (b) V. Busico, R. Cipullo, N. Friederichs, S. Ronca, G. Talarico, M. Togrou, B. Wang *Macromolecules* **2004**, *37*, 8201.

[7] G. W. Coates. PCT Int. Appl. WO2008/112133.

[8] (a) I. W. Hamley, "The Physics of Block Copolymers", *Oxford University Press*: Oxford, **2003**; (b) I. W. Hamley "Development in Block Copolymer Science and Technology" *John Wiley & Sons*. *Chichester*, **2005**.

[9] I. W. Hamley *Adv. Polym. Sci*. **1999**, *148*, 113.

[10] Y. L. Loo, R. A. Register, Crystallization Within Block Copolymer Mesophases. In: Development in Block Copolymer Science and Technology, ed. by I. W. Hamley, *John Wiley & Sons, Ltd.; Chichester*, **2004**, 213.

[11] A. J. Muller, V. Balsamo, M. L. Arnal *Adv. Polym. Sci*. **2005**, *190*, 1.

[12] A. J. Muller, M. L. Arnal, V. Balsamo *Lect. Notes Phys*. **2007**, *714*, 229.

[13] (a) R. Perret, A. Skoulios *Die Makromol. Chem*. **1972**, *156*, 143. (b) R. Perret, A. Skoulios *Die Makromol. Chem.* **1972** *156*, 291.

[14] H. Younes, D. J. Cohn *Biomed. Mater. Res*. **1987**, *21*, 1301.

[15] S. Nojima, M. Ono, T. Ashida *Polym. J.* **1992**, *24*, 1271.

[16] L. Sun, Y. Liu, L. Zhu, B. S. Hsiao, C. A. Avila-Orta *Polymer* **2004**, *45*, 8181.

[17] R. V. Castillo, A. J. Muller, M. C. Lin, H. L. Chen, U. S. Jeng, M. A. Hillmyer *Macromolecules* **2008**, *41*, 6154.

[18] S. B. Myers, R. A. Register, *Macromolecules* **2008**, *41*, 6773.

[19] C. De Rosa, R. Di Girolamo, F. Auriemma, M. D'Avino, G. Talarico, C. Cioce, M. Scoti, G. W. Coates, B. Lotz, *Macromolecules* **2016**, *49*, 5576.

[20] (a) R. Seguela, J. Prud'homme *Polymer* **1989**, *30*, 1446. (b) P. Rangarajan, R. A. Register, L. J. Fetters *Macromolecules* **1993**, *26*, 4640. (c) P. Rangarajan, R. A. Register, D. H. Adamson, L. J. Fetters, W. Bras, S. Naylor, A. J. Ryan *Macromolecules* **1995**, *28*, 1428. (d) P. Rangarajan, R. A. Register, L. J. Fetters, W. Bras, S. Naylor, A. J. Ryan, *Macromolecules* **1995**, *28*, 4932. (e) I. W. Hamley, J. P. A. Fairclough, F. S. Bates, A. J. Ryan *Polymer* **1998**, *39*, 1429. (d) D. J. Quiram, R. A. Register, G. R. Marchand, A. J. Ryan, *Macromolecules* **1997**, *30*, 8338. (e) V. Balsamo, F. von Gyldenfeldt, R. Stadler *Macromol. Chem. Phys.* **1996**, *197*, 3317.

[21] J. M. Eagan, J. Xu, R. Di Girolamo ,C. M. Thumber, C. W. Macoscko, A. M. LaPointe, F. S. Bates, Geoffrey W. Coates *Science* **2017,** 355, 814.

[22] G. Natta, P. Corradini *Nuovo Cimento Suppl*. **1960**, *15*, 40.

[23] F. Auriemma, C. De Rosa *Macromolecules* **2006**, *39*, 7635.

[24] C. De Rosa, F. Auriemma, *Crystals and Crystallinity in Polymers*; Wiley: Hoboken, NJ, **2014**.

[25] S. Brückner, S. V. Meille *Nature* **1989**, *340,* 455.

[26] F. Auriemma, C. De Rosa, T. Boscato, P. Corradini *Macromolecules* **2001**, *34*, 4815.

[27] F. Auriemma, C. De Rosa *Macromolecules* **2002**, *35*, 9057.

[28] Kimberly, A.; Chaffin, Frank S. Bates, Patrick Brant, Gary M. Brown *J. Polym. Sci., Part B* **2000**, *38*, 108.

[29] C. De Rosa, F. Auriemma, G. De Lucia, L. Resconi, *Polymer* **2005**, *46*, 9461.

[30] C. De Rosa, F. Auriemma, C. Perretta *Macromolecules* **2004**, *37*, 6843.

[31] Y. Men, G. Strobl *J. Macromol. Sci., Phys*. **2001**, *B40*, 775.

[32] C. De Rosa, F. Auriemma, R. Di Girolamo, O. Ruiz de Ballesteros, M. Pepe, O. Tarallo, A. Malafronte, *Macromolecules* **2013**, *46*, 5202.

[33] P. H. Geil, *Polymer Single Crystals*. John Wiley and Sons Inc., NewYork, **1963**. U. W. Gedde, *Polymer Physics*. Chapman & Hall, London, **1995**.

[34] (a) H. D. Keith, F. J. Padden, *Appl. Phys.* **1963**, *34*, 2409. (b) H. D. Keith, F. J. Padden, *J. Polym. Sci.* **1959**, *39*, 101.

[35] P. Corradini, V. Petraccone, C. De Rosa, G. Guerra, *Macromolecules* **1986**, *19*, 2699.

[36] O. Ruiz de Ballesteros, F. Auriemma, G. Guerra, P. Corradini *Macromolecules* **1996**, *29*, 7141.

[37] C. W. Bunn, *Trans. Faraday Soc.* **1939**, *35*, 482.

[38] T. Seto, T. Hara, K. Tanaka *Jpn. J. Appl. Phys.* **1968**, *7*, 31.

[39] F. C. Frank, A. Keller, A. O' Connor *Phil. Mag.* **1958**, *8*, 64.